Universiteit Antwerpen
Belgium

Beni-Suef University
Faculty of Science, Egypt

Search for Magnetic Monopoles with the CMS experiment at the Large Hadron Collider (LHC)

By

Mai Muhammed Hassan El Sawy
Assistant lecturer
Basic Science Department – Faculty of Engineering
The British University in Egypt (BUE)

A dissertation submitted to Beni-Suef University in Egypt and Antwerp University in Belgium in accordance with the requirements of the **bi-doctoral agreement (double degree)**
PhD in Physics , Beni-Suef University,
Doctor in de Wetenschappen: Fysica, **Universiteit Antwerpen**

Supervised by

Prof. Dr. Hany Saleh Hamdy
Professor of Atomic Physics
Department of Physics
Faculty of Science
Beni-Suef University
Egypt

Prof. Dr. Albert De Roeck
Professor of Particle Physics
Physics group, Faculty of Science
Antwerp University-Belgium
Staff member at CERN

Prof. Dr. Ali M. Khalaf
Professor of Theoretical Physics
Department of Physics
Faculty of Science
Al Azhar University
Egypt

2019

CERN-THESIS-2020-191

List Of Publications

1. "Magnetic monopole search with the full MoEDAL trapping detector in 13TeVpp collisions interpreted in photon-fusion and Drell-Yan production". *MoEDAL Collaboration, Phys.Rev.Lett. 123 (2019) no.2, 021802, arXiv:1903.08491 [hep-ex].*

2. "Searching for long-lived particles beyond the Standard Model at the Large Hadron Collider". *Submitted on 11 March 2019 to J. Physics G., arXiv:1903.04497 [hep-ex].*

3. "The CMS Trigger System". *CMS Collaboration, JINST 12 (2017) P01020, arXiv:1609.02366[hep-ex].*

4. "Measurements of the t-tbar production cross section in lepton+jets final states in pp collisions at 8 TeV and ratio of 8 to 7 TeV cross sections". *CMS Collaboration, Eur.Phys.J.C 77 (2017) 15, arXiv:1602.09024 [hep-ex].*

5. "Search for direct pair production of supersymmetric top quarks decaying to all-hadronic final states in pp collisions at $\sqrt{s} = 8\,TeV$". *CMS Collaboration, Eur.Phys.J.C 76 (2016) 460, arXiv:1603.00765 [hep-ex].*

6. "Search for supersymmetry in events with soft leptons, low jet multiplicity, and missing transverse energy in proton-proton collisions at $\sqrt{s} = 8\,TeV$". *CMS Collaboration, Phys.Lett.B 759 (2016)9 - 35, arXiv:1512.08002 [hep-ex].*

7. "Measurement of spin correlations in t-tbar production using the matrix element method in the muon+jets final state in pp collisions at $\sqrt{s} = 8\,TeV$". *CMS Collaboration, Phys.Lett.B 758(2016)321 - 346, arXiv:1511.06170 [hepex].*

8. "Search for anomalous single top quark production in association with a photon in pp collisions at $\sqrt{s} = 8\,TeV$". *CMS Collaboration, JHEP 04 (2016) 035, arXiv:1511.03951 [hep-ex].*

9. ”Reconstruction and identification of tau lepton decays to hadrons and tau neutrino at CMS”. *CMS Collaboration, JINST 11 (2016) P01019, arXiv:1510.07488 [hep-ex].*

10. ”Measurement of top quark polarisation in t-channel single top quark production”. *CMS Collaboration, JHEP 04 (2016) 073, arXiv:1511.02138 [hep-ex].*

11. ”Search for a light charged Higgs boson decaying to c s-bar in pp collisions at $\sqrt{(}s) = 8\,TeV$”. *CMS Collaboration, JHEP 12(2015) 178, arXiv:1510.04252[hep-ex].*

12. ”Transverse momentum spectra of b jets in p-Pb collisions at $\sqrt{(}s[NN]) = 5.02 TeV$”. *CMS Collaboration, Phys.Lett.B 754 (2016)59, arXiv:1510.03373 [hep-ex].*

13. ”Measurement of t t-bar production with additional jet activity, including b quark jets, in the dilepton channel using pp collisions at $\sqrt{(}s) = 8\,TeV$”. *CMS Collaboration, Eur.Phys.J.C 76 (2016) 379, arXiv:1510.03072 [hep-ex].*

14. ”Searches for a heavy scalar boson H decaying to a pair of 125 GeV Higgs bosons hh or for a heavy pseudoscalar boson A decaying to Zh, in the final states with h to tau tau”. *CMS Collaboration, Phys.Lett.B 755 (2016) 217, arXiv:1510.01181 [hep-ex].*

15. ”Measurement of transverse momentum relative to dijet systems in PbPb and pp collisions at $\sqrt{(}s[NN]) = 2.76\,TeV$”. *CMS Collaboration, JHEP 01 (2016) 006, arXiv:1509.09029 [hep-ex].*

16. ”Measurement of the differential cross sections for top quark pair production as a function of kinematic event variables in pp collisions at $\sqrt{s} = 7$ and $8\,TeV$”. *CMS Collaboration, Phys.Rev.D 94 (2016) 052006, arXiv:1607.00837 [hep-ex].*

17. ”Search for the associated production of a Higgs boson with a single top quark in proton-proton collisions at $\sqrt{(}s) = 8\,TeV$”. *CMS Collaboration, JHEP 06 (2016) 177, arXiv:1509.08159 [hep-ex].*

18. ”Measurement of the t t-bar production cross section in the all-jets final state in pp collisions at $\sqrt{(}s) = 8\,TeV$”. *CMS Collaboration, Eur.Phys.J.C 76 (2016) 128, arXiv:1509.06076 [hep-ex].*

19. ”Search for vector-like charge 2/3 T quarks in proton-proton collisions at $\sqrt{(}s) = 8\,TeV$”. *CMS Collaboration, Phys.Rev.D 93(2016)012003, arXiv:1509.04177 [hep-ex].*

20. ”Study of B meson production in p-Pb collisions at $\sqrt{(}s_N N) = 5.02\,TeV$ using exclusive hadronic decays ”. *CMS Collaboration, Phys. Rev Lett.116 (2016) 032301, arXiv:1508.06678 [hep-ex].*

21. ”Angular analysis of the decay $B^0 \to K^{*0}\mu^+\mu^-$ from pp collisions at $\sqrt{s} = 8\,TeV$”. *CMS Collaboration, Phys.Lett.B 753 (2016)424, arXiv:1507.08126 [hep-ex].*

22. ”Measurement of the CP-violating weak phase phi[s] and the decay width difference $\Delta\Gamma_{[}s]$ using the B_s^0 to $J/\Psi\phi(1020)$ decay channel in pp collisions at $\sqrt{(}s) = 8\,TeV$”. *CMS Collaboration, Phys.Lett.B 757(2016)97 - 120, arXiv:1507.07527 [hep-ex].*

23. ”Pseudorapidity distribution of charged hadrons in proton-proton collisions at $\sqrt{(}s) = 13\,TeV$”. *CMS Collaboration, Phys.Lett.B751(2015)143 - 163 , arXiv:1507.05915 [hep-ex].*

Declaration

I declare that the work in this dissertation was carried out in accordance with the requirements of the University's Regulations and Code of Practice for Research Degree Programmes and that it has not been submitted for any other academic award. Except where indicated by specific reference in the text, the work is the candidate's own work. Work done in collaboration with, or with the assistance of, others, is indicated as such. Any views expressed in the dissertation are those of the author.

Author signature ..... **Data** .....

© 2019 Mai El Sawy
All rights reserved. No parts of this book may be reproduced or transmitted in any form or by any means, electronic, mechanical, photocopying, recording, or otherwise, without the prior written permission of the author.

ABSTRACT

Title: **Search for Magnetic Monopoles with the CMS experiment at the Large Hadron Collider (LHC)**

By: **Mai Muhammed Hassan Abdel Maguid El Sawy**

A search for magnetic monopoles as an exotic long-lived particle, using a signature of a highly ionizing particle that deposits mostly of its energy in the Electromagnetic Calorimeter (ECAL) crystals, was performed with the CMS detector at the LHC using 33 fb^{-1} of 13 TeV proton-proton collision data. Monopole candidates were selected by reconstructing the trajectory of a highly ionizing particle in the tracking chamber, by the expected specific shower shape in the ECAL crystals. No evidence for magnetic monopole event is observed. We set a 95% confidence level upper limit of $23.9 - 14.7\,fb$ on the cross-section of Dirac magnetic monopole's production, with mass between 500 GeV and 3000 GeV.In addition, another search for magnetic monopoles, has been performed with the MoEDAL experiment at the LHC and it is also mentioned. In particular, the results of the analysis of the data from the Magnetic Monopole Trapper with a precision SQUID magnet are discussed.

Keyword: magnetic, monopole, quantization, Dirac, LHC, CMS

To my little cupcake and my ultimate love ”Roqia”

Acknowledgement

I would like to thank the Dean, Vice dean for postgraduate studies and Head of Physics Department at faculty of Science, Beni-Suef University, especially my supervisor, **Prof. Hany Saleh Hamdy** for his kind support and to believe in me. He made a great effort to convince the university management to initiate the bi-doctoral agreement with Antwerp University in Belgium. I cannot forget his advice to me when I was about to quit taking the risk to do this exotic search, he told me that exploring new ideas with a huge experiment and to get engaged with experts from all over the world is a chance I may never have again. Thank you Prof. Hany for everything you did for me to reach this stage. I would also like to thank my supervisor **Prof. Ali Khalaf** for his advice and his continuous encouragement, starting from my postgraduate studies till now.

I have to express my deepest gratitude and appreciation to my supervisor from Antwerp University **Prof. Albert De Roeck**, who puts me on the track of the particle physics field and for allowing me to start this wonderful adventure for almost 5 years. His trust in me that I will continue working on the thesis topic despite all the difficulties I faced during the past 5 years is appreciated and it encourages me to move on and overcome every difficult step. He gave me a very valuable and precious chance to visit the largest experiment in the world and to work in the most positive environment like **CERN**. He gave me the freedom to think and express my thoughts, to discuss the search ideas with experts and lead this search on my own under his supervision. Also, I would like to express my cardiac sincere appreciation to the University of Antwerp, Faculty of science, physics department for their financial and administrative support over the past 5 years. Thank you **Sarah**, to make my life easier. Thank you for doing your best to help me in all the ways when I sent you an email or request. Special thanks to **Prof. Pierre Van Mechelen**, team leader of the Antwerp physics group, for supporting me financially especially in the last year of my Ph.D. to visit CERN. Thanks to **Marleen** for helping me in all the accommodation matters at CERN. Special thanks to **Phat Srimanobhas**, without your help I would not get the Monopole Monte Carlo samples, sorry

for being so pushy and thanks for the efforts you did for this search.

Big thanks to CMS collaboration and administrative staff, especially **Kirsti Aspola**, CMS PPD Resources Manager, for her care and support. Thanks to **Prof. Archana Sharma** for her motivation and advice.

I would like also to thank the conveners of **Long-lived particles (LLPs)** group, **Exotica** group, **Trigger exotica contact** group and all professors who guided me through my search studies at CERN, especially **Sam Harper, Steven Lowette, Juliette Alimena, David Pytet**, and **Vladimir Ivantchenko**. Special thanks for the previous monopole team of run I, **Chris Cowden** and **Scott Wilber** for their help in the first year of my Ph.D.

Many thanks for the **RPC community**, especially **Prof. Gabriella Pugliese**, RPC project manager, who gave me the chance to work with the RPC detector, she is the most professional woman I have ever worked with. Thanks to my dear friends and colleagues from the RPC community, **Mehar Ali Shah** and **Mariana Filipova Shopova** who motivated me all the way to finalize my thesis and her comments were really important. Special thanks to Arka Santra for his support with the monopole production model, and his explanation to me each little detail.

I am also so grateful to my second home where I belong to, **British University in Egypt (BUE)** and the support I get from the vice president **Prof. Yehia Bahi El-den** and Dean of Engineering faculty **Prof. Maguid Hassan**. I also owe a lot to **Centre for Theoretical Physics (CTP) at BUE** and **Prof. Amr El Zant**. Thanks to **Dr. Yasser Assran** for revising my chapters and for the continuous discussion we were having for this search.

I also have to thank some of the scientific collaborators who supported me financially through my visits to CERN as The Egyptian Network for high Energy Physics (ENHEP), FB7 projects. Special thanks to Professor **Ludwik Dobrzynski** for his continuous support and motivation. Thanks to professors **Philippe Mine, Giuseppe Iaselli, Danial Denegri**, and **Nicola De Filippis** for their support through the FP7 project. I cannot forget the help of my colleagues, **Ashraf**, **Darwish**, **Haifa**, **Qamesh**, **Abdel Rahman**, **Eng. Yasser** and **Hammad** for the useful discussions and their help.

During my PhD journey, we lost one of the most respected professors, **Prof. Mohammed El Okr**, He was supporting me to the maximum whenever we met, RIP.

Additionally, I have to thank my family, especially my parents, sisters, and my mother-in-law for all their help, company, care, and their support during all the difficult moments of my PhD and for taking care of my baby girl during my studying period and my trips to CERN. **My Mom**, you are always my source of strength, I love you to the moon and back. **My Dad**, this was your biggest dream and I am happy to make it true.

Last but not least, I have to express my ultimate appreciation for my husband, **Ahmed Soliman**, for his support and for encouraging me to reach my goals. He has taken care of our little girl during my PhD journey, since she was born until now, her first year in school. He was doing his best to perform the two roles, the father and the mother for her. Thank you for letting me leave you for a few months every year to finish my studies and even now while I am writing my thesis. We have passed by very difficult periods, ups and downs and now it's the time for gathering as a family. **Roqia**, my wonderful daughter for whom this journey has just started. Thank you for being such a hero.

List of Abbreviations

ALICE A Large Ion Collider Experiment

ATLAS A Toroidal LHC ApparatuS

CERN European Organization for Nuclear Research

CL confidence level

TAS Transmit Antenna Selection

CSC Cathode Strip Chamber

DAQ data acquisition

DT Drift Tube

ECA electromagnetic calorimeter

FSR final state radiation

GSF Gaussian-sum filter

GUT Grand Unified Theory

HCAL hadronic calorimeter

HLT High-Level Trigger

IP ISR

L1 Level-1

LEIR Low Energy Ion Ring

LEP Large Electron Positron

LHC Large Hadron Collider

LHCb LHC Beauty

LLPs Long Lived Particles

LO leading order

MC Monte Carlo

MMTs The Magnetic Monopole Trapper Detector System

MoEDAL Monopole and Exotics Detector at the LHC

NLO next-to-leading order

PDF parton distribution function

PF particle flow

PS Proton Synchrotron

PSB Proton Synchrotron Booster

QCD Quantum Chromodynamics

QFT Quantum Field Theory

RF radio-frequency

RPC Resistive Plate Chamber

SIMP strongly interacting massive particle

SM Standard Model

SPS Super Proton Synchrotron

SUSY supersymmetry

TEC Tracker EndCaps

TIB Tracker Inner Barrel

TID Tracker Inner Disks

TOB Tracker Outer Barrel

TS Technical Shutdown

TRT transition radiation tracker

CONTENTS

1 Introduction **1**

1.1 Theoretical Concepts 4

1.1.1 The Standard Model of Particle Physics 4

1.1.1.1 The Particle Contents of the Standard Model (SM) 5

1.1.1.2 The Fundamental Interactions 8

1.1.2 Beyond the Standard Model (BSM) 10

2 Magnetic Monopoles **13**

2.1 Dirac Monopole 14

2.2 Dirac String 15

2.3 Magnetic Monopoles 17

2.3.1 Classical Electrodynamics 18

2.3.1.1 Symmetrizing Maxwell's Equation 18
2.3.2 The Schwinger Monopole 21
2.3.3 Monopole-Photon Coupling 21
2.3.4 Monopole in the Grand Unified Theories (GUTs) . . . 22
2.3.4.1 Charge Quantization and Monopole Mass in GUT Models 23
2.3.5 Monopoles in Electroweak Models 24
2.4 Particle Interaction in Matter 24
2.4.1 Passage of Monopoles through Matter 27
2.4.1.1 Energy Loss via Ionization 28
2.5 Monopole Detection Methods 31
2.5.1 Direct Detection Methods 31
2.5.1.1 Monopole Bound in Matter 32
2.5.1.2 High Ionizing Active Detection 33
2.5.1.3 Heavy Etching on Nuclear Track Detector . 33
2.5.1.4 Anomalous Tracks in Magnetic Field 34
2.5.2 Indirect Detection Methods 35
2.5.3 Searches at Electron-Positron Colliders 36
2.5.4 Monopoles at the LHC 37

3 The Large Hadron Collider (LHC) 39

3.1 The Large Hadron Collider (LHC) 39
3.1.1 LHC Overview and Injector Chain 40
3.1.2 Luminosity 42
3.1.3 LHC Magnets 44
3.1.4 Experiments of the LHC Machine 45
3.2 Compact Muon Solenoid detector (CMS) 46
3.2.1 The Coordinate System 48
3.2.2 Physics Goals of the CMS experiment 49
3.2.3 Superconducting Magnet - CMS soleniod 50
3.2.4 CMS Inner Detector - Tracker 51
3.2.5 The Electromagnetic Calorimeter (ECAL) 53
3.2.6 The Hadron Calorimeter (HCAL) 56
3.2.7 CMS Muon System 57
3.2.7.1 Drift Tube Chambers (DTS) 59
3.2.7.2 Cathode Strip Chambers (CSCs) 60
3.2.7.3 Data Acquisition and The CMS Trigger System 61
3.2.7.3.1 Level-1 Trigger (L1) 63
3.2.7.3.2 The High-Level Trigger (HLT) . . 65

4 Resistive Plates Chambers (RPCs) 67

4.1 Gaseous Particle Detectors 68

4.1.1 Modes of Operation 69
4.2 Resistive Plates Chambers (RPCs) 70
4.2.1 RPCs Development 70
4.2.2 RPCs General Design 71
4.2.3 RPCs Working Principle 72
4.2.4 RPCs System at the CMS Experiment 73
4.2.4.1 Gas Mixture 73
4.2.4.2 Conditions and Requirements 74
4.2.4.3 Detector Layout 74
4.2.4.3.1 Barrel RPCs 74
4.2.4.3.2 Endcap RPCs 76
4.3 RE±4 Endcap – RPCs at CMS Experiment 77
4.3.1 RE±4 - Performance During Run II at 13 TeV 79
4.3.1.1 Track Extrapolation Method (Tag and Probe Method) 79
4.3.1.2 RE4 Efficiency Performance 80
4.3.1.3 RPC Cluster Size Studies and performance . 81
4.3.1.4 Endcap RPCs Background rate 84
4.3.1.5 Currents Studies for RE4 Stations 85
4.3.2 RE±4 Commissioning and Re-validation During LS2 87
4.3.2.1 Re-validation of the RE4 at the Surface . . . 90

5 Data Analysis in CMS **96**

5.1 Proton-proton Collision's Physics 97

5.1.1 Monte Carlo (MC) Event Simulation 97

5.1.1.1 The Event Generation 97

5.1.2 Detector Simulation 101

5.1.3 Digitization 102

5.1.4 Event Reconstruction 102

5.1.4.1 Electron and Photon Reconstruction 103

5.1.4.2 Identification of Electron and Photon 104

5.1.5 Muon Reconstruction 105

5.1.5.1 Muon Identification 106

5.1.5.2 Jet Reconstruction 106

5.1.5.3 Particle Flow (PF) 107

6 Simulation of Magnetic Monopole in the CMS detector **109**

6.1 Exotic Long-Lived Particles 110

6.1.1 LLPs Interactions with Matter 111

6.1.1.1 Ionization of Electrically and Magnetically Charged LLPs 111

6.1.2 Hadronization of LLPs 113

6.2 Monopole Production in CMS Detector 113

6.2.1 Monopole Production - Event Generation 114
6.2.1.1 Implementation of Monopole model in MADGRAPH5_aMC@NLO 117
6.2.2 Monopole's Signature in CMS Subdetectors 118
6.2.3 Monopole's Signature in the Inner Detector 120
6.2.4 δ-ray Production Model 123
6.2.5 Monopole Simulation in GEANT4 124
6.3 Digitization of Simulated Signal 127
6.4 Events Reconstruction 128

7 Monopole Search **130**

7.1 Analysis Strategy 131
7.1.1 Monopole Tracking Reconstruction 132
7.1.1.1 Track Combining Algorithm 133
7.1.1.2 Track Ionization 134
7.1.2 Track Curvature 137
7.1.3 Electromagnetic Calorimeter Cluster Finding 137
7.1.4 Hadronic Calorimeter Isolation 142
7.1.5 Trigger Selections 143
7.1.6 Monte Carlo (MC) and Data 2016 Samples 145
7.1.6.1 Monte Carlo datasets 147

7.1.6.2 Datasets 2016 147
7.1.7 Monopole Identification 149
7.1.7.1 Signal Efficiency 150
7.1.8 Background Estimation - Using ABCD Method 154
7.2 Systematic Uncertainty 158
7.2.1 δ-rays Production Systematic Uncertainty 158
7.2.2 ECAL Systematic Uncertainties 160
7.2.2.1 Spike Topologies 161
7.2.2.2 ECAL Shower-Shape Systematic Uncertainty 162
7.2.3 dE/dx Cross-talk in the Tracker Sub-detector 164
7.2.4 Systematic Uncertainty in Data-driven Background Estimation 166
7.2.5 Systematic Uncertainty on the Integrated Luminosity . 168
7.2.6 Cross-Section Limits 169
7.2.7 Sensitivity Differences between LHC-experiments . . 170

8 MoEDAL experiment **172**

8.1 MoEDAL Experiment Overview 172
8.1.1 Track-Etch Detectors 174
8.1.2 The Magnetic Monopole Trapper Detector System (MMTs) 176
8.1.2.1 Magnetometer Measurement Procedures . . 178

8.1.3 MoEDAL Experiment Results for 13 TeV 178

8.1.3.1 MMTs Measuring Techniques 179

9 Conclusion **185**

A Appendix Title **189**

A.1 ECAL Noise 189

A.2 Spikes and Online Selection 191

A.2.1 Spike Mitigation Methods 192

A.2.1.1 Implementation Monopole model in MADGRAPH5_aMC@NLO 194

A.2.1.2 Velocity–dependent magnetic charge 196

LIST OF FIGURES

1.1 The inner structure of an atom. An indication of the size of each component is indicated 5

1.2 The Standard Model's particles contents[1] 8

1.3 A schematic diagram of the possible interactions between the constituents of the Standard Model ©Wikipedia 10

2.1 Maxwell's equations of electrodynamics, figure taken from [152] 14

2.2 Dirac String 16

2.3 Maxwell's equation with the effect of magnetic monopoles . . 18

2.4 The electric strength constant (left) and the magnetic strength constant (right) 22

2.5 GUTs show that forces are merging at high energies 23

2.6 Fractional energy loss per radiation length in lead as a function of electron or positron energy [104]. 26

2.7 Illustration of the stopping power $-\langle Ex \rangle$ for muons in copper as a function of $\beta\gamma = p/Mc$ [176] 27

2.8 Energy loss due to Ionization is indicated by the red line, the blue line for Bremsstrahlung, while the Pair production is indicated by the green line, the unit of γ is c_{-1} 28

2.9 Energy loss per unit length, dE/dx, for an electrically charged particle with $\mid z \mid = 68.5\,e$ (left) and for magnetic monopole of charge $\mid g \mid = 1.0\,g_D$ (right) as a function of the the particle velocity, β, for different materials[86] 30

2.10 Ionization energy loss for μ, π, k, p and monopole. 30

2.11 Feynman diagram of the process $Z \to \gamma\gamma\gamma$, which can be mediated by fermions and hypothetically by magnetic monopole. . 35

2.12 Summary of upper limits on production cross section as a function of $\sqrt{s}/2$ for several experiments that used data collected at different types of colliders 38

3.1 LHC Injector Chain 40

3.2 Integrated luminosity plot for 2016 data taken, delivered by the LHC and collected by the CMS 43

3.3 Overview of the integrated luminosity delivered to the CMS detector during run I (2010 - 2012) and run II (2015 - 2018) . . 43

3.4 Cross section of the LHC main dipole in its cryostat 44

3.5 LHC four main experiments 45

3.6 An overview of various layers of the CMS detector and their key characteristics 47

3.7 CMS Coordinate system 48

3.8 A schematic view of the CMS solenoid is shown as well as the steel return yoke and muon chambers around the magnet . . . 51

3.9 A transverse view of the pixel and strip tracker detectors showing the multiple barrel layers and endcap disks. 52

3.10 Schematic representation of the CMS silicon pixel detector . . 53

3.11 A 3D view of the barrel and forward pixel detector, consisting of 3 layers and 4 disks. 53

3.12 Inner tracker material's total thickness expressed in units of interaction lengths λ_1 (left) and radiation lengths X_o (right), as a function of the pseudorapidity η. TIB, TID, TOB, and TEC stand for "tracker inner barrel", "tracker inner disks", "tracker outer barrel", and "tracker endcaps", respectively. The two figures are taken from Ref [74] 53

3.13 $PbWO_4$ ECAL crystals with photo-detectors attached – a barrel crystal with APD capsule (left) and an endcap crystal with a VPT (right). 54

3.14 A schematic view of the CMS ECAL structure – Barrel (yellow), Endcap (green) and Preshower (orange). 54

3.15 A transverse view parallel to the beam line showing one quarter of the ECAL, with its barrel (EB), endcap (EE), and preshower (ES) detectors. 55

3.16 Longitudinal view of the hadronic calorimeter (HCAL) assembly. The barrel (HB), endcap (HE), outer (HO) and forward (HF) detectors are indicated 56

3.17 Photographs of the CMS HCAL – barrel HB (left) and endcap HE (right). 57

3.18 $r-z$ cross section of a quadrant of the CMS muon system, showing DT (yellow), CSC (green) and RPC chambers (light blue). The interaction point is at the lower left corner. 58

3.19 Transverse view of a DT cell (a) and schematics of a DT chamber (b) [77] 59

3.20 The CSCs operation principle 60

3.21 The structure of the WLCG tier-levels and their mapping among worldwide 62

3.22 Illustration of data flow in the CMS trigger system with the different trigger levels and event rates 63

3.23 Architecture of the Level-1 Trigger 64

3.24 HCAL tower layout 65

3.25 Schematics view of the general architecture of the CMS DAQ System 66

4.1 Illustration of an avalanche formation in a gaseous particle detector. 68

4.2 Gaseous particle detector's modes of operation 70

4.3 A schematic view of the different layers of an RPC (a) and illustration of RPC detecting principle (b). 72

4.4 View of the double gap design in the RPC 73

4.5 A schematic layout of one of the 5 Barrel wheels with the numbered sectors is shown. 75

4.6 A schematic illustration of the RPC Barrel η partitions 76

4.7 A quarter view of the CMS muon system (On the left), RPCs are the colored detectors in the endcap system. Endcap-RPCs detector' photograph during the installation of the CMS detector (on the right) 76

4.8 A schematic view of the RPC Endcap geometry 77

4.9 A schematic layout of RE+4 endcap-RPC with its 36 chambers per ring. 78

4.10 RE+4 (top) and RE−4 (bottom) efficiency performance over time, during run II 80

4.11 Overall efficiency of Endcap (top) for 2015-2018 data-taken, (bottom) RPC overall efficiency vs. time for 2016-2017 data-taken 81

4.12 Cluster Size, as the number of contiguous strips associated to a hit 82

4.13 Endcap Average Cluster Size 82

4.14 The history of the mean Cluster Size for the barrel for 2016 and 2017 physics data taking at 13 TeV. 83

4.15 Cluster size performance over time, during run II, for RE+4 (top) and RE−4 (bottom) 84

4.16 RPC hit rate vs instantaneous luminosity distributions for the RE±4 endcap-RPCs stations. 85

4.17 RE+4 and RE−4 Current vs. time (top). Currents vs. luminosity (bottom) of RE+4, RE−4 stations 86

4.18 RE+4 and RE−4 Current vs. Voltage 87

4.19 RE4 and CSCs overview in CMS 87

4.20 RE4, covered with RPC detectors before the dismounting (a), RE4 super module after dismounting (b) 88

4.21 RE4 laboratory with the dismounting disks 89

4.22 Extraction process of RE4 chambers, More photographs can be found in the following link: https://cds.cern.ch/record/2668394?ln=en. A video of the RE±4-supermodules removal can be viewed here https://drive.google.com/open?id=1Q6eDwRv69m973AQqlvOBhyCmEwGnprpt. 90

4.23 Illustration of the noise scan results for the one of the RPC detectors CMS-RE4-3-GHENT-048_A 91

4.24 RE4 super-modules with connections (left) to the HV scan rack (right) 91

4.25 Current vs. Hv for Trolley 02 super-modules in each gap . . . 92

4.26 Current vs. Voltage (before and after dismounting) 93

4.27 Gas Leak Test set-up with monitored screen 94

4.28 Gas Leak Test set-up with monitored screen 95

5.1 Illustration of an event shows the hard scattering and the ensuing parton shower (red), the hadronization (green) with hadron decays (dark green) and radiated photons (yellow), and the underlying event coming from beam remnants (blue) and multiple parton interactions (purple). Figure from ref. [110]. 98

5.2 The Parton Distribution Functions multiplied by the momentum fraction x at energy scales $Q^2 = 10\,GeV^2$ (left) and $Q^2 = 10000\,GeV^2$ (right) for the different valence and sea quarks and the gluons present in a proton, obtained in the NNLO NNPDF 3.0 global analysis. Figures taken from [41] 101

5.3 A slice of the CMS detector indicates the interactions of different types of particles when they travel through the detector . . 103

5.4 PF jets and Calorimeter jets at CMS 106

6.1 The Energy Loss for monopole (blue) is very high as compared with electric charged particles (red). [92] 111

6.2 Stopping Power $-\langle dE/dx \rangle$ for Dirac monopoles in aluminum as a function of β (left). The ratio of range to mass for Dirac monopoles in Aluminum as a function of $\beta\gamma = p/M$, calculated from the stopping power (right) [95] 112

6.3 A Feynman-like tree-level graphs for production processes of monopoles with generic spin S.(a): typical SM Drell-Yan process describing charged lepton production from quark-antiquark annihilation; (b) DY monopole-antimonopole pair production from quark annihilation 114

6.4 Transverse Momentun (p_T) 116

6.5 Pesuropaidity (η) 116

6.6 The approximate trajectory of monopole mass $1000\,GeV$, assuming a uniform solenoid magnetic field in the ALICE ($B = 0.5\,T$), ATLAS ($B = 2.0\,T$) and CMS ($B = 3.8\,T$) detectors at $\eta = 0$, for $|\,g\,| = g_D$ (left) 119

6.7 Signature of Magnetic Monopole is CMS detector via CMSSHOW program 120

6.8 Comparison of the dE/dx as produced in GEANT4 to an analytic formula for the monopole energy loss of Ahlen analogous to the Bethe formula 122

6.9 The origin of δ-rays which clearly cluster around the monopole trajectory 124

6.10 Screenshot of the GEANT4 validation for CMSSW_7_1_38 which is used for simulating the MC samples 127

6.11 Analysis Chain 128

7.1 Actual and fitted trajectories of monopoles 132

7.2 Cutting on the $dE/dx_{significance}$ improves discrimination power compared to a simple cut on the fraction of saturated strips. . . 135

7.3 Distributions of $dE/dx_Significance$ for each mass point simulated. 136

7.4 The $r-z$ curvature is not as useful a discriminant. 137

7.5 Domino construction step of "hybrid" algorithm 139

7.6 The average $E_{crystal}/E_{5\times5}$ for mass 1000 GeV, barrel (left), endcap (right) 140

7.7 Distribution of f_{51} in the ECAL endcap (left), and barrel (right) for all simulated monopole masses 141

7.8 Distribution of f_{51} in the ECAL after reconstructed the monopole candidates 141

7.9 The relative energy in the HCAL around monopole clusters in the ECAL 142

7.10 $HLT_Photon175_v^{\star}$ and L1 trigger path efficiencies vs. monopole masses 145

7.11 Joint distributions of the tracking discriminant and calorimetry discriminates for each monopole mass simulated after HLT and $E > 175\,GeV$ cut is applied to the ECAL cluster. Events are represented at most once in these figures in order to avoid double counting. 151

7.12 Illustration the relative efficiency of each major cut used in the analysis 153

7.13 ABCD Method 154

7.14 Scheme of double ABCD method used in the analysis 155

7.15 The distribution of f_{51} in the data collected compared to the same variable in the simulated monopole events. The red numbers represented the expected background and the black numbers are the actual counts observed in each region 156

7.16 The distribution of f_{51} in the data collected compared to the same variable in the simulated monopole events 157

7.17 The distribution of the $dE/dx_{significance}$ in the data collected compared to the same distribution in simulated monopole events. 157

7.18 The distribution of energy measured in the EE (left) and EB (right) in 5×5 clusters before any selections are applied for simulated monopole events. All simulated monopole mass points are represented by the various colors 161

7.19 The distribution of shower shape topology f_{51} in the ECAL for mass point 1000 GeV for $delta$-electron production off (green) and Spike typologies off (blue) along with default settings (red) 163

7.20 The joint distributions of the tracking discriminant and calorimetry discriminant for cases (a) Default setting , (b) Spike typologies off, (c) δ - ray production off 163

7.21 Observed dE/dx cross-talk 164

7.22 A schematic distribution of the dE/dx cross-talk clusters 165

7.23 A comparison of shapes of the f_{51} distribution in slices of the $dE/dx_{significance}$ in the 2016 dataset. All curves are normalized to unit area. 167

7.24 A comparison of shapes of the $dE/dx_{significance}$ distribution in slices of f_{51} the in the 2016 dataset. All curves are normalized to unit area. 167

7.25 Observed 95 % CL upper limits on the cross-section for Drell-Yan spin 1/2 monopole 169

7.26 ATLAS - Observed 95 % CL upper limits on the cross-section for Drell-Yan. Plot has been taken from [3] 171

8.1 A schematic view of three-dimensional MoEDAL detector (beside the yellow circle) 173

8.2 The polymeric bonds breaking caused by a crossing charged particle. 174

8.3 The latent track that occurred by particle's passage with charge Z and velocity $\beta = v/c$ (left). Two etch pit cones are formed on the sides of the foil (middle). A prolonged etching forms a hole (right). 175

8.4 The basic MoEDAL detector stack is consisting of three sheets of CR39 and 3 sheets of MAKROFOL with Lexan sheets separating the CR39 and MAKROFOL stacks. Sheet size is $25\,cm \times 25\,cm$. An $1\,mm$ thick aluminum housing is surrounding the stack. Total thickness of the stack is $3.6\,mm$. 175

8.5 A schematic diagram for SQUID apparatus. The sample passed in steps through the coil. The current in the superconducting coil is measured after each step. 176

8.6 Real photographs, taken by the author, for the magnetically shielded room at Zurich (top), the the SQUID magnetometer (middle), and the Aluminum samples (bottom) 177

8.7 Results of the calibration measurements for several currents ranges, with the superposition method using a magnetic dipole sample, and the solenoid method with $P = 32.4\, g_D/\mu A$. The dashed lines represent the expected plateau values in units of Dirac charge. 179

8.8 Magnetic pole strength (with Dirac charge units) measured in the 2400 Aluminium samples of the MMTs detector with exposing to $13\, TeV$ collisions during run II, with double scanning for each sample 180

8.9 Results of multiple pole strength measurements (in units of Dirac charge) for the 87 candidates samples. At least one of the two first measurement values was above the threshold $|g| > 0.4\, g_D$. Most of the values observed below the threshold, the presence of a monopole with $|g| \geq g_D$ is excluded. 181

8.10 Feynman-like diagrams for monopolem - antimonopole production via the Drell-Yan (left) and photon-fusion (right) processes at the LHC.[38]. 183

8.11 Cross-section upper limits at 95 % CLs for the combined DY and $\gamma\gamma$ monopole pair production model with β-dependent couplings in $13\, TeV$ proton proton collisions as a function of the mass spin $1/2$. The colors correspond to different monopole charges. The solid lines are cross-section calculations at leading order. 183

A.1 The energy found outside of the central strip vs. the fraction of energy found in the cluster for two monopole masses 700 and $1500\, GeV$ respectively. 190

A.2 The energy found outside of the central strip vs. the fraction of energy found in the cluster after a $100\, GeV$ energy cut for two monopole masses 700 and $1500\, GeV$ respectively. 190

A.3 The energy found outside of the central strip vs. the fraction of energy found in the cluster after a 175 GeV energy cut for two monopole masses 700 and 1500 GeV respectively. 190

A.4 illustration of spike shape and timing in the ECAL barrel . . . 191

A.5 A useful diagram showing the implementation of online spike filtering 193

A.6 Swiss-cross definition 194

A.7 Swiss cross distribution for monopole mass 1000 *GeV* before and after the cut of 0.95 194

LIST OF TABLES

1.1 Overview of the three Fermions generations in the Standard Model and their electric charge 7

1.2 Overview of the Standard Model Bosons with their masses, electrical charges and spin values are indicated [136] 7

2.1 The variables used in the Bethe equation 3.6 25

4.1 Trolley-02 current readings in μA, we disconnect this trolley on 16 August after completing its validation. 92

6.1 The variables used in the modified Bethe equation for monopole 112

7.1 Parameter values used in the clustering steps of the "hybrid" algorithm 140

7.2 HLT trigger paths with their L1 seeds 144

7.3 *HLT_Photon*175_$v^{\star}$ and its L1 seed efficiencies vs. monopole masses 145

7.4 Collections used in the Reconstruction step 146

7.5 Global Tag used for MC-2016 Datasets 147

7.6 Monte Carlo (MC) datasets for monopole masses points in RECO format 148

7.7 2016 DataSets - SinglePhoton 148

7.8 The JSON file and Global Tag used for Single Photon - 2016 Datasets 149

7.9 Pre-selections applied for monopole matching 149

7.10 Analysis selections cuts applied to identify the monopole candidate 150

7.11 CutFlow - Tabulated values of events simulated at each mass point after successive selection cuts are applied 152

7.12 N-1 - Tabulated values of events simulated at each mass point with all cuts except the indicated cut on the left column 152

7.13 This table itemizes the final acceptance and efficiency used in the estimation of the observed monopole production cross section limit. 153

7.14 The Relative efficiencies for each major cut in the analysis . . 154

7.15 The number of events observed in each region of the ($dE/dx_{significance}$, f_{51}) space. No events are observed in the signal region (9). . . 156

7.16 Systematic uncertainty for monopole mass 1000GeV when switching off the δ-electron production 159

7.17 Systematic Uncertainty for switching off the spike topologies in the PF-recHit step 162

7.18 Systematic Uncertainty in ECAL cluster shape distributions . . 162

7.19 dE/dx cross-talk Systematic Uncertainty 166

7.20 The estimated background contribution to the signal region based on various loose cuts and the associated relative systematic uncertainty on the background estimate. 168

7.21 The Systematic Uncertainties in the signal efficiency and background estimate. 169

7.22 Expected and observed production cross-section limit 170

8.1 95% C.L. mass limits in models of spin 0, spin $1/2$ and spin-1 monopole pair direct production in LHC pp collisions. The present results are interpreted for Drell-Yan and combined DY and photon-fusion production with both β-independent and β-dependent couplings. 184

CHAPTER 1

INTRODUCTION

The human understanding of the fundamental particles and interactions is one of the biggest challenges for more than 100 years. Our understanding of the universe and all of its constitutes is increasing exponentially. In the early of the 20th century, physicists discovered that the atom is composed of a fundamental particle such as an electron, which has been discovered by J.J. Thompson in 1897 and it was a real start to the field of particle physics. The other main composts of the atoms were then discovered, the positively charged protons and the neutrally charged neutrons.

Today our understanding of the composition of the atom has improved and we understand that there are other fundamental particles. Quarks are the smaller particles that compose the proton and neutron. After years of theoretical, experimental efforts and measurements to discover new particles and to prove the quantum mechanics theories, a united model has been developed which describes the electromagnetic, Strong, and Weak forces. The Standard Model of Particle Physics (SM) has been developed to describe the behavior of these fundamental particles, many experiments and extensive tests have been performed over the decades to assure the predictions of the Standard Model (SM). This model predicts the existence of top quark, tau neutrino and many more particles including the Higgs Boson which was recently discovered in 2012. Higgs

Boson was the last missing puzzle in the table contents of the Standard Model (SM) particles. The discovery of the Higgs has led to as many questions as answers. Physicists knew little information about the boson's properties from the experimental data, not so much that we must get more confident but we need to measure more properties of the Higgs.

Some open questions need explanations and answers, which the Standard Model (SM) could not have a clear answer for. For this reason, theorists had to search for a new theory that would complete the defects of the Standard Model (SM). As the Standard Model (SM) is not a complete theory of everything, it could not describe the dark matter, the gravity, and the asymmetry of matter and antimatter in the universe. As a result, many theories beyond the standard model (BSM) have been proposed, like extra dimension and Supersymmetry, to give a detailed description and explanation for everything around us in the universe in such a complete theory, which is; Beyond the Standard Model (BSM), the so-called "Theory of everything". It is also referring to the theoretical developments in explaining the weak points and deficiencies of the SM, which leads to exploring new physics at the TeV energy scale.

Fundamental particles are observed to possess electric and neutral charge. Only fundamental particles that possess non-neutral electric charge and photons (as a force carrier) have been observed to interact electromagnetically. Some discussions and experiments were held concerning the magnetic characteristic of the matter and there are some predictions about the existence of an isolated magnetic charge. Physicists have worked very hard to understand the nature of symmetries, like the symmetry between electricity and magnetism. One of the important pieces, that is still under investigation, is the existence of the magnetic monopole. A lot of searches have been performed to search for magnetic monopoles when strong theoretical arguments have been established, why should the magnetic monopole exist?

The Standard Model (SM) and Beyond Standard Model (BSM) theories can be examined experimentally in large colliders like the Large Hadron Collider (LHC) at the European Organization for Nuclear Research (CERN), LHC is a proton-proton accelerator which has been built to test all these theories. The LHC exists in a tunnel with $\sim 27\,km$ circumference and $\sim 100\,m$ deep beneath the surface near Geneva, Switzerland, that's why it is the largest particle accel-

erator in the world. LHC is the highest – energy accelerator with center-of-mass energy of $14\,TeV$ and $10^{34}\,cm^{-2}\,s^{-1}$ of luminosity. Two oppositely circulating beams of protons or lead nuclei collide at the main four intersection points which are the points of establishing the LHC's main experiments. The largest two experiments are the Compact Muon Solenoid (CMS) and Toroidal LHC Apparatus (ATLAS), which were built to record and reconstruct proton–proton collisions at a very high precision level.

One of the aims of the Large Hadron Collider (LHC) experiments is to set limits or discover exotic particle production within the TeV scale masses which have electric and/or magnetic charge and behave as highly ionizing particles (HIPs). In this chapter, we will discuss in detail the sensitivity of the LHC's experiments to high ionizing particles (HIPs) production. This includes the HIPs passage through a passive or active detector which is called direct detection, and for the case of magnetically charged particles, the induction method in which the magnetic monopole could be observed and detected when stopped in the material of the detector [86].

One of the main characteristics of the Highly Ionized particles (HIPs) is the ionization energy loss which is multiple times greater than any other minimum ionizing particles when passing/propagating through matter. Magnetic monopoles are considered to be exotic HIPs [20], while particles that carry electric and magnetic charges are called Dyons [182], and particles with high electric charge are called Q-balls [121]. Pairs of High Ionizing Particles (HIPs) may be produced through many processes during high energy collisions like particle–antiparticle annihilation, photon–photon fusion, or more processes involved in the high energy collisions. No such particles have been discovered up to date. Magnetic monopoles and Dyons are good examples of such High Ionizing Particles (HIPs).

In 1931, Dirac observed that the quantization of charge could be well understood as a consequence of angular momentum conservation if only one-pole of a magnetic charge existed [88]. This argument is the main motivation to search for magnetic monopoles that are trapped in the matter either cosmic rays [89] or particle colliders at the high energy frontier [117]. An approximate guideline to the value of a magnetic charge which could be held by a magnetic charged particle has been provided by Dirac's argument.

The following relation between electric charge q_e and any magnetic charge q_m : $q_e q_m = nh/m_0$, where m_0 is the vacuum permeability and n is an integer number and h is Planck's constant. If we replace the electric charge q_e with $q_e = ze$ (e is the elementary electric charge) and the magnetic charge $q_m = gec$ (where c is the speed of light), for $n = 1$ and $z = 1$, we will get $g_D = h/(m_0 e^2 c) = 68.5$, where g_D is the Dirac charge for magnetic monopole. This value shows that the electromagnetic coupling (monopole-photon coupling) is several thousand times higher than the coupling of a particle with electric charge. While Dirac's argument shows that the minimum fundamental unit for a magnetic charge is $g_D ec$. It is worth mentioning that predictions for monopole masses are uncertain.

Monopoles are general features of all theories where the $U(1)$ group of Electromagnetism is a subgroup of a broken gauge symmetry [48], which have masses very close to the unification scale. A lot of varieties of models have been proposed and some of these models enable the monopole masses to exist in the LHC's accessible range [120].

1.1 Theoretical Concepts

1.1.1 The Standard Model of Particle Physics

During 1970s, the Standard Model of elementary particle physics had reached its current formulation in which the Electromagnetic and Weak interactions are combined into the Electroweak interaction [19, 100, 181], and the Brout-Englert-Higgs (BEH) mechanism [159, 94, 108], and the addition of asymptotic freedom [105, 103] are combined into the theory of the Strong interaction. The Standard Model of Particle Physics (SM) is the relativistic Quantum Field Theory (QFT) which is used to describe the basic building blocks of matter and their interactions with each other [144]. Successfully, this theoretical model combines the Electroweak theory [122], which describes Electromagnetic and Weak interactions, with Quantum Chromodynamics (QCD), that describes the Strong interactions. This theory also incorporates three of the fundamental forces. Despite describing the Electromagnetic force, Weak force and Strong

interactions, the description of the fourth interaction which is Gravity has not yet been discovered.

1.1.1.1 The Particle Contents of the Standard Model (SM)

Everything around us is composed of atoms, which is containing negatively charged electrons and a positively charged nucleus contains protons and neutrons. A proton consists of up and down quarks. These quarks and the electrons are the basic fundamental particles called Fermions. Figure 1.1 illustrates the inner structure of an atom.

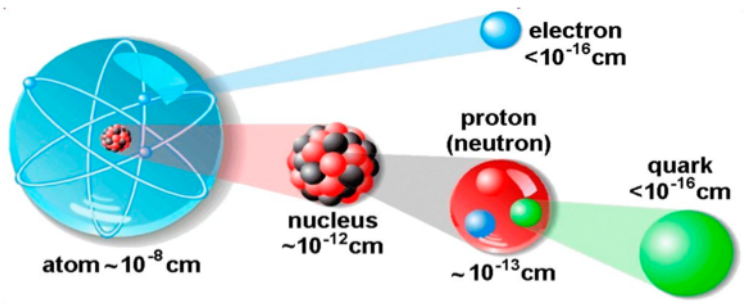


Figure 1.1: The inner structure of an atom. An indication of the size of each component is indicated

The SM's particle content is consisting of the most fundamental structure of matter which known up to date and it is divided into main categories according to its properties:

- **Fermions**, which are the composition of all of the stuff around us. Fermions are particles with half-integer spin (spin $1/2$), in the unit of $\hbar$, which interact with each other by the exchange of other particles called Gauge Bosons (spin 1). and they are classified into two main types – **Leptons and Quarks**. Leptons, which include electrons, muons, taus, and barely - massive neutrinos. Quarks, which are a fundamental composite of protons and neutrons, are subjected to the Strong interaction by the existence of gluons, that is why they have a color charge.

Quarks and leptons have been observed to be subdivided into three generations (twelve flavors fermions), six quarks and six leptons with increasing mass, where each generation is heavier than the previous one. Details of the Fermions of the SM with their masses and electrical charge and spin information is summarized in table 1.1, which shows that each of the vertical groups has the same electrical charge. Also, each particle of the Standard Model contents table has an anti-particle. Antiparticles are having an opposite charge besides the same properties as their corresponding particles, with another quantum number. Antiparticles are having a bar above the same particle symbol, e.g. the quark (q) has an antiquark q, but only for the charged lepton I^- and the positively charged sign is reserved for the anti leptons I^+.

For quark families, each generation is composed of two quarks, depending on their masses. one-up (u) and one-down (d) in the first, charm (c) and strange (s) in the second and top (t) and bottom (b) in the third. One charged and one neutral particle forms the lepton generations. The first generation of the leptons contains electron (e), the second contains muon (μ) and the third contains (τ), while the electrically neutral leptons are called neutrinos (ν) – electron- (νe), muon - $(\nu\,\mu)$ and tau neutrino $(\nu\,\tau)$. Neutrinos only interact via the Weak interaction and they can be detected in specially dedicated experiments due to the complications of their observation.

The interactions of the Quarks are through the Electroweak [141] and Strong forces because they are holding an electric charge, color charge, and weak iso-spin. No observations have taken place for Quarks as free particles due to the Strong interaction property. Confinement (a Strong interactions property). Quarks are forming bound states of colored neutral particles called Hadrons (baryons and mesons). The interaction of Leptons is only through Electroweak force since they have zero color charge. For neutrinos, the interaction is only via the Weak force as they are also not electrically charged. Fermions obey the Fermi exclusion principle and they possess weak iso-spin and hyper change which means that they interact weakly and electromagnetically, unlike electrically neutral neutrons.

Table 1.1: Overview of the three Fermions generations in the Standard Model and their electric charge

Generation	Quarks				Leptons			
1	u	up	d	down	e	electron	ν_e	electron neutrino
2	e	charm	s	strange	μ	muon	ν_μ	muon neutrino
3	t	top	b	bottom	τ	tau lepton	ν_τ	tau neutrino
El. charge (e)	+2/3		-1/3		-1		0	

- **Bosons**, particles that mediate how Fermions interact with one another, like a photon, the particle of light, and the particle that carries the electromagnetic force, Z and $W^{\pm}$ boson and gluons (g). Bosons are force carriers with integer spin 1.

  Higgs Boson is the only scalar particle with spin 0. A summary table for the SM Bosons is shown below, including the force carriers. Table 1.2 shows an overview of the Bosons with their masses and electric charge and spin information.

Table 1.2: Overview of the Standard Model Bosons with their masses, electrical charges and spin values are indicated [136]

Boson	Mass (GeV)	El. charge (e)	Spin
γ (photon)	0	0	1
g (gluon)	0	0	1
W^+, W^-	80.385 ± 0.015	± 1	1
Z	91.188 ± 0.002	0	1
H	125.09 ± 0.24	0	0

A summary diagram of the basic particles in the Standard Model (SM), which is sorted by generations and ordered concerning their masses, is shown below in figure 1.2. It is worth mentioning that neutrinos are described as particles with no mass.

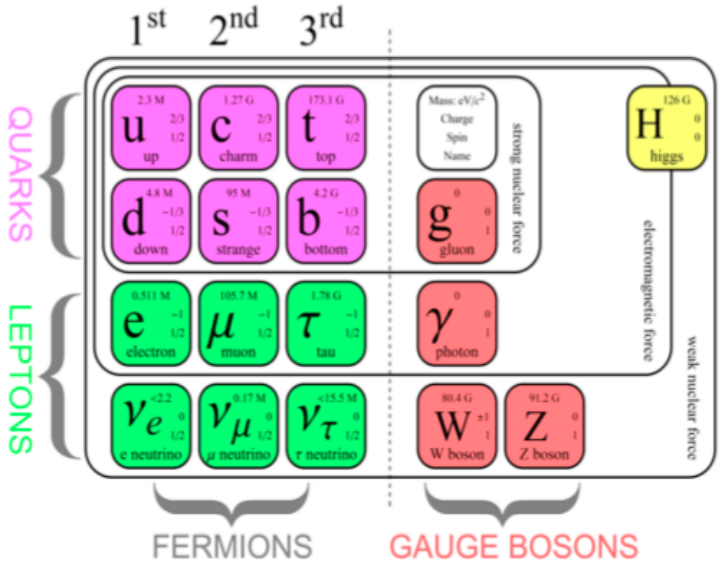


Figure 1.2: The Standard Model's particles contents[1]

1.1.1.2 The Fundamental Interactions

In Nature, there are four types of fundamental interactions in which the elementary particles interact with each other through them, *The Strong Force*, *the Weak Force*, *Electromagnetism* and *Gravity*. Our world is controlled by two of those fundamental forces which are *Gravity* and *Electromagnetism*. The force which binds the quarks together and holds the proton and the neutrons in the nuclear is so-called "The Strong Force". The force which is responsible for the interaction of neutrinos and other leptons with matter and the radioactive decay of unstable nuclei is "The Weak Force". The Standard Model (SM) is only describing three out of the four fundamental forces. Gravity is not included due to the difficulties in combining quantum mechanics and general relativity. The effect of the Gravity on the interactions described by the Standard Model (SM) is almost negligible since the Gravity is an order of 10^{40} weaker than the Electromagnetic force [102].

The fundamental interactions of the SM are mediated by Gauge Bosons and there is a special boson for each fundamental force behind the interaction which is used to carry it. The Electromagnetic force interaction acts between the electrically charged particles and the photon is the mediator force carrier. This

force governs all electrical and magnetic interactions. The Strong and Weak (nuclear) forces have a very limited range and the Strong force is mediated by the gluon and has a range of about $\sim 10^{-15}\,m$ and due to the large mass of the weak force's mediators $W^{\pm}$ and Z bosons [131], the Weak force has a shorter range.

The charged particles, with colored charges, interact by exchanging gluons. Constantly, quarks change their color charges because they exchange gluons with other quarks. There are 3 color charges and corresponding three anti-color charges. Each quark has one of the color charges while each anti-quark has one of the anti-color charges. In a baryon, a combination of green, red, and blue is color neutral. Mesons are color neutral because they carry combinations as red and anti-red. Gluons can carry a color and an anticolor charge, as their emission and absorption always change color and the QCD calculations predict eight different kinds of gluons. The decay of particles is described by the Weak Nuclear force as in the radioactive processes. This force acts on all the Standard Model fermions. Depending on whether the neutral Z boson or the W bosons are mediating the process, the Weak interactions are divided into neutral (similar to the electromagnetic interactions which mediated by the photon) and charged interactions, while a neutrino is involved by the neutral interactions. It is important to note that the neutrinos can only be mediated by Z boson while, due to the conservation of charge during an interaction, a W boson will always link particles with an electrical charge difference of $1\,e$, as charged lepton and neutrinos or an up and down quark.

The last puzzle piece of the SM contents table is the recently discovered Higgs boson [97, 2, 66] which gives mass to the fermions, the $W^{\pm}$ and Z bosons and itself via the Brout-Englert-Higgs mechanism [61, 94, 108]. The massless particle that mediating the Electromagnetic force is photons (γ), and for the Weak force, the mediators/force carriers are the charged W^{+} and W^{-} bosons and the neutral $Z0$ boson, with massive masses $m_w = 80.399 \pm 0.023\,GeV$ and $m_z = 91.1876 \pm 0.0021\,GeV$ [105], while the gluons (g) are the Strong force carriers. According to the QCD, there are eight different gluons with zero mass which have a color charge and they can also interact with each other. The color charge comes in three flavors – red (r), green (g) and blue (b).

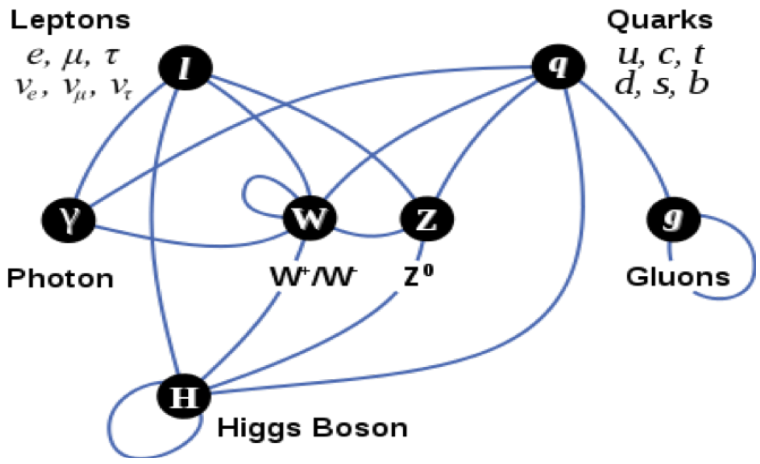


Figure 1.3: A schematic diagram of the possible interactions between the constituents of the Standard Model ©Wikipedia

There is an extremely Strong force that keeps the planets in their orbits around the stars, but in particle physics, Gravity is the fourth known fundamental force. The mediator (graviton) of the Gravity has not been found yet and Gravity is not unified with the SM. Figure 1.3 shows the allowed interactions between the SM's particles.

In conclusion, the Standard Model of particle physics (SM) is the most successful Quantum Field Theory (QFT) that describes all the basic particles and their interactions so far. The combination between the Electromagnetic and Weak interactions gives the Electroweak (EWK) theory, while Quantum Chromodynamics (QCD) describes the Strong interaction. An additional mechanism, the Higgs mechanism, adds the mass of particles that describes the Electroweak symmetry breaking. A more detailed review of the mathematical foundation of the SM in the theory of gauge symmetries can be found in [133].

1.1.2 Beyond the Standard Model (BSM)

The Standard Model of Particle Physics (SM) is a very successful theory, tested, and questioned for more than a century. Still, it seems not entirely compatible with the ultimate description of nature. There are several questions and problems both theoretical and phenomenological that do not have an explana-

tion in the SM, Why do we observe matter and almost no antimatter?. Are quarks and leptons fundamental?. Why can't the SM predict a particle's mass?. Why are there 3 generations of quarks and leptons?. How does gravity fit into all of this?, these questions and more need answers, unfortunately, the Standard Model cannot give a clear explanation for many questions.

One of the major problems with no explanation in this theory is the so-called hierarchy problem – it comes from the huge difference in the scales of magnitude for Electroweak physics $m_z \sim 10^2\,GeV$ and the fundamental gravity scale - Plank mass scale – $m_p \sim 10^{19}\,GeV$. The SM already describes all fundamental interactions but the gravitational one, so no new physics is expected in between these two scales. Another major problem is the unification of the coupling constants. There is a belief that following the good unification of the Electromagnetism and Weak interaction, it will be possible to unify all fundamental interactions and thus describe them by a single symmetry group.

Unfortunately, no evidence for this unification possibility is observed so far, so new physics at higher energies must be searched. Gravitational interactions are also not defined in the SM which makes the model incomplete by itself. There is also no explanation of the observed existence of neutral non-baryonic matter. It is called Dark Matter and based on cosmic microwave background studies it is six times more than baryonic (SM postulated) matter in the universe [177]. Another cosmological problem with no explanation is the asymmetry between matter and anti-matter. Many promising models have been introduced throughout the years in order to extend or replace the Standard Model. So far there is no experimental evidence for accepting or rejecting any of them.

The main analysis work that has been done in the presented thesis is to search for one of the long-lived exotic particles, Magnetic Monopole, at the $13\,TeV$ center of mass-energy proton-proton collision with the CMS experiment. In 1931 by Dirac and many experimental searches have been dedicated to searching for the monopole.

Due to the highly ionizing properties of a magnetic monopole, we use this feature to look for regions with high ionizing tracks in the Silicon tracker of the CMS detector and a very narrow energy deposits in the electromagnetic calorimeter (ECAL) sub-detector with a very little or no radiation in the hadron

calorimeter (HCAL). Events with narrow calorimeter clusters matched to a highly ionizing track are selected as signatures of a monopole.

This thesis is structured into 9 chapters. At first, in chapter 1, a brief overview of the Standard Model and its particle contents are discussed. An introduction of Magnetic monopole is presented in chapter 2 and a detailed overview of its characteristics and motivations for this search, and some other types of monopole and its history. Also a brief discussion on the matter interactions. We will give brief information on the recent searches for magnetic monopoles. Chapter 3 describes the physics and construction of the Large Hadron Collider (LHC) and the detailed construction of the CMS experiment, which is used to produce the needed events and the data recorded for this analysis work. In chapter 4, there will be a description of the Resistive Plates Chambers (RPC) detector which is installed in the muon system of the CMS experiment, performance of $RE \pm 4$-endcap RPCs and the author's contribution during the Ph.D. studies in LS2 commissioning services will be discussed. A step by step overview of the data analysis strategy at CMS is presented in Chapter 5, to understand how the particle detector can observe such particles correspond to the interactions between colliding particles. Events from the collision are simulated and reconstructed with the needed information to finalize the study. Chapter 6 is discussing the event generation and simulation of magnetic monopoles and the recent implementation of the monopole model in one of the MC generators. The results of the presented analysis will be discussed in chapter 7. An introduction to the MoEDAL experiment is given in chapter 8 with the doctoral candidate's contribution in the 2018 analysis with a comparison between CMS, ATLAS, and MoEDAL sensitivities. Last, the conclusion is in chapter 9.

CHAPTER 2

MAGNETIC MONOPOLES

”The discovery of the mysterious hypothetical particles would provide a tantalizing glimpse of new laws of nature beyond the standard model”, Arttu Rajantie [152]

In the modern world, Electricity and Magnetism are existing everywhere forming the basis of our technology. They are well described and fully understood using classical electrodynamics, e.g. James Clerk Maxwell’s formulas in 1864. Also, a part of the Standard Model (SM) has been described by Quantum Electrodynamics (QED). However, there is a basic aspect of Electromagnetism that we still do not understand, which is Magnetic Monopole [151]

Electricity and magnetism together form the so-called phenomena “Electromagnetism”. Protons and electrons (positive and negative electric monopoles) have been known to exist. Magnetic charges (south and north poles) also exist and always show up in pairs, unlike the electric charge which can be separated. Magnets always have two poles (north and south). We do not have any theoretical reasons why magnetic monopoles could not exist with only one pole (north or south). 88 years ago, Paul Dirac introduced the magnetic charge as a way to explain the quantization of electric charge [88]. The existence of magnetic monopoles would also lead to the symmetry between Electricity and Magnetism i.e., will symmetrize Maxwell’s equation. Huge efforts from

the theorists as well as experimentalists have been done to prove the existence of the magnetic charged particle. Many theories have predicted a large scale of monopole masses that could be found in many different detector searches [165].

In classical electrodynamics, magnetic monopoles are not prohibited, since they would symmetrize the theory. Maxwell shows that the laws which govern Electricity and Magnetism are symmetric, which can be seen through the Maxwell equations of electrodynamics. These equations have a duality symmetry in the vacuum, i.e. the magnetic terms can be used instead of electric terms. Only when electric charge and currents are presented, the symmetry is broken. If the magnetic monopoles exist, the duality symmetry is restored as shown in figure 2.1, and we would expect their existence. Experiments at that time show that the magnetic charges do not exist, that's why Maxwell did not include them in his equations [130].

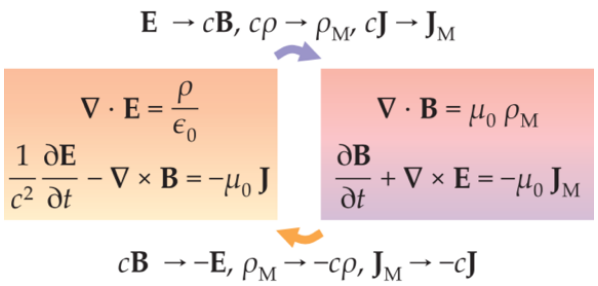


Figure 2.1: Maxwell's equations of electrodynamics, figure taken from [152]

2.1 Dirac Monopole

From the famous paper of Paul Dirac in 1931, he showed that magnetic monopoles could be explained by quantum electrodynamics and it may give a clear explanation to the charge quantization [88]. The relationship between the charge of magnetic monopole and electric charge is given by

$$eg = \frac{n\hbar c}{2} \tag{2.1}$$

Where g, e are the magnetic and electric charge, n is an integer number. From the above relation we can find an expression for the fundamental magnetic charge, the so called "Dirac charge" [8]:

$$g_D = \frac{\hbar c}{2e} = \frac{e}{2\alpha} \approx 68.5\, e \tag{2.2}$$

Where α is called the fine structure constant and is given by $\alpha = e^2/(\hbar c) \approx 1/137$, it represents the coupling between electron and photon. The force between the monopole and anti-monopole is given by $(137/2)^2$, which is approximately 4700 times higher than the force between electric charges. This may be a good reason to explain why until now we can not detect separated monopoles pairs in nature.

Since there is no perturbative calculations for the monopole production cross section experimentally, we can not predict the mass of Dirac monopole, but we can generally assume that the radius of monopole could equal the classical electron's radius:

$$r_M = \frac{g^2}{m_M c^2} = r_e = \frac{e^2}{m_e c^2} \rightarrow m_M = \frac{g^2 m_e}{e^2} \tag{2.3}$$

For such a fundamental magnetic charge, this relation gives the relatively large mass equals to $2.4\, Gev$ [39].

2.2 Dirac String

In the first half of the 20th century. Paul Dirac has worked on establishing the existence of Magnetic monopoles within the framework of Electromagnetism and quantum mechanics. He predicted that the existence of monopoles can be described by quantum mechanics and it could explain the electric charge's quantization [88].

Dirac's model in figure 2.2 shows that in a magnet each pole is connected to the other pole with a line of singularity called *"Dirac String"*. This string is acting as zero thickness idealized solenoid and the lines of the magnetic field remain continuous since the magnetic flux, which is carried by the string, is traveling from south pole to north pole. Because of this reason and also the effect that would be on the electrically charged particles, the Dirac string could be observed easily. However, in quantum mechanics, if the two - pole's magnetic charge g has the same correct value, the electrically charged particles will not be affected by the presence of the Dirac String. The value of the magnetic charge is given by the Dirac quantization charge [89].

$$g = \frac{2\pi\hbar}{\mu_0 e} n \tag{2.4}$$

Where e is the electric charge of a particle, $\hbar$ is Planck's constant, and n is an integer number. No experiment could observe the string if the quantization condition is satisfied by the electric charges of the particles. Thus, an argument has been raised by Dirac, that the string does not exist. With the help of this theoretical description, the two poles at the two ends of the string are real and they would appear as separate particles, i.e. magnetic monopoles.

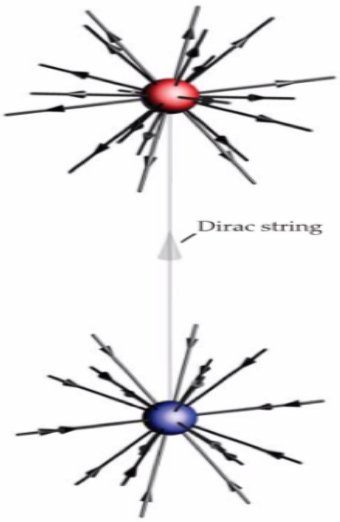


Figure 2.2: Dirac String

The quantization condition gives us information regarding the charge of the magnetic monopole g, which is very strong compared to the electric charge. First, it shows us the magnetic force that acts between two magnetic monopoles, each of them with Dirac charge g_D, would be 4700 times greater than the force between two electrons. Second, the electric charge is quantized if monopoles would exist.

As mentioned, Dirac string could be detected however if the change in the phase is a multiple of 2π the string would not be detected.

$$ge = \frac{\hbar c}{2} n \quad or \quad g = \frac{n}{2\alpha} e \quad from \quad \frac{4\pi eg}{\hbar c} = 2\pi n \qquad n = 1, 2, 3, ... \tag{2.5}$$

Where g is the magnetic charge and α is the fine structure constant which equals $\alpha = \frac{1}{137}$. This leads to the conclusion of the Dirac quantization condition below, which states that the presence of a magnetic monopole leads to the quantization of charge, expressed as $g\,q = nh\,/\,\pi_o$, where n is a positive integer number.

There are many other scenarios one could reach to observe the quantization condition [129] which reinforces the above conclusion. To determine the fundamental magnetic charge, which is known as Dirac charge g_D, last equation (2.5) could be written in terms of e and the fine structure constant $\alpha = \frac{\pi_o e^2 c}{2h}$ assuming $n = 1$, the equation (2.2) will be:

$$g = \frac{n}{2\alpha}(ce) \quad \longrightarrow (n = 1) \quad g_D = \frac{ce}{2\alpha} \tag{2.6}$$

2.3 Magnetic Monopoles

In this section, we will discuss some of the theories that demand the existence of the magnetic monopoles. Some of the important characteristics of monopole will be discussed as well as interactions of monopole with the mat-

ter.

2.3.1 Classical Electrodynamics

2.3.1.1 Symmetrizing Maxwell's Equation

Classically, the well-known Maxwell's equations describe the asymmetry of the electric and magnetic fields, as no magnetic monopole had ever been seen, the isolated magnetic charges are kept out from Maxwell's equation – making them asymmetric. A magnetic monopole restores the symmetry to equations of Maxwell [88]. Figure 2.3 represents the equations of Maxwell with and without the effect of magnetic monopoles.

Name	Without Magnetic Monopoles	With Magnetic Monopoles
Gauss's law:	$\vec{\nabla} \cdot \vec{E} = 4\pi\rho_e$	$\vec{\nabla} \cdot \vec{E} = 4\pi\rho_e$
Gauss' law for magnetism:	$\vec{\nabla} \cdot \vec{B} = 0$	$\vec{\nabla} \cdot \vec{B} = 4\pi\rho_m$
Faraday's law of induction:	$-\vec{\nabla} \times \vec{E} = \frac{\partial \vec{B}}{\partial t}$	$-\vec{\nabla} \times \vec{E} = \frac{\partial \vec{B}}{\partial t} - 4\pi\vec{J}_m$
Ampère's law (with Maxwell's extension):	$\vec{\nabla} \times \vec{B} = \frac{\partial \vec{E}}{\partial t} + 4\pi\vec{J}_e$	$\vec{\nabla} \times \vec{B} = \frac{\partial \vec{E}}{\partial t} + 4\pi\vec{J}_e$

Figure 2.3: Maxwell's equation with the effect of magnetic monopoles

Where E and B represent the electric and magnetic fields respectively. ρ_e and J_e represent electric charge and current densities. This replacement is not forbidden theoretically. As P. Dirac described "The Theoretical reciprocity between Electricity and Magnetism is perfect " [23].

On the other hand, the new modified equations do not predict the magnitude of the magnetic charge and current density and we can not derive the quantization of charge from those equations [89]. Maxwell's equations are the

equations which describe the asymmetry between electric and magnetic fields, are indicated below as follow:

$$\vec{\nabla} \cdot \vec{\mathbf{E}} = 4\pi\rho_e \tag{2.7}$$

$$-\vec{\nabla} \times \vec{\mathbf{E}} = \frac{\partial \vec{B}}{\partial t} \tag{2.8}$$

These equations determine the electric field which is generated with charge density ρ_e, it states that electric field lines are propagating from positive charges and ends (terminated) on the negative charge, i.e. the electric field is diverging away from the positive charge. Similarly, another two equations that describe the magnetic field is illustrated below

$$\vec{\nabla} \cdot \vec{\mathbf{B}} = 0 \tag{2.9}$$

$$\vec{\nabla} \times \vec{\mathbf{B}} = \frac{\partial \vec{E}}{\partial t} + 4\pi\vec{J_e} \tag{2.10}$$

Where J_e is the electrical current density which determines the magnetic field. The magnetostatic equations show that the magnetic field B is curling around the current and it does not diverge which means the lines of the magnetic field don't originate or terminate anywhere. This explains the zero divergence in this equation $\vec{\nabla} \cdot \vec{\mathbf{B}} = 0$, which shows the absence of the magnetic charge as the electric charge. The theory integrates the results of experimental observation where none of the magnetic charges or magnetic currents have been observed and only the electric charge and current densities are the main sources of both electric and magnetic fields. If the magnetic charge happened to exist, it would have both magnetic current and charge density analog to the electric charge.

The existence of magnetic monopoles would lead to some modifications in Maxwell's equations which would lead to the symmetry in describing the

electric and magnetic field, as below.

$$\vec{\nabla} \cdot \vec{\mathbf{B}} = 4\pi\rho_m \tag{2.11}$$

$$-\vec{\nabla} \times \vec{\mathbf{E}} = \frac{\partial \vec{B}}{\partial t} + 4\pi\vec{J_m} \tag{2.12}$$

By introducing the magnetic charge and current density J_m, Monopole's magnetic charge g would equal to the integral of the magnetic charge density ρ_m.

In conclusion, by introducing the magnetic monopoles, Maxwell's equations would be symmetric for both electric and magnetic fields under the duality of transformation

$$\begin{pmatrix} \vec{E} \\ c\vec{B} \end{pmatrix} = \begin{pmatrix} \cos\xi & \sin\xi \\ -\sin\xi & \cos\xi \end{pmatrix} \cdot \begin{pmatrix} \vec{E'} \\ c\vec{B'} \end{pmatrix} \tag{2.13}$$

$$\begin{pmatrix} c\rho_e \\ \rho_m \end{pmatrix} = \begin{pmatrix} \cos\xi & \sin\xi \\ -\sin\xi & \cos\xi \end{pmatrix} \cdot \begin{pmatrix} c\rho'_e \\ \rho'_m \end{pmatrix}$$

Where c is the speed of light and ξ is the transformation parameter. Symmetrize Maxwell's equation is only possible by introducing the magnetic monopoles and then the electric and magnetic fields could be considered to be simple transformation of one another i.e. such a transformation leads to $\vec{E} \to \vec{B}$ and $\vec{B} \to -\vec{E}$ for transforming between the two fields, $c\rho_e \to \rho_m$ and $\rho_m \to c\rho_e$, for $\xi = \pi/2$ for the transformation between the sources of the fields.

2.3.2 The Schwinger Monopole

After a few decades, J. Schwinger had extended the prediction of Dirac's theory in order to study monopole's relativistic invariance [163]. He found that the vector potential which presents a solution for the field of magnetic monopoles [166] can be explained as follow:

$$\overrightarrow{\mathrm{A}}(\overrightarrow{\mathrm{r}}) = \frac{\mu_o g}{4\pi r}\cot\theta\hat{\phi} \tag{2.14}$$

By this definition, it may lead to many quantization conditions other than the scenario that Dirac proposed by Dirac, $gq = \frac{2nh}{\mu_o}$. This shows that the lowest magnetic monopole charge would be twice the Dirac charge. It is also worth maintaining that Schwinger's work had generalized the condition of quantization to study Dyons, which is the particle with both electric and magnetic charge [164].

$$q_1 g_1 - q_2 g_2 = \frac{2nh}{\mu_o} \tag{2.15}$$

where q_1, g_1 and q_2, g_2 are the electric charge and magnetic charge of the dyons.

2.3.3 Monopole-Photon Coupling

The fine structure constant α, which is the strength of the coupling between the photon and the electron, can be used to define the monopole-photon coupling by

$$\alpha = \frac{\mu_o e^2 c}{4\pi\hbar} \quad \overset{e\to g=ng_D/c}{\longrightarrow} \quad \alpha_m = \frac{\mu_o g_D^2}{4\pi\hbar c} n^2 \tag{2.16}$$

The strength of the coupling between the electron–photon is given by the

fine structure constant and similarly the strength of the coupling between the magnetic monopole and photon which is called magnetic coupling constant, and this can be defined by replacing e^2 with $g^2 = (ng_D/c)^2$.

This indicates that the strength of magnetic coupling is almost 4 orders of magnitude greater than the fine structure constant for electron–photon coupling. The magnetic coupling constant is $\alpha_m \approx 34.24$, for $n = 1$. This is the second feature of the magnetic monopole along with the quantization condition. Figure 2.4 represents the electric strength coupling (left) and the magnetic strength coupling (right).

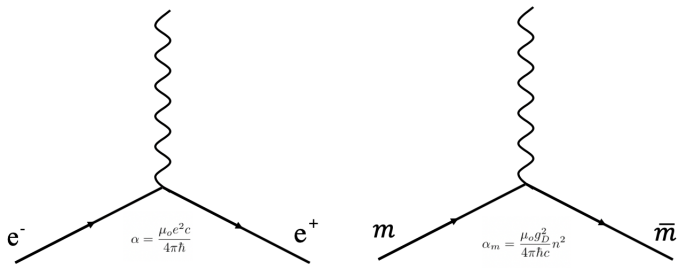


Figure 2.4: The electric strength constant (left) and the magnetic strength constant (right)

2.3.4 Monopole in the Grand Unified Theories (GUTs)

Independently, t' Hooft [111] and Polyakov [145] showed that the existence of the magnetic monopoles has been predicted by the Grand Unified Theories (GUTs), where the electromagnetism $U(I)$ group is embedded in larger compact non-Abelian group.

This is the same case as the case of the standard model, in which $SU(2)_L \times U(I)_Y$ symmetry breaks down to $U(I)$ symmetry of electromagnetism which results in rising the electroweak monopoles. However, some arguments showed that when this symmetry group undergoes spontaneous symmetry breaking [180, 43], it does not admit monopole solutions. GUT models have proposed another solution called "The Hedgehog Configuration", in which the scalar field's direction is coupled to the spatial direction because the vacuum's sym-

metry is almost broken when the vacuum state of the scalar field assumed a specific direction

$$\phi^a = \nu \frac{r^a}{r}, \qquad a = 1,2,3 \tag{2.17}$$

2.3.4.1 Charge Quantization and Monopole Mass in GUT Models

The quantization of charge, as a result of the existence of monopoles, which was predicted by Dirac theory, arises in the GUT models when the $U(I)$ group of electromagnetic is embedded into a higher rank of the semi-simple non-Abelian group. GUTs models that described symmetry breaking spontaneously, did not predict any solution for the monopole.

Dirac's theory of magnetic monopoles could not fully predict the mass of the monopole. On the other hand, the GUT models have predicted the magnitude of the mass of the magnetic monopole to be equal to $M \cong 137 m_x$, where m_x is the vector boson's mass [183]. GUTs models predict that the Strong, Electromagnetic, and Weak forces are merging at high energies $\sim 10^{18}$, as shown in figure 2.5.

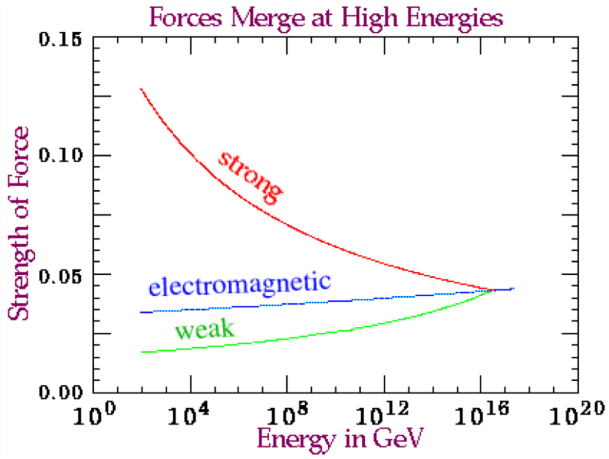


Figure 2.5: GUTs show that forces are merging at high energies

In GUT models, the vector boson's mass is equal to the unification scale

mass ($10^{16}\,GeV$) [36]. Thus, the magnetic monopole mass which is predicted by GUT models is of order $10^{18} GeV$ which is currently outside the reach of the current particle colliders.

Unlike the theory of Dirac for magnetic monopoles, GUT models have predicted the mass of the monopole. Classically, this prediction is obtained because the energy of the monopole's configuration is at rest, which corresponds to the mass of the monopole. Monopole configuration energy is composed of the Abelian fields' energy outside the monopole core, R_c, which is related to the reciprocal of the mass of the vector boson of the model $R_c \sim (mx)^{-1} \sim (ev)^{-1}$ and the energy of the scalar field inside the core.

2.3.5 Monopoles in Electroweak Models

In the Framework of the standard model, magnetic monopoles are believed not to exist. However, there are monopole-like solutions, known as Electroweak monopole, which have been proposed to be possible in the Standard Model electroweak sector [180] [43].

These Electroweak monopoles obey Schwinger's charge quantization condition (see equation 2.1), and this leads to a minimum charge of $2\,g_D$. The difference between GUT monopoles and Electroweak monopoles is that there is no well-defined mass for the Electroweak monopoles, like Dirac monopoles. However, recently there are some developments have been predicted that the monopole mass is of an order of $4-10\ TeV$ [118, 93], such mass range could be produced at the current particle's colliders, such as LHC and possible future circular colliders (FFC).

2.4 Particle Interaction in Matter

To understand how to distinguish between different particles in the CMS detector, we should discuss the passage of fundamental particles through the matter. Primarily, charged particles interact through inelastic collisions with

electrons and atomic nuclei of the matter [104, 102, 106]. There are two possibilities for interactions with the atomic electrons, either Excitation or Ionization processes. When a particle passes through the matter and interacts with the atomic electron, it can excite the electrons to a higher energy state, and a photon is emitted when the electron de-excite to the ground state. This photon can be detected as a scintillation light. Also, the passing charged particle can ionize the atomic electron, in a way that the electron is completely separated from the atom. The ionization energy loss's mean rate of a charged particle in this case can be described by the famous Bethe Bloch equation:

$$-\left\langle Ex \right\rangle = KQ^2 \frac{Z}{A}\frac{1}{\beta^2}\left[\frac{1}{2}\ln\frac{2m_e c^2\beta^2\gamma^2 T_{max}}{I_e^2} - \beta^2 - \frac{\delta(\beta\gamma)}{2}\right] \tag{2.18}$$

The variables used in the Bethe equation are summarized in the below table.

Table 2.1: The variables used in the Bethe equation 3.6

Symbol	Definition	Value/Units
m_e	Electron mass	0.511 MeV
r_e	Electron radius $= e^2/4\pi\varepsilon_0 m_e$	$2.82\,fm$
Q	incident particle's charge	
Z	Atomic number of the material	
A	Atomic mass of the material	$g\ mol^{-1}$
N_A	Avogadro's number	$6.022\times10^{23} mol^{-1}$
K	$4\pi N_A r_e^2 m_e$	$K/A = 0.307 MeV g^{-1} cm^2 for A = 1 g mol^{-1}$
β	Speed per unit c of the incident particle	
γ	$\frac{1}{\sqrt{1-\beta^2}}$	
T_{max}	Maximum kinetic energy which transferred to a free electron in a single collision	MeV
I_e	Mean excitation	eV
$\delta(\beta\gamma)$	Density effect correction to ionization energy loss	

Electron's energy loss inside the matter is represented in figure 2.6. The dominant process for the electron/positron energy loss at low energies is the Ionization process. logarithmically, the ionization rates fall off with energy and linearly, the bremsstrahlung losses dominate above few tens of MeV in most of the materials. In the CMS detector, the bremsstrahlung process is dominating for electrons which are traveling with energies above a few GeV.

Charged particles can interact with the nuclei of the matter they pass through.

When the particle interacts with the nucleus, a photon is emitted and this can represent radiation. The incident particle undergoes bremsstrahlung radiation, this happens when the charged particle gets deflected by the nucleus and loses an amount of significant energy. If the incident particle is a hadron, it can interact via the Strong force with the nucleus of the matter and this interaction will create quarks and antiquarks, which could be combined in several ways to form mesons and baryons, such a process called Hadronization.

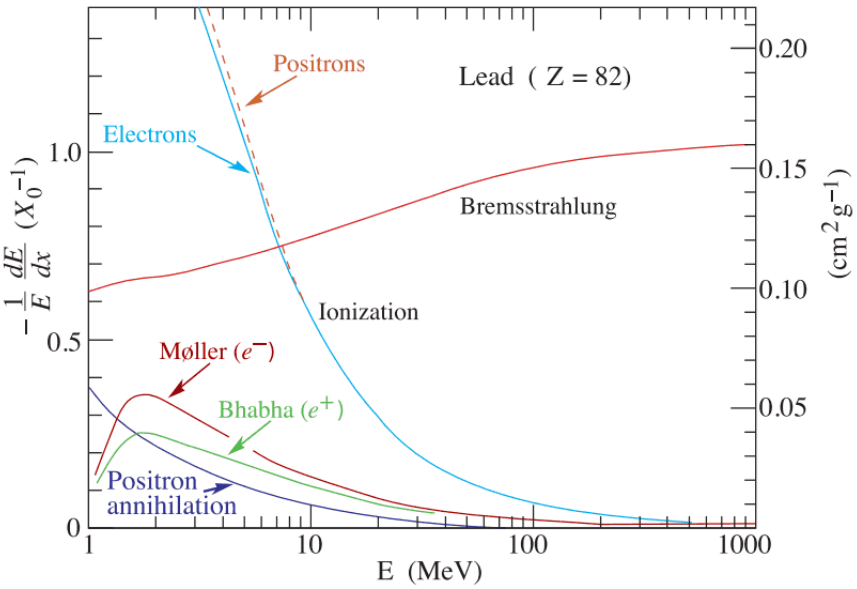


Figure 2.6: Fractional energy loss per radiation length in lead as a function of electron or positron energy [104].

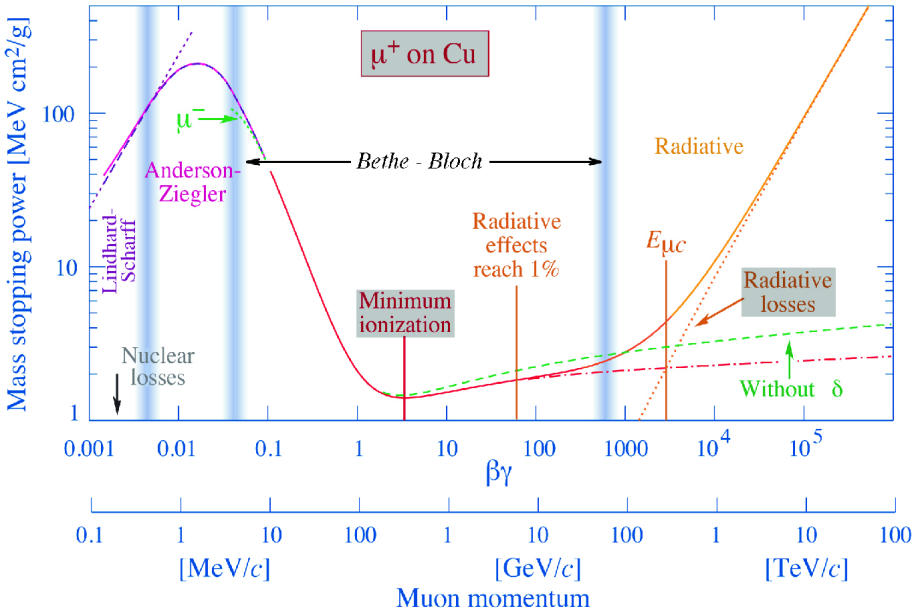


Figure 2.7: Illustration of the stopping power $-\langle Ex\rangle$ for muons in copper as a function of $\beta\gamma = p/Mc$ [176]

The behavior of muons particles when interacting with the matter is described in figure 2.7. The distribution represents an illustration of the stopping power $-\langle Ex\rangle$ for muons in copper material as a function of $\beta\gamma = p/(Mc)$. Solid curves show the total stopping power while the vertical bands indicate boundaries between different approximations. If the momentum of the muons is sufficiently low (less than a hundred GeV), they will lose energy in the detector through the Ionization process. If their momentum is greater than a hundred GeV, they will lose energy via radiation. For photons, the Photoelectric effect dominates at low energies, while for energies of a few MeV, the dominant process is the Compton effect. Pair production process dominates when the photon energy increases above $1\,GeV$.

2.4.1 Passage of Monopoles through Matter

The interaction of the magnetic monopole with the electromagnetic field is similar to the interaction of electrically charged particles. In the presence of electromagnetic field, a particle with electric and magnetic charge is experiencing a force which is known as Lorentz force, which expressed as follow:

$$F = q(\vec{E} + \vec{v} \times \vec{B}) + g(\vec{B} - \vec{v} \times \frac{\vec{E}}{c^2}) \tag{2.19}$$

Thus, both monopole and highly electrically charged objects (HECOs) are considered to be highly ionizing particles (HIPs). Most of the HIPs have a very unique distinguishable parameter, which is dE/dx, the energy loss inside the matter. Three mechanisms are considered in the energy loss of the charged particles. *Ionization* of the medium, *Bremmstrahlung* and *Pair Production*.

The energy losses in the range of $\gamma < 10$, for Pair Production and the Bremsstrahlung, are negligible. In particle colliders, the dominant energy loss process for the magnetic monopole is the Ionization. Figure 2.8 shows a comparison of the energy loss of monopole with mass $1000\,GeV$ and charge $\mid g \mid = 1.0\,g_D$ in argon for the different three mechanisms.

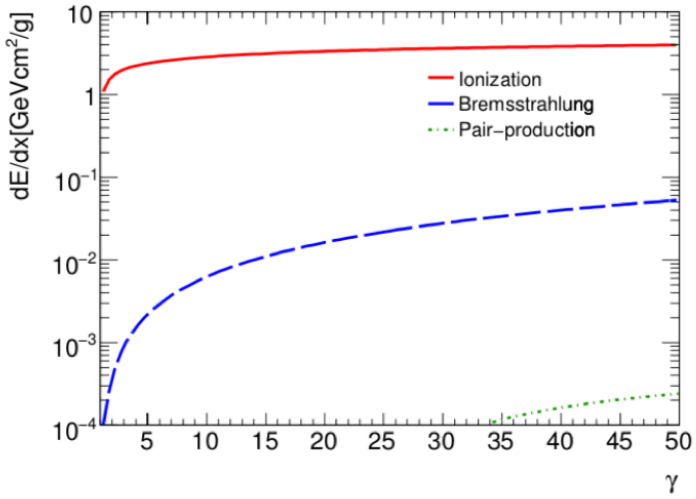


Figure 2.8: Energy loss due to Ionization is indicated by the red line, the blue line for Bremsstrahlung, while the Pair production is indicated by the green line, the unit of γ is c_{-1}

2.4.1.1 Energy Loss via Ionization

When the charged particles transverse through the matter, they lose their energies, either by interacting with the atomic electrons of the matter, which

cause liberation of electrons from the atoms of the material, or by colliding with the nuclei of the atom, this results in displacing the atom from the lattice which causes non-ionizing energy loss. When the magnetic monopole traverses through matter, large energy depositions are expected to exist due to ionization and the strength of the interaction of the orbiting electron of the medium and the magnetic field of monopoles. To study the interaction of monopoles with the medium, The Bethe-Bloch formula for an electrically charged particle can be modified by substituting βg for $z e$.

Monopole's energy loss consists of two regimes, a high - momentum transfer regime (close interaction) and a low - momentum transfer regime (distance interaction). Kazama, Yang, and Goldhaber (KYG) had introduced a model of the former regime which they solved the equation of Dirac for an electron in the existence of the magnetic field of a monopole [116]. While the latter regime has been modeled using the dipole approximation. The energy loss formula takes into account the close and distance interactions as they based on the first - order Born approximation, which was developed by Ahlen [25], with an accuracy of about 3 % for monopole with $\beta \geq 0.2$ and $\gamma \geq 100$. The energy loss formula for the monopole is given by:

$$-\left\langle Ex \right\rangle = Kg^2\frac{Z}{A}[\ln\frac{2m_e c^2\beta^2\gamma^2}{I} + \frac{k(g)}{2} - \frac{1}{2} - \frac{\delta}{2} - B(g)] \tag{2.20}$$

Where $g = ng_D$ represents the magnetic charge, βc is the monopole's speed. $k(g)$ is the KYG correction (introduced by Kazama, Yang, and Goldhaber) which is the result of the relativistic cross-section calculations, and $B(g)$ is the Bloch correction.

Figure 2.9 presents the energy loss per unit length, dE/dx, for an electrically charged particle with $\mid z \mid = 68.5\, e$, left, and for magnetic monopole of charge $\mid g \mid = 1.0\, g_D$, right, as a function of the the particle velocity, β, for different materials.

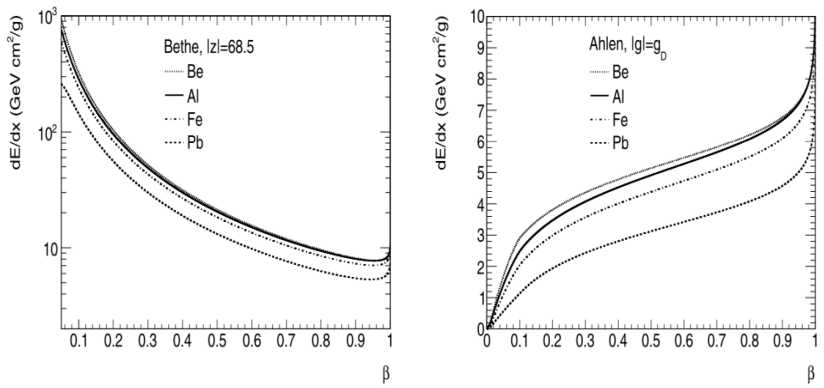


Figure 2.9: Energy loss per unit length, dE/dx, for an electrically charged particle with $\mid z \mid = 68.5\,e$ (left) and for magnetic monopole of charge $\mid g \mid = 1.0\,g_D$ (right) as a function of the the particle velocity, β, for different materials[86]

The ionization energy losses for some electrically charged particles and monopoles due to ionization are shown in figure 2.10. It is very obvious that the energy loss for magnetic monopoles is about four orders higher than any other electrically charged particle due to the magnitude of the magnetic charge compared to the electric charge $g^2 \sim 4692$.

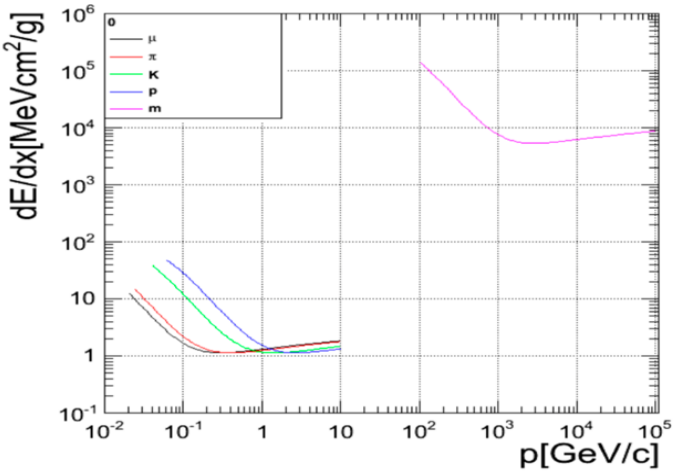


Figure 2.10: Ionization energy loss for μ, π, k, p and monopole.

2.5 Monopole Detection Methods

Furthermore, with the prediction of magnetic monopoles in GUT models by Hooft-Polyakov [111, 145], the search for such a particle became so interesting. Several detection techniques have been developed to search for magnetic monopoles as a result of the prediction of monopoles which may lead to explain the charge quantization [88]. By taking advantage of the production of large ionization due to the passage of monopoles through the matter, different detection methods have covered a range of techniques and technologies. Besides the highly ionizing signature of the monopoles, in the presence of the magnetic field, they are accelerated in a different way than any other particle with an electric charge. This is the main reason for detecting the monopoles as anomalous tracks in detectors with an existing magnetic field.

The most sensitive detection technique for monopoles that bound in the matter is the divergence of the monopole's magnetic flux, which is the most ultimate signature of a monopole that sets it apart from any other highly electric charged particles. The deviations from the Standard Model (SM) predictions in such processes where photons are present, to which monopole couple very strongly, may be observed. Due to the high coupling between monopole and photon, in the SM processes, the deviations from the SM predictions may be observed. The most common detection methods which are used in the direct and indirect searches for magnetic monopoles will be briefly discussed.

2.5.1 Direct Detection Methods

Directly, monopoles would be detected when they pass through the matter. The condition of quantization, equation 2.1, shows that Dirac charges g_D is almost equivalent to 68.5 $(c\,e)$. Monopole acts as a highly ionizing particle with such an electric charge equivalent. Monopole's energy loss is therefore very large and the monopoles deposit all their kinetic energy and get trapped in the material. The development of the detection methods has taken place to detect the existence of magnetic monopoles that are bound in the matter and their passage through the material. Some of the commonly used methods for

monopoles detection are discussed below.

2.5.1.1 Monopole Bound in Matter

During the phase transition in the early universe, monopoles may have been produced. They may be accelerated by the magnetic field to relativistic speeds, while some may be trapped or binding to the atomic nuclei of the matter with energies of the order of $100\,keV$ [130]. GUT models have predicted that presence of monopoles bound in matter such as lunar rocks [155], meteorites [112] and in the earth's crust [47].

For the other type of monopole produced at particle colliders, which can be found trapped in matter. For monopoles produced in a high energy collision, some kinetic energy is required to be able to make the monopole pass the first layer of the inactive material before it reaches the active parts of the detector. That's why there is a high probability for monopoles to be stopped in the beam-pipe. Also, another source of trapped monopoles, is the materials surrounding the interaction points of high energy colliders [79, 114].

The most common detection method for magnetic monopoles, which is trapped in a matter through passing a sample of material like rocks or parts of a particle detector, is the "SQUID" magnetometer which is a superconducting loop coupled to a superconducting quantum interference device. An induced current in the system is produced by an increase in the magnetic flux through the loop that is generated by a monopole. On the other hand, while a full passage through the loop, a magnetic dipole would not induce a net current. The variation in the magnetic flux can be detected by the "SQUID magnetometers" and it is as small as a quantum of magnetic flux $\phi_o = h/2\,e$, for a monopole with charge g, the total magnetic flux $\phi_g = \mu_o g_D = h/e$ and this indicates that a monopole with Dirac charge g_D would have twice the total flux of the quantum magnetic flux.

Despite detecting the monopoles that are bound in matter, primarily, through the induction technique, the measuring of the flux of monopoles in cosmic rays has also been implemented. By using a SQUID magnetometer, it has been measured as a single candidate with a consistent expected signal from a monopole

with charge g_D and this is one of the famous experimental results by Cabrera [55].

Also, another method for the detection of monopoles bound in the matter was by applying a strong magnetic field on the sample to be able to extract the rapped monopoles. Then a complementary method is used to detect these extracted monopoles [35].

2.5.1.2 High Ionizing Active Detection

As described before, monopoles are highly ionized particles and their energy losses are about 4 orders larger than the energy losses of any other electric particle of unit charge e. Most of the particle detectors are designed with the ability to measure the dE/dx for the electrically charged particles. For this reason, when a monopole passes through such a detector a unique signature can be observed. Through ionization, fast-moving monopoles lose a huge amount of energy by producing energetic δ-rays. Depending on the detection method, this could be observed and measured with a large amount of collected charge or light produced which can be considered as a highly ionizing particle. The energy losses are not well understood for the very slow monopoles ($\beta < 0.01$) and it is expected that monopoles become bound to atomic nuclei [146].

The most fundamental detection method to measure energy losses is ionization. Semiconductor trackers, drift chambers, and scintillators are examples of detectors that measure the dE/dx.

2.5.1.3 Heavy Etching on Nuclear Track Detector

To identify the highly ionizing particles, nuclear track detector (NTD) or plastic foils are widely used to search for magnetic monopoles in cosmic rays [40, 134] and also at high – energy particles colliders [143, 20]. In order to minimize the amount of material in which monopoles could be trapped in, plastic foils are added in a way that surrounds the interaction points at colliders. With passing the highly ionizing particles through the NTD, the plastic foil is dam-

aged due to the displacement of the lattice atoms [95] which created the high ionization and the non-ionization energy loss. The value of the energy loss dE/dx could be measured.

NTD foils are then etched by soaking the foils in a chemical bath which dissolves the damaged part of the foil, in order to make sure that the damage created is because of the passage of monopoles. From the geometry of the etch pit cones, one can determine and study the energy loss rate of the passage particle dE/dx under a microscope.

In a ballon-brone experiment, the NTD technology was used in cosmic rays, to study objects with a large electric charge. Evidence for the existence of a fast-moving magnetic monopole with charge $2\,g_D$ has been observed [147].

2.5.1.4 Anomalous Tracks in Magnetic Field

Monopoles are accelerated along the magnetic field, unlike electrically charged particles that experience a force perpendicular to the direction of the field. The Lorentz force equation (equation 2.19), describes the interaction of monopoles with the magnetic field. By immersing the tracking detectors in a known magnetic field, the momentum of charged particles can be measured. Generally, the track reconstruction algorithms for a particle, assume that the particle possesses an electric charge and no magnetic charge and the particle's momentum can be measured from the curvature of the track.

For magnetically charged particles, they produce anomalous tracks and their trajectories would be followed in a different plane in particle accelerators. It is immersed in a solenoid magnet in which a magnetic field in the z-axis direction is produced, and it could record curved (circular) tracks in x–y plane and straight tracks in the $r-z$ plane. On the other hand, a monopole follows a parabolic trajectory in the $r-z$ plane and a straight track in the transverse $x-y$ plane.

In the existence of a magnetic field, as the energy losses are considered, the actual trajectory of a monopole differs from a perfect parabola. This detection technique has been used in many searches at particle colliders [53, 98]. It is

highly important to note that there is a huge amount of δ-rays produced along the trajectory of a monopole and the algorithm for the track reconstruction may have some difficulties to recognize the monopole – like a particle in such tracking detectors.

2.5.2 Indirect Detection Methods

Monopoles can be detected in an in-direct way through the effect of high order contributions to the processes of the Standard model. At a particle collider, the decay of Z boson could be mediated by monopoles.

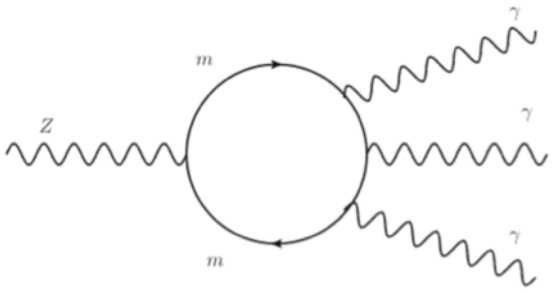


Figure 2.11: Feynman diagram of the process $Z \to \gamma\gamma\gamma$, which can be mediated by fermions and hypothetically by magnetic monopole.

In processes that give rise to multi-photon final states, as shown in figure 2.11, virtual monopoles can mediate these processes. At the Large Electron-Positron (LEP), the $L3$ experiment has been searched for monopoles signature, indirectly by using the process $Z \to \gamma\gamma\gamma$ [15]. By the existence of monopoles which would couple to the z boson, the process which is suppressed in the SM has an enhanced cross-section and the results are consistent with Quantum Electrodynamics (QED) background expectations. This lead to a lower limit of monopole mass at $520\,GeV$ and a branching ratio limit $BR(Z \to \gamma\gamma\gamma) < 0.8 \times 10^{-5}$.

Based on the high monopole-photon coupling, which is much higher than the electron-photon coupling, $D0$ experiment, at Tevatron, has established another indirect search method for monopoles at $\sqrt{s} = 1.8\,TeV$ [9]. Virtual monopoles are expected to give rise to photon-photon re-scattering as described in [99, 87].

With no effect observed over the background, lower 95% C.L. limits of 610, 970, or 1580 GeV on the mass of spin 0, $1/2$ and 1 Dirac monopole of charge equal to $1.0\,g_D$ is set.

2.5.3 Searches at Electron-Positron Colliders

At Large Electron-Positron Collide (LEP) collider, there two experiments has searched for magnetic monopoles which produced in $e^+\,e^-$ collisions at $\sqrt{s} = 91.1\,GeV$. A dedicated experiment, MODAL experiment, has been built around the LEP interaction points which used NTD foils [119]. As monopoles are highly ionized particles, they are expected to produce tracks while passing through the foils. No monopole-like tracks were found in the NTDs. By using the Drell-Yan mechanism as a mechanism for the monopole production, the MODAL experiment has set limits on the monopole cross-section in 1992. Drell-Yan mechanism became the benchmark model for most of the collider's searches. 70 pb was the upper production cross-section limit for this experiment [143]. There is another experiment with 0.3 pb cross-section production limit, assuming the Drell Yan mechanism, which used NTD foils, located around the beam pipe and OPAL detector's parts with $4\,\pi$ coverage. Both experiments were only able to rule out monopoles of mass $m < 45\,GeV$ due to the limitation of the LEP collider. All the previous results apply for monopoles of charge 1.0 and $2.0\,g_D$.

The limits from LEP were later exceeded by OPAL at LEP2 with data from $e^+\,e^-$ collisions at $\sqrt{s} = 206.3\,GeV$ [81]. The detection techniques of this search varied from that of previous searches at LEP. OPAL made use of its jet chamber to identify high ionization deposits and trajectories that bent in a plane parallel to its solenoidal magnetic field. In the absence of an observation, upper limits on the production cross-section were set to 0.05 pb for monopoles of charge $\mid g \mid = 1.0\,g_D$ and masses in the range $45 - 102\,GeV$, assuming Drell-Yan production. It can be concluded that the combination of the results from all LEP and LEP2 searches effectively excludes monopoles of mass $m < 102\,GeV$.

2.5.4 Monopoles at the LHC

ATLAS and MoEDAL experiments are the most recent colliders searches for the magnetic monopole. In run I, ATLAS experiment has searched for magnetic monopoles with data from proton–proton collision at $\sqrt{s} = 7\,TeV$ [5]. Combining the measured parameters from several subdetector (transition radiation tracker TRT and the electromagnetic calorimeter EM) of ATLAS experiment to be able to identify monopoles with mass range $200 - 1500\,GeV$. An upper limit of $2\,fb$ was set on the production cross-section for monopoles of charge $1.0\,g_D$, using the Drell-Yan mechanism as a benchmark for the monopole production. A variation in the upper cross-section limits from $0.2\,pb$ to $0.02\,pb$ was obtained for monopole masses $200 - 1200\,GeV$. In the selected data, No monopoles event was observed by ATLAS in run I.

During run I of the Large Hadron Collider (LHC) there was a search that was done with ATLAS detector using an integrated luminosity of $7.0\,fb^{-1}$ with $8\,TeV$ proton-proton collision data. They used a highly ionizing particle's signature which stopped in the electromagnetic calorimeter. Through a combination of the measured ionization in the transition radiation tracker (TRT) and the energy deposition's shape in the electromagnetic calorimeter, candidates were selected.

Zero observations have been found in the signal region. The search was very sensitive by setting an upper limit on the cross-section production for monopole masses and all charge points simulated. They showed in that the model that the upper limit on the production cross-section of $0.5\,fb$ was independently obtained for masses between $200\,GeV$ and $2500\,GeV$ and for magnetic charge rang of $0.5\,g_D$ and $\leq \mid g \mid \leq 2.0\,g_D$ and electric charge range of $20 \leq \mid z \mid \leq 60$. They used the Drell-Yan pair production mechanism of spin $1/2$ and spin 0.

Improvements have occurred with these results on the upper limits on the cross-section production for masses and charges of the high ionizing particles and extended the limits to higher masses ($> 1500\,GeV$). For the first time at the LHC, monopoles with magnetic charge larger than $1.0\,g_D$ (up to $1.9\,g_D$) and stable exotic particles with electric charge larger than $\mid z \mid = 17$ (up to $\mid z \mid = 60$) were probed. The results of ATLAS experiment at run II are indicated later in chapter 7 with a comparison with CMS search.

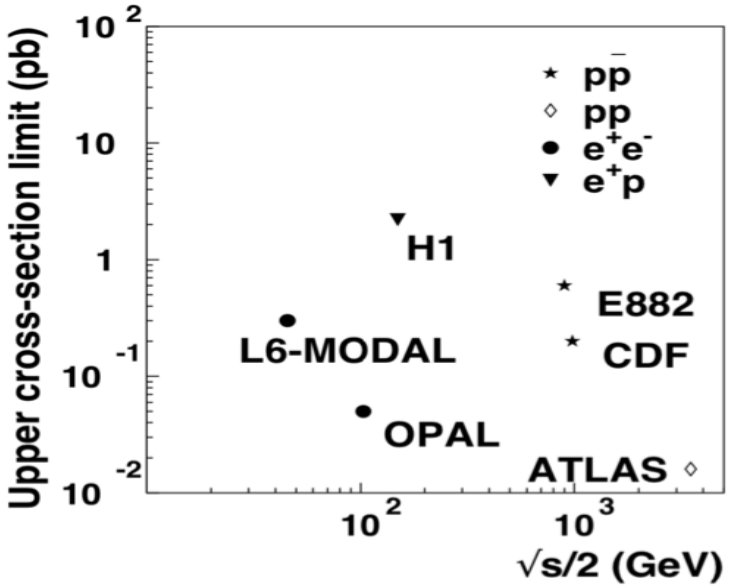


Figure 2.12: Summary of upper limits on production cross section as a function of $\sqrt{s}/2$ for several experiments that used data collected at different types of colliders

.

The searches are going on, a huge effect on physics could happen by discovering magnetic monopoles. Monopole's properties would enable us to explore some fundamentals of the new physics which are not possible with other particles. As magnetic monopoles are stable and highly ionizing particles, we could extract them easily from the trapping detector. Also, the interaction of monopoles with the electrically charged fermions would depend on physics in a very sensitive way at very high energies.

The importance of Electricity and Magnetism in technology is highly recognized, which indicates that magnetic monopoles could have some practical applications, however, this would be very specialized as the cost of producing such a particle is very high. Figure 2.12 presents a summary of the upper limits on the production cross-section obtained by searches performed by several experiments with data from different types of particle colliders.

CHAPTER 3

THE LARGE HADRON COLLIDER (LHC)

3.1 The Large Hadron Collider (LHC)

In order to find responses for the current open questions of particle physics and discover new particles, experiments with large multi-layers detectors have been built at particle colliders. The Large Hadron Collider (LHC) is the largest particle accelerator in the world. It is located at the *European Organization for Nuclear Research* (CERN) in Geneva, Switzerland. At LHC, two protons beams are being accelerated at energies of $6.5\,TeV$ in opposite direction along a $27.6\,km$ path, $100\,m$ underground, to record $13\,TeV$ centre of mass-energy in the proton-proton collisions. The Standard Model can be probed in several ways and we can perform many searches for particles beyond the standard model by using the recorded data from the generated collisions at the interaction points along the accelerator ring.

A detailed description of the LHC and its main experiments is presented in the next sections. LHC experiments have been built around the interacting points of the LHC. In particular, the Compact Muon Solenoid (CMS), the general-purpose experiment will be described in more detail.

3.1.1 LHC Overview and Injector Chain

In the already existing Large Electron-Positron (LEP) collider tunnel, the LHC was installed. Its circumference is 27.6 km. It accelerates the charged particles, protons, or lead ions. The maximum collision energy and the luminosity that could be reached by the LHC, are the main specifications for the machine. The highest energy is required to be able to detect new heavy particles, predicted by many theories beyond the standard model.

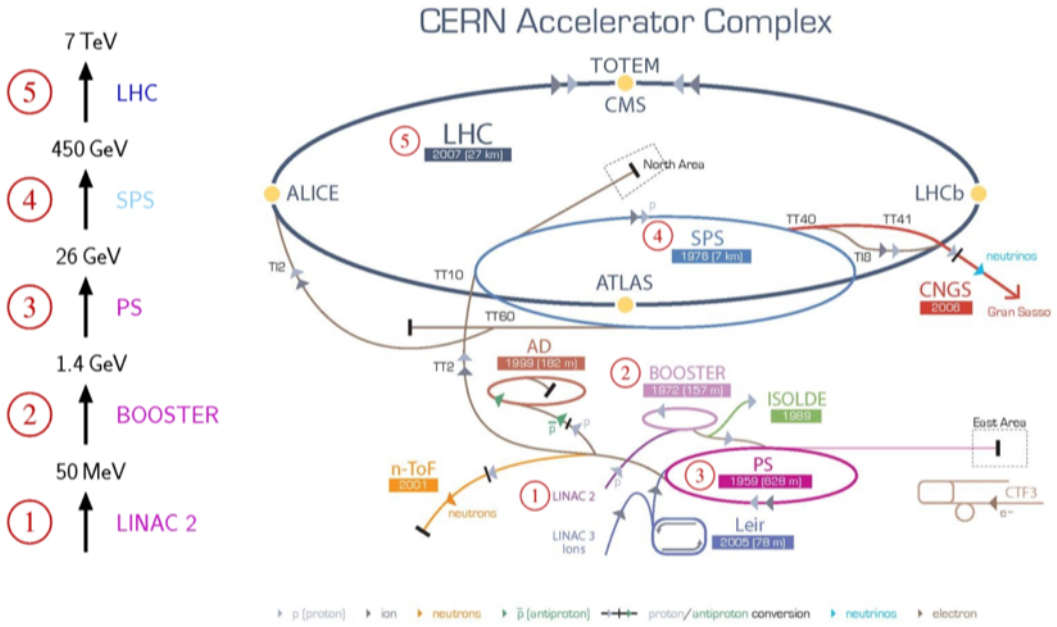


Figure 3.1: LHC Injector Chain

The colliding particles at the probed energies are not the protons or lead ions but their constituents, which carries a fraction of the momentum of the proton. The LHC machine is an ideal instrument for extrapolation at high energies. A wide energy range could be covered by collisions. The colliding particles (protons or lead ions) need to be accelerated gradually. This injection process relies on a chain of several pre-accelerators at CERN, as illustrated in figure 3.1.

In the case of proton beams, a bottle of hydrogen is the source of protons. Through ionization of the hydrogen atoms, the protons are separated and later

accelerated up to $50\,MeV$ by *LINAC2*, a linear accelerator. Then, the proton beams are transferred to a circular accelerator: *the Proton Synchrotron Booster* (PSB), which accelerate the proton to the energy of $1.4\,GeV$. After they have been accelerated in the *Proton Synchrotron* (PS), the proton beams are injected into the *Super Proton Synchrotron* (SPS) with the energy of $26\,GeV$. Finally, the proton beams are injected in the opposite direction to the LHC with the energy of $450\,GeV$ and with a speed almost equal to $99.99\,\%$ of the speed of light.

For accelerating the lead ions, before being injected in the *Low Energy Ion Ring* (LEIR), first they got accelerated in several linear accelerators: *LINAC3* at an energy of $4.5\,MeV$ per nucleon, later energy of $72\,MeV$ per nucleon, then they follow the same path as the protons through the PS where they are accelerated up to $5.9\,GeV$. At SPS, they are accelerated up to $177\,GeV$. At LHC, the recorded centre of mass-energy so far for the heavy ions in 2015 and 2016 respectively, were $5.02\,TeV$ and $8.16\,TeV$ for lead-lead ($Pb-Pb$) and proton-lead ($p-Pb$) collisions.

The protons are kept on the circular path by 1232 superconducting dipole magnets which are used to produce a magnetic field of $8\,T\cdot m$ to keep the proton beam on its circular trajectory. These superconducting magnets, with liquid Helium, are cooled down to $1.9\,K$. To reach the design field of $8.33\,T$, they are supplied with a current of $12\,kA$. Each proton bunch contains almost 10^{11} protons, and each beam contains up to 3564 bunches. The maximum momentum of the accelerator is limited to:

$$p = B/\rho = 8.33\,T\,/\,2804\,m = 7\,TeV/c \tag{3.1}$$

ρ is the bending radius of the tunnel. By radio frequency (RF) cavities in which an oscillating electric field is produced. Protons are accelerated to the desired energies.

The protons are concentrated and focused in bunches by strong quadrupole magnets at the interaction points, to achieve a high design luminosity of $10^{34}\,cm^{-2}\,s^{-1}$ The radio frequency (RF) is $400\,MHz$, which confines the protons beams into buckets of $2.5\,ns$. About 35640 buckets are allowed through the LHC circum-

ference, which would result in 37.5 cm bunch crossing spacing. 25 ns is corresponding to one bunch per 10 RF buckets. With these limitations requirements, the number of bunches in the machine is a maximum of 2808.

3.1.2 Luminosity

The instantaneous luminosity $L\,(cm^{-2}\,s^{-1})$ is one of the key parameters of a particle collider as well as the high event rate. For the process with the number of events N and cross-section σ, the event rate is

$$NT = \mathcal{L}\sigma_{event} \tag{3.2}$$

The luminosity is related to the parameters of the LHC proton beam. By assuming a Gaussian beam size, the instantaneous luminosity is given by:

$$\mathcal{L} = \frac{\gamma f k_B N_p^2 F}{4\pi\varepsilon_n \beta^*} \tag{3.3}$$

Where γ is the Lorentz factor, f is the revolution factor, k_B is the total number of bunches, N_p is the number of protons per bunch, β^* is the betatron function at the interaction point (IP). The luminosity delivered by LHC during the 2016 run and recorded by CMS are presented in figure 3.2.

Designing and construction of LHC were completed in 2008 after almost 25 years of effort and hard work, and the scientists have started the commissioning of the machine. On 19 September 2008, an electric arc developed inside a bus bar during a powering test led to extensive mechanical damage to one of the LHC sectors due to a large release of helium and a pressure wave. As a result of this incident, the first collisions of one bunch per beam with energy of 900 GeV has been delayed until late 2009. A centre of the mass-energy of 7 TeV has been used for the collisions during 2010 and 2011, and then increased to 8 TeV in 2012. In 2010, the instantaneous luminosity was also increased from $2 \times 10^{32}\,cm^{-2}\,s^{-1}$ to be $6 \times 10^{33}\,cm^{-2}\,s^{-1}$ in 2012.

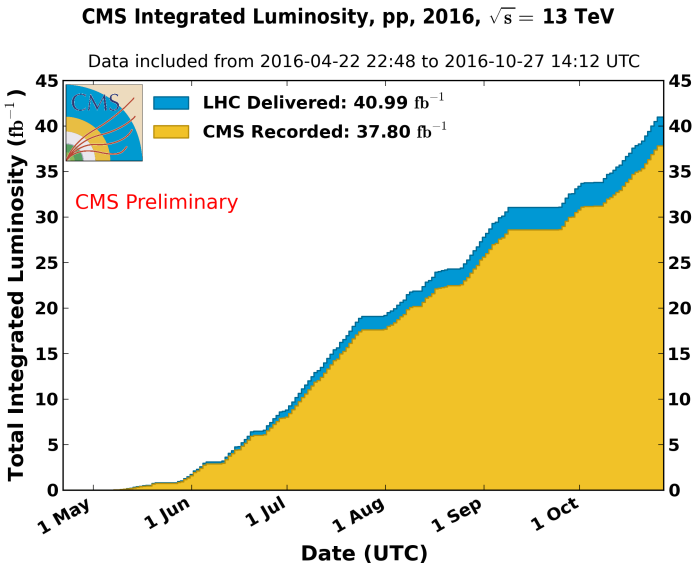


Figure 3.2: Integrated luminosity plot for 2016 data taken, delivered by the LHC and collected by the CMS

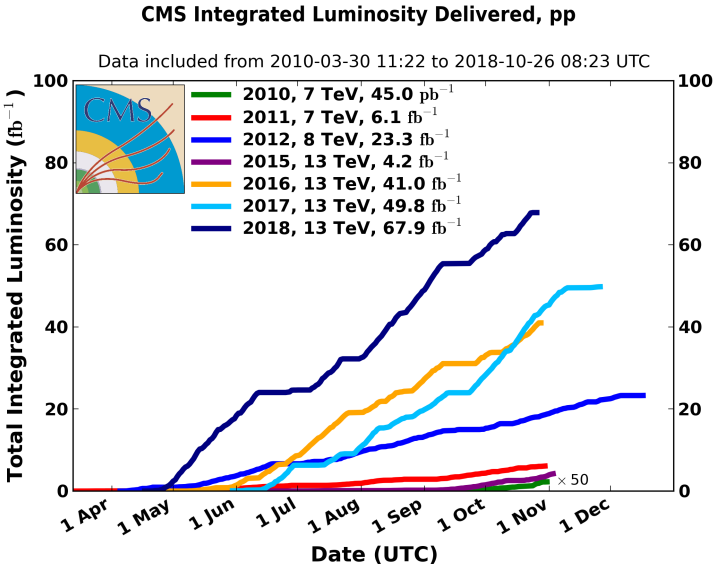


Figure 3.3: Overview of the integrated luminosity delivered to the CMS detector during run I (2010 - 2012) and run II (2015 - 2018)

An integrated luminosity of 45.0 pb^{-1}, 6.1 fb^{-1} and 23.3 fb^{-1} were delivered during the 3 years of data taking in run I. After run 1, the first long shutdown (LS1) which last for 2 years, was used to solve the discovered problems since the start-up of the machine in 2008. And also, to upgrade some parts

of the detectors located around the interaction points on the LHC ring. During 2015, the machine has started its run II operation, at a centre of mass-energy of 13 TeV, then during 2016, the luminosity of the machine has been increased to deliver a total of 41 fb^{-1} of data, as shown in figure 3.2. The evolution of the integrated luminosity delivered within time is illustrated in figure 3.3.

3.1.3 LHC Magnets

In order to accelerate particles into a circular path as in LHC, this requires a huge magnetic force to be able to keep the beams in this curved path. To achieve this with the tunnel's space constraints, a new two-in-one magnet design (twin-bore magnets) has been used for the LHC, which consists of two coils with a common infrastructure and cryostat [125].

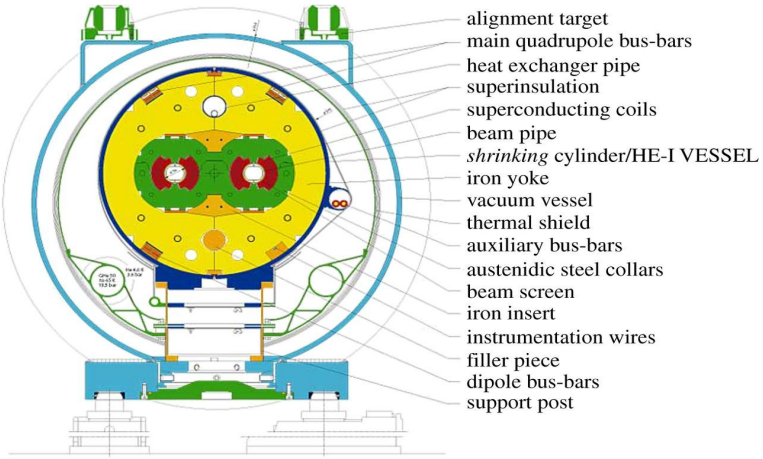


Figure 3.4: Cross section of the LHC main dipole in its cryostat

The cross-section design of the main dipole magnets of the LHC is presented in figure 3.4. In the centre there are two beam pipes with a diameter of 54 mm each and the separation between them is almost 194 mm. A superconducting coil, made of superconducting ($NbTi$) cables, is surrounding the beam pipes. These superconducting cables have to be cooled down to 1.9 K. The steel collars hold the coils in place and the magnetic yoke that surround the coils are forming the cold mass of the magnet. A vacuum vessel insulated the cold mass, is immersed in superfluid Helium, the coolant of the magnetic system, of 1.9 K.

in total, 30*tons* of dipole magnets, with a cryostat diameter of 0.914*m* and 15*m* long have been built by industry [156].

3.1.4 Experiments of the LHC Machine

Taking into consideration the complexity and high cost of the LHC accelerator, it is highly important to get the most benefits from its scientific reach. That's why the protons are accelerated and collide at four points along the LHC ring, as shown before in figure 3.1.

At the four interaction points (IPs), where the proton beams or lead ion beams can collide, large particle detectors are built, and their main function is to record the generated collisions. At (IP1) and (IP5), two independents general-purpose detectors, ATLAS [6] and CMS [62] experiments are located. Both of these experiments are general-purpose detectors that cover a wide range of high energy physics, at high luminosity and constructed from many layers, which have an onion-like structure around the Interaction point to collect all generated particles from escaping the detector.

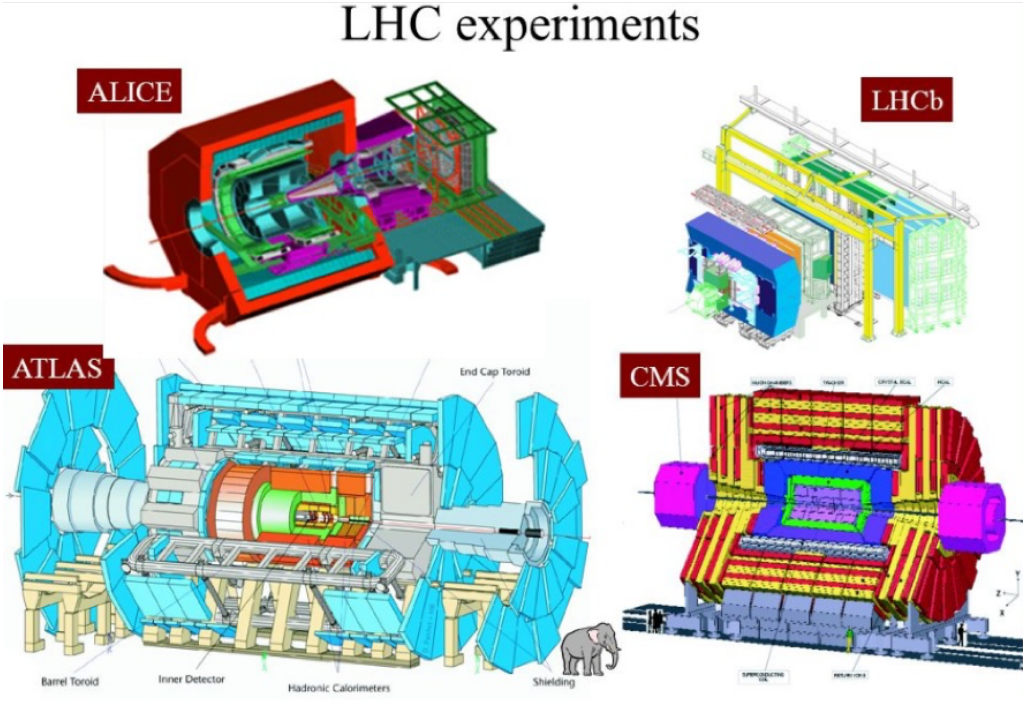


Figure 3.5: LHC four main experiments

A third detector, ALICE is located at (IP2) [7]. It is specialized to the collisions of heavy ions at low instantaneous luminosities ($10^{27}\,cm^{-2}\,s^{-1}$). Information about and study of the quark-gluon plasma is performed. A fourth detector, LHCb, is located at (IP8) receiving an instantaneous Luminosity of few orders of $10^{32}\,cm^{-2}\,s^{-1}$. Matter and anti-matter asymmetry in the universe are studied with the usage of LHCb, besides the studying of b quarks. Figure 3.5 represents the four main LHC experiments.

3.2 Compact Muon Solenoid detector (CMS)

The search topic described in this thesis was performed using 2016 data which was collected with the CMS detector. The Compact Muon Solenoid (CMS) is a general-purpose detector located at one of the interaction points of the LHC ring. It consists of many layers of particle physics detectors, which meet the requirements of the LHC physics.

A silicon tracker, the closet layer to the interacting point which is providing a high charged particle momentum resolution, followed by an Electromagnetic calorimeter (ECAL), to ensure good energy resolution for electromagnetic particles, and Hadronic calorimeter (HCAL), to measure the energy of hadrons, a very powerful solenoid magnet surrounding these calorimeters with $3.8\,T$, and outer there is a muon detector.

Both calorimeters are situated inside the powerful superconducting magnet. The design of the detector has improved the resolution of the energy by reducing the material density in front of the calorimeters. The CMS detector is $21.6\,m$ long and it has a diameter of $14.6\,m$ and weighs about $12400\,tons$. An overview of various layers of the CMS detector and their key characteristics is shown in figure 3.6.

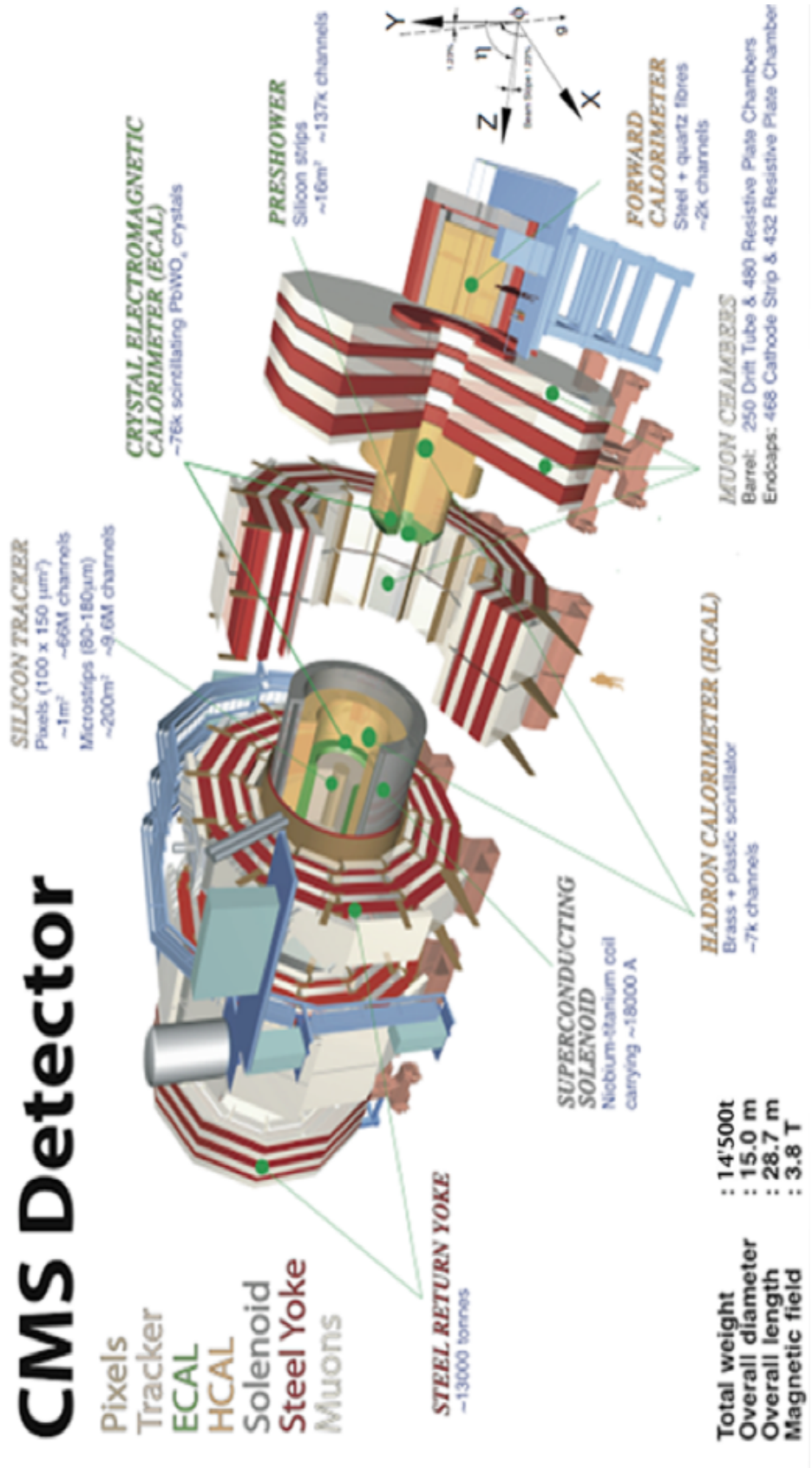


Figure 3.6: An overview of various layers of the CMS detector and their key characteristics

3.2.1 The Coordinate System

The global design of the CMS coordinate system is at the IP, using a right-handed coordinate system, the $x-axis$ is pointing to the centre of the ring of LHC and perpendicular to the proton beams, while $y-axis$ is vertical and pointing upward, the $z-axis$ is anti-clockwise along the beam pipe. For the hadron collisions at the LHC, the transverse components of the total energy and the missing energy are the measurable components since the total energy of the partons is unknown. Invariant quantities are used, such as the transverse momentum p_T. In the z direction, along the beam pipe, the pseudorapidity is given by

$$\eta = \ln\left(\tan(\theta/2)\right) \tag{3.4}$$

Where θ is the polar angle between the $z-axis$ and the particle momentum direction. Since along the $z-axis$, the differences in pseudorapidity are invariant under Lorentz boosts, the polar angle is converted into the pseudorapidity. If the pseudorapidity is 0, θ will be equal to $\pi/2$ (perpendicular to the beam) and if pseudorapidity is infinite, θ will be 0, the direction is parallel to the beam. Figure 3.7 represents the CMS Coordinate system.

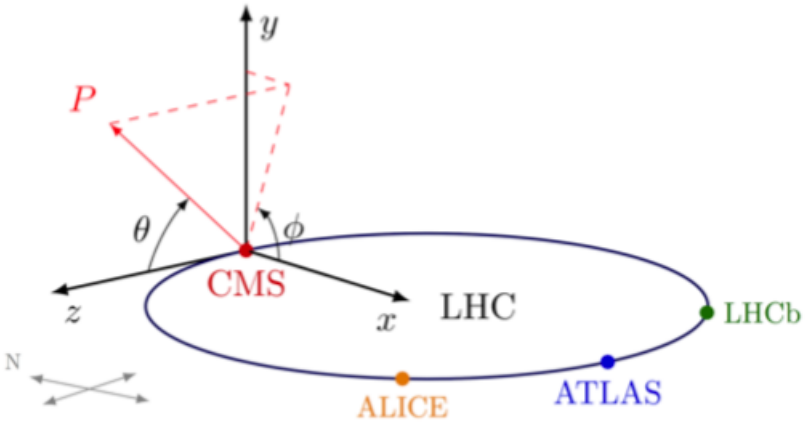


Figure 3.7: CMS Coordinate system

Another interesting quantity is the transverse momentum p_T, which is de-

fined as the momentum contained in the transverse plane (i.e. perpendicular to the beam and is given by $p_T = \sqrt{p_x^2 + p_y^2}$). In the final state of the collision, the momentum of the particles should be balanced in the transverse plane due to the conservation of the momentum before and after the collision. Therefore, the transverse momentum of a particle will be used, defined as

$$p_T = p \cdot \sin\theta \tag{3.5}$$

3.2.2 Physics Goals of the CMS experiment

CMS experiment has been constructed to search for *Higgs Boson* and new physics beyond the Standard Model. Its design has been based on the requirements of the following goals:

1. High performance to ensure precise measurement of muons in the outer layer of the CMS experiment. It searches for the clearest signature of a possible decay mode for the Higgs boson.

2. The second layer of the CMS detector, the electromagnetic calorimeter (ECAL), provides a high-resolution method to detect and measure electrons and photons. This is highly needed for the discovery of a light Higgs boson via its decays into two photons. A precise measurement of the energies of electrons is also important when the Higgs boson decay to Z.

3. Tracking system with high-quality detection features gives the best momentum and impact parameter measurement for tracks which can be achieved. It is highly important to have a good tracking system to measure the decay of a light Higgs boson into pairs of bb quarks.

To meet the above requirements, the CMS experiment is composed of the following sub-systems

- Solenoid magnet.
- Trackers.
- Electromagnetic calorimeter (ECAL).
- Hadronic calorimeter (HCAL).
- Muon system.

3.2.3 Superconducting Magnet - CMS soleniod

The powerful superconducting solenoid of the CMS experiment [21] is almost 100000 times stronger than the earth's magnetic field. It is used to achieve precise measurements of the momentum p of the charged particles which cross the detector. The paths of the issue of the particle from the collision are bend by the magnetic field.

The CMS magnet is the largest superconducting magnet ever built. The CMS magnet, developing a magnetic field of $3.8\,T$ is the real backbone of the CMS experiment. It has a length of $12.9\,m$ and its inner diameter is $6\,m$. The magnetic field is closed with $12500\,tones$ of steel return yoke which contains the muon detector. Due to the large inner radius of the inner coil, the tracker and both calorimeters can fit inside it. Outside of the magnet, there are five separate dodecagonal wheels along z forming the barrel yoke ($YB-2$ to $YB+2$). They can be moved and give access to the installed detectors inside it. The Endcap consists of three steel disks on each side ($YE-1$ to $YE-4$ and $YE+1$ to $YE+4$).

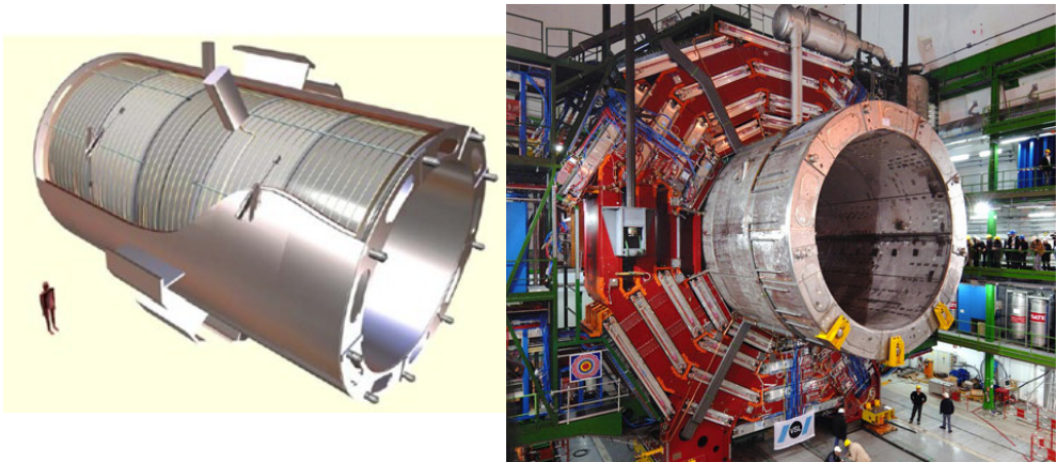


Figure 3.8: A schematic view of the CMS solenoid is shown as well as the steel return yoke and muon chambers around the magnet

Figure 3.8 shows a schematic view of the CMS solenoid as well as the central steel return yoke equipped with muon chambers all around the magnet.

3.2.4 CMS Inner Detector - Tracker

The innermost layer of the CMS detector, which is the closest part to the IP, is the tracking system [115, 54]. The CMS inner tracker sub-detector is a silicon-based detector and it consists of an inner silicon pixel detector, followed by a strip detector providing precise 3D hits, needed for the reconstruction of the interaction vertex and tracking seeding. The main purpose of this sub-detector is to reconstruct the charged particles' trajectories precisely and measure their momentum. The tracker detector covers a range up to $|\eta| < 2.5$ in pseudorapidity [115]. The tracker is a system of two independent sub-detectors with separate cooling, powering, and read-out schemes. The Tracker has an overall length of $5.4\,m$ and an outer diameter of $2.4\,m$.

The CMS silicon strip tracker [173] is composed of more than 10 million readout channels of a total active area of $200\,m^2$ set of about 15000 silicon modules. It surrounds the pixel detector up to a distance of $116\,cm$ from the beam pipe, all along $5.6\,m$. The strip detector is divided into four subsystems, the Tracker Inner Barrel (TIB), has four barrel layers, the Tracker Outer Barrel

(TOB), has six barrel layers, the Tracker Inner Disks (TID) and the Tracker EndCaps (TEC), each has three and nine disks respectively. An overview of the CMS tracker layout is shown in figure 3.9, with its subsystems – Pixel.

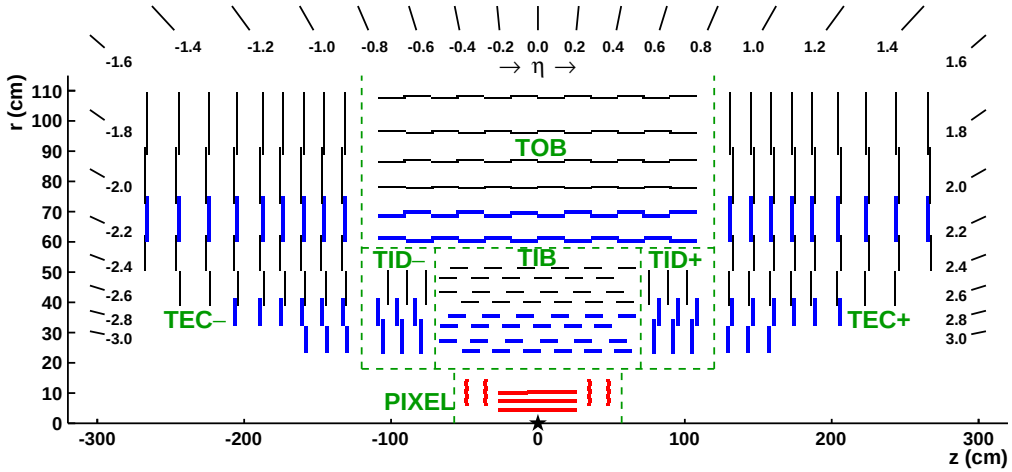


Figure 3.9: A transverse view of the pixel and strip tracker detectors showing the multiple barrel layers and endcap disks.

The inner pixel detector [91] is made out of pixels with a dimension of $100 \times 150\,\mu m$, these pixels are arranged in the tracker detector in three barrel and two Endcap layers and cover an active area of $1.1\,m^2$. The barrel silicon strip detector is surrounding the pixels at 3, 6.8, 10.2, and 16 cm, while the Endcap disks are located at 24.1, 34.5 and 46.5 cm, from the interaction point. In total, an implementation of about 66 million pixel sensors [67] into 285 mm tick n-type bulk and p-type backside, with the dimension of $100 \times 150\,\mu m$ define the CMS pixel detector. The signals produced by these sensors are read by 15840 readout chips (ROC). The silicon strip tracker provides two-coordinate measurements for at least four hits in the pseudorapidity range of $\mid \eta \mid < 2.4$. Figure 3.10 represents a schematic of the CMS silicon pixel detector, and figure 3.11 presents a 3D view of the barrel and forward pixel detector, consisting of 3 layers and 4 disks.

Charged particles that cross the tracker volume have to pass through a significant amount of material, as shown in figure 3.12. The tracker's sensors are mounted onto a carbon fibre and graphite support structure with on-detector electronics which are needed to enable a fast response time.

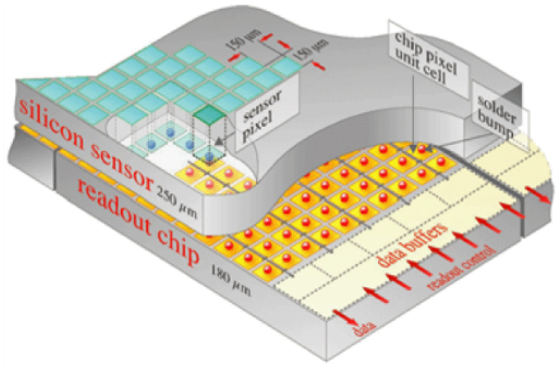


Figure 3.10: Schematic representation of the CMS silicon pixel detector

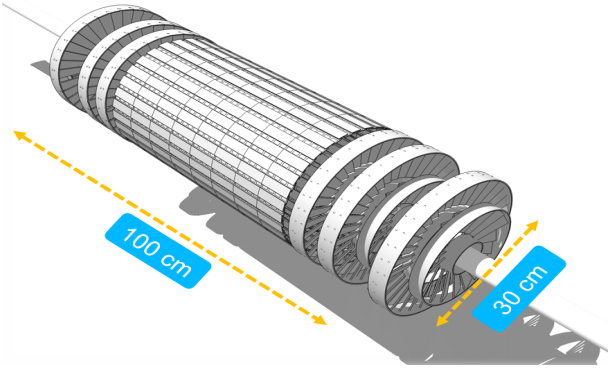


Figure 3.11: A 3D view of the barrel and forward pixel detector, consisting of 3 layers and 4 disks.

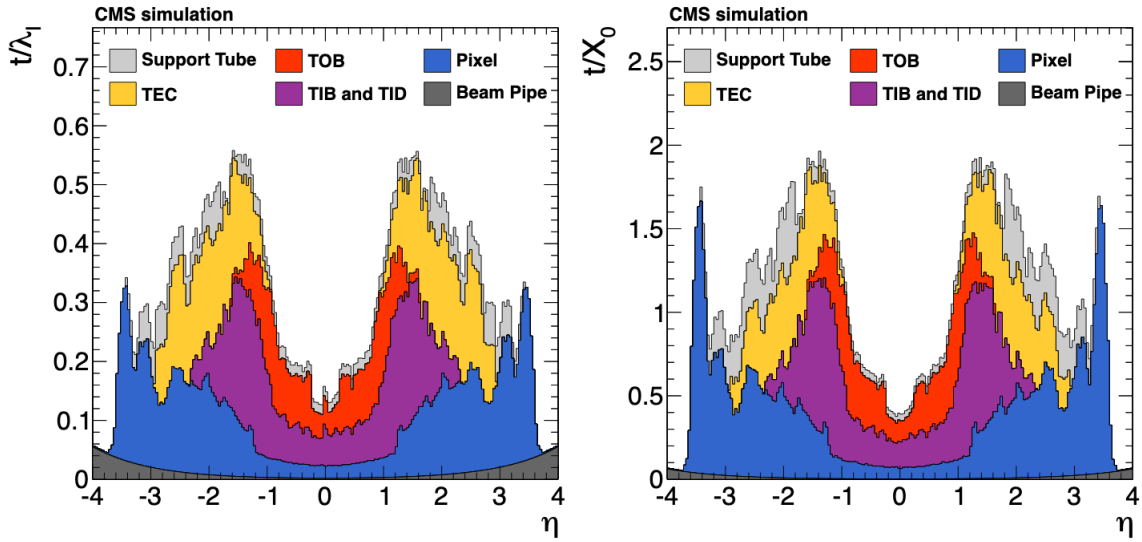


Figure 3.12: Inner tracker material's total thickness expressed in units of interaction lengths λ_I (left) and radiation lengths X_o (right), as a function of the pseudorapidity η. TIB, TID, TOB, and TEC stand for "tracker inner barrel", "tracker inner disks", "tracker outer barrel", and "tracker endcaps", respectively. The two figures are taken from Ref [74]

3.2.5 The Electromagnetic Calorimeter (ECAL)

Following the tracking system, CMS detector has the Electromagnetic calorimeter (ECAL), to measure the energy of the electron and photon [52].

The ECAL consists of 75848 lead-tungstate ($PbWO_4$) crystals arranged in a central barrel section (EB) within pseudorapidity coverage up to $\eta = 1.48$, and on Endcap section with an extending coverage up to $\eta = 3.0$ (EE). The density of the ($PbWO_4$) crystals is very high ($\rho = 8.28 g/cm^3$) with short radiation length ($X_0 = 0.89\,cm$). These crystals also have a very good radiation resistance. Avalanche photodiodes (APDs) are reading the scintillation light in the barrel, while vacuum photodiodes (VPTs) [75] are used in the endcap region. Figure 3.13 shows the $PbWO_4$ ECAL crystals with photo - detectors attached – a barrel crystal with APD capsule and an endcap crystal with a VPT.

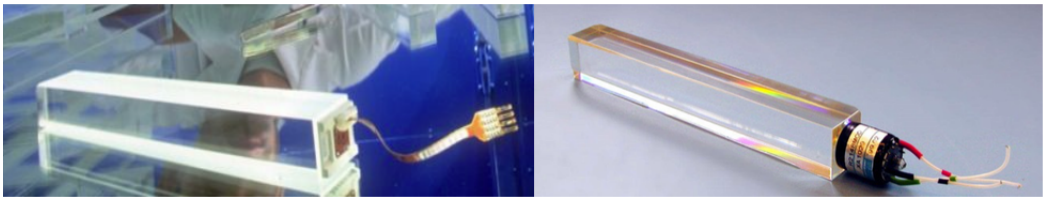


Figure 3.13: $PbWO_4$ ECAL crystals with photo-detectors attached – a barrel crystal with APD capsule (left) and an endcap crystal with a VPT (right).

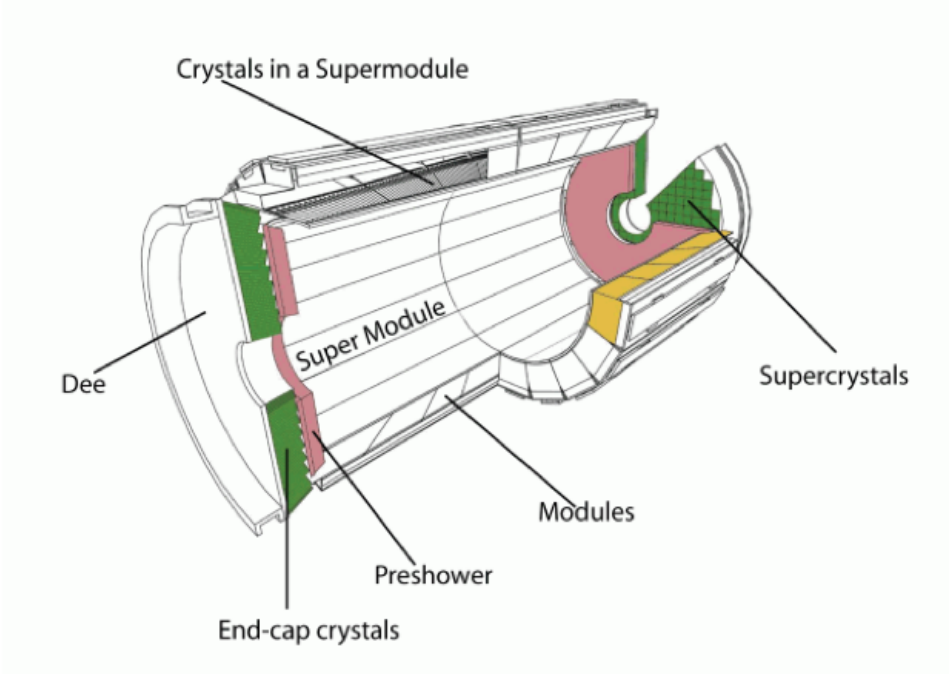


Figure 3.14: A schematic view of the CMS ECAL structure – Barrel (yellow), Endcap (green) and Preshower (orange).

The ECAL-Barrel (EB), which covers the range of $\eta = 1.48$, has an inner

radius of 129 cm. It consists of 36 supermodules, each supermodule is made of 20×85 crystals. Each crystal has a length of 230 mm producing 25.8 radiation lengths (X_o) and weight 1.5 kg. The Crystals are placed slightly turned to avoid cracks between them. The crystal axis makes a 3-degree angle for the nominal interaction point direction in the azimuthal Φ and η projections.

The Endcap (EE) of the ECAL, have 4-half disks called "Dees", each of those disks is holding 3662 crystals. Endcap disks cover the pseudorapidity range $1.479 <| \eta |< 3.0$ with 2.15 m away from the interaction point. The crystal front face cross-section is $28.62 \times 28.62\, mm^2$ and has 220 mm in length which corresponds to 24.7 X_o. A schematic view of the ECAL layout is shown in figure 3.14.

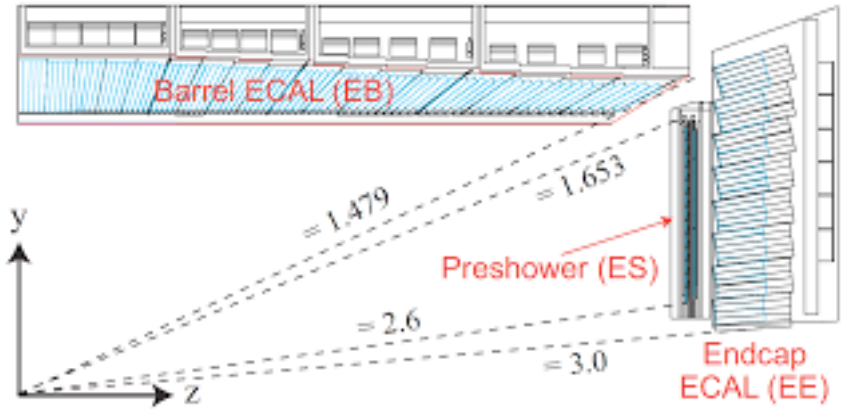


Figure 3.15: A transverse view parallel to the beam line showing one quarter of the ECAL, with its barrel (EB), endcap (EE), and preshower (ES) detectors.

A Preshower (PS), is installed in front of the two endcaps [124]. The Preshower (PS) is 20 cm thick and it consists of two layers of silicon strip sensors and leads plates of 2 and 1 X_O. It has been designed to improve the resolution in the forward region at $1.653 <| \eta |< 2.6$, to resolve the two photons of a π_o (neutral pions) decay and also to provide information on the identification of the electron against the minimum ionizing particles. Figure 3.15 shows a transverse view parallel to the beamline showing one-quarter of the ECAL, with its barrel (EB), endcap (EE), and preshower (ES) detectors.

3.2.6 The Hadron Calorimeter (HCAL)

To complete the CMS calorimeter system the Hadron Calorimeter was installed around the ECAL. The main aim of the HCAL is to measure the energy of charged and neutral hadron and participates in the estimation of missing transverse energy of each event [72].

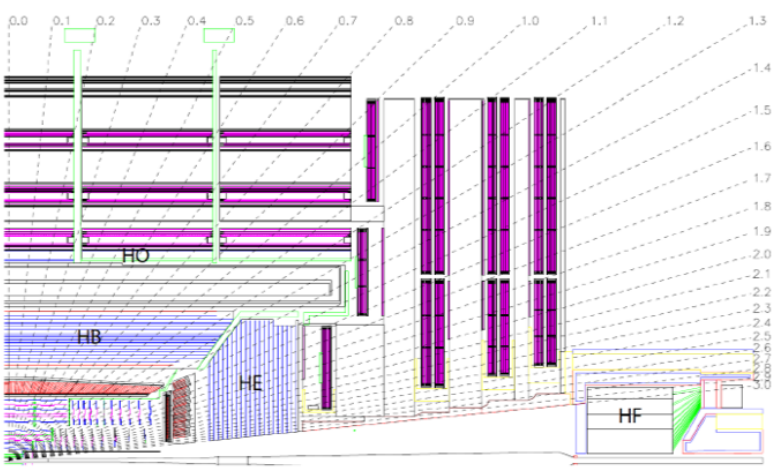


Figure 3.16: Longitudinal view of the hadronic calorimeter (HCAL) assembly. The barrel (HB), endcap (HE), outer (HO) and forward (HF) detectors are indicated

The HCAL is a compact sampled system which is located between the ECAL and the superconducting magnet of the CMS, and it is initiating a cascade of secondary particles for the hadrons by several layers of non-magnetic brass absorbers and fluorescent scintillators. HCAL is consisting of a coaxial barrel (HB) within $\eta < 1.3$, an endcap calorimeter (HE) region up to $\eta < 3$, and down to the beam pipe in the forward region a forward calorimeter with coverage up to $\eta < 5.2$ in the (HF). In the central region, the ECAL and HCAL barrel's stopping power becomes not sufficient to contain the entire hadron showers of the energetic jets, the HCAL was extended outside the solenoid with an outer calorimeter (HO), using scintillators and the coils of the magnet as an absorber.

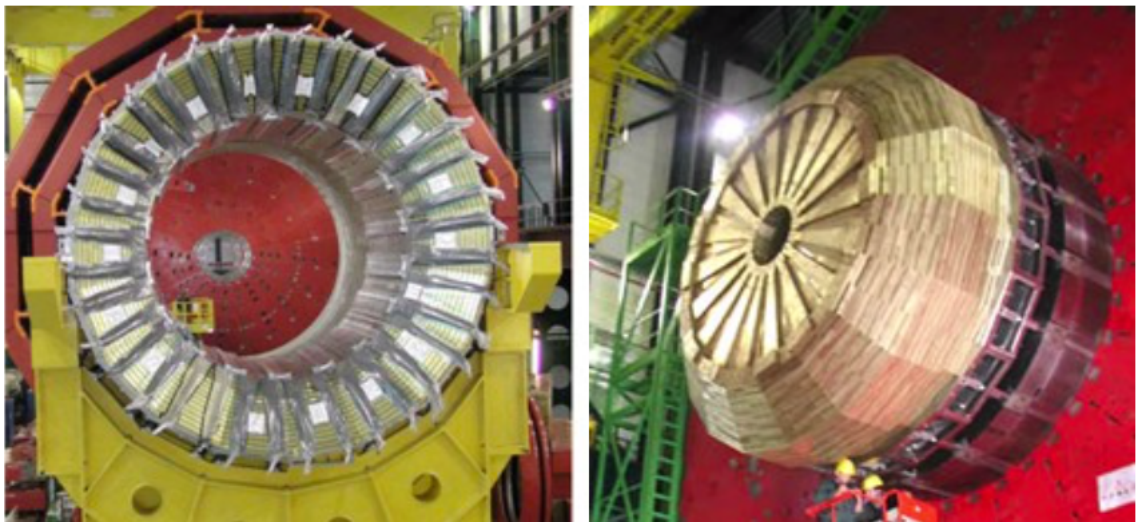


Figure 3.17: Photographs of the CMS HCAL – barrel HB (left) and endcap HE (right).

The HB and HE scintillator tiles are grouped in towers, readout with Hybrid photodiodes (HPDs) through wavelength-shifting fibers. The energy of the particles is accessed to the total amount of light collected over the layers within a given tower. A quarter view of the hadronic calorimeter (HCAL) assembly is shown in figure 3.16. Real photographs of the HCAL detector are shown in figure 3.17.

3.2.7 CMS Muon System

The outermost layer of the CMS detector, one of the features keys of the CMS experiments, totally placed outside the solenoid, is the extensive muon detection system. The main tasks of this sub-detector are muon identification and its measurement necessary for event triggering at the first level.

The CMS muon system parts are embedded in the magnet iron yoke constraining the lines of the magnetic field and placed behind the calorimeter and the magnet coil. It consists of three different types of gas ionization technologies. the Drift Tubes (DT) which are installed in the barrel ($|\eta| < 1.2$), lower in background noise and occupancy. In Endcap, Cathode Strip Chambers (CSCs) are used in the region of $0.9 < |\eta| < 2.4$. Low muon rates, which are expected to exist in the barrel, are detected by the DTs and thus they have a slower re-

sponse time than the CSCs, which are covering larger pseudorapidity ranges. Both DTs and CSCs systems are providing precise space and time measurements. Resistive Plate Chambers (RPCs) are placed in both barrel and endcap regions providing a fast time response of few *ns* and independent trigger measurements. A schematic view of the muon system in the CMS is shown in figure 3.18.

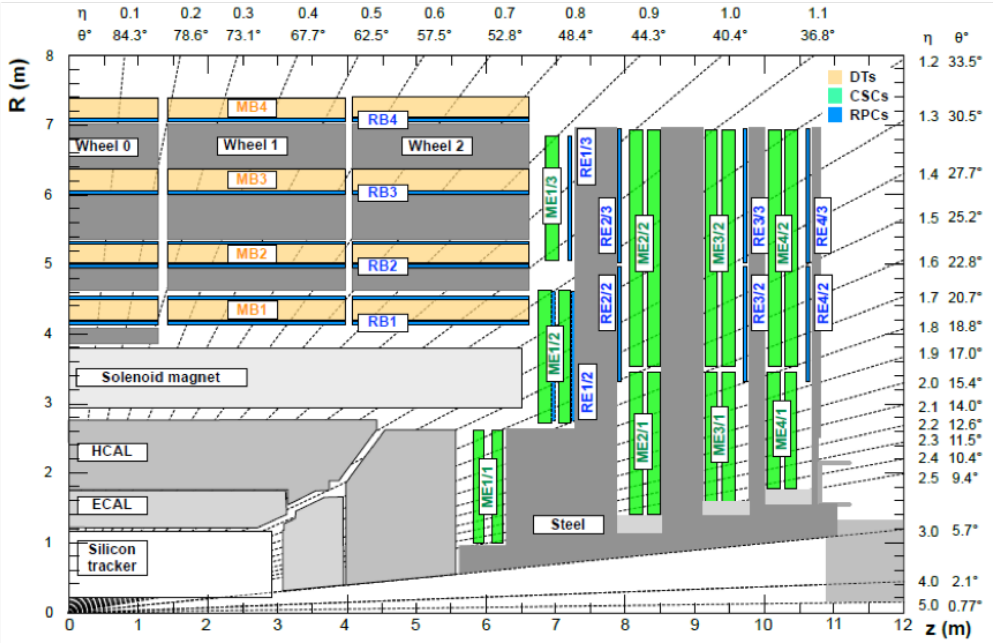


Figure 3.18: $r-z$ cross section of a quadrant of the CMS muon system, showing DT (yellow), CSC (green) and RPC chambers (light blue). The interaction point is at the lower left corner.

The Barrel part at the muon system is divided into five independent wheels, wheel 0, wheel ± 1, and wheel ± 2. Each one of these wheels is subdivided into 12 sectors with azimuthal angle Φ covering 30°. Each sector has four stations integrated into the yoke of the magnet.

The Endcap muon detector is composed of four muon stations $ME1$, $ME2$, $ME3$, and $ME4$. Each of the muon stations contains Cathode Strip Chamber (CSC) up to $\eta = 2.4$ and a dedicated trigger detector RPCs up to $\eta = 2.1$. Details of the working mechanism of RPCs and its construction is described in detail in chapter 4.

3.2.7.1 Drift Tube Chambers (DTS)

The Drift Tubes system (DTs) [76] are gaseous detectors, part of the barrel of the CMS muon system, covering the region $\eta < 1.2$. DTs were built with a rectangular drift cell of dimension $13 \times 42\,mm^2$, as shown in figure 3.19 (a). Gold plated stainless steel wire of $50\,\mu m$, served as anode power supplied at $3.6\,kV$, and the cathode consists of two $50\,\mu m$ thick aluminum electrodes on the short edge of the drift cells supplied at $(-1.8\,kV)$. At $1.8\,kV$, the long edges contain $50\mu m$ thick aluminum field electrodes. The drift cells are spread along the full length of $2.5\,m$ or the width of the DT chambers with $42\,mm$ separation distance between the anode wires.

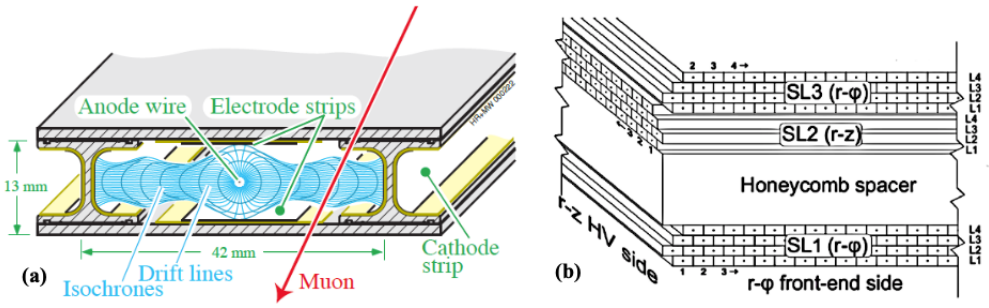


Figure 3.19: Transverse view of a DT cell (a) and schematics of a DT chamber (b) [77]

The barrel region of the muon system is equipped with DTs, which consist of 4 coaxial stations ($MB1$, $MB2$, $MB3$ and $MB4$), which are forming concentric wheels (Wheel 0, Wheel ± 1, Wheel ± 2), these wheels are segmented into 12 sectors surrounding the beamline. The muon system contains about 250 DT chambers. Super Layer (SL) is the smallest independent unit of the DT design. Each chamber is formed from 3 SLs with 4 layers of staggered drift cells. A schematic view of a DT chamber is illustrated in figure 3.19 (b). The innermost and outermost SLs wires are parallel to the line of the beam and provide a track measurement in the bending $r-\Phi$ wires of the inner SLs measure the position of the hits in the $r-z$ plane. The innermost SL does not exist in the fourth station ($MB4$), placed outside the return yoke, and to its Φ coordinates, it can measure only the hit position. This configuration for the DT results in two measurements in Φ and one measurement in z position per station for each muon coming from the interaction point.

Passing through the layers of the detectors, it creates electrons and ions, which drift toward and away from the wire of the anode respectively. When the electrons reach the strong electric field close to the wire, it creates an avalanche that is transformed into an electrical signal on the anode. In each DT chamber, the maximum draft time is 400 ns, for the working gas mixture 85 % Ar and 15 % CO_2. The drift velocity in the DT cells is almost constant.

3.2.7.2 Cathode Strip Chambers (CSCs)

The Cathode Strip Chambers (CSCs) Systems [96] are also gaseous detectors. On each endcap, there are 540 integrated gaseous detectors in 4 layers ($ME1$, $ME2$, $ME3$, and $ME4$). They are covering a range of pseudorapidity of $0.9 < |\eta| < 2.4$ [184], the CSCs operation principle is illustrated in figure 3.20, An electron avalanche is caused through a gas gap when a muon is passing the gas detector, providing a signal on the anode wires and inducing a charge on the cathode strips. Each CSC is a multi-wire chamber composed of 7 copper-clad panels and forms 6 gas gaps layers.

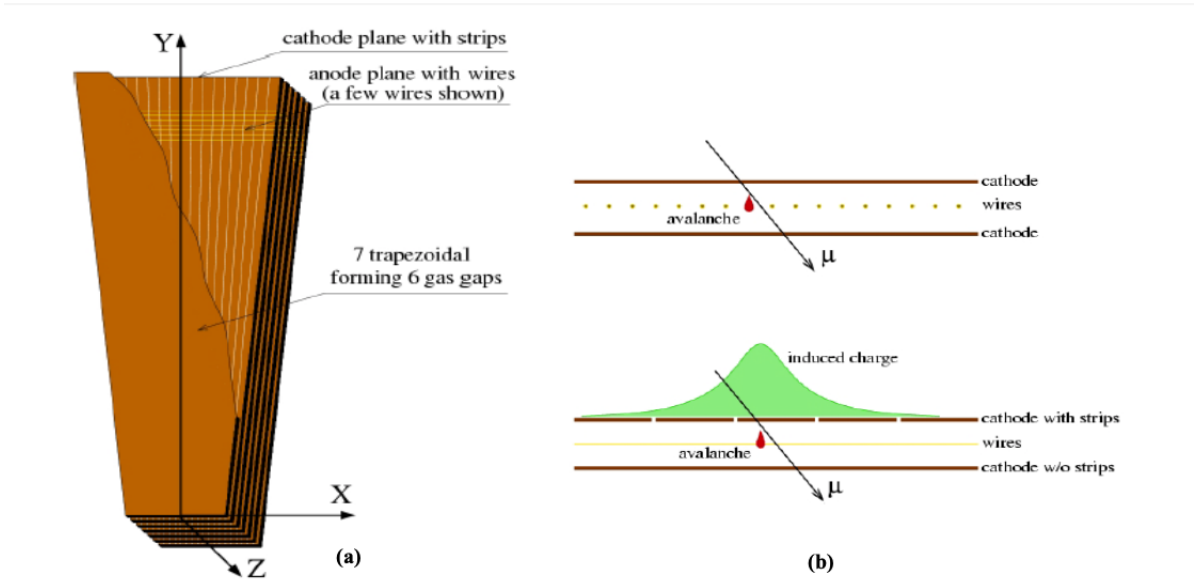


Figure 3.20: The CSCs operation principle

For $ME1$ chambers, the gas gaps are 6 mm and 9.5 mm for the rest of the chambers. The cathode strips with different widths of 3 to 16 mm are etched on

each copper panel. The azimuthal coordinates of passing muons, crucial for the exact estimation of their transverse momentum, are measured using these strips. Between each cathode strips layer, there are anode wires. The anode wires are oriented normal to the strips and provide passing muons radial coordinates. The potential that held the wires is $2.9 - 3.6\,kV$, with the CSC standard gas mixture - 50 % CO_2, 40 % Ar and 10 % CF_4 filling the gaps.

3.2.7.3 Data Acquisition and The CMS Trigger System

Data that has been selected by L1 and HLT, needs to be stored somewhere to be transferred to the institutes that are involved in the analyzing process. Storing these huge amounts of data needs specific requirements and huge amounts of storing servers and this is achieved through the Worldwide Large Hadron Collider Computing Grid (WLCG).

The resources of computing service are combined in most of the participating institutes at the LHC experiments to build world-wide centres, see figure 3.21. WLCG is composed of three tier-levels which are distributed among these centers around the world. *Tier-0*, is the storage space where the data collected by the experiments, and then these data is distributed to other tier-levels (*Tier-1* and *Tier-2*) centers. These levels are responsible for reprocessing and storing the data for analyzing and also we can use these tier-levels computing centers to store the simulated MC samples which are produced officially. We, physicists, can access *Tier-2* centers and analyze the data. *Tier-0* is located at CERN, and then the distribution of data takes place among 7 centers of *Tier-1*, which are located at France, Italy, Germany, Spain, UK, Taiwan, and the US, and then it is further distributed to more than 50 centers of *Tier-2*.

The CMS Data Hierarchy, as we discussed above there is three data tier in the CMS experiment:

- RAW-data format, which contains the full information of an event, raw detector information, from the *Tier-0* (i.e. from CERN). We can not use the RAW data format directly for analysis.
- RECO, (RECOnstructed data), which is the output of the first-pass pro-

cessing which is done by Tier-0. It contains the reconstructed physics objects with very detailed information (huge in size). It can be used for analysis but due to its huge size, the CMS experiment does not store RECO data format anymore, only for specific and limited samples).

- AOD, (Analysis Object Data), which is a reduced version of the RECO format that contains all the necessary reconstructed information to perform the analysis. MiniAOD and NanoAOD are now available.

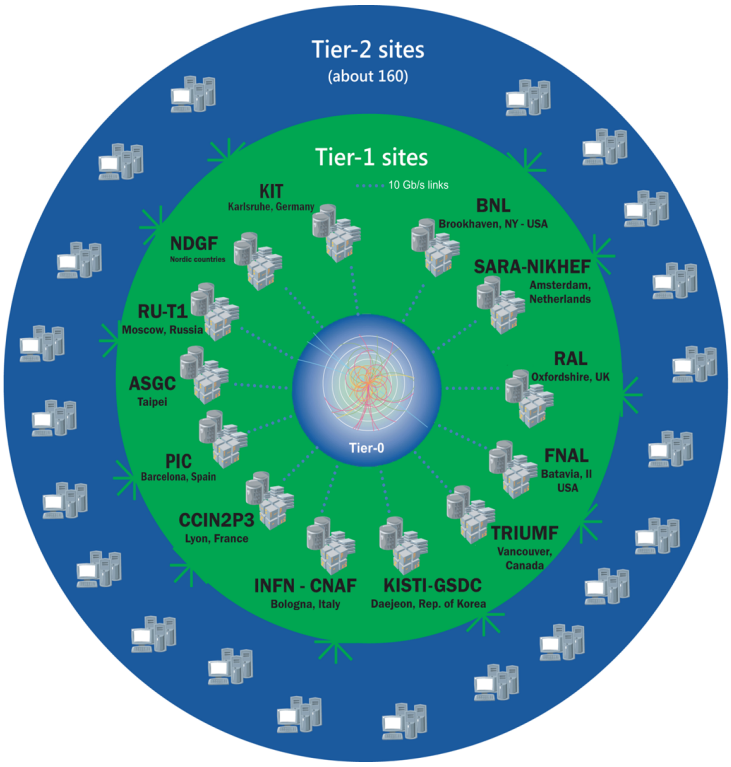


Figure 3.21: The structure of the WLCG tier-levels and their mapping among worldwide

At the Large Hadron Collider (LHC), at the designed luminosity is $10^{34}\,cm^{-2}\,s^{-1}$, a rate of $40\,TB/s$ is expected from almost 22 proton-proton events occurring in every bunch crossing. LHC experiments are analyzing, selecting, and collecting these data but due to a limited storage capability, the data rate is many orders of magnitude higher than the available storage space. Therefore, it is required to seriously reduce the amount of data collected until it reaches the maximum rate of the accepted data which is about $100\,MB/s$, which corresponds to 100 events per second ($100\,Hz$ data-taking).

All the data are going in a buffer of $3\mu \cdot s$ for the time the Level-1 Trigger (L1) provides the selection decision and lets the DAQ after that to transfer to the High-Level Trigger (HLT) only the data validated by the L1.

The data reduction process is done through a two-step trigger system, used in the CMS detector. Level-1 Trigger (L1) and High-Level Trigger (HLT) [70] are the two steps required for such a reduction. The Level-1 reduces the collected event rate to less than $100\,kHz$, and then the HLT trigger step is providing the final output event rate of $100\,Hz$ [73]. Figure 3.22 illustrates the data flow in the CMS Trigger system with different trigger levels and event rates.

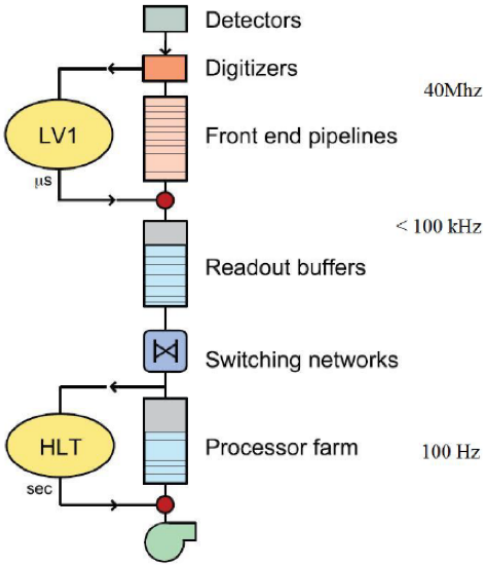


Figure 3.22: Illustration of data flow in the CMS trigger system with the different trigger levels and event rates

3.2.7.3.1 Level-1 Trigger (L1)

The Level-1 trigger [70] is an online hardware electronic trigger system, which gives the first decision on whether to keep the experimental data or not, directly after these data are recorded by the experiment. Within $3\,\mu s$ after each collision, this decision is made. After passing the L1 trigger, the event rate is reduced from $40\,MHz$ to $100\,kHz$, which is low enough to transfer the data to computer servers. Events are then selected upon their interesting signatures based on the creation of local objects like electrons, photons, muons. and jets

besides the transverse missing energy E_T. They use information from trigger towers in $\eta - \phi$ space issued from the calorimeters and muon system.

Calorimeter Trigger, the Muon Trigger, and the Global Trigger are three major subsystems implemented in the L1 trigger system. Figure 3.23 shows the structure of these subsystems. The sum of the local energy from the individual readout towers of the ECAL, HCAL, and HF, known as "the Trigger Primitive Generator (TPG)" are preserved by the calorimeter trigger [69]. For the three subsystems of the muons, (DT, CSC, and RPC, have their trigger logic process, which transfers the four best candidates of muons for combination in the muon global trigger.

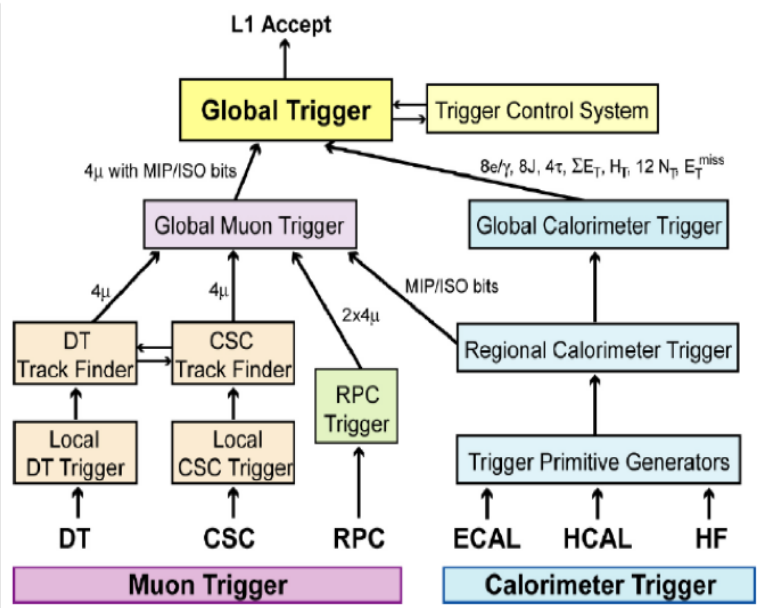


Figure 3.23: Architecture of the Level-1 Trigger

In the HCAL barrel and endcaps, the TPG corresponding to the layout of the tower is shown in figure 3.24. Given the HCAL tower layout. In the ECAL, the TPGs are built in the barrel, combining 5×5 crystal arrays, and in endcaps a layout is used which follows the HCAL trigger towers.

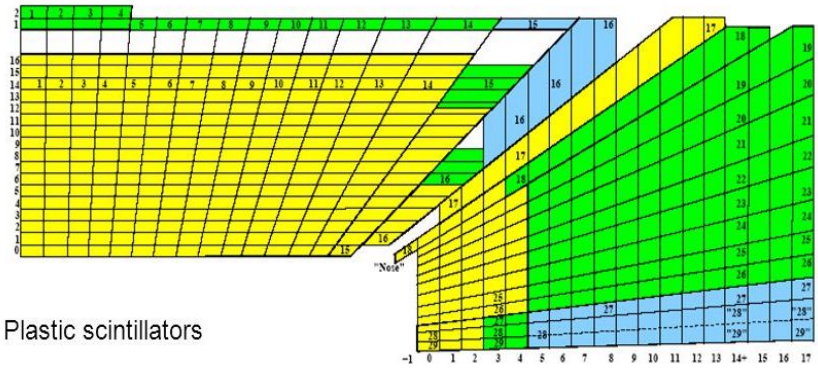


Figure 3.24: HCAL tower layout

3.2.7.3.2 The High-Level Trigger (HLT)

The second step of the Trigger system is the High-Level Trigger (HLT) [73], in which the HLT processes all events which have been accepted by L1 Trigger and transferred to a computer farm, were software based on the offline filters process these events by using different reconstruction algorithms. For permanent storage, only events that pass at least one of the HLT criteria are kept. After this step, the event rate is reduced from $100\,kHz$ to $100\,Hz$, which is the limit of the disk storage. To accept only the interesting events, execution of complex physics selection is made by HLT algorithms on a farm of commercial processors. Each of these processors has an access to the L1 raw data and it analyzes one event with procession time up to $1\,s/event$. A minimal amount of information from the detector "trigger objects" is reconstructed to reject a maximum background event in future analysis. Unnecessary calculations are avoided by using fast algorithms of several stages of the virtual trigger level for selection and reconstruction, to reject events as early as possible. The coming out information from the HLT primary data sets are stored in Tier 0, at CERN, of the Worldwide LHC Computing Grid (WLCG) network [101] and then distributed around the entire network for CMS collaboration, for easy access.

The output of the L1 trigger is read out by The Data Acquisition (DAQ) System [73]. It merges all the event fragments from several front-end devices, into a complete event. After this step, the event passes to the Event Filter Farm, where the HLT algorithms are running. Figure 3.25 shows the general architec-

ture of the DAQ system.

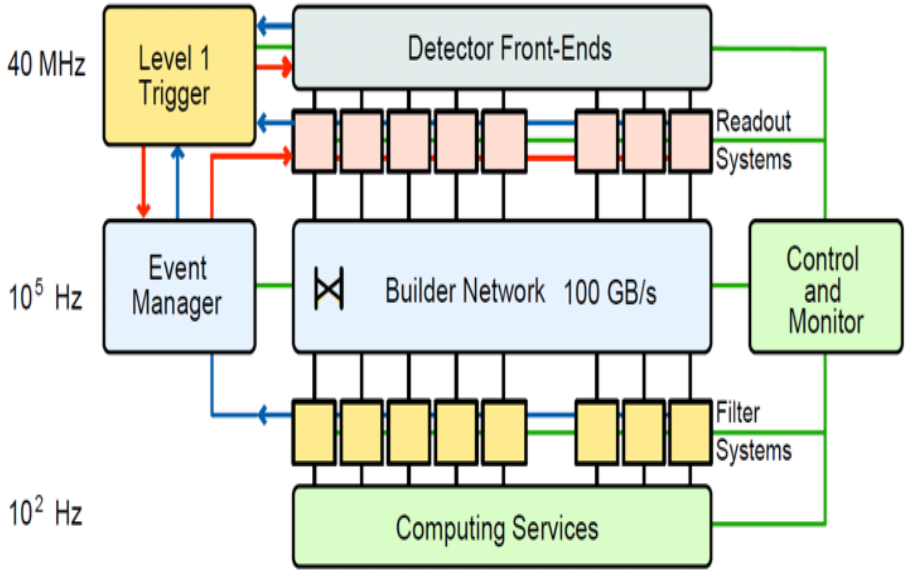


Figure 3.25: Schematics view of the general architecture of the CMS DAQ System

CHAPTER 4

RESISTIVE PLATES CHAMBERS (RPCS)

Over complicated background at the LHC, Muon candidates provide such a clean signal for detecting interesting events. At high luminosities, the reconstruction and triggering abilities for muons are highly important concepts for CMS. The fast-Resistive Plate Chambers are a crucial part of the CMS detector as they are playing a key role in the process of selection muon events.

A brief introduction is given in this chapter on the gaseous detectors, which are the main features of the *Resistive Plate Chambers* (RPCs) and trigger system, and some characteristics of gas mixtures which are used to detect charged particles in a gaseous detector. Also, an overview of the *Resistive Plate Chambers* (RPCs) is given in this chapter. Their design, their working principle, and how they are configured in the CMS experiment are also discussed. We will focus mainly on the installed *RE*4 – endcap stations performance, their commissioning during LHC-run II, and the 2nd long shutdown (LS2).

The doctoral candidate took a role in the data quality monitoring and offline performance analysis of data recorded during LHC-run II as data manager shifter during 2016, 2017, and 2018, and also the participation in the commissioning of services and operations which are currently ongoing, during LS2, related to the *RE*4–endcap RPCs in the CMS experiment.

4.1 Gaseous Particle Detectors

For many decades, gaseous particle detectors have played a crucial role in the field of High Energy Physics (HEP) experiments and they developed throughout the years. Starting with Rutherford [158] who invented the single-wire proportional counter, to a wide range of fast and efficient detectors with better resolution and reasonable cost [162].

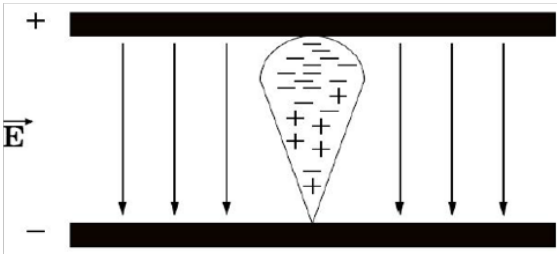


Figure 4.1: Illustration of an avalanche formation in a gaseous particle detector.

Despite the huge variety of gaseous detector types and techniques, the basic principle of detection remains the same. When a particle passes through a gaseous medium, they ionize the constituents of the medium. An external electric field is accelerating the resulting electrons and ions as free charges. The secondary electrons may cause an avalanche through the secondary ionization process. The geometry of the gaseous detector, and the gas used are depending on the electric field. The avalanche can create a spark or a streamer which propagates from the anode to the cathode. Based on the layout of the detector electronics, the position and the time resolution of the path of the particle could be determined and measured in a precise way. Figure 4.1 shows a schematic view of an avalanche caused in gaseous. A signal is induced on read-out electrodes because of the propagation of the resultant free charge carriers. Electronics can give a precise position and time information for the particle's path.

4.1.1 Modes of Operation

Based on the applied electric potential and the ionization phenomenon, the modes of operation of RPC are classified as follows:

- **Avalanche mode**: When a charged particle passes through the gaseous medium, it produces primary ions. These ions, being accelerated by the electric field, collide with the gas molecule to produce secondary ionization.

- **Streamer mode**: In this mode of operation, the applied electric field is large and consequently electron gain may go up to 10^8. The secondary ionization continues until there is a breakdown of the gas and a continuous discharge takes place.

Gaseous particle detector's modes of operation can be summarized, as

shown in figure 4.2:

- **Region I**: At very low voltage, charge begins to be collected, but recombination is still dominant.

- **Region II**: All electron-ion pairs are collected before recombination (plateau).

- **Region III**: Above the threshold voltage VT, multiplication is observed and in the proportional mode gain of ($> 10^4$) can be achieved as the detected charge is proportional to the original charge deposition. Eventually, space charges are built up around the anode, which leads to loss of proportionality.

- **Region IV**: In the Geiger-Muller mode photons are emitted by the deexciting molecules, which spread to other parts of the counter, thus triggering a chain reaction along the length of the anode (size of the induced signal is independent of the original energy deposition).

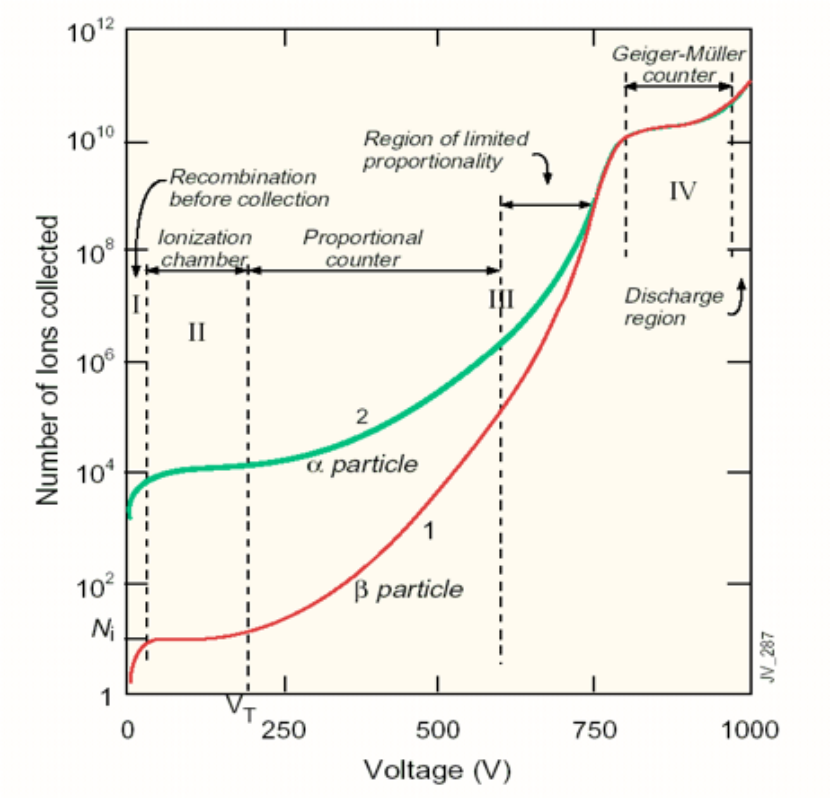


Figure 4.2: Gaseous particle detector's modes of operation

4.2 Resistive Plates Chambers (RPCs)

4.2.1 RPCs Development

As discussed before in chapter 3, the muon detector of the CMS experiment uses three types of gaseous particle detectors in order to identify the muon [179]; *Drift Tubes* (DTs) in the barrel region, *Cathode Strip Chambers* (CSCs) in the endcap regions and the *Resistive Plate Chambers* (RPC) in both regions of barrel and endcaps. The main function of the DTs and CSC detectors is to obtain a precise measurement of the position and momentum of the muon, while the RPC chambers are mainly acting as trigger detectors to provide quick information for the Level-1 trigger.

During the past 3 decades, *Resistive Plate Chambers* (RPC) was chosen and

used for many colliders and cosmic rays' experiments. The main advantage of the RPCs is that they are combining very good time resolution of $\sim 1\,ns$, sufficient spatial resolution, high gain, simple design, and low cost.

In the early seventies, RPCs were developed as parallel chambers with a bulk resistivity of $(10^{10} - 10^{12}\,\Omega \cdot cm)$. [137, 138]. Later in the early eighties, chambers with two-plates were constructed, which consisted of two *High-Pressure Laminate* (HPL), high – resistivity Bakelite plates that contain a low-pressure gas mixture [160]. In the nineties, the avalanche mode was introduced to the RPCs [58, 83] in order to increase their capabilities rate to $kHz \cdot cm^{-2}$ range. Based on these developments that have been performed through the years, RPCs are a leading choice to be used in high rate experiments of large areas.

4.2.2 RPCs General Design

RPCs are very simple in design. They consist of two resistive electrodes with bulk resistivity of $(10^{10} - 10^{12}\,\Omega \cdot cm)$, usually coated by a conductive material, as Graphite. RPCs use the technique of two resistive electrodes with gas detecting volume in between.

The two electrodes are placed on rectangular plastic frames with a constant separation distance between each other by small plastic separators, to ensure electrical and mechanical stability. A schematic view of an RPC and its principle of operation is shown in figure 4.3. The gap between the two electrodes is filled by a gas mixture containing organic gas, like $C_2H_2F_4/iC_4H_{10}/SF_6$, with a high UV absorption feature to be able to reduce the secondary avalanches. For controlling the charge multiplication, a strongly electronegative gas is used. A voltage difference on the electrode is applied.

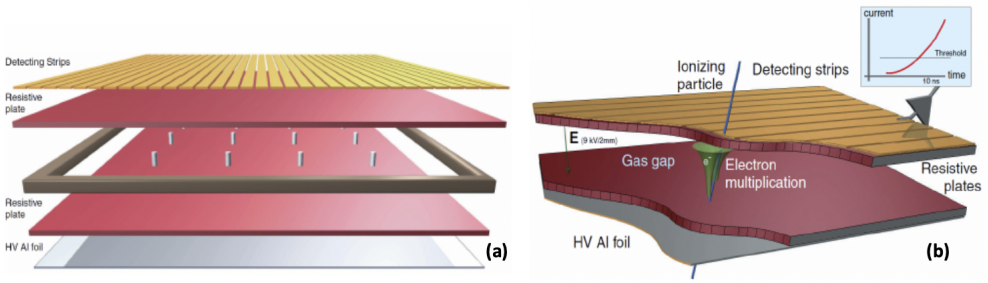


Figure 4.3: A schematic view of the different layers of an RPC (a) and illustration of RPC detecting principle (b).

4.2.3 RPCs Working Principle

The working principle of the RPCs is based on the ionization process which occurs in the gas when an ionizing particle is passing through the active medium in the presence of an external field. The free charges carriers are accelerated and start an avalanche. A cluster of electrons obtained after the ionization is the main source of the avalanche multiplication [12]. Electron charge is developed inside the gap, which drifts toward the anode. Then the signal of the charge induced is picked up by the conductive strips, like Aluminum or copper, which are placed on the top of the graphite coating layer and insulated by a mylar foil. The charge, collected on the electrodes, is compensated by the applied HV power by moving them outside the gap.

Streamer mode is used to operate RPCs through the gas gap, with the described configuration. The charge which results from the passage of the ionizing particle is about 100 pC and incident flux of about 100 Hz/cm^2. This mode has been tested and it is not suitable for high-rate experiments and therefore, it is not suitable to use with the LHC environment. To increase the capability rate, we can use the avalanche mode, by keeping the gain factor of the gas lower than 10^8, and the avalanche can grow to a maximum of 25 pC, which allow the incident rate to be an order of kHz/cm^2 [185]. RPCs are suitable in experiments like CMS at LHC due to its high rate capability.

4.2.4 RPCs System at the CMS Experiment

RPC system at the CMS experiment consists of 1056 double gap chambers, which operate in avalanche mode [13]. They are constructed from two High-Pressure Laminate (HPL) Bakelite gaps which contain gas space of 2 mm between the plates [73]. The two gaps are placed on top of each other, with a copper read outplaced between them, and Mylar sheets are placed in a way to isolate the readout strips from the graphite. A Schematic view of the double gap design in the RPC is shown in figure 4.4.

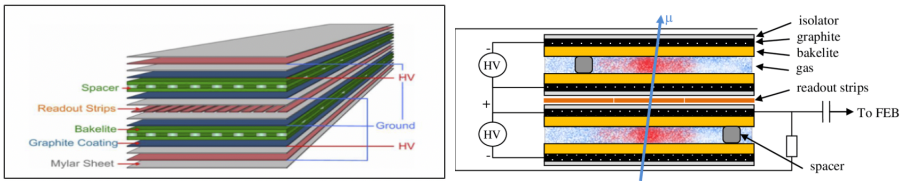


Figure 4.4: View of the double gap design in the RPC

In each gap, the plates are separated by a grid of $10 \times 10\, cm^2$, made of plastic, called "*Spacer*". It is used to avoid any contact between the plates, because of the electric attraction between them. The inner surface of the gap is coated with linseed oil [123] to make the surface smooth and to quench the photons of Ultraviolet (UV) [10]. While the outer surface of the gap is coated by a conductive paint of graphite and forming the ground and high voltage electrodes.

4.2.4.1 Gas Mixture

The CMS standard gas mixture, which we used also in RPCs, is composed of 3 components:

- 95.2% $C_2H_2F_4$, the charge carrier gas [57].
- 4.5% iC_4H_{10}, a quencher gas in order to absorb UV photons from molecule de-excitation.

- 0.3% SF_6, which used to control the excess electrons through its high electron affinity [11].

4.2.4.2 Conditions and Requirements

RPCs should have good timing resolution [77], having an average cluster size of ~ 2 strips (the number of contiguous strips fired by muon), having high efficiency, $> 95\%$, and having the ability to withstand long term operations and high background radiation.

It is highly important to have a fast timing performance, to be able to trigger the events efficiently. The trigger needs almost $25\,ns$ to identify the muon candidates and this requires only a few nanoseconds of time resolution.

4.2.4.3 Detector Layout

The layout of the CMS RPC system is controlled by many parameters. The need to trigger on the passing muon's transverse momentum p_T is one of the main steps that control the layout of the RPCs in the CMS experiment. To measure the transverse momentum p_T of the muon, one can study the bending of the muon in the magnetic field of the CMS. The muon is required to cross at least 3 layers out of 4 in the muon system. Muon system layers, which are interleaved with the steel return yoke, are ensuring the maximum bending of the muon's track between them. The RPC detector is divided into two regions, based on the CMS configuration - Barrel region covering a pseudorapidity range of $|\eta| < 1.2$ and endcap region covers the region $0.9 < |\eta| < 1.9$, with 1056 chambers in total. The RPC system has more than $110,000$ electronic channels and covers a sensitive area of $3500\,m^2$.

4.2.4.3.1 Barrel RPCs

The Barrel system consists of 480 RPCs, which are distributed along the beam pipe among 5 wheels equally, $Wheel\,0$, $Wheel \pm 1$, $Wheel \pm 2$. Each

one of these wheels consists of 4 stations with an increasing radius of R ($RB1$, $RB2$, $RB3$, and $RB4$), which interferes with the steel return yoke. Each of the barrel RPC stations is composed of 2 or 3 RPC units, called "rolls". Figure 4.5 represents a schematic layout of one of the 5 Barrel wheels with the numbered sectors shown. The two inner stations have two layers of RPCs with DTs in the middle, and each of the two outer stations consists of one RPC's layer and one layer of DTs.

Each of the wheels is divided into twelve sectors ($S01 - S12$), according to the azimuthal angle Φ direction, same as the construction of the return yoke of CMS. Due to mechanical reasons, $RB3$ and $RB4$ are further divided to $+$ and $-$ along Φ in all sectors apart from $S04$, $S09$ and $S11$ in $RB4$. Since $RB4/S09$ and $RB4/S11$ are in the feet of the barrel wheel, they consist of only a single RPC chamber. $RB4/S04$ is divided even more along 4 chambers $-$, $++$, $+$, and $--$.

The chambers are also divided into 2 partitions with respect to the pseudo-rapidity, called rolls - forward and backward [76], based on the trigger requirements, Only RB2in in $Wheels -1$, 0, $+1$ and RB2out in $Wheels -2$, $+2$ are divided into 3 rolls (forward, middle and backward), as shown in figure 4.6.

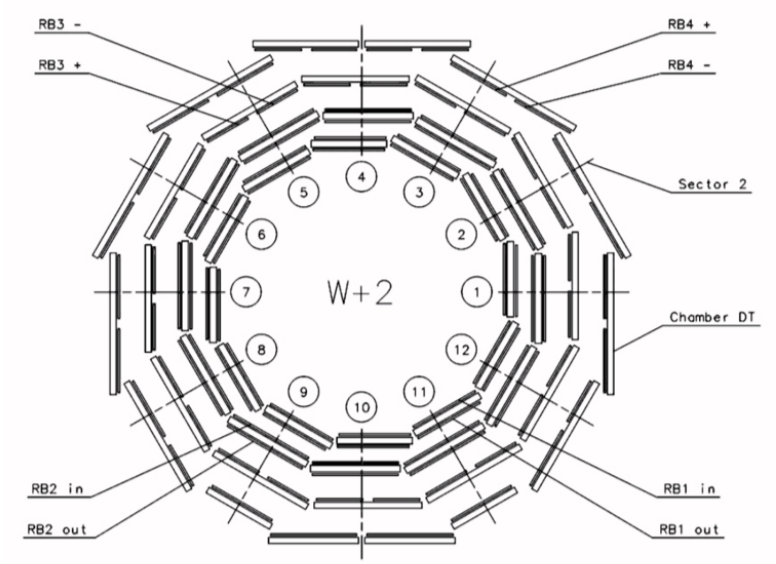


Figure 4.5: A schematic layout of one of the 5 Barrel wheels with the numbered sectors is shown.

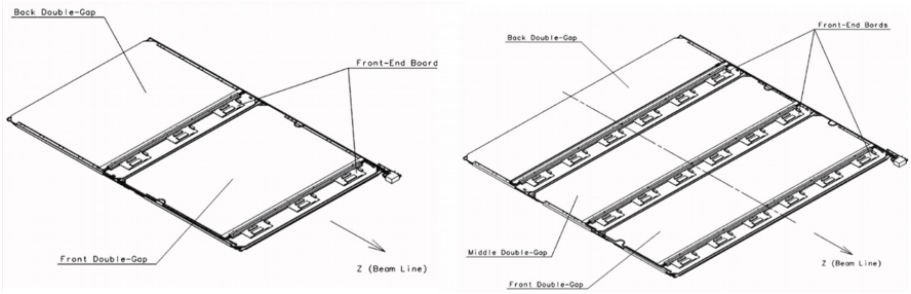


Figure 4.6: A schematic illustration of the RPC Barrel η partitions

4.2.4.3.2 Endcap RPCs

The design of the endcap-RPCs is almost the same as the design used in the Barrel system. The main difference between them is the geometry aspects and segmentation which are related to the geometry of the CMS detector. Figure 4.8 (left) shows a quarter view of the CMS muon system, RPCs are the colored detectors in the endcap system. Figure 4.7 (right) shows endcap-RPCs detector's photograph during the installation of the CMS detector.

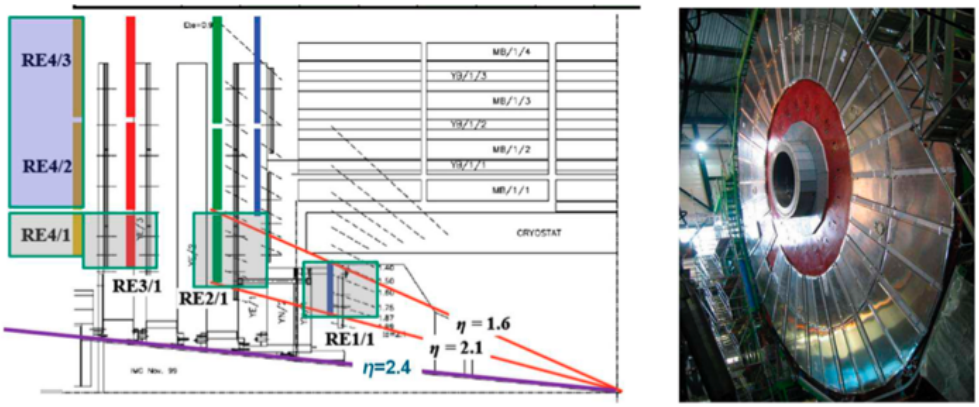


Figure 4.7: A quarter view of the CMS muon system (On the left), RPCs are the colored detectors in the endcap system. Endcap-RPCs detector' photograph during the installation of the CMS detector (on the right)

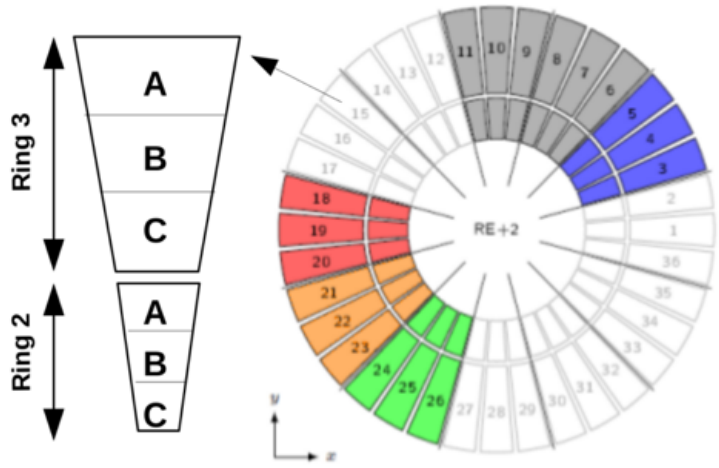


Figure 4.8: A schematic view of the RPC Endcap geometry

The endcap – RPCs system is consisting of 576 RPCs which compose the 4 disks on both sides of each of the endcap regions (positive and negative), $RE \pm 1$, $RE \pm 2$, $RE \pm 3$ and $RE \pm 4$. The two disks for the 4th stations (both positive and negative) are formed with 144 RPC detectors and installed in the muon system during the 1st Long Shutdown (LS1) upgrade (2013-2014). Each disk of the endcap stations is divided into 36 super-modules, along Φ with two concentric rings, ring 2 ($R2$), and ring 3 ($R3$) with three rolls per ring, labeled A, B, and C with respect to increasing η. An overview of the RPC Endcap geometry is given in figure 4.8.

4.3 RE$\pm$4 Endcap – RPCs at CMS Experiment

One of the major tasks during the 1st Long Shutdown (LS1) period (2013-2014), was adding the 144 newly built endcap-RPC detectors for the upgrade of the muon system in the forward region ($\eta < 1.6$). In the following period of data-taken of run II, starting from 2015, monitoring of the performance of the newly installed RE$\pm$4 chamber was of great importance.

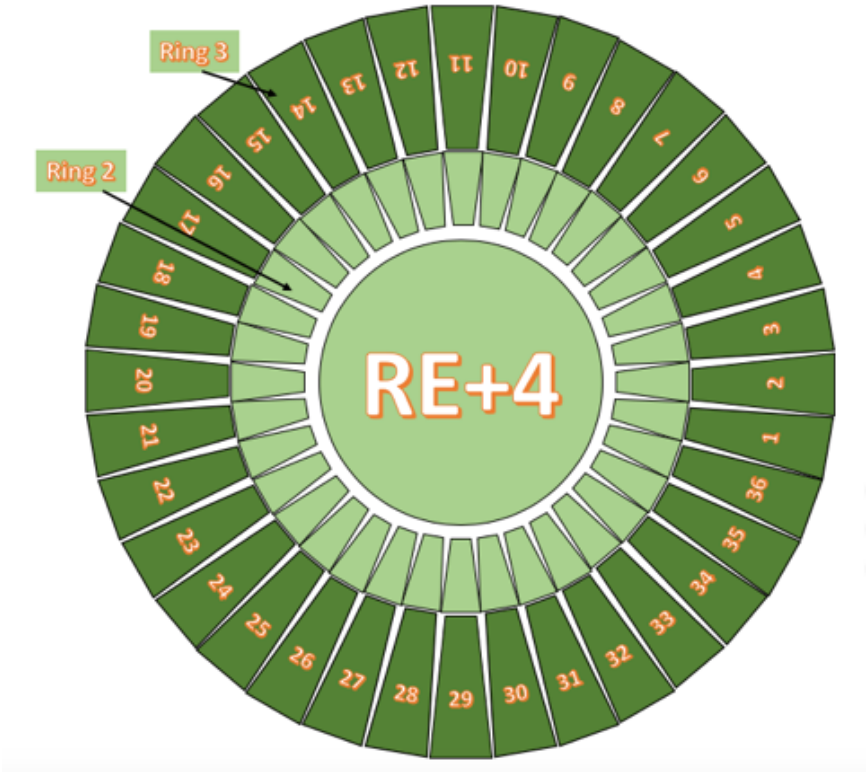


Figure 4.9: A schematic layout of RE+4 endcap-RPC with its 36 chambers per ring.

As the instantaneous luminosity of the LHC is increased gradually. It is expected that this increase will occur above the design value of $10^{34}\ cm^{-2}\,s^{-1}$ at $14\,TeV$, during the phase 2 of LHC. In order to prepare the LHC machine and its experiments for this process, two periods of the Long Shutdown (LS) are scheduled after each run. Several detector upgrades are planned, by CMS collaboration, to be performed during these periods [49]. For the muon detection system, the low p_T threshold for Level-1 muon trigger should be maintained and to ensure this, an extension of the fourth layer of endcap – RPCs in both regions is added to the RPC system during 1st Shutdown period (LS1).

The new two stations (disks) are composed of 144 High-Pressure Laminate (HPL) double gap RPCs, operating the avalanche mode, with the same design of the existing endcap RPCs chambers. There are 36 RPCs super-modules in the $RE4$ endcap disk (negative and positive disks). Each super-module is composed of two rings ($RE4/2$ and $RE4/3$) with a height of 1.66 and $1.93\,m$, respectively, as represented in figure 4.9.

4.3.1 RE±4 - Performance During Run II at 13 TeV

After two years of a technical stop, 1st Long Shutdown (LS1) period in 2013 and 2014, the Large Hadron Collider (LHC) at CERN has re-started working again with colliding proton beams at recorded breaking center of mass of $13\,TeV$ for the first time in May 2015. This is the beginning of the run II period of the high luminosity, which lasts for 4 years.

We have given a brief description of the RE±4 – endcap-RPCs system, and in this section, we will focus on the results of the system performance, such as Efficiency and Cluster Size, but first, we need to explain the method that has been used in the next subsection.

4.3.1.1 Track Extrapolation Method (Tag and Probe Method)

Efficiency studies are obtained using the Tag-and-Probe method with a single muon triggered dataset. Probe muons are reconstructed by using the tracker muon algorithm, which is independent of the RPC system, requiring at least one segment to be matched in local x position within $3\,cm$ and pull ≤ 3. Probe muons are also required to have at least $20\,GeV$ in transverse momentum [157].

The reconstruction algorithm of the "*RPCMuon*" [65] is included in the standard reconstruction of run II. The algorithm starts from the inner track and finds the matched RPC hits, "*RPCRecHits*" along its trajectory. The track extrapolation is done, and the results of this extrapolation are stored in the muon objects. The track extrapolation method is used to measure the efficiency of RE4 endcap-RPCs. *TrackerMuon* [149] identification on the muon is required and it is done by extrapolating inner tracks to muon systems to find the matching DT/CSC segments. The *TrackerMuon* and *RPCMuon* reconstruction are designed to run independently and to be complementary algorithms to each other. *Tag and Probe* method is used to remove bias from the triggers which start from the *SingleMuon* dataset, require one muon (tag) to pass identification and isolation cuts but also require to be matched to the trigger object to accept the event. Then we select another muon (probe) in the event to study the efficiency, requiring TrackerMuon identification and/to form $Z \rightarrow \mu\mu$ resonance.

4.3.1.2 RE4 Efficiency Performance

We focused on monitoring the performance parameters of the endcap-RPC system, specially RE−4 and RE+4, such as Efficiency [1], cluster size and currents through run II data-taken. The RPC efficiencies are measured during 2015-2018, which are comparable and in agreement with the expectations. The efficiency distribution for RE±4 - endcap RPCs is shown in figure 4.11, (top) distribution for RE+4 and (bottom) distribution for RE−4. Figure 4.11 (top) represents the overall efficiency distribution of endcap-RPCs vs. the number of rolls (η partitions) during run II of the LHC for the endcap region. The underflow entries are from rolls with efficiency lower than 70%, caused by known hardware problems - threshold control at that time, chambers switched off because of gas-leak problems. Figure 4.11 (Bottom) represents the performance of the overall RPC efficiency vs. time for the 2016 and 2017 data.

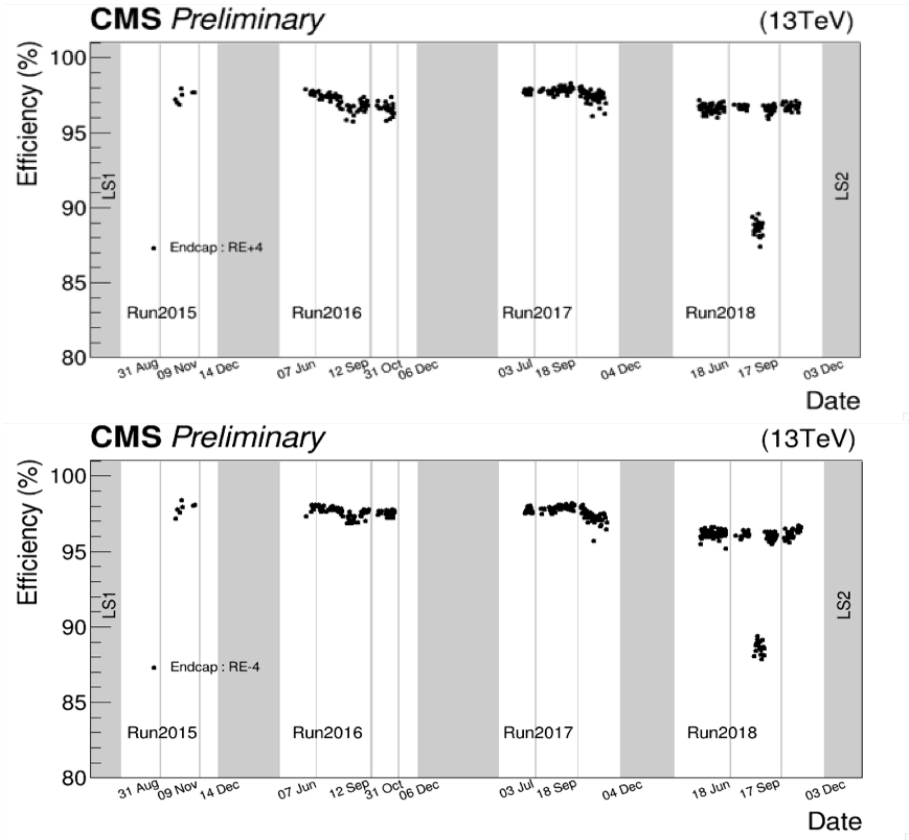


Figure 4.10: RE+4 (top) and RE−4 (bottom) efficiency performance over time, during run II

[1] Efficiency is defined as the ratio between the number of chamber signals in a fixed time window and the number of triggers.

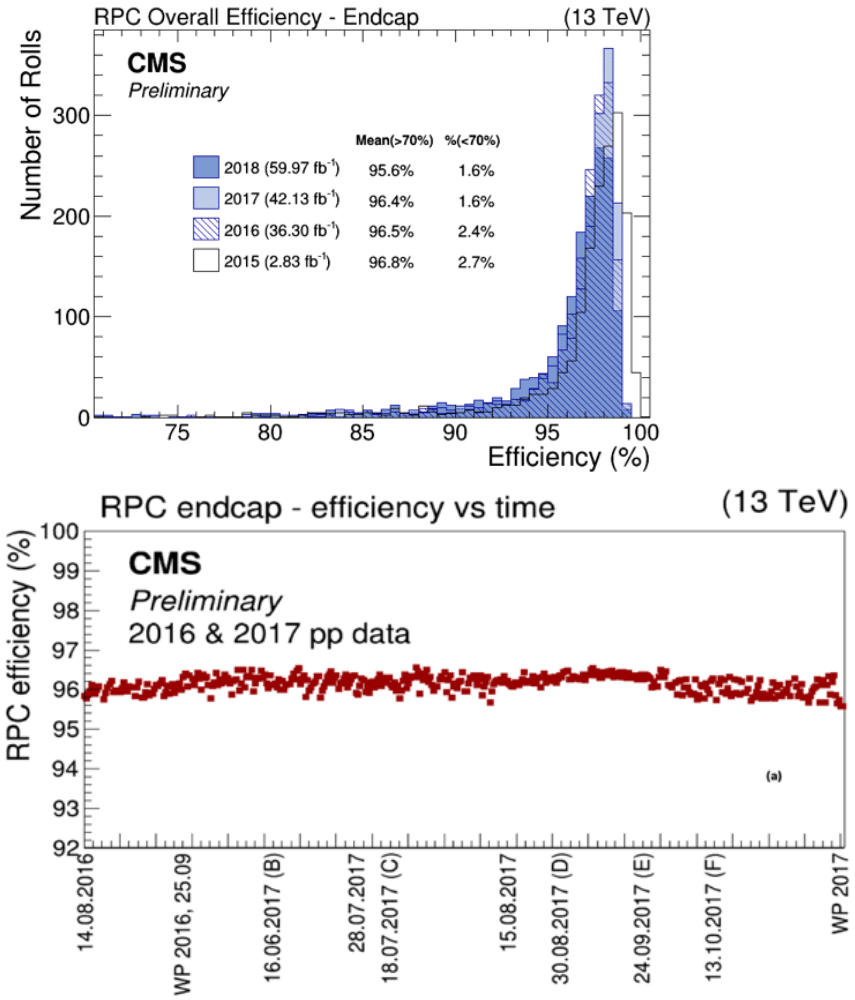


Figure 4.11: Overall efficiency of Endcap (top) for 2015-2018 data-taken, (bottom) RPC overall efficiency vs. time for 2016-2017 data-taken

4.3.1.3 RPC Cluster Size Studies and performance

The chamber Cluster Size [2], see figure 4.12, is monitored during run II, run by run, to guarantee the system stability. Figure 4.13 shows the cluster size distributions for the RPC - endcap measured during 2017 and 2018. Figure 4.14 shows the distribution of the cluster size for the endcap-RPCs overtime during 2016 and 2017. We found that these analysis results are very useful in monitor-

[2]The Cluster size (CLS) of the RPCs is defined as "the number of adjacent strips fired when an avalanche is produced in the RPC", i.e. the number of contiguous strips associated to a hit

ing the stability of the RPC system for different operational and environmental changes.

During run II, the performed studies show that the mean value of the cluster size of the RPC system is $\sim$ 2 strips, which is One of the achieved greatest successes is to keep the cluster size stable over time with this average value which is the same as CMS TDR [68], which is in agreement with the trigger requirements for ≤ 3 strips.

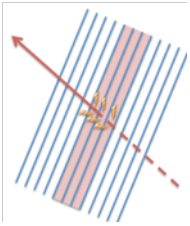


Figure 4.12: Cluster Size, as the number of contiguous strips associated to a hit

A special focus on the RE$\pm$4-chambers cluster size performance is illustrated below in figure 4.14, (top) for RE+4 endcap-RPCs, (bottom) for RE$-$4 endcap-RPCs

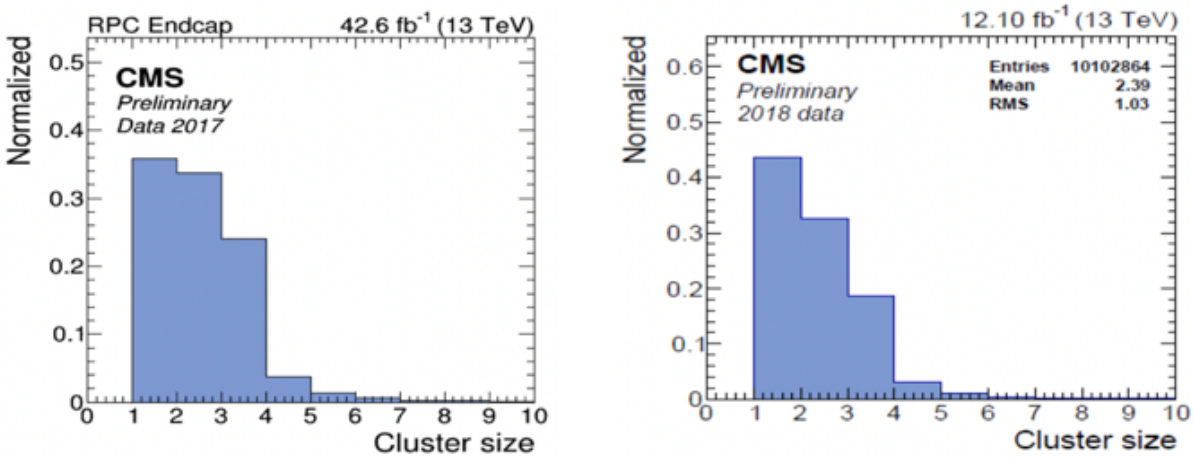


Figure 4.13: Endcap Average Cluster Size

Performance results of RE$\pm$4-endcap that are discussed in this section are measured using *tag and probe* technique. As shown in figures 4.11 and 4.15

each point corresponds to an average efficiency or cluster size per station in a given LHC fill. Data points with low statistics or temporary problems are excluded from the distributions. The $x-axis$ is representing the date while the $y-axis$ is the average efficiency of cluster size for the detector part under study. Vertical grey lines and areas correspond to the planned technical stops (TS) and year-end technical stops ($YETS$).

The history of the efficiency and cluster size follows the changes of the applied high voltage working points and changes of the *Isobutane* concentration in the working gas mixture. The spread in 2015 cluster size distribution is caused by a threshold control problem, solved in October 2015. A small drop of the RE+4 and RE−4 cluster size in 2016 is caused by a temporary Low Voltage (LV) problem, solved at the end of August 2016. The drop in the efficiency during 01-August-2018 was caused by a known configuration setting problem at that time.

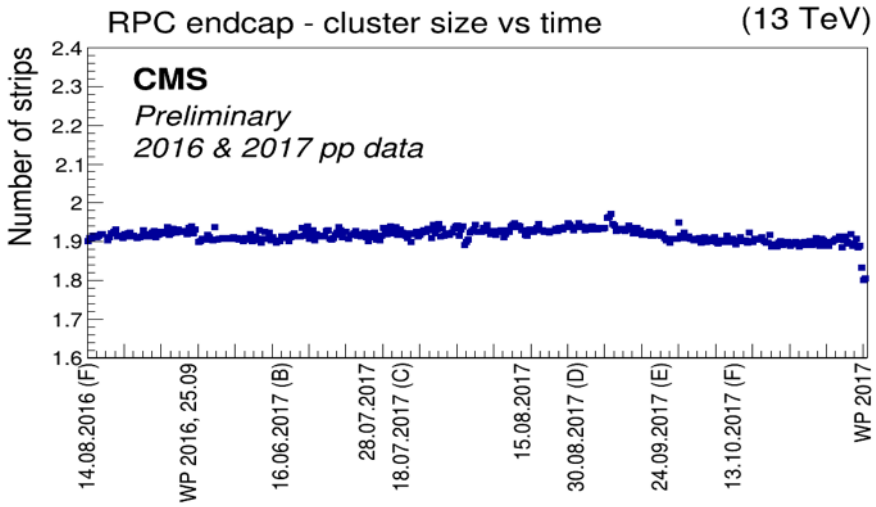


Figure 4.14: The history of the mean Cluster Size for the barrel for 2016 and 2017 physics data taking at 13 TeV.

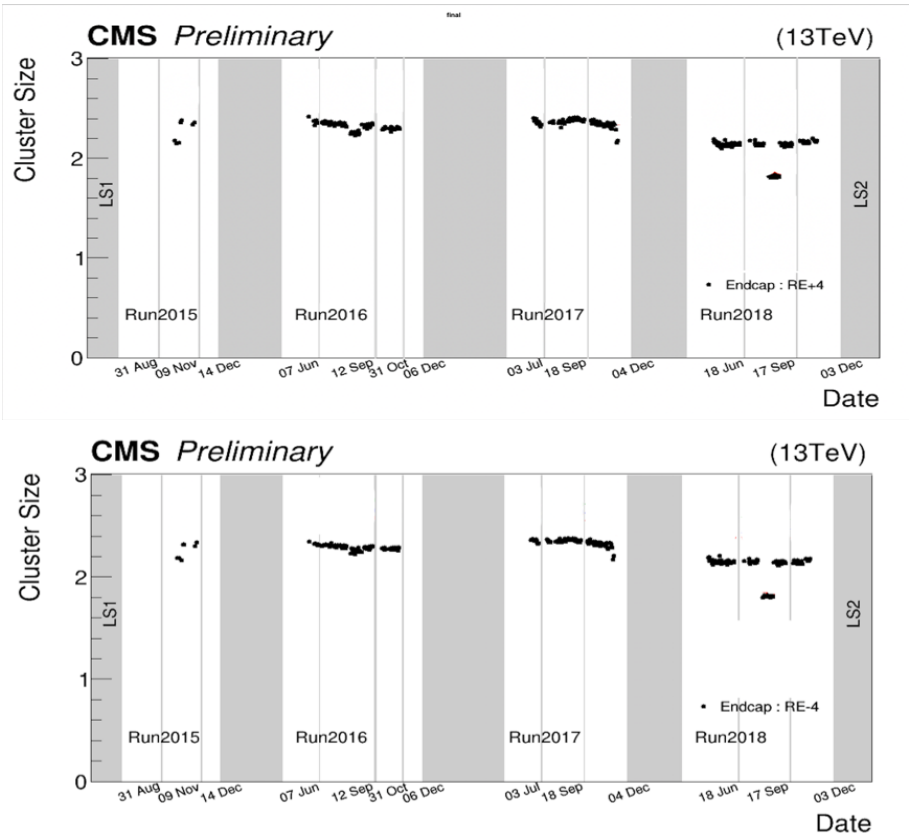


Figure 4.15: Cluster size performance over time, during run II, for RE+4 (top) and RE−4 (bottom)

4.3.1.4 Endcap RPCs Background rate

One of the most important factors in monitoring the performance of the CMS muon system is the *background radiation*. A clear understanding of the background rate plays an important role in the performance of the muon system. During the LHC proton-proton collision runs, the RPC hit rate is measured at the strip level. The strip rate is calculated by using the incremental counts of the RPC trigger Link Boards. The incremental counts are taken during typical time intervals of the order of 100 s. Then, the resulting rates are averaged over the total run - time and normalized to the strip area. The instantaneous luminosity is averaged over the same run - time. Normalized rates in Hz/cm^2 are presented. No trigger selection is applied at this stage, resulting in an inclusive measurement of the radiation background rates [150, 82]

Figure 4.16 shows the RPC hit rate vs. instantaneous luminosity distributions for the RE±4 endcap-RPCs stations. Results are obtained with 2018 proton-proton collision data with selected runs of stable beams and the number of colliding bunches larger than 600. Luminosity values are provided by the official CMS luminosity tool, mean rate values are defined as the average rate on all the rolls in the corresponding station.

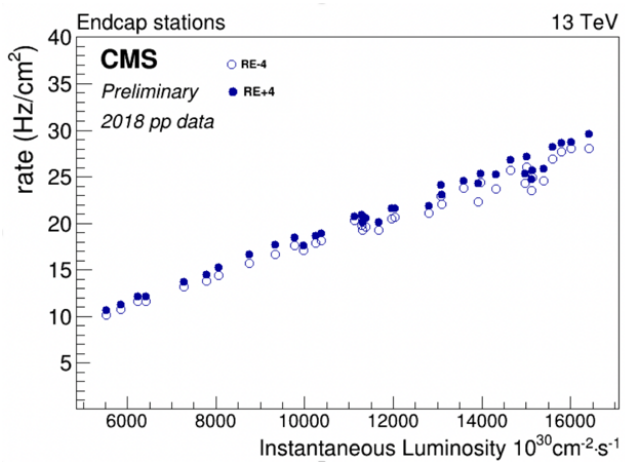


Figure 4.16: RPC hit rate vs instantaneous luminosity distributions for the RE±4 endcap-RPCs stations.

4.3.1.5 Currents Studies for RE4 Stations

- **Currents vs. Time and Integrated Luminosity**

  From the beginning of 2018 to September of the same year, a higher ohmic current [3] has been observed in RE−4 compared to RE+4. After the gas flux was doubled in $RE-4$ (Mid-September) a significant change in its behavior has been observed, up to the point in which it drops below RE+4 curve. The ohmic current increase is directly correlated with the background. In RE4 the background rate is about $40\,Hz/cm^2$ and the gas flow is $1.1\,V/h$.

[3] Ohmic current is defined as current with no beam, up to around $7000\,V$, in the range where there is no gas amplification contribute and the current, follows the ohmic law. The ohmic current values are monitored at $6500\,V$, and Cosmic current, is defined as current with no beam, at working point voltage, in the region of the gas amplification

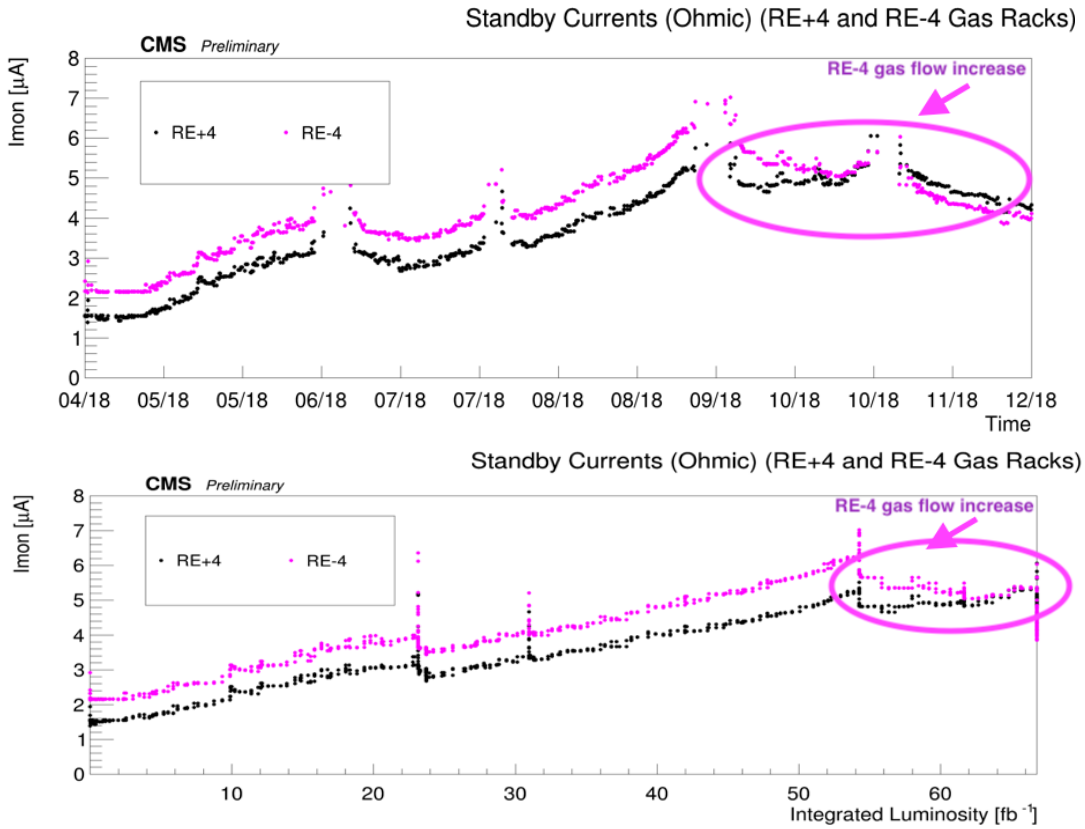


Figure 4.17: RE+4 and RE−4 Current vs. time (top). Currents vs. luminosity (bottom) of RE+4, RE−4 stations

The currents measured in RE+4 and RE−4 RPC stations in endcap are plotted in figure 4.17. The measured currents are plotted vs. time (top), and integrated luminosity (bottom).

- **Currents vs. voltage**

The currents, measured in different years for RE±4 endcap-RPCs stations, as a function of the High Voltage (HV), for example, one of the RE −4 RPC chambers is shown in figure 4.18. The lowest curve depicts the currents measured in the middle of September in 2016. The blue and green markers correspond to currents measured in July and October in 2017, and the purple ones - to currents measured in the beginning of 2018.

As it might be seen from the plot, the current increases as collisions go

on. From the near end of 2017 to April 2018 we observe that the current decreases significantly during the Year-End Technical Stop ($YETS$).

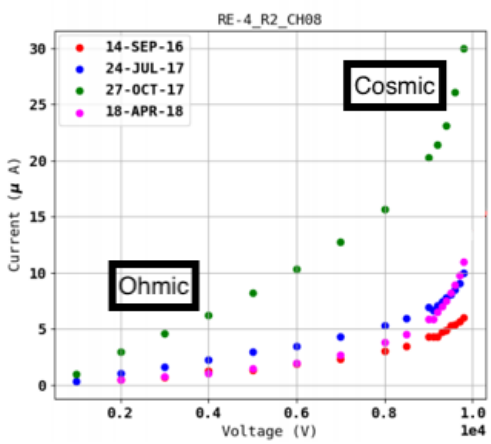


Figure 4.18: RE+4 and RE−4 Current vs. Voltage

4.3.2 RE±4 Commissioning and Re-validation During LS2

The RE±4 endcap-RPCs chambers are installed on the Cathode Strip Chambers (CSCs) mounting posts on the 3rd endcap yoke's backside. Figure 4.19 shows a drawing of the RE4-RPCs modules installed on the CSCs [135].

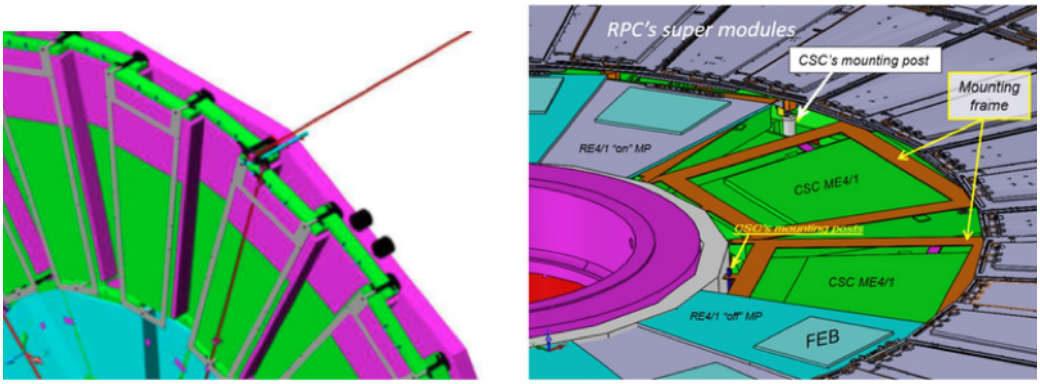
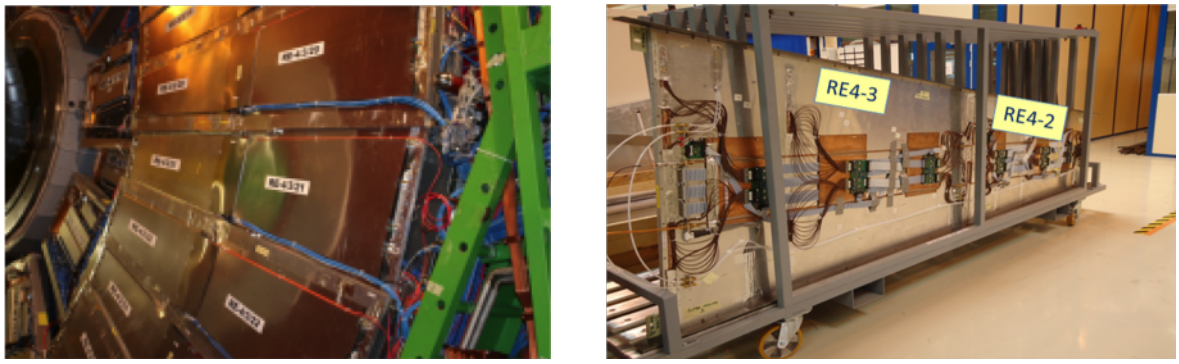


Figure 4.19: RE4 and CSCs overview in CMS

The endcap-RPC trigger logic requires hits in at least three layers, which was causing a drop in the efficiency to almost 80 %. By enabling three out

of four trigger logic with the RE4 champers, the RPC endcap performance efficiency has increased to 95 % [179].

After 4 years of running the LHC machine during run II, the 2nd long shut down (*LS*2) of LHC is scheduled during 2019/2020. RE4 endcap-RPCs were dismounted in March 2019 to spare space for neighboring CSC detector electronics refurbishment. Both the dismounted stations are planned to be reinstalled in November 2019 and April 2020 after performing several quality control procedures to ensure that no damage has been done and these chambers will be operating properly during run III.



(a) (b)

Figure 4.20: RE4, covered with RPC detectors before the dismounting (a), RE4 super module after dismounting (b)

The main reason for dismounting these chambers is the upgrade of CSC electronics, which requires the CSCs to be taken from the CMS cavern to the surface to replace the chamber's electronic boards and to test the new ones. This procedure is needed for the phase 2 upgrade of the CSCs system, to be able to handle the higher Level-1 trigger rate and latency, and also to replace some components that won't survive the large radiation dose.

Endcap-RPC *LS*2 upgrade project was designed to perform the major quality control tests to all the chambers of the RE$\pm$4, to ensure that all components of the chambers are working properly after the dismounting and to fix/replace damaged components, which were monitored and discovered during run II. Figure 4.20 shows real photographs of the RE4 disk before (a) and after (b) the dismounting.



Figure 4.21: RE4 laboratory with the dismounting disks

A new laboratory is built at the beginning of 2019, at the surface of the *P*5 site to store the *RE*4 chambers, dismounted from the CMS detector. It provides special environmental conditions for temperature and humidity as well as safety sensors, which are monitored daily to ensure a suitable environment for the chambers.

This laboratory is not only for storing the RE$\pm$4 chambers but also for performing important validation procedures, for fixing any part of the components of the chambers that were affected or damaged during run II and also for testing overall components. Each chamber goes through a certification procedure with some major tests such as gas leak tests, cooling tests, as well as High voltage stability, and noise measuring tests for all the electronic FEBs to spot any noisy or dead readout channels. Figure 4.21 shows the new laboratory built for these chambers. Figure 4.22 shows the RE4 endcap-RPC chambers extraction.



Figure 4.22: Extraction process of RE4 chambers, More photographs can be found in the following link: https://cds.cern.ch/record/2668394?ln=en. A video of the RE±4-supermodules removal can be viewed here https://drive.google.com/open?id=1Q6eDwRv69m973AQqlvOBhyCmEwGnprpt.

4.3.2.1 Re-validation of the RE4 at the Surface

Seventy two super chambers (RE+4 and RE−4 stations) were dismounted in March 2019 to free space for CSC extraction for electronic refurbishment. RE+4 stations are going to be reinstalled inside CMS in November 2019. Some quality control tests have been performed in the newly built lab with a controlled environmental condition to re-validate all the detectors. This included performing the noise scan on the detectors to confirm the functionality of the detector's front-end boards (FEBs) and to spot any dead or noisy readout channels, based on the noise rate histogram results. Figure 4.23 below illustrates the noise scan results for one of the RPC detectors CMS-RE4-3-GHENT-048_A. Strip number 16 in this detector represents an example of a single noisy strip. That is due to the very high noise rate in that strip per unit area which was

approximately 4400 Hz/cm^2.

Moreover, the high voltage has been turned on and kept at 6 kV for each of the 6 super modules carried on a single trolley and the current readings have been recorded regularly using a web detector control system (web DCS).

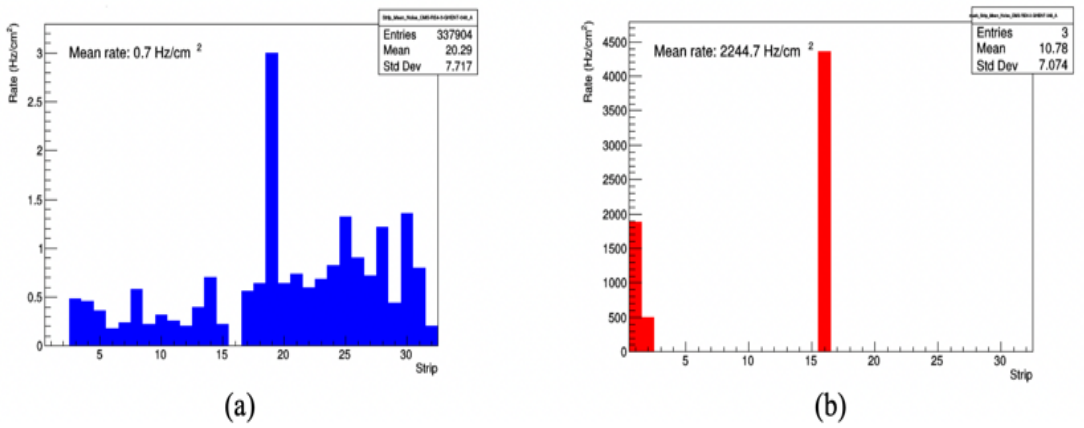


Figure 4.23: Illustration of the noise scan results for the one of the RPC detectors CMS-RE4-3-GHENT-048_A



Figure 4.24: RE4 super-modules with connections (left) to the HV scan rack (right)

Table 4.1 shows a sample result for current readings from trolley-02 at different dates. In this table, "SMs" stands for Super Modules and $P0$ is the expected Ohmic current that was determined by extrapolating the decreasing current's slope by end of run II. All SMs were kept at a constant voltage of 6 kV.

Figure 4.24 shows one of the connected trolleys with the gas pipes and HV scan cables during the test (left) and the HV scan rack (right) used to control the process and monitor the results and behavior of the current during the scan.

Table 4.1: Trolley-02 current readings in μA, we disconnect this trolley on 16 August after completing its validation.

SMs	20 Jul 2019	30 Jul 2019	06 Aug 2019	16 Aug 2019	P0 from fits 2018
26	4.7	3	2.8	-	2.5
28	12	7	6	5.2	4.1
22	15	7	4	-	4.5
24	6	4	4	-	4.7
18	7	5	4	3.2	2
20	6	4.3	4.2	-	4.4

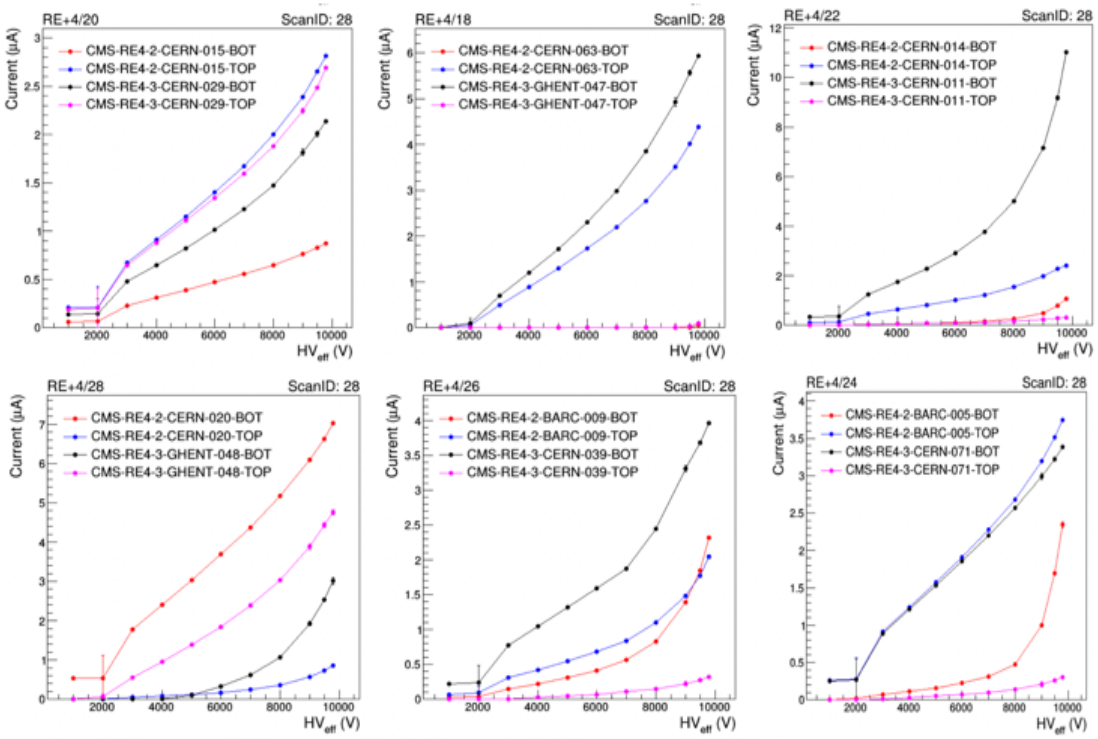


Figure 4.25: Current vs. Hv for Trolley 02 super-modules in each gap

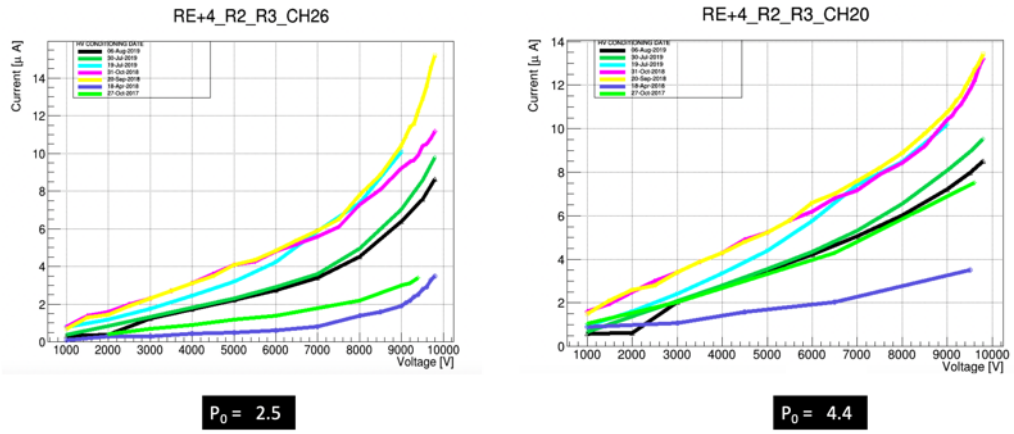


Figure 4.26: Current vs. Voltage (before and after dismounting)

It can be seen from the table that as the super modules are kept at high voltage for a long period of time, the resulting current value decreases and is expected to approach the corresponding value of $P0$. It can also be observed that the SMs with a relatively high value of current initially, tend to have a significant rate of reduction in its value at the beginning and then this rate of reduction itself decreases as the current approaches the corresponding value of $P0$. Finally, some other SMs have shown that the currents can be decreased much faster if higher voltage values are used.

Since the increase of currents appears to be reversible as it decreases back to initial value over time as data taking stops, a conclusion can be made that there is no damage to the inner electrode surface and no permanent damage to the electrode resistivity. The current increases are due to a high concentration of pollutants (HF) which is not effectively removed by the gas flow and thus forms a thin conductive layer on the inner electrode surface and decreases surface conductivity. The RPC gas mixture is mainly composed of F-gas. The decomposition of this gas under electrical discharge produces Fluorine ions which can produce HF [28]. Gas flux cleans this layer and HV helps burn any deposit after data-aking is stopped and the system is kept flushing with gas. Figure 4.25 shows the current distribution for Trolley 02 super-modules in each gap. Figure 4.26 shows the current distribution for two of the super-modules as a function of voltage for HV scans which has been done starting from July 2017 till August 2019 (before and after dismounting comparison).

In conclusion, during my service work period in 2019, 4 Trolleys, each trolley holds 6 super-modules, (T01, T02, T06, T03) from RE+4 are completely validated and closed, by replacing all the insulating protections, final checks for all the connections/groundings and putting back the aluminum covers. The work is still ongoing on the rest of the trolleys.



Figure 4.27: Gas Leak Test set-up with monitored screen

Another main mild-stone for the re-validation process is the gas leak test. The gas flow is controlled by measuring the stability of applied pressure of $10\,mbar$ using a pressure sensor, in a fixed time of $600\,sec$. The gas leak rate should be less than $0.2\,mbar/10\,min$ at 2 liters.

As shown in figure 4.27, the gas leak test is performed by using a special set up (with a photograph for the doctoral candidate while preparing the chamber

pipes to connect the gas pipes and high voltage cables), with a nitrogen bottle as a gas injector and bubble input and output system to monitor any issue that may exist in the input injector process or the output bubbling tubes (shown in figure 4.28, for gas leak test (right) and the one used for HV scan test (left)). If there are no bubbles (gas indicator) appearing in the output tubes, this is an indicator that the tested gap is broken. Also, by monitoring the behavior of the injected gas pressure with the time and calculating the slope of the plateau after switching off the injection sensor, the actual leaking rate for the gap can be obtained. Below is an example of the tested gaps with the results of the gas leak test.



Figure 4.28: Gas Leak Test set-up with monitored screen

In conclusion, RPC systems have stable performance after running in extreme conditions for more than 7 years and no obvious aging effects have been observed. The system is ready to participate in the upcoming High Luminosity-LHC program.

CHAPTER 5

DATA ANALYSIS IN CMS

This chapter gives a brief explanation of how to generate and simulate events in the CMS detector as well as the reconstruction process. And mainly, it will describe the generation step of monopole events and the simulation process of monopole interactions in the CMS detector. It is also important to discuss some important information about the Long-lived particles (LLPs) and their signature in the detector. The development of experimental studies is always guided by fundamental theories. In order to be able to analyze the recorded data by the CMS detector, we have to reconstruct the obtained signals which come from the different parts of the CMS detector, to identify any particles in the event. Also, one of the main purposes of the analyzing process is to compare the experimental results with the theory.

In this chapter, we will give a brief introduction to the description of the event structure at the LHC with the steps needed to simulate the event which will interact with the layers of the CMS detector. Also, we will explain in detail the Monte Carlo generator program which we used in this research.

5.1 Proton-proton Collision's Physics

To generate an event in a proton-proton collision, we have to generate the complete process starting from the colliding protons in the LHC till the final observed particle. Each of the final observed particles is detected in a specific layer of the CMS detector depending on the type of that particle in its final state.

There is dedicated software for the CMS experiment, which allows us to simulate, reconstruct and analyze the recorded data. CMS software (CMSSW), is a set of tools and algorithms to produce the Monte Carlo (MC) simulation samples and also to reconstruct the recorded data which produced in the CMS detector [46, 71]. First, a brief description of the Monte Carlo (MC) simulation process will be given, and then we will describe the data formats, which are used in both real data and MC.

5.1.1 Monte Carlo (MC) Event Simulation

In order to start the MC event simulation, there are two main steps which should be done in order: **the event generation**, which a proton-proton collision is generated and simulate the particles that appear in the detector layers, and **the detector simulation**, which will explain how the generated particles will behave inside the detector.

5.1.1.1 The Event Generation

According to the composite nature of the protons, the event structure at the LHC is complicated. There are many generators which can be used to generate events with the required conditions for each particle, such as **Pythia** [171], **Madgraph** [33, 107]. The first step of producing the MC samples is called "*GEN step*". The hard scattering process is simulated during this step, which is the interaction between the quarks and gluons (partons) in the proton-proton collision. Then it creates the interesting physics process we need. The mo-

mentum of the protons is known but the partons momentum within the protons is constantly in flux. Thus, the generators use *Parton Distribution Function* (PDFs), which is important to describe partons to have a certain momentum and it is determined by the momentum fraction of the parton and the transferring momentum. Since the current theories can not derive the PDFs, they are measured experimentally. Then the generator is modeling the short-lived particles after the step of simulating the hard scattering. Then the partons hadronization is simulated and create the parton showering. The last step in generating events is the "*underlying event*", which is the soft partons interaction and pile-up is modeled.

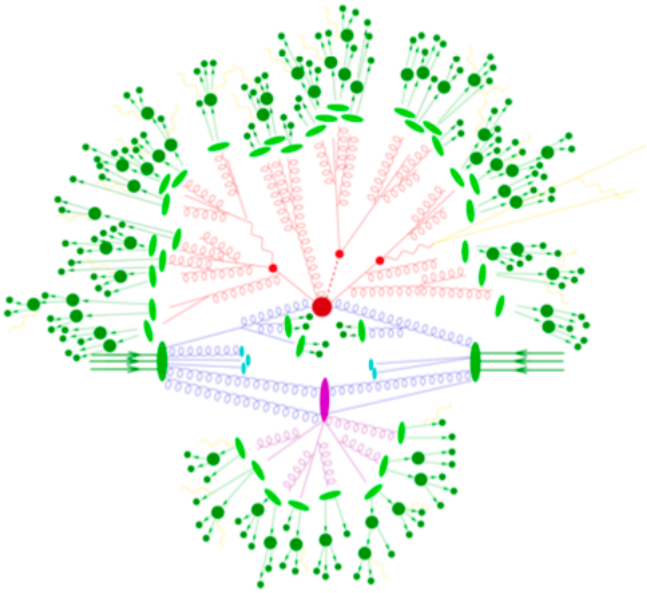


Figure 5.1: Illustration of an event shows the hard scattering and the ensuing parton shower (red), the hadronization (green) with hadron decays (dark green) and radiated photons (yellow), and the underlying event coming from beam remnants (blue) and multiple parton interactions (purple). Figure from ref. [110].

Figure 5.1 demonstrates the event structure and shows the hard interaction (red), surrounded by a tree-like structure. Due to the partons color charge, their involvement in the hard interaction process will create a parton shower consisting of radiation cascade from QCD processes. The red color indicates the outgoing partons and the blue color indicates the incoming partons. Then the resultant partons will be hadronized because of color confinement (green

color), with radiation of photons (yellow) and hadron decays (dark green). The last step is the purple interaction which represents the secondary interaction between the remaining constituents of the proton. Besides these multiple interactions of the partons, additional pile-up interactions can occur and it can generate the event. All these steps must be counted when we generate events using any generator. The sub-processes which are used to generate an event can be summarized as follow:

- **Hard scattering and Parton Distribution Functions**

  Each of the colliding protons is formed of quarks and gluons (partons), the proton's momentum is distributed among its partons depending on the Parton Distribution Function (PDF) used. At a given momentum transfer, two partons will interact from the colliding protons, with a certain probability. PDFs can be determined experimentally and they are available from various groups, e.g. NNPDF [41], MSRT/MSTW [127], CTEQ [148]. Figure 5.2 shows an example of PDFs obtained by the NNPDF group.

  PDFs $f(x, Q^2)$, where x is the momentum fraction of the proton and Q^2 is the momentum transfer scale are described in the figure, where the valence quarks in the proton (up and down) have a momentum fraction which is larger than the fraction momentum of the remaining sea quarks, which shown as virtual quark - antiquark pairs forming from gluons and they are annihilating again. Then the PDFs convoluted with the hard scattering's matrix element, where the two colliding partons produce high energetic final state particles.

  The generator which is used in this search in such a process is MADGRAPH5_aMC@NLO, a detailed description of the model used in this search will be discussed in the next chapter.

- **Parton Showers** As mentioned, the hard scattering produces partons that can be branched into other partons and they in turn create a secondary partons shower associated with a radiation cascade from QCD processes. This radiation is mainly categorized into two types of radiation depending on its origin. The first type is called the *Initial State Radiation* "ISR", which is produced from the colliding partons. The second type which is produced from the outgoing partons, called *Final State Radiation* "FSR".

The detail of the perturbative method to involve these types of radiation in the generation process is described in [37, 90]

- **Hadronization** Following the step of the showering, is the hadronization step, where the colored particles produced in the parton shower are transforming into color neutral hadrons. Phenomenological models are used for such a process. The showering and hadronization steps, which used to perform this search are done via "*PYTHIA 8*" [172, 170], which is a generation event software that includes hard (soft) interactions, PDFs, ISR and FSR parton shower, fragmentations and decays. PYTHIA is using a set of parameters tunes to reproduce the experimental data.

- **Underlying event**

  In general, the colliding protons share a small fraction of their energy with the colliding partons. the rest of the energy remains in the beam remnant, which continues its path in the original direction. Since the proton is formed of many partons, more partons can collide with the other proton's partons, (since we assumed in the previously described processes that only one parton from each of the protons are participating in such a process), this results from a multi-partons interactions (MPI) so that the hadronization of the multi-partons interaction (MPI) and beam remnant are referred to *"underlying event"*.

- **Pile-up**

  Two types of pile-up could occur, *In-time pile-up* (PU) collisions, which produced from the proton' scattering in the same bunch crossing of the hard interaction process. *Out-of-time pile-up* collision, which produced from the next or previous proton bunch crossings.

After passing through this chain of essential processes to generate events, we have to combine this information to a detector simulation framework.

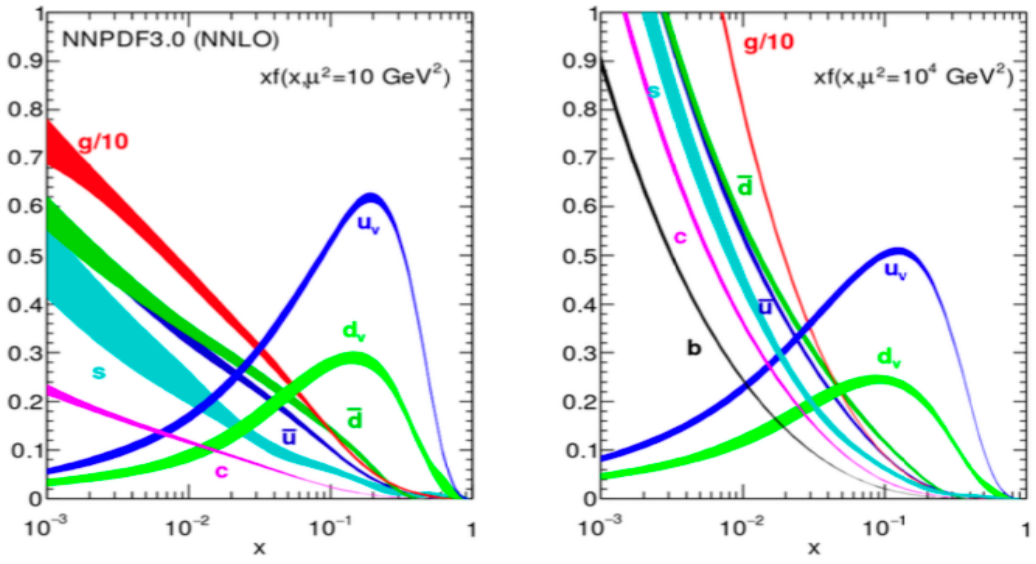


Figure 5.2: The Parton Distribution Functions multiplied by the momentum fraction x at energy scales $Q^2 = 10\,GeV^2$ (left) and $Q^2 = 10000\,GeV^2$ (right) for the different valence and sea quarks and the gluons present in a proton, obtained in the NNLO NNPDF 3.0 global analysis. Figures taken from [41]

.

5.1.2 Detector Simulation

After generating events through the parton shower and hadronization, they are passed to the simulation step of the CMS detector and being processed by a simulation toolkit called ”GEANT4 ” [29].

Interaction between particles and the material of the detector need to be simulated and it is well described in the toolkit with the effects of these interactions, such as *Bremsstrahlung* of electrons, ionization energy loss of charged particles and showering of photons, electrons and hadrons in the detector calorimeters as a result of the particles are passing through the detector layers.

The CMS - GEANT4 simulation package is installed inside the CMS software, which contains the detector’s geometry with sensitive layers designed to detect the charged particles. It also contains information about the dead mate-

rial regions which contain cables, support structure, and cooling pipes. Also, a precise magnetic field's map is included to be able to simulate the charged particle's curvature properly

5.1.3 Digitization

After the simulation of the detector *"SIM step*", the digitization process takes place, which gives information regarding the electronic response produced inside the detector by the hits occurring in the active layers of the detector material. In such a way the event content is the same as the real detector output. Also by adding the hits of the generated proton-proton interactions to the hits which results from the main interaction, the pile-up effect is included.

The simulation algorithm used in this search was imported specially for monopoles, as the interaction of new particles that can be produced by special models is not always inserted inside the software package by default. Detailed description of the method of importing the monopole model in GEANT4 will be discussed in the next chapter.

5.1.4 Event Reconstruction

Each layer of the CMS detector is designed to identify and reconstruct specific types of particles. Figure 5.3 presents a visualisation of the charged particles interactions that occur inside the CMS detector, starting from the interaction point to the outer layers of the CMS detector.

We generate minimum bias events for the pile-up and the obtained events from the simulation step can be directly reconstructed, using the CMSSW reconstruction algorithm. Besides applying the reconstruction method to the MC simulated samples, it is also applied to reconstruct the real data coming from the detector. The reconstruction chain is performed as follow:

- First, track reconstruction is performed, with a particular track reconstruction algorithm for electrons and muons. For monopoles, a special

track combiner algorithm is used, which will be described later in detail.

- Calorimeter deposits, which occur by charged particles, are grouped into clusters and a special reconstruction algorithm called "Particle Flow (PF)" is used to improve the reconstruction step. PF algorithm improves the reconstruction performance of jet and hadronic τ decay, as well as the determination of the missing transverse momentum and electron and muon identification.

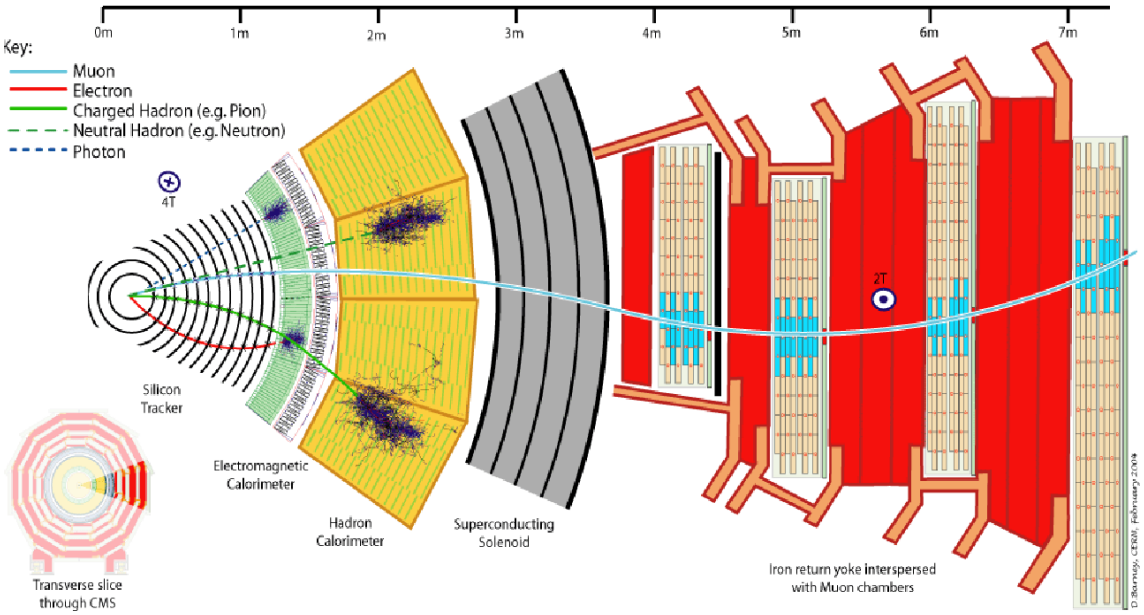


Figure 5.3: A slice of the CMS detector indicates the interactions of different types of particles when they travel through the detector

5.1.4.1 Electron and Photon Reconstruction

Information from the tracker and calorimeters of the CMS detector is used to reconstruct the electrons. As a result of the huge amount of material exist in the tracker, bremsstrahlung process occurs and electrons will emit photons, these photons in turns will convert into pairs of $e^+ e^-$, which can radiate secondary photons.

In the electrons reconstruction process, a *Gaussian-sum filter* (GSF) candidate is used as a first starting step [174]. To reconstruct the electron track from tracker hits, taking into account the bending of the electron's track in the magnetic field, the *GSF* candidates are obtained by two various methods. The first method used is the *ECAL-based approach*, which is grouping the clusters of the ECAL into superclusters to collect the electron's energy and the photons from the bremsstrahlung process in a small η and a large ϕ. Then the position of the hits in the layers of the tracker is estimated by the energy and position of the supercluster.

The second method is the *Tracker-based approach*, which is used to find any electrons has been missed by the first method, the ECAL-based method. In such a method, tracks with transverse momentum ($> 2\,GeV$) are used. some requirements are needed for the number of hits and X^2 of the fit. The electron seeds formed with the two above methods are combined and used in the full electron tracking as an input.

By using the *Particle Flow* (PF) algorithm, the resultant electron tracks are matched to ECAL clusters. ECAL superclusters seed with transverse energy larger than $10\,GeV$ (and not matched to any GSF track) is selected as an indication of the reconstruction of an isolated photon candidate. By using an analytical function for energy and pseudorapidity, an energy correction has been taken into account in the calculations of the total energy of the accumulated ECAL clusters due to the energy loss in the reconstruction process. At low transverse momentum and $\mid \eta \mid = 1.5$, the applied correction is almost 25 %. the magnitude of an electron's energy is determined from a combination of the momentum of the GSF track and the corrected energy, while the electron's direction is obtained from the GSF track. The corrected energy and the direction of the photon and the direction are obtained from the used supercluster.

5.1.4.2 Identification of Electron and Photon

Starting with a *supercluster* in the ECAL, electrons, and photons can be reconstructed. The sums of energy deposits of the particle showering in the ECAL are forming the so-called Superclusters. If a track seed from the pixel detector is matched to a supercluster in the ECAL, the GSF electron is pro-

duced, otherwise, the supercluster is reconstructed as a photon.

If the GSF electron could be distinguished from a hadron, we can count it as an electron candidate. To perform this step, many criteria are used, such as the supercluster width in η direction should be small, the deposition of energy in the ECAL must be higher than the deposition in the HCAL cells, and to separate the GSF electron candidate from the muon candidate. If these requirements/criteria are fulfilled, the electron candidate passes the PF algorithm and becomes a PF electron.

5.1.5 Muon Reconstruction

Two complementary methods are used to perform the muon tracking process. The first method, which is based on standalone muons, is reconstructing the muons through the hits that occurred in the muon detectors by using pattern recognition. Then, the hits are merged to form a global muon track by matching the standalone muons to tracks in the tracker detector. Muons which are reconstructed from this method are having a worse momentum resolution compared to the next reconstruction method below. The momentum resolution is improved by the global muon fit at muon momenta higher than $200\,GeV$.

Due to the large multiple scattering in the return yoke, the muon with momenta less than $10\,GeV$, fails the conditions of the global muon which needed to enable the muon to penetrate more than one muon detector plane. Since the tracker-only muon reconstruction method requires only one muon segment, it is more efficient to be used. In the tracker detector, if the transverse momentum for each track is higher than $0.5\,GeV$ and the total momentum is higher than $2.5\,GeV$, the track is therefore extrapolated to the muon system. By finding only one matching track segment, it can be selected as a muon candidate.

Either as global or tracker muon or both, 99% of the muons are reconstructed due to the geometrical acceptance of the muon system. It can be possible for global and tracker muons that share the same track, to be merged into a single candidate. If part of the hadron shower reaches the muon system, charged hadrons can be mis-reconstructed as muons. To improve the identification of muons, the algorithm of particle flow (PF) muon identification should match

the depositions of energy in the calorimeters with the track of the muon.

5.1.5.1 Muon Identification

Some identification criteria should be applied to ensure the quality of the reconstructed muon when using it for physics analysis. several identification levels exist, which denote as "*tight*", "*medium*", and "*loose*". The most widely used criteria are tight and loose identifications. Muons are required to be either global or tracker only muon if we use loose identification. And for the tight identification, it is required for the muon to be only a global muon, which is identified as a muon by using the PF algorithm.

5.1.5.2 Jet Reconstruction

By using anti-k_T algorithm [56], we can reconstruct the jets[78] which can cluster the particles generated from the event simulation, or the reconstructed particles by the PF algorithm (PF jets), or the depositions of energy in the calorimeters (Calo jets).

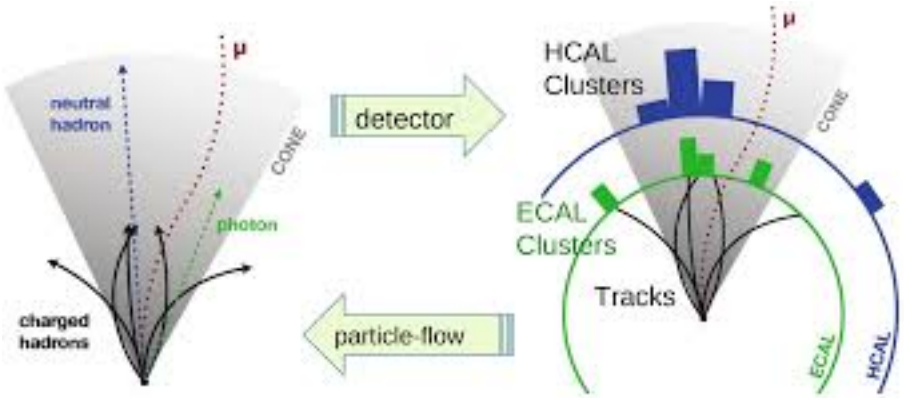


Figure 5.4: PF jets and Calorimeter jets at CMS

The particle's transverse momentum p_T (also called k_T) and the distance between the particles are taken into account when these procedures are performed. We can define the distance between the particles as

$$\triangle R_{ij} = \sqrt{(\eta_i - \eta_j)^2 + (\phi_i - \phi_j)^2} \tag{5.1}$$

Where i and j represent a pair of particles, and The parameter R determines a jet. PF hadrons are forming the PF jets by using the primary vertex direction of the particle. The hadronic showers created from quarks and gluons are defined as Jets. Anti-k_T algorithm, used in the CMS to identify the jets, is merging the closer neighboring particles. This step is iterated continuously until all the PF hadrons have been gathered to form a PF jets, which is a cone and its size is proportional to R. Figure 5.4 presents the formation of the PF jets and Calorimeter jets.

5.1.5.3 Particle Flow (PF)

Reconstruction algorithm of the Particle flow (PF) is responsible for combining information from the various sub-detectors of the CMS experiment [169]. It is also linking tracks from the inner tracker with calorimeter clusters and tracks of the muons. When each particle is identified properly, a full picture of the events is completed.

Few requirements have to be fulfilled to perform PF reconstruction, first, the large volume of the inner tracker is needed, for precision and high-efficiency tracking. Also to be able to distinguish between charged and neutral particles in the subdetectors and having a good resolution of the transverse momentum, a high magnetic field is necessary. Finally, the calibrated calorimeter is important for good energy resolution and also, to distinguish between charged and neutral particles.

Tracks, ECAL and HCAL clusters plus the tracks - clusters links, are the basic components for the PF reconstruction algorithm. By using matching/link algorithms, tracks and clusters are matched and linked together to form the so-called ”blocks”. The main purpose of the PF reconstruction algorithm, besides preventing double counting of particles, is to link subdetector’s information to give a global picture of the particles produced in the event of collisions.

First, the PF algorithm identifies the tracks of the charged particles, electron and muon. Besides, a special designed clustering PF event reconstruction algorithm is used to reconstruct the calorimeter clusters. If the deposited energy in the cell of the supercluster is above a given seed threshold, the seed is identified to have the maximum local energy with respect to the neighboring cells. Then, by using a link algorithm, the PF elements are connected, in the various subdetector, to avoid any doubling counting. This link algorithm creates blocks of such elements and by defining a geometrical distance between these elements, the quality of the matching between these elements is quantified. The shortest distance between the elements is chosen. To be more precise, matching between a track in tracker subdetector and a calorimeter cluster is done by extrapolated the last hit in the tracker to the nearest calorimeter cluster. The matching distance is defined by the distance between the extrapolated track and the nearest cluster in (η, ϕ) plane.

In order to improve the performance of the muon identification, the identification algorithm of PF muon is matching the muon tracks to the muon energy deposits in the calorimeters (ECAL, HCAL). Finally, the obtained PF blocks from the matching step, are then classified as electrons, isolated photons or muons, while the remaining elements are identified as *PF charged hadrons* or *PF neutral hadrons* of *PF photon*.

In conclusion, identification of electrons is done first and the electron candidates are removed from the PF reconstruction algorithm. When there is no track in the tracker subdetector, the particle could be identified as a neutral particle. But if there is no track in the inner tracker and there is an energy deposit in the ECAL, the formed block is identified to be a photon, and if the energy deposited in the HCAL, the formed block will be identified as neutral hadron.

CHAPTER 6

SIMULATION OF MAGNETIC MONOPOLE IN THE CMS DETECTOR

In this chapter, we will give a brief overview on the Long-Lived particles and their signature in the detector. A detailed description of the monopole event generation model that has been used in this search will be explained. Then, we will discuss in detail the signature of magnetic monopoles in the sub-detectors of the CMS, specially the Inner Tracker and the Electromagnetic calorimeter (ECAL) with a full description of the simulation process of the monopole in the detector.

The doctoral candidate is the principle responsible for generating the monopole events using the described model and producing the LHE files for each monopole mass simulated. The Les Houches Event file format (LHE) is an agreement between Monte Carlo event generators and theorists to define Matrix Element level event listings in a common language. Also, an official presentation has been delivered by the doctoral candidate in the CMS-MC exotica group to be able to request the official MC samples with the used model, to validate the results later.

6.1 Exotic Long-Lived Particles

Numerous theories beyond the SM have predicted the existence of long-lived particles (LLPs). Experimentally, some searches can be performed in the LHC and particularly the CMS experiment. Supersymmetry (SUSY) is one of the extension theories of the SM of particle physics which predicted the LLPs. This theory enables us to solve the hierarchy problem, the gauge coupling unification at the Planck scale, and provides us with dark matter candidates [132].

Long-lived exotic particles are considered to have long lifetimes, and they can travel for few kilometers, i.e. LLPs do not decay at the interaction point of the collision and they travel some distance. Only we are interested in LLPs that their decay lengths are very close to the scale of the detector which lose most of their energies in the material of the detector (ionization).

The unique features of the detectors are used to search for LLPs as they enable us to find new physics beyond the Standard Model. Usually, detectors require a special trigger, unique reconstruction algorithms and they also need discriminating variables to identify them in the detector layers. As discussed in chapter 1, the Standard Model theory is precise to explain the fundamental particles and their interactions, but it is not yet complete. Thus, we have to look for new physics beyond the SM as there are no massive LLPs in the SM theory. Furthermore, LLP's signatures in the detector are very unique, if there is any evidence for these particles to exist, this will lead to a discovery.

A magnetic monopole is considered to be an exotic long-lived particle, which can be detected at particle colliders. As mentioned in chapter 2, the magnetic monopole is a hypothetical particle with an isolated magnet with only one pole (north or south). However, till now all the observed magnetic particles have two poles with zero magnetic charge. At current colliders, monopole searches can be conducted as they are highly ionizing particles, and it is very easy to distinguish between monopole and any other minimum ionizing particles. Besides, monopoles have been developed by many other theoretical models.

In the following section, we will describe how these particles will look in

the detector, through the ionization process.

6.1.1 LLPs Interactions with Matter

There are different ways for the LLPs' signature inside the detector. The basic way of the LLPs interaction with matter is ionization. When a particle passes through the detector material, it can easily interact with the atomic electrons or the nuclei of the atoms. For LLPs, the ionization process is the result of the interaction with the atomic electrons, while the hadronization process is the result of the interaction between the LLPs and the atomic nuclei.

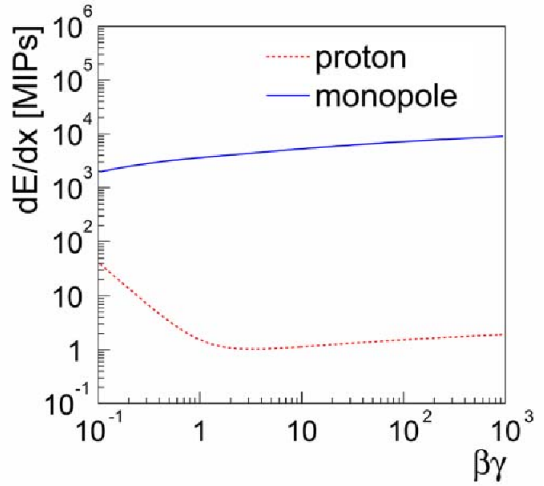


Figure 6.1: The Energy Loss for monopole (blue) is very high as compared with electric charged particles (red). [92]

6.1.1.1 Ionization of Electrically and Magnetically Charged LLPs

The basic electromagnetic interaction between LLPs and the matter is ionization. Energy loss via ionization for an electrically charged LLP is described by the Bloch-Bethe formula (equation 2.16) and for monopoles (equation 6.1) is used. It is the same as the equation of the energy loss of the electrically charged particles with replacing ze with g and inserting the factor $(1/\beta^2)$. Since Dirac monopoles have a magnetic charge of order of $137\,e/2$, the ionization loss of

the magnetic monopole would be an order of several thousand times greater (almost 4700 times higher) than any electrically charged particle with charge e. Figure 6.1 indicates that the energy loss for monopole (blue) is very high as compared with electric charged particles (red). Table 6.1 shows the used variables in the modified Bloch Bethe formula for monopole.

$$-\left\langle Ex \right\rangle = K\frac{Z}{A}g^2\left[\ln\frac{2m_e c^2\beta^2\gamma^2}{I} + \frac{k(|\,g\,|)}{2} - \frac{1}{2} - \frac{\delta}{2} - B(|\,g\,|)\right] \tag{6.1}$$

Table 6.1: The variables used in the modified Bethe equation for monopole

Symbol	Definition	Value/Units		
I	Mean Ionization potential	eV		
$k(\|\,g\,\|)$	Correction term	0.406	for	$g=1$
		0.346	for	$g=2$
$B(\|\,g\,\|)$	Correction term	0.248	for	$g=1$
		0.672	for	$g=2$

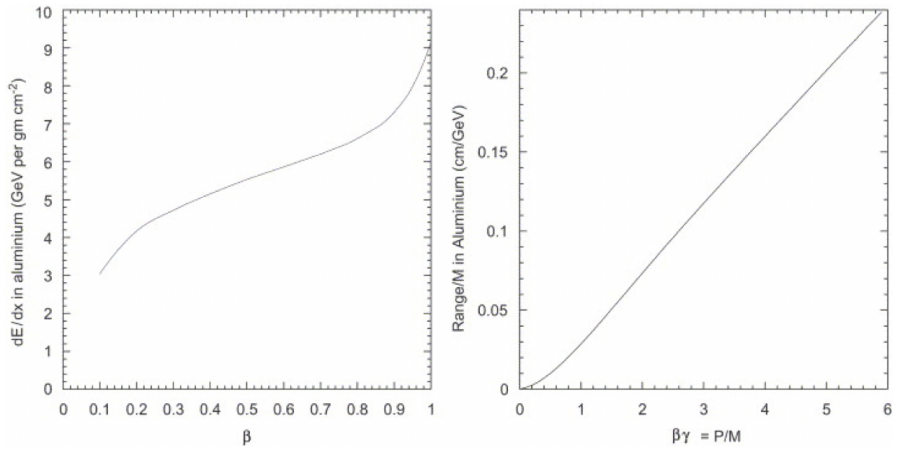


Figure 6.2: Stopping Power $-\langle dE/dx\rangle$ for Dirac monopoles in aluminum as a function of β (left). The ratio of range to mass for Dirac monopoles in Aluminum as a function of $\beta\gamma = p/M$, calculated from the stopping power (right) [95]

The stopping power for Dirac monopoles in aluminum as a function of their speed β is shown in figure 6.2 (left). It shows that the monopole slows down when the ionization becomes less dense. The right figure shows the ionization range normalized to the mass of Dirac monopoles, as a function of $\beta\gamma = p/M$. Monopoles give a very striking ionization signature in the matter.

6.1.2 Hadronization of LLPs

Hadronization process is the result of the interaction between colored LLPs with the atomic nuclei of the detector material, through which picking up a light quark or gluon. These LLPs could be mesons or baryons, they are called R-hadrons, which they can change their charge if they continue to harmonize the detector material [95].

6.2 Monopole Production in CMS Detector

The generation and simulation processes for monopole will be discussed in detail, using frameworks such as GEANT4 and Madgraph5 generators which are currently used to estimate the acceptance for several sub-detectors parts in the current search. The search method adopted relies on highly ionizing tracks in the tracker sub-detector with many saturated hits and confined energy deposits in the calorimeter.

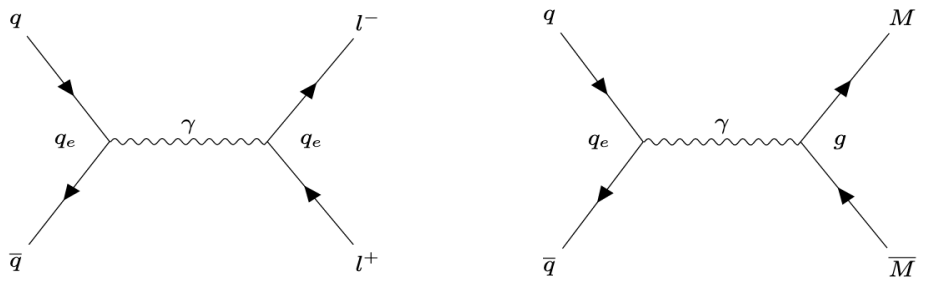
Magnetic monopole gains energy from the magnetic field generated from the solenoid, and unlike SM particles, monopole tracks are expected to have some curvature along the axis of the beam. Both, the track path and the calorimeter transverse cluster shape are consistent with magnetic charge dynamics in a uniform magnetic field. Such a strategy applies to any massive highly charged stable particle. In this thesis, the analysis is assumed to be searching for massive Dirac monopoles using the Drell-Yan mechanism as a benchmark for this search, which provides a scenario with relativistic kinematics for monopoles produced in the proton-proton LHC collisions. Since the calculations of the cross-section in any case do exist but they are calculated in perturbation theory

which is not valid due to the high coupling constant involved in the monopole process, so these calculations are not reliable. We, therefore, set limits on the monopole cross-section production.

In the next subsection we will discuss the event generation model and how we generate events for simulated monopole signals (Monte Carlo Samples).

6.2.1 Monopole Production - Event Generation

There are two main processes for monopoles to be produced at the LHC from proton–proton collisions, Drell-Yan and Photon fusion processes are used for monopole production in an effective $U(1)$ gauge field theory's framework, which obtained from conventional models that describe the interaction of monopole spin 0, $1/2$, 1, magnetically charged fields with ordinary photons, taking into account the electric-magnetic dualization.



(a) Typical SM Drell-Yan process

(b) DY monopole-antimonopole pair production

Figure 6.3: A Feynman-like tree-level graphs for production processes of monopoles with generic spin S.(a): typical SM Drell-Yan process describing charged lepton production from quark-antiquark annihilation; (b) DY monopole-antimonopole pair production from quark annihilation

A Feynman-like tree-level graph is shown, for monopole production processes with generic spin *S*, in figure 6.3 (a) shows a Typical Standard model Drell-Yan process in producing charged lepton from quark–antiquark annihilation, (b) shows Drell-Yan monopole-antimonopole pair production from quark annihilation.

The first step to producing MC samples in any analysis is the step of event generation. For a particular physics process, this step produces the desired final state particles. In our current search, the final state particles are monopole-antimonopole. In order to generate different types of physics processes, one can use any of the available event generators.

MADGRAPH5_aMC@NLO [34] is one of the tree-level matrix element generators, is used in this search with a recent implementation of the magnetic monopole model for Drell Yan mechanism – spin $1/2$ with a magnetic charge equal to $1.0\,g_D$ for 10 mass points (500, 700, 1000, 1200, 1500, 1700, 2000, 2500, 2700, $3000\,GeV$) with $100K$ events each. We selected a large number of mass points since no constraints are placed on the monopole mass in any theory. The simulated particles through the step of event generation are called "truth particles" and they are not the same as particles created from the reconstruction step.

Using the Drell-Yan mechanism, simulated monopole events are generated of spin $1/2$ pair-produced monopoles. Monopole production mechanism is not well understood although monopoles are predicted by models with masses in the TeV scale. A monopole interacts with matter differently compared to electric charged particles as electrons, hadrons, and muons, which are used in particle colliders measurements and searches. MADGRAPH5_aMC@NLO is used to generate events for the pair-produced spin $1/2$ monopoles model in proton-proton collisions at centre of mass-energy of $13\,TeV$ using the Drell-Yan kinematics are produced. Samples of 100000 events were generated for each mass point and charge $1.0\,g_D$ with Parton distribution function (PDF): NNLOPDF.

To ensure that only the energetic monopoles will reach the Electromagnetic calorimeter to be simulated, we need to set a limit on the minimum transverse momentum p_T by optimizing its value using computing resources. Magnetic monopole generation models have been imported to the Madgraph5 generator recently. Recent MadGraph5 versions (version $\geq$ 2.6.5) have in-built updated monopoles.

Generator Level Kinematics Distributions

The Kinematics of the monopoles on the generator level are plotted for all mass points has been generated via Madgraph.

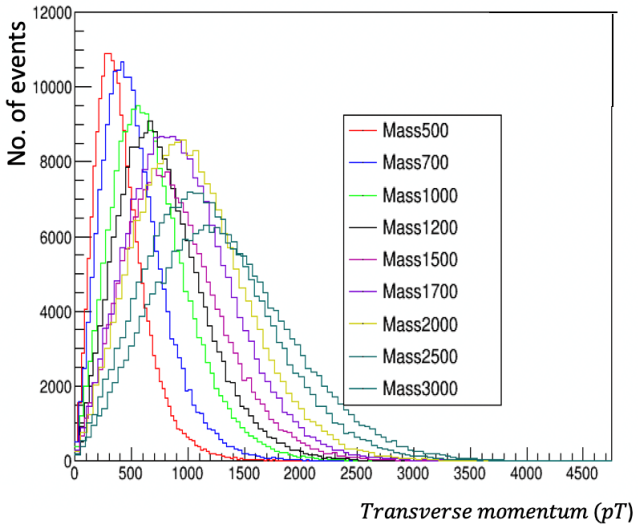


Figure 6.4: Transverse Momentun (p_T)

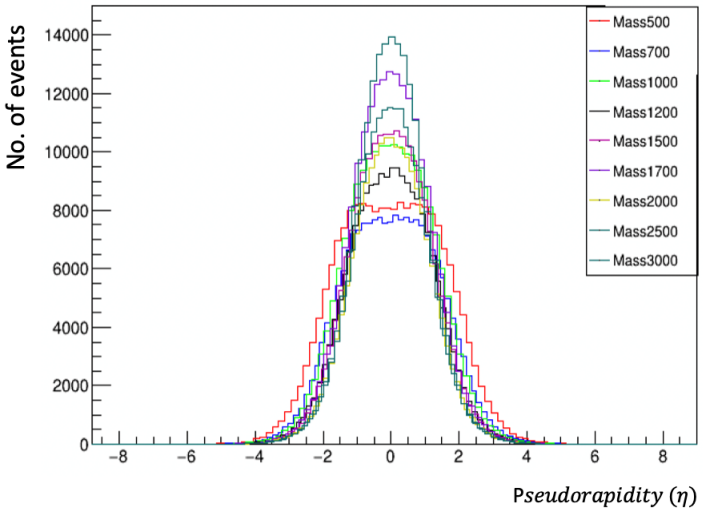


Figure 6.5: Pesuropaidity (η)

Figure 6.4 shows that the monopole is a very energetic particle and by higher masses have higher energy ranges, and figure 6.5 represents the η distribution for all mass points of generated monopole and it shows that most of the monopoles events produced within the acceptance of the ECAL, $-3.0 < \eta < 3.0$.

6.2.1.1 Implementation of Monopole model in MADGRAPH5_aMC@NLO

For such relativistic fast monopoles with relative velocity $\beta = 1$, passing through materials, a large number of electron-positron pairs are produced which can be used as a sign for the monopole's presence [38, 161]. The study of slowly moving monopoles with $\beta << 1$, will be excluded from the present work. This thesis focuses on the electromagnetic interactions of monopoles of spin $S = 1/2$ (see Appendix A.2.1.1).

The monopole velocity β is used in the Drell-Yan model is given by Lorentz invariant expression in terms of the monopole mass M and the square of the center of mass-energy of the incoming particles (Photon or anti quarks), $\sqrt{s} = 2E\gamma/q$

$$\beta = \sqrt{1 - \frac{4M^2}{s}} \tag{6.2}$$

"There are no accurate theoretical calculations of the monopole production cross-section". Only Leading Order models can be used for the Feynman diagram. For Feynman diagram calculations, we use the perturbative approach, i.e. we have many terms in the cross-section calculations.

1. LO - Leading Order to tree level
2. NLO - Next to leading order of first-order loop diagram to next to Leading order or second-order loop diagram and so on.

For processes where the effective coupling is less than 1, the terms in b and c are less than terms in a. For monopoles, the coupling is $68.5 \gg 1$ so

terms b and c will be larger than terms in a, this is the reason why perturbative calculations are not possible. Here we only calculate the tree-level diagram and ignore higher order terms. We ignore them not because they are smaller in value than *LO* terms but because we don't know how to handle higher order terms.

It is reasonable to assume that a proper field theory treatment of monopole pair production would reproduce the Drell-Yan electron production with the duality transformation applied. Events are generated through the developed spin $1/2$ monopole β-dependence model in MADGRAPH5_aMC@NLO via the Drell-Yan process. Monopole PID is ± 411000, which GEANT4 recognizes as a magnetic monopole and treats it as a particle having the fundamental magnetic charge g and no electric charge. Monopole masses ranging from 500 to 3000 *GeV* have been simulated.

6.2.2 Monopole's Signature in CMS Subdetectors

A wide range of signatures could be found for the LLPs. A few of these particles could pass through the detector layers with an unusual signature, as monopoles. They could have very highly ionized tracks, while other LLPs could have lifetimes to be decayed in the detector.

Also, other particles could be so heavy and exhibit a complete stop in the detector and later after some time, they could decay. For Dirac monopoles, the dE/dx signature is one of the discriminated variables to detect the magnetic monopole. To search for monopoles at colliders, there are two discriminated variables, that combined to identify the monopole candidates, related to the inner tracker and electromagnetic calorimeter sub-detectors.

First, we should look for high dE/dx tracks in the inner tracker detector, the track of the magnetic monopole in the inner tracker is a parabolic track, which is curved in the $r-z$ plane due to the existence of magnetic field, unlike any other electric charged particles.

Monopole has a unique feature related to the track. It is well known that the trajectory of the electrically charged particles bends in the $x-y$ plane which

perpendicular to the magnetic field, but in the case of monopoles, the magnetically charged particles that accelerated along the direction of the magnetic field, they are bending in the $r-z$ plane and this cause the electromagnetic calorimeter cluster reconstruction which produced by the monopole track after applying some pre-selections for the matching process. Figure 6.6 shows that The monopole trajectory of mass $1000\,GeV$ is bending in the z plane, assuming a uniform solenoid magnetic field in the 3 main experiments at the LHC (CMS, ATLAS and ALICE experiments).

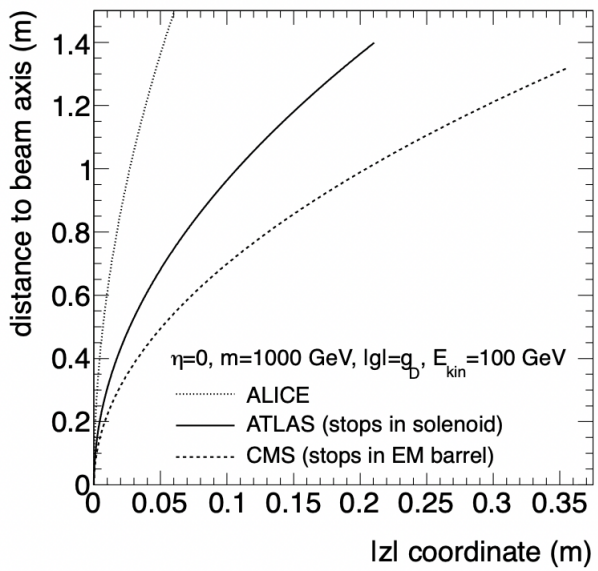


Figure 6.6: The approximate trajectory of monopole mass $1000\,GeV$, assuming a uniform solenoid magnetic field in the ALICE ($B=0.5\,T$), ATLAS ($B=2.0\,T$) and CMS ($B=3.8\,T$) detectors at $\eta=0$, for $\mid g \mid = g_D$ (left)

Second, a narrow ECAL cluster could be taken as a magnetic monopole signature in the ECAL. Figure 6.7 presents the simulation of magnetic monopole (monopole - antimonopole) in the CMS detector via CMSSHOW program, it shows the straight track in an $x-y$ plane (yellow line), unlike most other charged particle which has a curved track in the $x-y$ plane. A narrow energy deposition in the ECAL cluster (red narrow cone), which for other particles is spread more among neighboring crystals.

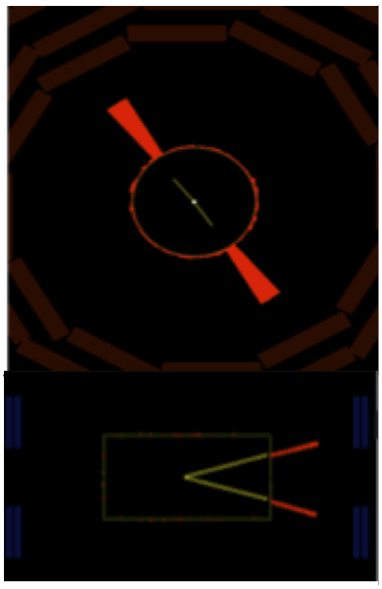


Figure 6.7: Signature of Magnetic Monopole is CMS detector via CMSSHOW program

Magnetic monopoles deposit most of their energies in a single ECAL crystal (cell) of the ECAL 5 $\times$ 5 cluster. However, this would make them look like an ECAL spike!. Spikes are one of the noise sources at some of the colliders, specifically for CMS detectors (see Appendix A.2.1). In CMS, there are some spike cleaning selections which will be discussed later.

There is another prediction that states that monopoles could be stopped in the inner tracker of the detector, around the interaction point or get trapped in the beam pipe, due to the large value of the dE/dx of the monopoles and they bound to the atomic nuclei of the detector material or beampipe.

6.2.3 Monopole's Signature in the Inner Detector

There are many differences between monopoles and other electrically charged particles such as the high ionization produced by monopoles due to the absence of the inverse squared β dependence and the existence of a high magnetic charge compared to the electric charge in the energy loss by ionization equations. Also the dominance of the ionization process over pair production and Bremsstrahlung processes for the monopoles and other electrically charged particles. This determines the signature of monopoles in the CMS sub-detector.

The first layer that the monopole must pass through is the beryllium beam pipe that surrounds the interacting point, just before the tracker sub-detector. A magnetic monopole with low kinetic energy may stop and would be trapped in the CMS beam pipe. Monopoles with high kinetic energy could travel through the beam pipe and enter the inner tracker.

Also, a current beam pipe study is under way in MoEDAL experiment with a collaboration with CMS experiment, to search for magnetic monopoles in the beam pipe of CMS detector which was replaced in 2013.

The two main properties to distinguish between monopole track and other ordinary particle's tracker:

- The track left by a monopole traveling through the tracker sub-detector would be more ionized with multiple orders of magnitude other than a normal track by any other charged particles and this leads to saturating the energy loss (dE/dx) measurements.
- The monopole would experience a force along the magnetic field which is the reason to curve its track toward the positive and negative z direction.

However, because of the curvature in the z direction, the standard tracking algorithm is extremely inefficient to identify the monopole's track. A new algorithm has been developed to find the monopole tracks. The details will be discussed in chapter 7, section 7.1.1

First, we need to understand how monopoles are produced at Colliders?

Generating monopole events is performed using the Drell-Yan mechanism spin $1/2$ monopole pairs. There are two main reasons to use this model: (1) It is the benchmark used by the previous monopole searches in other experiments. (2) Dirac monopole would lead to a new duality transformation which connects the electric and magnetic quantities. It is reasonable to assume that a proper field theory treatment of monopole pair production would reproduce the Drell-Yan electron production with duality transformation applied. This process populates a wide range of phase space with monopole whilst attempting to keep model dependent assumption to a minimum [84].

Then, the interaction of the generated monopole events in the CMS detector is simulated using GEANT4 [22]. GEANT4 is a software program which simulates the passage of the charged particles through the detector and measures the energy loss dE/dx, measures and calculates the trajectory of each particle step by step, handles the interactions of the particle with the material detector and its motion in the magnetic field. The software for simulating magnetic monopoles in GEANT was initially developed as additional code [44], but is now included in GEANT4 software [31, 30]. The monopole energy loss in the matter is treated according to the full model developed by S.P. Ahlen, including higher-order corrections such as density and Bloch corrections [25, 26, 24, 27].

A monopole team in CMS, starting from 2011, has been working on a series of comparisons between the full GEANT4 simulation and analytic calculations such as the Bethe formula for monopoles. Figure 6.8 shows a comparison of the dE/dx as produced in GEANT4 to an analytic formula for the monopole energy loss of Ahlen analogous to the Bethe formula. The GEANT4 values (data points) are obtained by building a histogram binned in β-γ of the energy lost by the monopole divided by the step size. This distribution is then fitted to a Landau distribution and the most-probable value is reported. This doesn't include higher-order corrections (such as density correction) that the simple formula does not include.

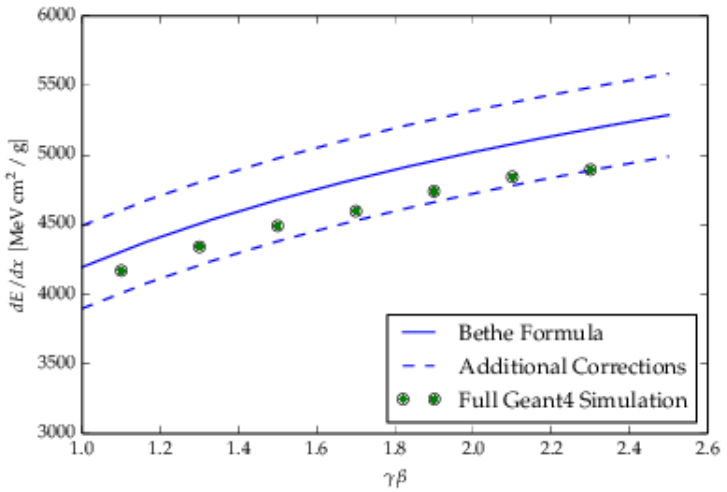


Figure 6.8: Comparison of the dE/dx as produced in GEANT4 to an analytic formula for the monopole energy loss of Ahlen analogous to the Bethe formula

This accounts for some of the discrepancies. The remaining discrepancy is likely we are comparing MPV of Landau to the mean energy loss from Bethe-Bloch formula, this can be quite different: without a cutoff the mean of Landau is infinite!. To do this comparison fully correctly, we need to account for the energy procedure used by GEANT4. But already at this point, the discrepancy between full-blown GEANT4 and our simple analytic model is a maximum 4 % effect. Note that the curves for non-monopoles are several orders of magnitude below this curve.

In summary, there is some evidence which is used to determine the monopole's signature in the two subdetectors: The silicon tracker and Electromagnetic Calorimeter (ECAL) at the CMS detector. When monopole interacts with matter, it interacts differently than other charged particles, such as electrons, photons, muons, and charged or neutral hadrons, because usually the unit electric charge is commonly assumed in most of the searches and measurement at particle detectors. There are some important differences between monopole and other charged particle, which are:

- The highly ionizing tracks produced by the monopoles because of the large value of magnetic charge compared to the electric one ($g = 68.5\,e$).
- The absence of the term $(1/\beta^2)$ in the equation of energy loss due to ionization for monopole, equation 6.1.
- The dominance of the ionization process as a mechanism for energy loss.

6.2.4 δ-ray Production Model

Monopoles can cause liberation of electrons from the material of the inner layers of the CMS detector. These knocked off electrons are called "δ-rays or δ-electrons", which usually have kinetic energy, of an order of few keV, more than other electrons which results from the ionization process. More details on the production of δ-rays can be found in [51]. Figure 6.9 shows the origin of δ-rays which cluster around the monopole trajectory. The δ-ray's energy which produced in the collision is subtracted from the kinetic energy of the monopole.

By using the default GEANT4 classes, the ionization δ-ray's energy loss is also simulated.

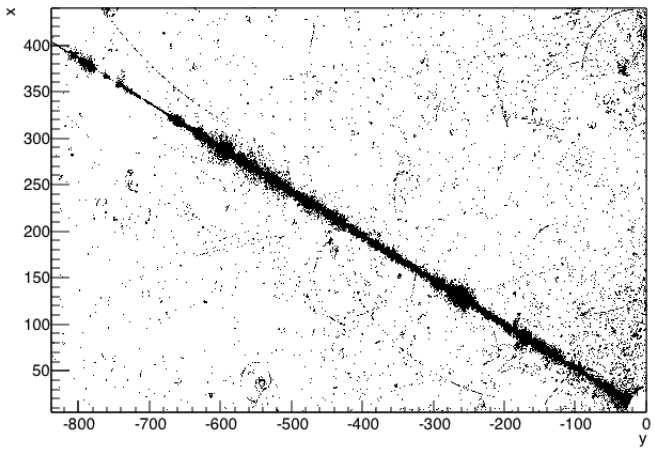


Figure 6.9: The origin of δ-rays which clearly cluster around the monopole trajectory

Based on equation 6.1, The models of monopole energy loss and the production of δ-ray are imported and used in GEANT4 with an associated uncertainty of 3 % [51]. The topological shower – cluster shape variable in the ECAL (f_{51}), which is used in this search as one of the discriminated variables to identify the monopole, could be affected by the production of δ-ray. The production of δ-ray can be adjusted in GEANT4 simulation package for monopoles (which is taken as a systematic uncertainty item).

δ-rays are explicitly generated above a configurable energy threshold in the CMS detector. The acceleration of the monopole in a magnetic field is implemented by providing a new equation of motion, which depends on the local magnetic field and electric field, to the GEANT4 numerical integration algorithm. The δ-ray production model is implemented in the CMSSW in the class **CMSmplIonisationWithDeltaModel**.

6.2.5 Monopole Simulation in GEANT4

To simulate an event, we have to take into consideration everything that could happen in the detector. The acceleration of the magnetic monopole in a

magnetic field is implemented by providing a new equation of motion, which depends on the local magnetic field and electric field, to the GEANT4 numerical integration algorithm. We must consider the following information:

- The interaction of the particles which we generated by the event generator with the material of the detector.
- Digitization phase simulation
- Event reconstruction, globally and locally.

The generated events - four vectors are processed by PYTHIA, one of the Monte Carlo simulation software [171], which adds the parton shower and hadronization effects and the decays of the products of the proton proton collisions simulation. The next step after using the desired event generator to generate monopole events is to model the detector's response to the passage of monopole through its sub-detectors. The simulation step should contains the following:

1. Detailed description of the detector: type of each subdetector's material, the shape of each sub-detector, geometrical hierarchies and the position of each component of the sub-detector of the CMS detector.
2. CMS magnetic field's description
3. Various of the physical processes in the event, which occur inside the detector for all types of particles (e^{-1}, γ, μ, π^o, k, neutrinos, protons and monopole): Physics interactions, such as, transportation equation, decay information, ionization process, bremsstrahlung and inelastic processes as well as multiple scattering.
4. Propagation of particles with their tracks inside the detector under the effect of the magnetic field.
5. Finally, tracking parameters, selection cuts, corrections and specific tuning for the simulation software

After fully simulating the process for monopole with all the above-needed requirements, the following step is "Digitization", which uses the output sample of the simulation step in a form of hits and uses the position of entering the particle to a sensitive volume of the detector. This step is mainly working on the detector electronics and converting the analog signal to the digital one. It also works on emulating the Level–1 trigger electronics.

As discussed before, the three main mechanisms to describe the interaction of electromagnetically charged particles with the material of the detector and their energy losses, [24, 27] are Ionization, pair production, and bremsstrahlung. In the case of magnetic monopoles, the ionization energy loss, which given by equation 6.1, is directly proportional to g^2. Monopoles with higher speed (higher β) are likely having a higher ionization. The energy loss equation of monopoles and the KYG and B corrections are implemented in class CMSmplIonisationWithDeltaModel in the GEANT4 package.

In 2010, GEANT4 simulation CMS – software didn't include any information regarding simulation of the magnetic charged particles when passing through matter. Therefore a custom simulation package has been developed and added to the CMSSW package, *cmssw/SimG4Core/*, this package includes the correct equations of motion in the electromagnetic fields (equation 1.16) for the magnetic charged particles, transportation equation and the computing of the energy deposition by monopoles in the unit of the magnetic charge g_D (equation 1.18) with taking into account the δ-rays production. Below are the classes that have been imported to the CMS-GEANT4 simulation software that are related to magnetic monopole simulation.

(MonopoleEquation - CMSMonopolePhysics - MonopoleTransportation - MonopoleIonization)

The simulation package for monopole is based on the developed package used in the monopole search in 2011. Few new fixes were introduced recently (March 2019) into physics models and in transportation code. Specifically, some discussions were done with the GEANT4 developers team and they have checked CMS and ATLAS simulation packages for Monopole ionization and they found that the threshold for the δ-ray produced should be modified. By default, monopole ionization produces δ-electrons above some threshold. In these

fixes, which integrated the threshold of the δ-electron production is limited and cannot be extremely small, only energetic δ-electrons are produced. Modification for monopoles ionization is merged to the CMS software and updates were integrated into CMSSW 7_1_*X*, 10_2_*X* and 10_6_*X*. It will also integrate into all recent validated versions of the CMS software.

For validation, the monopole ionization model in GEANT4 has been then compared with the ATLAS model and after the GEANT4 team confirmed that they are consistent, they gave us the green light to reproduce, privately, our MC samples again and request the official samples from the CMS MC-team. Figure 6.10 presents a screenshot of the validation and fixes performed in the code interface.



Figure 6.10: Screenshot of the GEANT4 validation for CMSSW_7_1_38 which is used for simulating the MC samples

6.3 Digitization of Simulated Signal

To produce an event content similar to the real detector's output, the effect of the detector that comes from the electronic sensor response that is produced by the hits in the detector's active material is simulated. Also, by adding the

detector hits of the generated proton-proton interactions on top of the hits which result from the main interaction, the effect of pileup is included. This is called the Digitization step.

Digitization of the simulated Monte Carlo samples is the next step after the GEANT4 simulation using the CMSSW.

RunIISummer15GS + RunIISummer16DR80Premix are the campaigns that have been used to digitize the simulated monopole samples using the suitable pileup profile. The per-channel data from the detector is called *Digis* and it shows the pulse shape of the detector and is used in the reconstruction of the hit's energy and time in the calorimeter.

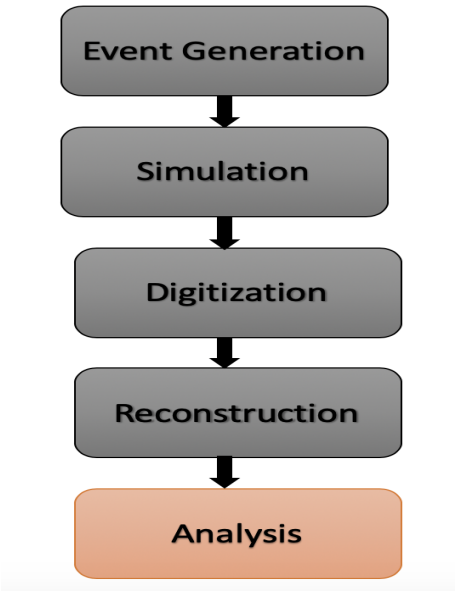


Figure 6.11: Analysis Chain

.

6.4 Events Reconstruction

The next step is to reconstruct the digitized simulated monopole sample on an event-by-event basis. New physics objects are identified mainly, at this stage, from the reconstructed tracks and energy depositions in the clusters of

the EM calorimeter like charged leptons, photons, jets and missing transverse energy. A detailed study on the monopole reconstruction in the CMS sub-detectors is given in the next chapter. A schematic diagram is shown in figure 6.11 represents the analysis chain.

CHAPTER 7

MONOPOLE SEARCH

As explained in chapter 6, we have generated the monopole events with the Standard Drell-Yan (DY) process through the Madgraph generator and performed the simulation process using PYTHIA and GEANT4 programs. We studied the standard case, spin $1/2$ monopole with $1.0\,g_D$ for mass points range $500-3000\,GeV$. Particle identification code (*PID*) is translated to t As explained in chapter 6, we have generated the monopole events with the Standard Drell-Yan (DY) process through the Madgraph generator and performed the simulation process using PYTHIA and GEANT4 programs. We studied the standard case, spin $1/2$ monopole with $1.0\,g_D$ for mass points range $500-3000\,GeV$. Particle identification code (*PID*) is translated to the *PID* of the monopole, which is ± 411000 to be recognized as a magnetic monopole and it is then treated as a particle with fundamental magnetic charge g and with no electric charge. It is worthwhile to mention that all the Monte Carlo (MC) samples used in this search have been re-produced with the latest update generation model [38, 161] and the whole results in this chapter were obtained by using the official MC samples after testing the steps of the analysis chain with our private MC samples produced in the first years of the search. Usually after obtaining the signal efficiency using all the selections along with the trigger, we were asked to present our results and the used production model to the Long-Lived Particles (LLPs) group at CMS-CERN. It requested from the MC contact

group to re-produce our MC samples officially, with high statistics (see section 7.1.2 for MC official samples). We will also discuss the signature of a magnetic monopole, and explain how we reconstruct the monopole signature in the CMS sub-detectors with the monopole identification selections.

In this chapter, we will discuss our analysis strategy and the reconstruction of monopole events based on its signature in the CMS sub-detectors. Also, we will discuss the HLT path we used and its effect on our signal samples. MC and Data datasets will be indicated with the collections used in creating our final analysis chain step. We will discuss how we choose the discriminated variables used to identify the monopole candidates in the event with the parameters used in the pre-selection and tight selections cuts with their relative efficiencies for each mass point and last, we will calculate the signal efficiencies after all selections are applied and to obtain the final acceptance that we will use, later, in the cross-section limit calculations.

In order to estimate the background which is surviving after the final selections, a data-driven method, double ABCD method, is adopted and discussed in detail. The systematic uncertainties for the MC signal and background estimation will be obtained. Last, we will calculate the cross-section mass limit. A comparison of the sensitivity between ATLAS and CMS experiments will be given and discussed.

7.1 Analysis Strategy

In this analysis search we will consider the 2016 data-taken with centre of mass-energy $13\,TeV$, by looking for an event with a highly ionizing track and narrow energy deposits in the calorimeter cluster. There are some pre-selections we used to perform the matching between the track found in the tracker and the narrow seed crystal of the calorimeter. When this matching is done, if an event passes the analysis tight selections, some cuts will be applied later on the discriminated variables, and the trigger HLT path, it will be selected as a monopole candidate.

The discriminated variables we used in this search are based on a combi-

nation of tracking $dE/dx_{significance}$ and Calorimetry f_{51} parameters which are used to identify the monopole in the sub-detector and determine the Signal region. In the next sections, we will discuss how we select these parameters and their definitions.

7.1.1 Monopole Tracking Reconstruction

As mentioned before, monopoles gain energy from the magnetic field generated by the solenoid, tracks are expected to have some curvature along the beam axis, unlike other electrically charged particles. Tracking is the, first, important part of the reconstruction process. Combining the hits found in the tracker, as a result of passing the charged particle, to form the charged particle trajectories. After forming the track of the charged particle, we have to apply some pre-selections to extrapolate this track to other sub-detectors.

The Tracking algorithm in CMS is used to reconstruct the trajectory of the produced charged particles from the collision, using the local track parameters to define any helical trajectory, like p_T, η, ϕ, z_0 and d_0. There are two parts we should take in considerations; Pattern Recognition (hits come from one particle) and Fitting (best fit/estimate of track parameters). For high ionizing particles like monopoles, we are more interested in high-momentum tracks (high p_T) than low-momentum tracks (low p_T).

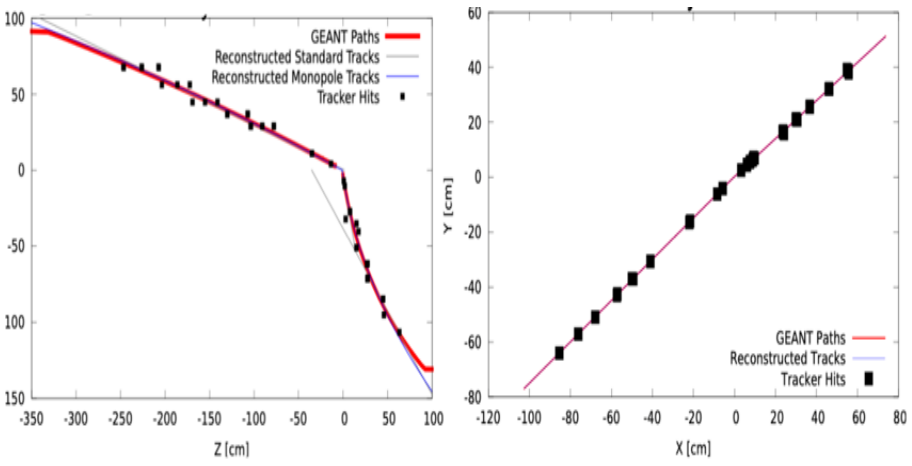


Figure 7.1: Actual and fitted trajectories of monopoles

First, to produce the monopole candidates we need to study the track of the monopole in the tracker sub-detector. As previously discussed, the track left by a magnetic monopole traveling through the tracking chamber would be multiple orders of magnitude more ionized than a normal track, saturating the dE/dx measurement.

Additionally, the particle would experience a force along the magnetic field, causing the track to curve toward the positive or negative z direction (straight tracks in $x-y$ plane). Due to these two properties, a monopole track would be easily distinguishable from an ordinary track. However, because of the curvature in z, the standard tracking algorithm is extremely inefficient at identifying monopole tracks. An algorithm has been developed, which finds monopole tracks by combining multiple straight tracks (in $x-y$ plane) into a single curved track. The detail of the new algorithm used is described in the next sub-section.

7.1.1.1 Track Combining Algorithm

The developed Track Combiner Algorithm is combining the straight track segments which arise from the standard track algorithm into sets of track segments that could have come from the same particle, to be a curved one. Starting from a specific segment, the combiner algorithm scans through all other segments if it has not yet assigned to a set. Tracks with p_T less than $5\,GeV$ are ignored. A segment is assigned to a set if its tracking hits satisfy two separate fits when combined with the other tracking hits in the set.

- The first fit is a *circle* in the $x-y$ plane, this is standard for the projection of helical track segments into this plane.

$$y = a + Sign(c) \star \sqrt{c^2 - (x-b)^2 - c} \tag{7.1}$$

  Where x and y is the system coordinate which rotates in the polar angle of the first hit in the detector frame ϕ_o. This fit has parameters a, b and c. The circle fit ensures that we don't miss any potential monopoles that may be electrically charged as in our signal MC, it will only give straight tracks in the $x-y$ plane.

- The second fit is to a *parabola* in the $r-z$ plane,

$$z = d + f\rho + g\rho^2 \tag{7.2}$$

Where d, f, g are the fit parameters . Note that a track from a particle with magnetic charge 0 would satisfy these fits (with the parabola degenerating into a straight line), as would a particle with electric charge 0 (with the circle degenerating into a straight line). This fit is changed by using GEANT4 to output the true position of the monopole and checking the true trajectory against the result of the track fit. Figure 7.1 shows an example of true and fitted trajectories.

The six parameters a, b, c, d, f and g from the two fits are saved as properties of the track set and they are used to extrapolate the track to the Calorimeter. The $x-y$ fit results in the usual track parameters ϕ_o, d_o and q/p_T. while $r-z$ fit results in the usual z_o and η along with the magnetic curvature d^2z/dr^2. The track-fit parameters cuts are indicated in table 7.9.

7.1.1.2 Track Ionization

When the monopole's track sets are established, then we can measure the ionization for each set. The standard dE/dx measurements which use the harmonic average of dE/dx hits in the track is weighting low-energy hits much more than high-energy hits. The dE/dx measurements for a monopole is very sensitive (because monopole tends to large saturated dE/dx hits) to the fluctuations of the smaller hits, as they are near a boundary or lower-energy hits, as they have been included in the reconstructed monopole track by accident. This is the reason, we instead measure the fraction of the dE/dx measurements that are saturated to give better separation between highly ionizing monopoles and background (which is minimum ionizing).

Because of the detector noise, tracks with the minimum ionizing hits (background) end up with a standard number of hits in the tracker layers, in addition to a set of saturated strips that raise the number of the fraction of standard dE/dx measurements. On the other hand, a monopole would have many real saturated strips plus small number of unsaturated strips and to improve such a separation between the monopole and the background, we take into account the

total number of strips and the fraction of the saturated strips and have combined them into only single parameter which is $dE/dx_{significance}$.

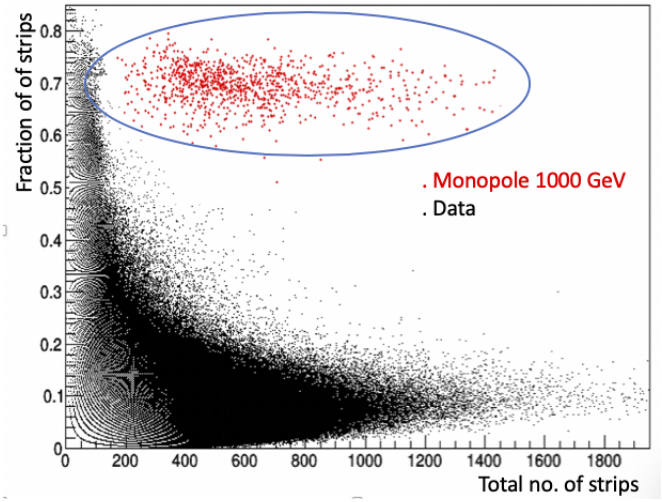


Figure 7.2: Cutting on the $dE/dx_{significance}$ improves discrimination power compared to a simple cut on the fraction of saturated strips.

In the calculation of the $dE/dx_{significance}$ measurements, we assume that in the background, due to noise, every single strip has a small probability to be saturated. This probability is not independent since there are parameters such as the track's angle that affects this probability, however, this effect is small.

In order to estimate this probability, we have fitted the "saturated fraction" distribution in the background tracks that have a high number of track hits (background tracks located in the lower right of figure 7.2. In this figure, we plotted the fraction of saturated hits versus the total number of strips for monopole MC mass 1000 GeV and 2016 Data. For monopoles, the number of saturated strips are very close to the total number of the strips, i.e. the fraction of saturated strips, for monopoles, is approximately close to one (~ 1), and this is indicated in the red dots.

This distribution gives a probability of 0.07 for the background hits to be saturated in the region of the large number of strips per track which the monopole signal lies. We used the binomial function to calculate the probability of the saturated strip's number in the track which could have occurred by

chance, the $dE/dx_{Significance}$ is given by:

$$dE/dx_{Significance} = \sqrt{-\log BinomialI(0.07, NStrips, SaturatedStrips)} \quad (7.3)$$

Where Binomiall (p,n,k) is the binomial probability that at least k trials out of n are successful if each trial has a probability of p. It was implemented in ROOT as TMath::BinomiaII(). 0.07 is the average number of saturated tracker strips over the total number of strips per track. It was calculated by looking only at tracks with at least 200 tracker strips, which is the region where monopoles would be expected, (The average saturation fraction is very different in the "low number of strips" region). We have plotted the $dE/dx_{Significance}$ for different monopole's mass points and the distribution shows the high value of $dE/dx_{Significance}$ which will be used as the track discriminant for monopole identification, see figure 7.3.

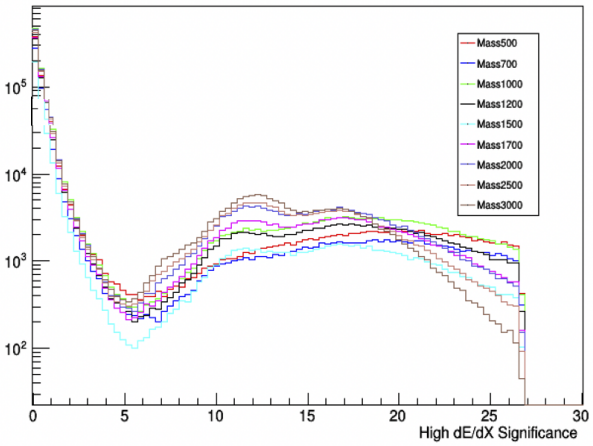


Figure 7.3: Distributions of $dE/dx_Significance$ for each mass point simulated.

We have performed a quick study for the 13 TeV data to re-estimate the probability of background strips to be saturated in the high number of tracks region, and we got approximately the same number by varying the cuts of the number of strips.

7.1.2 Track Curvature

Monopoles that have enough momentum to travel through the tracking chamber and continue to the electromagnetic calorimeter will have a relatively small curvature that's why the $r-z$ curvature, figure 7.4, of a monopole track is not useful as ionization to be used as a discriminant parameter for monopole identification. However, with larger statistics, it might be possible to look at the distribution of tracks in d^2z/dr^2 and look for a monopole component. This would allow a more sophisticated analysis with later data.

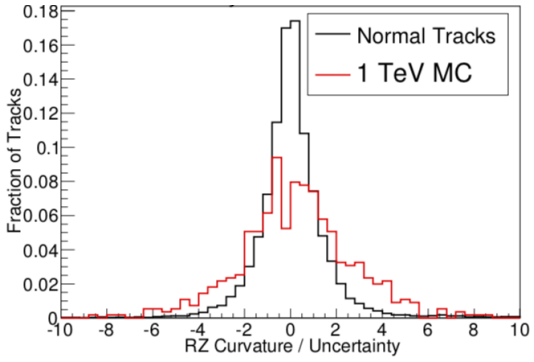


Figure 7.4: The $r-z$ curvature is not as useful a discriminant.

7.1.3 Electromagnetic Calorimeter Cluster Finding

As mentioned previously, Dirac monopoles are expected to lose energy in the electromagnetic calorimeter (ECAL) due to ionization which is the dominant process for the monopole energy loss. Monopole energy is deposited in the ECAL strips with a very small amount, or no, energy in the HCAL, the next layer in the CMS detector. The ECAL cluster shape tracks the monopole through the ECAL crystals.

There are two clustering algorithms in which the energy is grouped into clusters through them, the "Hybrid" and "Island" [128]. In the electromagnetic barrel (EB), the energy which is deposited in the nearby crystal is clustered by the Hybrid algorithm.

Hybrid Algorithm is clustering the energy based on the $\eta - \phi$ geometry of the EB. The strategy is to start from a seed crystal "dominoes"of 1×3 crystals (in $\eta - \phi$) which aligned with crystals in the center in η to be added for N_{step} steps in $\pm\phi$. If one of these seed crystals has energy larger than Ewing (Threshold for 5 crystals), then it is spread to 1×5 crystals, otherwise, they are eliminated from the cluster if they have energy less than E threshold. Finally these dominoes are clustered in ϕ, based on their energies, to form super-clusters.

The Island clustering algorithm builds clusters in the opposite way than the fixed shape of clusters formed by the hybrid algorithms. The island algorithm starts with The Island clustering algorithm dynamically builds clusters as opposed to the fixed shape of clusters found by the hybrid algorithm. This algorithm starts with a list of seeds and removes seeds adjacent to higher energy seeds. Then, for each seed, the algorithm scans in $\pm\phi$ collecting energy in crystals until a rise (or hole) is detected. Another scan, one crystal over in η, for $\pm\phi$ occurs. The algorithm continues to step in $\pm\eta$ after each scan in ϕ until a rise (or hole) is detected. All collected crystals cannot be used in another cluster.

One technical background which is reduced by the track matching requirement is the anomalous signal in ECAL crystals [140], particularly in the EB. The variables developed to mitigate these anomalous signals [139] [64] [50], referred to as spike events, flag monopole clusters at a high rate. Filters designed to reject such anomalous signals are employed at L1, the HLT, and offline reconstruction. The L1 spike filter assigns a single bit to each 1×5 (η, ϕ) strip in the 5×5 trigger tower. If two or more cells in a strip are above a $350\,MeV$ threshold, the bit is set to 1. The 5 bits of the 5 strips are OR'ed together. For a value of 1, the tower is accepted, and for a value of 0, the tower is rejected as a spike-like event. Towers with less than $12\,GeV$ of energy are ignored. In the HLT, cuts are placed on the timing and the ratio of energy in 4 neighboring cells to the seed cell, the "Swiss-cross" variable, is applied.

Similar selections to the HLT are employed in the offline reconstruction, in which two separate collections are populated by default. There is a collection of clean clusters that pass the offline spike rejection filter and unclean collection consisting solely of clusters that do not pass the offline spike rejection filter. These two collections can be combined by adding a CMSSW module to the

configuration file. By using this combined collection of ECAL clusters, we avoid spike rejections, but the triggers have already rejected the spike events!

- **The Superclustering Algorithm in the ECAL**

In the ECAL barrel, the hybrid algorithm is used based on $\eta - \phi$ geometry. First, it starts to look for the seed crystals which have higher transverse energies above a certain given threshold $E_{T,hybseed}$. These crystal dominoes are then aligned in η with the seed crystal, depending on the seed crystal energy, the dominoes are containing 3 or 5 crystals. This procedure to form the crystals dominoes is repeated for all the crystals, with the seed crystal, which are aligned in η in each direction along ϕ direction, limited to a maximum no. of crystals N_{crys}. Only above a certain given threshold $E_{threshold}$, these dominoes are kept. Then the dominoes are clustered in ϕ and it is required for each formed dominoes cluster to have a seed domino with an energy larger than a given threshold E_{seed}.

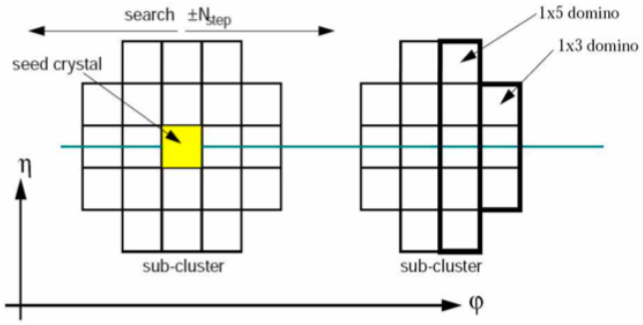


Figure 7.5: Domino construction step of ”hybrid” algorithm

The resultant clusters are combined to form the so-called “*supercluster*”. By summing all the energies of the individual crystals that form the supercluster, the total energy can be computed for each supercluster. Table 1.1 is representing the parameter values used in the clustering steps of the ”hybrid” algorithm. Figure 7.5 illustrates the construction of the domino with a table of the parameters introduced in the hybrid algorithm.

Table 7.1: Parameter values used in the clustering steps of the ”hybrid” algorithm

Parameter	Value
$E_{t,hybseed}$	1 GeV
E_{wing}	0 GeV
N_{crys}	17 crystals
E_{thresh}	0.1 GeV
E_{seed}	0.35 GeV

Monopole track matching requirements have reduced one of the technical backgrounds which is the anomalous signal in ECAL crystals [140], especially in EB. The variables were developed to mitigate these ECAL anomalous signals, spike events [139, 64, 50], which flag monopole clusters at a high rate. There are some filters designed to reject such anomalous signals which are employed at L1, the HLT and offline reconstruction, will be discussed in detail in the next section.

For monopole analysis, according to the algorithm above, clusters of 5 $\times$ 5 crystals are tested to check which seed (crystal with the maximum energy) is found. In this analysis, we have considered all crystals by combining the flagged crystals with the swiss-cross variables and late time checks.

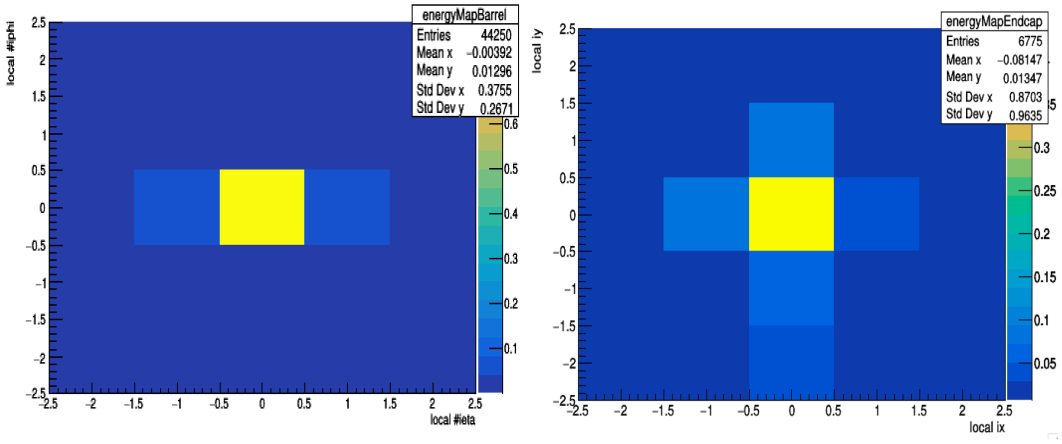


Figure 7.6: The average $E_{crystal}/E_{5\times5}$ for mass 1000 GeV, barrel (left), endcap (right)

In the offline analysis, a combined collection of clean and unclean clusters are formed and evaluated. For monopole, the energy in the seed crystal is al-

most equal to the energy in the 5×5 crystals, since the monopole deposits all of its energy in the seed crystal, so the ratio of the seed crystal energy to the energy of the 5×5 crystals should approximately equal 1, or slightly > 1. Figure 7.6 shows that the average $E_{crystal}/E_{5\times5}$, for monopole mass $1000\,GeV$, barrel (left) and endcap (right), which should be (< 1) in each bin of clusters tagged to monopoles in MC simulation. Energy in the barrel is more to spread in η direction than in the ϕ direction.

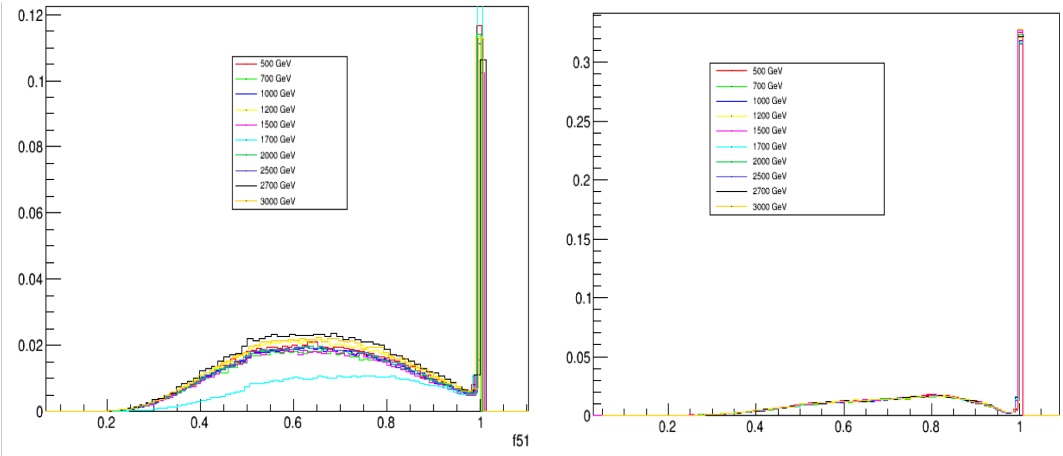


Figure 7.7: Distribution of f_{51} in the ECAL endcap (left), and barrel (right) for all simulated monopole masses

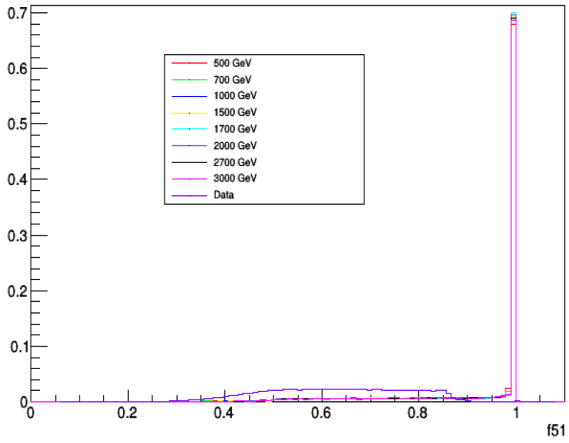


Figure 7.8: Distribution of f_{51} in the ECAL after reconstructed the monopole candidates

We identify monopoles in the ECAL by employing a topological cluster shape variable, f_{51} which is defined as the fraction of energy in the $5 \times 1, (\eta - \phi)$

strip central to the 5×5 cluster. Figure 7.7 shows the distribution of f_{51} in the ECAL barrel and endcap for all simulated monopole masses. If the energy flow in monopole clusters is rotationally symmetric, one would expect these distributions to be comparable. We combined the two distributions into one single parameter (seedFrac), by performing matching between the barrel and the endcap, as we combine the monopole candidates at the ntuple level, see figure 7.8.

7.1.4 Hadronic Calorimeter Isolation

Dirac monopoles are expected to rapidly lose energy in the electromagnetic calorimeter (ECAL) with little associated radiation in the HCAL. We computed the sum of energy which is deposited in an annulus in the HCAL of radii $0.1 < \triangle R < 0.4$ around the ECAL crystal, i.e. the activity found near the ECAL clusters. HCAL isolation is defined as, the hadronic energy of all caloTowers in the first segmentation of the HCAL. To identify the monopole, we put a pre selection cut on the HCAL isolation to be less than $10\,GeV$. Figure 7.9 shows the energy distribution in the HCAL around the ECAL clusters in MC samples, divided by the total energy (HCAL plus ECAL of the cluster).

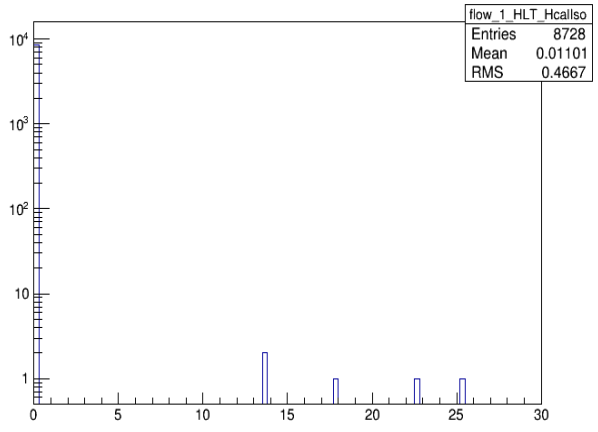


Figure 7.9: The relative energy in the HCAL around monopole clusters in the ECAL

7.1.5 Trigger Selections

The CMS trigger menu is very rich in having several HLT paths with L1 seeds, which each of them is dedicated to select interesting events for each physics process. During the simulation of the MC samples and the data taking, The reconstruction of the trigger is a process that uses the algorithm of each path to be applied to the reconstructed physics objects.

As in this search, we will use *SinglePhoton* datasets 2016 and besides the pre-selection and tight selections which are applied to our data and MC samples to identify monopoles events, we are using single photon trigger, which monopoles and photons are required to pass. An unprescaled trigger path, "$HLT_Photon175_v^{\star}$", which is a single photon trigger with E_T cut of $175\,GeV$ and loose H/E (energy in the HCAL/energy in the ECAL) cut, is used in the current search. The reason to use an unprescaled trigger is because prescaled triggers limit the statistics when going to high p_T.

Triggers can be either *prescaled* or *unprescaled*. A prescale is a means to reduce the rate of a trigger without adding additional cuts by simply only accepting a fixed fraction of the triggers output. At CMS only integer prescales are used, a prescale of 4 means only 1 out of every 4 events passing the trigger are accepted. Prescales can be applied at both L1 and HLT. For a prescale value of X at L1, only 1 out of X events which fire the trigger are accepted while for a prescale value of Y at HLT, the HLT trigger is only run for 1 out of Y events for which its L1 seed has accepted. The two definitions are functionally the same, i.e. we reduce the rate by 1/prescale value and this saves significant CPU time.

The unique properties of monopole signature in the ECAL show that monopole may look like a spike and this limits our options in choosing the suitable trigger we might use. We have made a trigger study to check the efficiency of every available trigger of the HLT paths menu and after a discussion with the trigger contact group, they have nominated a few HLT Paths which we can use, indicated in table 7.2.

After testing the efficiencies of these paths, we selected $HLT_Photon175_v^{\star}$ trigger path along with L1 seeds to be used in the current search.

Table 7.2: HLT trigger paths with their L1 seeds

HLT Path	L1 Seed
*HLT_Photon*175_*v*⋆	L1_SingleEG30 OR L1_SingleEG34 OR L1_SingleEG40 OR L1_SingleJet170 OR L1_SingleJet180 OR L1_SingleJet200 OR L1_SingleTau100er OR L1_SingleTau120er
*HLT_PFMET*300_*HBHECleaned_v*⋆	L1_ETMHF70 OR L1_ETMHF80 OR L1_ETMHF90 OR L1_ETMHF100 OR L1_ETMHF110 OR L1_ETMHF120 OR L1_ETMHF150
*HLT_ECALHT*800_*v*⋆	L1_SingleEG40 OR L1_SingleEG42 OR L1_SingleEG45 OR L1_SingleEG50 OR L1_SingleJet170 OR L1_SingleJet180 OR L1_SingleJet200 OR L1_HTT300er OR L1_HTT320er OR L1_HTT340er OR L1_HTT380er OR L1_HTT400er OR L1_HTT450er OR L1_HTT500er OR L1_ETMHF70 OR L1_ETMHF80 OR L1_ETMHF80_HTT60er OR L1_ETMHF90 OR L1_ETMHF90_HTT60er OR L1_ETMHF110 OR L1_ETMHF110_HTT60er OR L1_ETMHF120 OR L1_ETMHF120_HTT60er OR L1_ETMHF150
*HLT_PFMETNoMu*120_*PFMHTNoMu*120_*IDTight_v*⋆	L1_ETMHF70 OR L1_ETMHF80 OR L1_ETMHF90 OR L1_ETMHF100 OR L1_ETMHF110 OR L1_ETMHF120 OR L1_ETMHF150

The main source of the inefficiency of our signal is the trigger, whose efficiency is in the range of $\sim 8-10.5\,\%$ for mass points range from $500-3000\,GeV$. Most of the efficiency of selected trigger comes from monopoles which hit the endcap of the ECAL, where the spike killer topologies is applied for Barrel (no spikes in the endcaps), the spike killing algorithm ensures that the detector will only trigger on monopoles that hit close to the ECAL cell boundary.

The effects of the trigger selection due to L1 pre-fires in the ECAL when comparing the Data and the MC, are not taken into account in great detail as they are very small effects for Single photon datasets. Missing Transverse Energy (MET) triggers are also could be useful to use, as their efficiencies are higher ($\sim 28-30\%$), than the photon triggers.

We do not use MET triggers because they make use of a failure in the system (one of the two monopoles not detected, may be because of the spike killer), but perhaps one could use these paths in future studies. Actually, we need more information from the events to reconstruct our events. The calculated efficiencies of the HLT path used and its L1 seed path are indicated in table 7.3 for all mass points in the search, with an Illustration of these efficiencies in figure 7.10.

Table 7.3: *HLT_Photon*175_$v^\star$ and its L1 seed efficiencies vs. monopole masses

Mass	500	700	1000	1200	1500	1700	2000	2500	2700	3000
L1 eff. %	53.15	55.91	57	58.59	58.88	59.11	59.31	60.08	59.86	59.97
HLT eff. %	5.71	7.32	9	9.437	9.458	9.85	9.86	9.73	9.34	8.98

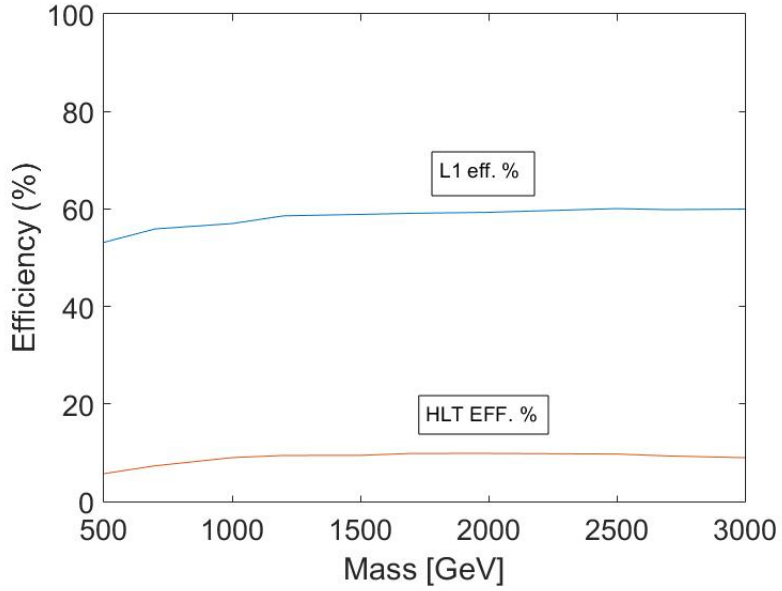


Figure 7.10: *HLT_Photon*175_$v^\star$ and L1 trigger path efficiencies vs. monopole masses

7.1.6 Monte Carlo (MC) and Data 2016 Samples

As discussed, mainly we have two keys to reconstruct the monopole candidates (Tracking and ECAL clustering). Thus, we need some additional object collections on top of AOD and MiniAOD to perform the analysis, as there are some uncleaning cuts in AOD and MiniAOD, and also to study properly the reconstruction of the monopole trajectories in the tracker.

Due to the large size of Reco format data, the collaboration only keeps data with AOD/MiniAOD format with less size and doesn't keep Reco format anymore, unless some analysis needs the Reco format data for important reasons. One of our challenges was to study carefully which collections we need and to represent our search strategy to the CMS community to be able to request

a special Rereco data format. Table 7.4 indicates all collections needed in this search for the tracking and ECAL cluster finding algorithms. End of 2017, we succeeded to get the approval of the Data group to produce our Rereco datasets with the required trigger HLT path, to perform our study on 2016 Data for magnetic monopole.

The two main keys to reconstruct the monopole candidates are summarized as follow:

- Tracking, as discussed before, to combine track segments that possibly come from magnetically charged particles.

- ECAL Cluster Finding, we have to combine *clean* and *unclean* collections to avoid spike rejection filters in the offline analysis.

Table 7.4: Collections used in the Reconstruction step

Tracking collections	ECAL clustering collections
Reco::TrackExtra-generalTracks_*_* *_siStripCluster_*_* *_siPixelCluster_*_*	*_hybridSuperCluster_*_* *_multi5x5SuperCluster_ multii5x5EndcapSuperCluster_, *_multi5x5SuperCluster_, uncleanOnlyMulti5x5Endcap,BasicCluster_* SuperCluster_* *_ecalRecHit_EcalRecHitsEB_ *_ecalRecHit_EcalRecHitsEE_

We are using a clean and unclean clusters collection. Clean collections, which pass the offline spike rejection filter, and Unclean clusters collections, which consist of clusters that don't pass the offline spike rejection. These two collections can be combined by adding CMSSW module to the configuration and by using this combined collection of ECAL clusters, we avoid spike filters in the offline analysis.

7.1.6.1 Monte Carlo datasets

In the first years of our study, we have worked with privately produced MC samples for all points masses, calculating the signal efficiencies with trigger path HLT_Photon175_v and adjusting our selections. We tried our best to cope with all the recent development that has been done for the monopole production model and results were recalculated. Early in 2019, again we have regenerated our MC samples privately with the latest model [161] and during this process we initiated a discussion with one of the experts in GEANT4 who are responsible for importing GEANT4 configuration files to the CMSSW, to make sure that we are using the up-to-date version, before requesting the official MC signal samples from the Data Group. Due to the conflict that discovered in GEANT4 model (see section 6.2.6), we have requested the official samples for all mass points with $\sim 100\,K$ events just after the fixing of the GEANT4 simulation with the ionization of monopole and get the green sign that all fixes were imported to the CMS software (CMSSSW). We succeeded to, officially, get 10 MC datasets with Reco format, one Reco format sample for systematic study (δ-ray production set to off).

The GlobalTag used in this search is indicated in table 7.5. and all the MC samples that have been produced are indicated in table 7.6.

7.1.6.2 Datasets 2016

In this thesis, we are studying the data of 2016 data-taken. For future studies, we will continue working on the 2017 and 2018 datasets as well.

We performed our analysis on the Single Photon datasets (see table 7.7). Eight datasets with total integrated luminosity of $33\,fb^{-1}$ have been produced specially for monopole study for data2016-07Aug17 Legacy Reprocessing. GlobalTag and JSON file information are indicated in table 7.8.

Table 7.5: Global Tag used for MC-2016 Datasets

Global Tag	80X_mcRun2_asymptotic_2016_TrancheIV_v6

Table 7.6: Monte Carlo (MC) datasets for monopole masses points in RECO format

Monte Carlo Datasets
/Monopole_SpinHalf_M-500_DY_13TeV_TuneCUETP8M1/RunIISummer16DR80Premix-PUMoriond17_80X_ mcRun2_asymptotic_2016_TrancheIV_v6-v2/GEN-SIM-RECO
/Monopole_SpinHalf_M-700_DY_13TeV_TuneCUETP8M1/RunIISummer16DR80Premix-PUMoriond17_80X_ mcRun2_asymptotic_2016_TrancheIV_v6-v2/GEN-SIM-RECO
/Monopole_SpinHalf_M-1000_DY_13TeV_TuneCUETP8M1/RunIISummer16DR80Premix-PUMoriond17_80X_ mcRun2_asymptotic_2016_TrancheIV_v6-v2/GEN-SIM-REC10
/Monopole_SpinHalf_M-1200_DY_13TeV_TuneCUETP8M1/RunIISummer16DR80Premix-PUMoriond17_80X_ mcRun2_asymptotic_2016_TrancheIV_v6-v2/GEN-SIM-RECO
/Monopole_SpinHalf_M-1500_DY_13TeV_TuneCUETP8M1/RunIISummer16DR80Premix-PUMoriond17_80X_ mcRun2_asymptotic_2016_TrancheIV_v6-v2/GEN-SIM-RECO
/Monopole_SpinHalf_M-1700_DY_13TeV_TuneCUETP8M1/RunIISummer16DR80Premix-PUMoriond17_80X_ mcRun2_asymptotic_2016_TrancheIV_v6-v2/GEN-SIM-RECO
/Monopole_SpinHalf_M-2000_DY_13TeV_TuneCUETP8M1/RunIISummer16DR80Premix-PUMoriond17_80X_ mcRun2_asymptotic_2016_TrancheIV_v6-v2/GEN-SIM-RECO
/Monopole_SpinHalf_M-2500_DY_13TeV_TuneCUETP8M1/RunIISummer16DR80Premix-PUMoriond17_80X_ mcRun2_asymptotic_2016_TrancheIV_v6-v2/GEN-SIM-RECO
/Monopole_SpinHalf_M-2700_DY_13TeV_TuneCUETP8M1/RunIISummer16DR80Premix-PUMoriond17_80X_ mcRun2_asymptotic_2016_TrancheIV_v6-v2/GEN-SIM-RECO
/Monopole_SpinHalf_M-3000_DY_13TeV_TuneCUETP8M1/RunIISummer16DR80Premix-PUMoriond17_80X_ mcRun2_asymptotic_2016_TrancheIV_v6-v2/GEN-SIM-RECO
/Monopole_SpinHalf_M-1000_DY_13TeV_TuneCUETP8M1/RunIISummer16DR80Premix-PUMoriond17_MDRoff_80X_ mcRun2_asymptotic_2016_TrancheIV_v6-v2/GEN-SIM-RECO
/Monopole_SpinHalf_M-1000_DY_13TeV_TuneCUETP8M1/RunIISummer16DR80Premix-PUMoriond17_80X_ mcRun2_asymptotic_2016_TrancheIV_v6-v2/GEN-SIM-RAW

Table 7.7: 2016 DataSets - SinglePhoton

DataSets 2016
/SinglePhoton/Run2016B-EXOMONOPOLE-07Aug17_ver1-v1/USER
/SinglePhoton/Run2016B-EXOMONOPOLE-07Aug17_ver2-v1/USER
/SinglePhoton/Run2016C-EXOMONOPOLE-07Aug17-v1/USER
/SinglePhoton/Run2016D-EXOMONOPOLE-07Aug17-v1/USER
/SinglePhoton/Run2016E-EXOMONOPOLE-07Aug17-v1/USER
/SinglePhoton/Run2016F-EXOMONOPOLE-07Aug17-v1/USER
/SinglePhoton/Run2016H-EXOMONOPOLE-07Aug17-v1/USER
/SinglePhoton/Run2016G-EXOMONOPOLE-07Aug17-v1/USER

Table 7.8: The JSON file and Global Tag used for Single Photon - 2016 Datasets

JSON file	Cert_271036-284044_13TeV_23Sep2016ReReco_Collisions16_JSON.txt
Global Tag	80X_dataRun2_2016LegacyRepro_v

7.1.7 Monopole Identification

Monopole candidates are constructed from a track which extrapolated to the face of ECAL and matched to the nearest ECAL cluster. We have applied preselection to the track fit parameters, $\triangle R$, which is the distance between the track and ECAL cluster is required to be less than 0.5, $\triangle R$ is calculated as

$$\triangle R = \sqrt{(\phi^2) + (\eta^2)} \tag{7.4}$$

HCAL isolation, which is the total energy in the HCAL (the hadronic energy of all caloTowers in the first segmentation of the HCAL)in the region $0.1 < \triangle R < 0.4$ around the ECAL cluster centre must be less than $10\,GeV$. Table 7.9 summarizes the pre-selections used to match the monopole track with the nearest ECAL cluster.

Table 7.9: Pre-selections applied for monopole matching

Pre-selections	Cuts	Value
Circular fit parameters	$\mid XYPar0 \mid\rightarrow \quad d_o = \sqrt{(a-c)^2 + b^2 - \mid c \mid}$	$<$ 0.6 cm
	$\mid XYPar2 \mid\rightarrow \mid \phi_o - \arctan(\frac{b}{c-a}) \mid$	$<$ 1000
Parabola fit parameters	$\mid RZPar0 \mid\rightarrow Z_o = \mid d \mid$	$<$ 10 cm
	$\mid RZPar1 \mid\rightarrow \eta_o = \mid f \mid$	$<$ 999
	$\mid RZPar2 \mid\rightarrow \rho - Z$ curvature = $\mid g \mid$	$< 0.005\ cm^{-1}$
Matching parameters	$\triangle R = \sqrt{(\eta)^2 + (\phi)^2}$	$<$ 0.5
	HCAL isolation	$<$ 10 GeV

We have applied a cut on the energy deposits in the ECAL which is required to be $E > 175\,GeV$. Also, events must pass the trigger selection. In order to identify the event as a monopole candidate, it must pass the tight selections on $dE/dx_{significance}$ (defined in section 7.1.1.2) and f_{51}, (defined in section 7.1.3.).

If a track/cluster pair has $dE/dx_{significance}$ of at least 9 and $f_{51} > 0.85$, we identify this event as a monopole candidate. Table 7.10 summarizes the tight selection cuts for the analysis search plus the loose cuts that used in the background estimation (ABCD method) that will be discussed later.

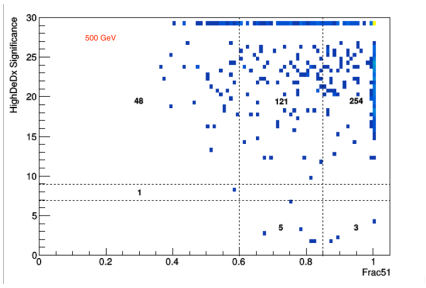
Table 7.10: Analysis selections cuts applied to identify the monopole candidate

	Cuts	Value
Analysis cuts	Energy deposition in ECAL	>175 GeV
	HLT_Photon175_v	
Discriminated variables	$dE/dx_{Significance}$	$\geq$ 9
	f_{51}	$>$ 0.85
Loose cuts	$dE/dx_{Significance}$	$\geq$ 7
	f_{51}	$>$ 0.60

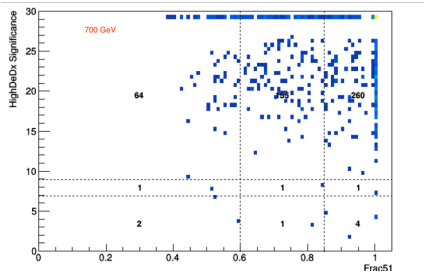
7.1.7.1 Signal Efficiency

We have studied the signal efficiencies from MC simulated events for all the masses range involved in this analysis for each major selection cut. Table 7.11 is the Cut-Flow table that represents the number of simulated monopole events that pass successive cuts, in order, i.e. the row with dEdXSig cut is the number of events that pass all selection cuts.

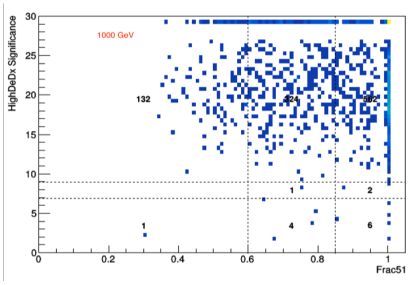
Table 7.12 is the (N-1) table that represents the number of events passing all selections cuts except the cut indicated in the left column, i.e. the row with NoTRG means that this is the number of events that pass all selection cuts except the trigger (HLT path).



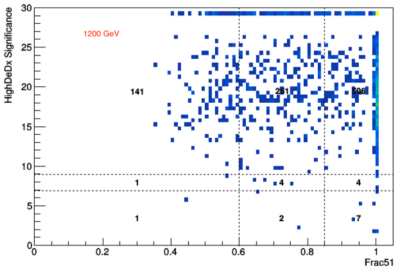
(a) 500 GeV



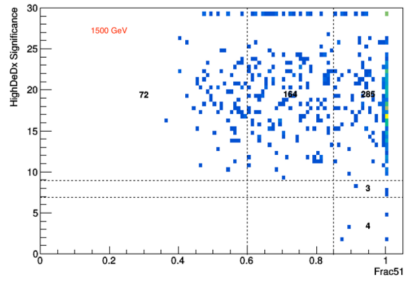
(b) 700 GeV



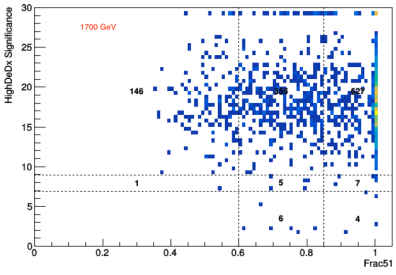
(c) 1000 GeV



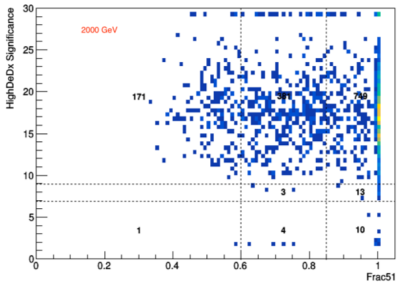
(d) 1200 GeV



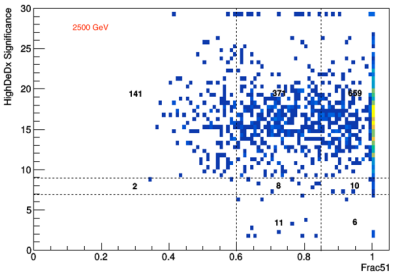
(e) 1500 GeV



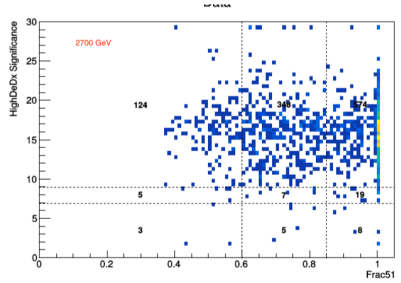
(f) 1700 GeV



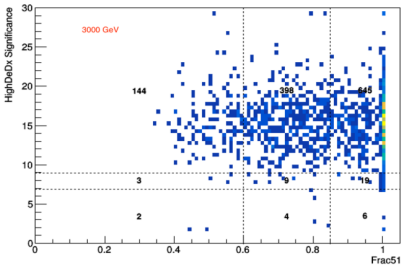
(g) 2000 GeV



(h) 2500 GeV



(i) 2700 GeV



(j) 3000 GeV

Figure 7.11: Joint distributions of the tracking discriminant and calorimetry discriminates for each monopole mass simulated after HLT and $E > 175\,GeV$ cut is applied to the ECAL cluster. Events are represented at most once in these figures in order to avoid double counting.

Table 7.11: CutFlow - Tabulated values of events simulated at each mass point after successive selection cuts are applied

	500 GeV	700 GeV	1000 GeV	1200 GeV	1500 GeV	1700 GeV	2000 GeV	2500 GeV	2700 GeV	3000 GeV
Generated	85000	61000	100000	77000	41200	79200	98000	92200	82000	98000
TRG	4860	4467	8728	7267	3897	7802	9666	8975	7659	8801
QualityCuts	2347	2174	4501	3604	2003	3930	5016	4751	4066	4709
ECut	318	293	576	505	279	563	713	731	575	675
F51Cut	235	202	378	326	170	353	470	466	368	436
dEdXSigCut	235	202	378	326	170	353	469	466	366	436

Table 7.12: N-1 - Tabulated values of events simulated at each mass point with all cuts except the indicated cut on the left column

	500 GeV	700 GeV	1000 GeV	1200 GeV	1500 GeV	1700 GeV	2000 GeV	2500 GeV	2700 GeV	3000 GeV
Generated	85000	61000	100000	77000	41200	79200	98000	92200	82000	98000
NoTRG	2265	2016	3972	3214	1832	3541	4515	4155	3604	4333
NoQualityCuts	387	345	627	525	275	608	804	786	615	705
NoECut	1592	1404	2812	2324	1266	2477	3228	3068	2627	3005
NoF51Cut	318	293	575	505	279	563	712	730	573	674
NodEdXSigCut	235	202	378	326	170	353	470	466	368	436

The offline selection cuts on f_{51} have efficiencies above 50 % , above 90 % for $dE/dx_{significance}$ and above 11 % for the cluster energy. However, the trigger selection has much lower efficiency of $\sim$ 10% even after the offline selections are applied.

The largest source of inefficiency is the trigger selection, as shown in table 1.14. For the events passing the trigger selection, monopole identification is relatively efficient. The table represents the relative efficiencies for each major cut used in the analysis and the values indicated in the table are illustrated in figure 7.12. The acceptance times efficiency is 0.40 % for 1500 GeV monopoles, and the acceptance times the efficiency for all the monopole masses simulated are given in table 7.13.

Monopole with mass near 2500 GeV has the peak efficiency. Higher mass monopoles are produced more centrally and thus hit the lower efficiency barrel region instead of the endcap. Lower mass monopoles tend not to have enough momentum to reach the calorimeter. The rules below have been obeyed to calculate the relative efficiency and the acceptance ($A \times e$)

$$Relative\,efficiency = \frac{number\,of\,events\,after\,selections}{number\,of\,events\,after\,selections\,except\,the\,mentioned\,cut}$$

$$Signal\,efficiency = \frac{number\,of\,events\,after\,all\,selection\,cuts}{number\,of\,events\,before\,selections\,applied}$$

Table 7.13: This table itemizes the final acceptance and efficiency used in the estimation of the observed monopole production cross section limit.

Mass	500 GeV	700 GeV	1000 GeV	1200 GeV	1500 GeV	1700 GeV	2000 GeV	2500 GeV	2700 GeV	3000 GeV
A $\times e$	.0027	.0033	.00378	.0042	.0041	.0044	.00478	.005	.00446	.0044

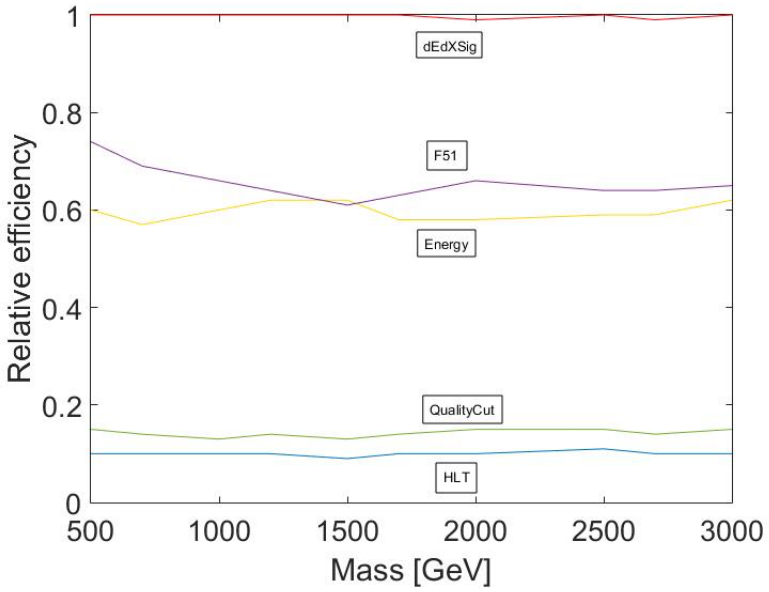


Figure 7.12: Illustration the relative efficiency of each major cut used in the analysis

Table 7.14: The Relative efficiencies for each major cut in the analysis

Mass(GeV)	HLT	Quality Control	Energy Cut	f_{51}	$dE/dx_{Sig.}$ Cut
500	0.10	0.60	0.15	0.74	1
700	0.10	0.57	0.14	0.69	1
1000	0.10	0.60	0.13	0.66	1
1200	0.10	0.62	0.14	0.64	1
1500	0.09	0.62	0.13	0.61	1
1700	0.10	0.58	0.14	0.63	1
2000	0.10	0.58	0.15	0.66	0.99
2500	0.11	0.59	0.15	0.64	1
2700	0.10	0.59	0.14	0.64	0.99
3000	0.10	0.62	0.15	0.65	1

7.1.8 Background Estimation - Using ABCD Method

Basic ABCD method: If the two discriminated variables that defining the signal region are uncorrelated (the shape of variable 1 distribution independent of variable 2 distribution), then we can proceed by using the ABCD method, satisfies the below rule which a data-driven estimate of background under a signal. Figure 7.13 illustrates the basic concept of the ABCD method.

$$N_D = \frac{N_c \times N_A}{N_B}$$

where N_D is the number of event in the signal region (background) N_A and N_B are the numbers of events in region A and B N_C is the number of events in the control region.

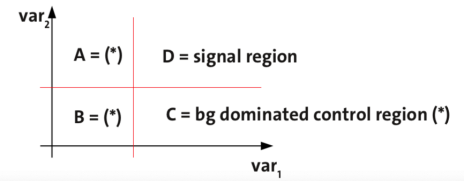


Figure 7.13: ABCD Method

In our analysis, we use a double ABCD method which is divided into 9 regions, to calculate the expected background in the signal region. This means to allow for an intermediate check of the background estimate. If we see issues we can adapt before we look at the signal region. Figure 7.14 represents a scheme of double ABCD method that was used in the analysis with 9 domains. Each of the 9 regions is given a unique with the following number scheme:

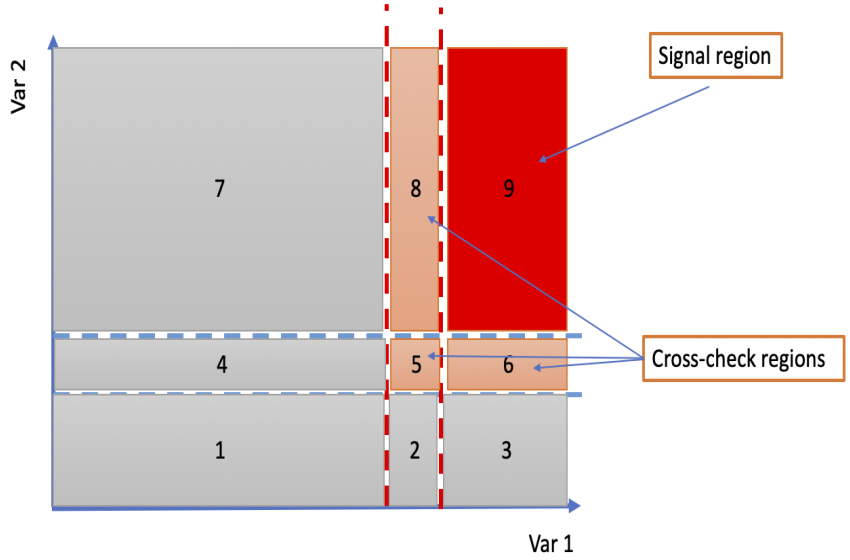


Figure 7.14: Scheme of double ABCD method used in the analysis

The domain is divided into 9 regions as follows:

$$0 \leq f_{51} \leq 0.6, \quad 0.6 < f_{51} \leq 0.85, \quad 0.85 < f_{51} \leq 1$$
$$0 \leq dE/dx_{sig} \leq 7, \quad 7 < dE/dx_{sig} \leq 9, \quad 9 < dE/dx_{sig} \leq \infty$$

The region at large $dE/dx_{significance}$ (> 9) and f_{51} (> 0.85) is the signal region. Each event populates this distribution once. For events with multiple candidates, only the candidate with the largest $dE/dx_{significance}$ is added to the joint distribution.

Initially, the four regions in the upper-right of this distribution (regions 5,

6, 8, and 9) were left blinded and the unblinded data was used to calculate the optimal position for the tighter $dE/dx_{significance}$ cut. The expected backgrounds in regions 8, 5, and 6 were then estimated using the ABCD method. Once those regions were checked to have good agreement with data, the expected background in the actual signal region was calculated and the signal region was unblinded. The background estimate is calculated by multiplying the contents in regions 3 and 6 by the ratio of contents in regions 7 and 8 to the contents of regions 1, 2, 4, and 5. The unblinded distribution of LHC collision data events recorded by CMS are shown in figure 7.15. The number of observed events in each region is also provided in Table 7.15.

The number of event observed in the 2016 dataset passing the trigger selection in each region are tabulated below:

Table 7.15: The number of events observed in each region of the ($dE/dx_{significance}$, f_{51}) space. No events are observed in the signal region (9).

Region	1	2	3	4	5	6	7	8	9
No. of events	19085	13814	1068	51	21	1	5	4	0

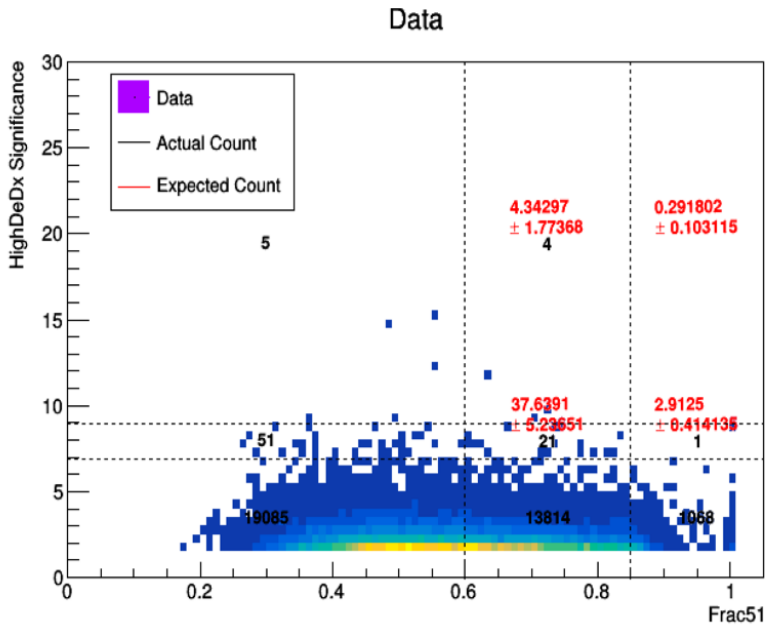


Figure 7.15: The distribution of f_{51} in the data collected compared to the same variable in the simulated monopole events. The red numbers represented the expected background and the black numbers are the actual counts observed in each region

The expected background estimation obtained using the double ABCD method is 0.2918 ± 0.103. We observe zero events in the signal region in $33\,fb^{-1}$ of $13\,TeV$ proton proton collision data. Figure 7.16 shows the distribution of f_{51} in the data collected compared to the same variable in the simulated monopole events. Figure 7.17 shows the distribution of the $dE/dx_{significance}$ in the data collected compared to the same distribution in simulated monopole events.

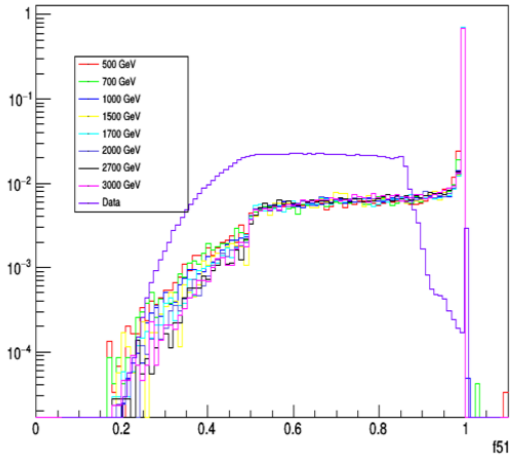


Figure 7.16: The distribution of f_{51} in the data collected compared to the same variable in the simulated monopole events

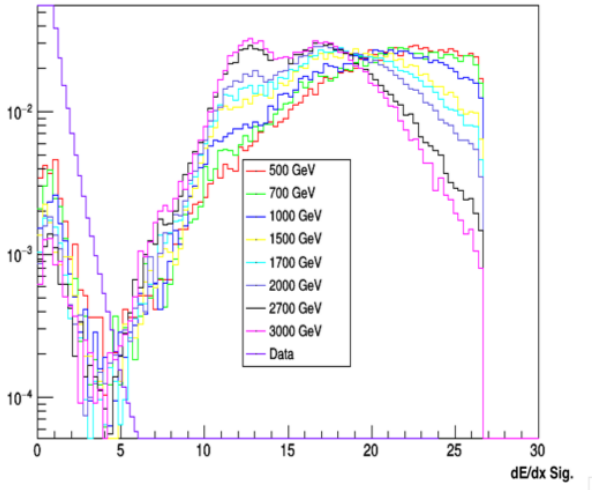


Figure 7.17: The distribution of the $dE/dx_{significance}$ in the data collected compared to the same distribution in simulated monopole events.

Distributions of simulated monopole events in the regions described above is shown in figure 7.11 for the mass points generated.

7.2 Systematic Uncertainty

Multiple effects can be a reason for uncertainty in the monopole efficiency. For example, the default settings of the GEANT4-CMS simulation software are treated as the nominal conditions and to study the systematic effects we have re simulating a sample of monopole mass $1000\,GeV$ for $g_D = 1$ with Drell-Yan process by changing the default status of these parameters. The systematic variation is introduced at the analysis level since the change in the default CMS simulation was not feasible, The systematic sources in our analysis are listed as follow:

- δ - electron production
- ECAL systematic uncertainties (shower shape and spike typologies).
- dE/dx cross-talk in the inner tracker.
- integrated luminosity for 2016 Data.
- Background estimation uncertainties.

The following subsections will discuss the various systematic uncertainties that were considered in this search.

7.2.1 δ-rays Production Systematic Uncertainty

The simulation of monopole interactions with matter is one of the largest uncertainties. As we discussed before, δ- electron ray production by monopole is varied up and down by 3 % [27]. By default, monopole ionization produces δ-electron above some threshold. The propagation of low energy electron rays

is limited by the GEANT4 simulation software in CMS, this is done by not simulating the δ-electrons below a certain kinetic energy threshold. As in such cases, the energy loss by the electrons is added to the monopoly's energy loss continuously during the simulating steps of the propagated trajectory. This threshold is defined as a distance parameter in GEANT4 and it is internally converted to the energy units. To achieve the best simulation precision, we need to minimize this parameter. The best proposal for CMS from the GEANT4 experts is to switch off the δ-electron production parameter in the simulation step and reproduce the MC sample and study the difference in the efficiencies. For mass 1000 GeV about 86000 events were fully simulated using the option of switching off this parameter in the GEANT4 and it was officially produced as an MC sample. The efficiencies were recomputed and the results are mentioned in table 7.16.

In the current versions of CMSSW simulation package, the threshold of the kinetic energy of the δ-electron produced is limited, only energetic δ-electron are produced. i.e. electrons with energy below the minimum kinetic energy are not simulated.

Table 7.16: Systematic uncertainty for monopole mass 1000 GeV when switching off the δ-electron production

Systematic uncertainty (for monopole mass 1000 GeV)	δ-ray production (off)	δ-ray production (on)
number of events generated	86200	100000
number of events passed selection cuts	296	378
Signal efficiency	0.00343	0.00378
Systematic uncertainty %	**9.25%**	

We changed the thresholds to understand the systematic uncertainty, but it is not easy to do it consistently for a complicated detector such as CMS. This can be studied with the standalone example for monopoles in GEANT4 later in future studies. The alternative proposal for CMS is to disable the δ-electron production For that it was enough to customize only one flag "Process.g4SimHits.Physics.MonopoleDeltaRay = cms.untracted.bool(False)".

By disable delta electrons, the range of monopoles should not change, only energy depositions in the tracker and ECAL will be different, that's why we also

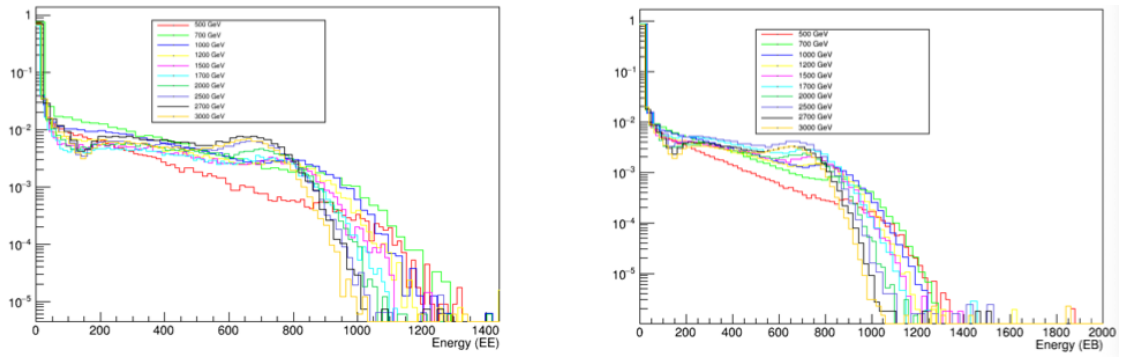
studied the systematic uncertainties in the shower shape in the ECAL clusters, which will be discussed later. We have calculated the systematic uncertainty for δ-electrons production off, and it found to be 9.2 %, which is a very small effect.

7.2.2 ECAL Systematic Uncertainties

Systematic uncertainties due to the online selection in the ECAL can be obtained by disabling the GEANT4 modeling described in the previous section. The online spike filtering is based on topological shower shapes in the ECAL. Therefore, uncertainty in the spike filter efficiency is subject to uncertainties in the shower shape of the energy deposit left by a monopole. The large mass of the monopoles simulated leads ionization to dominate over radiative processes as the preferred energy loss mechanism.

By disabling the simulation parameter which determines the modelling of the ionization energy loss, the ECAL cluster shape dependence is also probed. The systematic uncertainties quoted in table 7.17, include the simulation of the trigger selection. Any effect arising from the saturation of ECAL cells is negligible since most of the energy depositions are well below this threshold, see figure 7.18.

The 175 GeV energy threshold applied toward monopole selection rejects ECAL noise (see Appendix A.1), and a broad energy spectrum observed in simulated events suggests that systematic uncertainties arising from calibration effects are negligible. Since fluctuations in measured energy are small compared to the width of the energy distribution, the impact of calibration uncertainty on acceptance is also small. Figure 7.18 shows the distribution of energy of 5×5 ECAL clusters before any selection is applied from simulated monopole events (all mass points are represented by the various colors). Monopoles show a broad energy spectrum which effectively ends below 1700 Gev. The ECAL saturation at 2 TeV has a negligible effect since very few clusters are expected to reach near that energy. The broad energy spectrum suggests that uncertainties due to calibration on acceptance are small.



(a) (b)

Figure 7.18: The distribution of energy measured in the EE (left) and EB (right) in 5×5 clusters before any selections are applied for simulated monopole events. All simulated monopole mass points are represented by the various colors

7.2.2.1 Spike Topologies

Very small effect of the systematic uncertainty is attributed to the spike killing algorithm in the offline selection, because all ECAL clusters are considered regardless of the flags set by the offline reconstruction. We switched off the spike topologies (see appendix A.2), *swiss-cross* and *timing*, at the Particle flow rechit level by setting the following parameters to False for the ECAL Barrel and Endcap: *particleFlowRecHitECAL_cfi.py class /RecoParticleFlow/PFClusterProducer/*

$$timingCleaning = cms.book(False)$$
$$topologicalCleaning = cms.bool(False)$$

The systematic uncertainty in the case of switching off the spike topologies is equal to 0.5% as quoted in table 7.17.

Table 7.17: Systematic Uncertainty for switching off the spike topologies in the PF-recHit step

Systematic uncertainty (for monopole mass 1000 GeV)	Spike topologies (off)	Spike topologies (on)
number of events generated	4200	100000
number of events passed selection cuts	16	378
Signal efficiency	0.0038	0.00378
Systematic uncertainty %	**0.5%**	

7.2.2.2 ECAL Shower-Shape Systematic Uncertainty

We studied the ECAL cluster shower shape topology f_{51} after disabling the production of δ-electron (green color) in GEANT4 simulation software and compare it between the distribution of the default setting (red color) for the same mass point 1000 GeV.

Besides, we switched off the spike typologies (blue color) and performed the same comparison of the shower shape in the ECAL is plotted below in figure 7.19. We calculated the difference of the mean of the distribution of f_{51} for the two cases to be compared with the default sample. The Systematic uncertainty effect was found to be very small $\sim 2.4\%$. The systematic uncertainties are quoted in table 7.18. Figure 7.20 shows the joint distributions of the tracking discriminant and calorimetry discriminant for case (a) Default setting, (b) Spike typologies off, (c) δ-rays production off, the three cases are for monopole mass 1000 GeV. We can see from these distributions the differences in the signal regions.

Table 7.18: Systematic Uncertainty in ECAL cluster shape distributions

Systematic (Shower Shape)	Spike typologies off	δ-electron production off	Default
Mean (from the distribution)	0.827	0.847	0.849
Systematic uncertainty %	**2.5%**	**0.14%**	

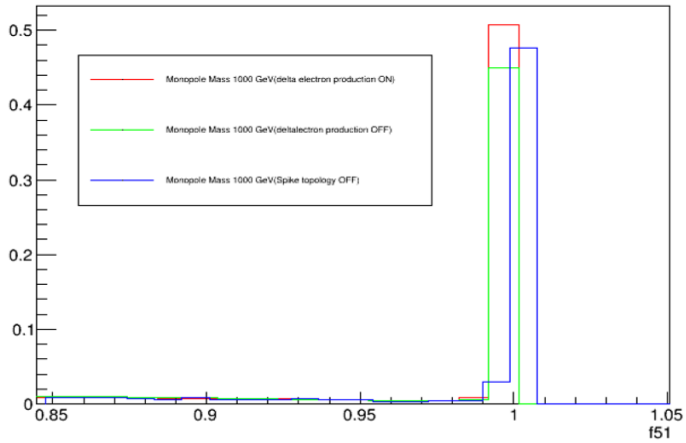
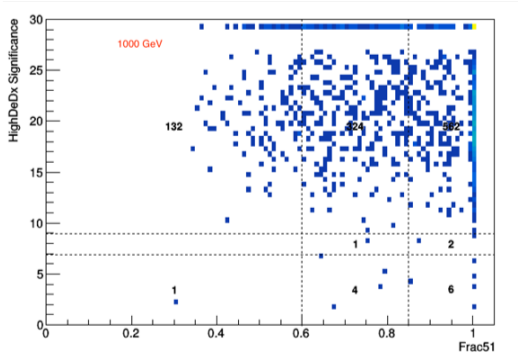
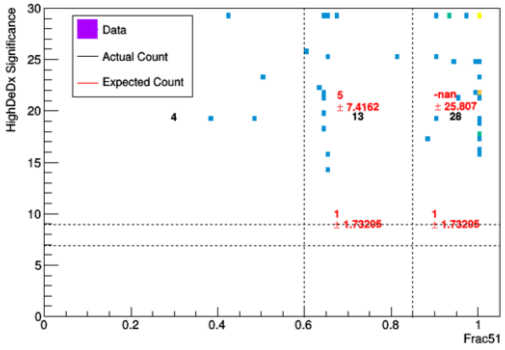


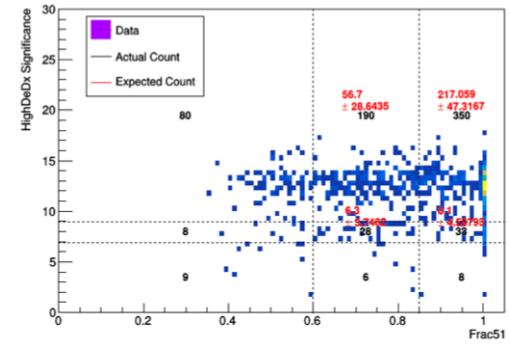
Figure 7.19: The distribution of shower shape topology f_{51} in the ECAL for mass point 1000 GeV for $delta$-electron production off (green) and Spike typologies off (blue) along with default settings (red)



(a) Default



(b) Spike off



(c) δ-ray production off

Figure 7.20: The joint distributions of the tracking discriminant and calorimetry discriminant for cases (a) Default setting , (b) Spike typologies off, (c) δ - ray production off

7.2.3 dE/dx Cross-talk in the Tracker Sub-detector

The dE/dx response is more complicated due to a large number of strips involved in each track measurement. The electronic cross-talk in the tracking chamber affects the dE/dx measurements, particularly since monopoles are expected to saturate many of the tracking strips. The systematic uncertainty is intentionally overestimated by simulating with the amount of cross-talk 10 % up and down, which gives an uncertainty of 0.28 % and 1.11 % respectively.

In order to understand what is the dE/dx cross-talk [167], here is just a summary of the study we did. In Data the reconstructed clusters are referred as "observed clusters", cluster with three strips in the cross-talk is a coupling between neighboring strips, as shown in figure 7.22, there is a coupling between the central strip and the first two neighbor strips (x_1) and also a coupling with the second two neighbor strips (x_2).

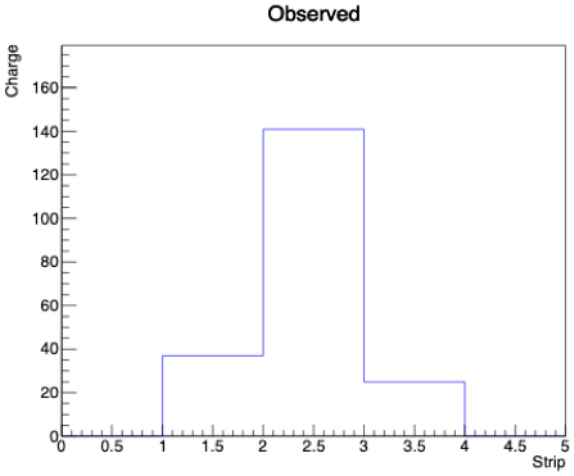


Figure 7.21: Observed dE/dx cross-talk

The dE/dx cross-talk parameters should be understood as the following:

$$Q_0 = par[0]xQ$$
$$Q_\pm 1 = par[1] \times Q$$
$$Q_\pm 2 = par[2] \times Q$$

Where Q is the total charge "deposited" within the silicon volume under the strip "0", Q_0 is the charge "collected" under that strip, and $Q_\pm 1$ are the 2 closest neighbor strips, and $Q_\pm 2$ the 2 next ones.

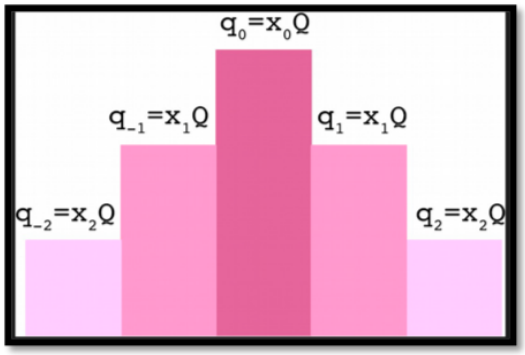


Figure 7.22: A schematic distribution of the dE/dx cross-talk clusters

A measurement campaign has been done during 2018 and they observed variations compared to run I. The variation was about 20 % and is known with small statistical uncertainty. There is a constraint between the parameters to impose the charge conservation: The cross-talk must verify that

$$x_0 + 2x_1 + 2x_2 = 1 \tag{7.5}$$

To perform the systematic study, we kept $par[2]$ unchanged as it is small value and we changed x_0 with 10 % up and down of its original values that indicated in the SiStripSimParameters_cfi.py configuration file in the CMSSW

Mixing Module package, and then we determine the value of x_1 that satisfy above condition in equation (7.5).

In the configuration file, SiStripSimParameters_cfi.py in the MixingModule package in the digi. step of the MC production, we have modified the cross-talk parameters using a command like:

$$process.SiStripSimBlock.CouplingConstantDecIB1 = cms.vdouble(X,Y,Z)$$

Where X,Y,Z are the new values we want to inject after changing the 10 %. Inside the file there are 14 commands to describe the whole tracker module typologies in "Dec" mode, 2 for TIB, 2 for TOB, 3 for TID, 7 for TEC, which are in total 14 parameters should be changed. It means that the efficiencies are all compatible with each other which implies that the impact of the cross-talk is below $\sim$ 10 % (relative uncertainty on our efficiency). Our test shows compatible results within error bars (10 %). In that case, we assume that if the effect exists, it is subdominant compared to the other uncertainties. Results are quoted in table 7.19.

Table 7.19: dE/dx cross-talk Systematic Uncertainty

Systematic uncertainity (for monopole mass 1000 GeV)	dE/dx cross talk 10% up	dE/dx cross talk 10% down	dE/dx cross talk Default
number of events generated	28000	28000	100000
number of events passed the track parameter fit cuts	10006	10111	35619
Signal efficiency	0.357	0.36	0.35619
Systematic uncertainty %	**0.28%**	**1.11%**	

7.2.4 Systematic Uncertainty in Data-driven Background Estimation

The collision data taken is sliced by the tracking and calorimetry variables to study uncertainties in the shape of the distribution. Figures 7.23 and 7.24 Show the one-dimensional distribution of the discriminant variable f_{51} and $dE/dx_{significance}$ respectively, in slices of the other variable. These distributions are normalized to the unit area for the purpose of comparing the shape of distributions. The distributions of f_{51} vary in shape depending on the

$dE/dx_{significance}$ slice taken. The shape of the overall distribution is dominated by the shape of the lowest $dE/dx_{significance}$ slice since the number of events in each slice rapidly decreases at large $dE/dx_{significance}$.

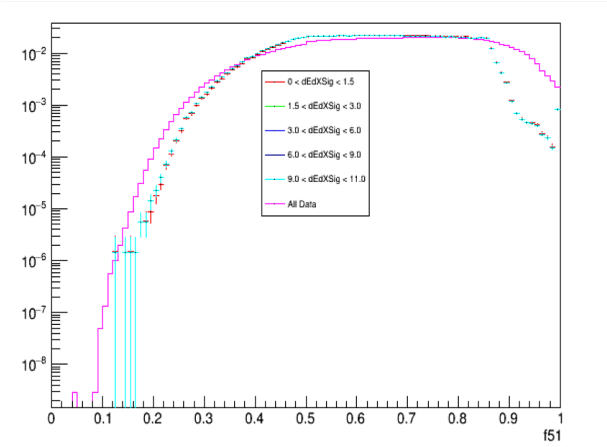


Figure 7.23: A comparison of shapes of the f_{51} distribution in slices of the $dE/dx_{significance}$ in the 2016 dataset. All curves are normalized to unit area.

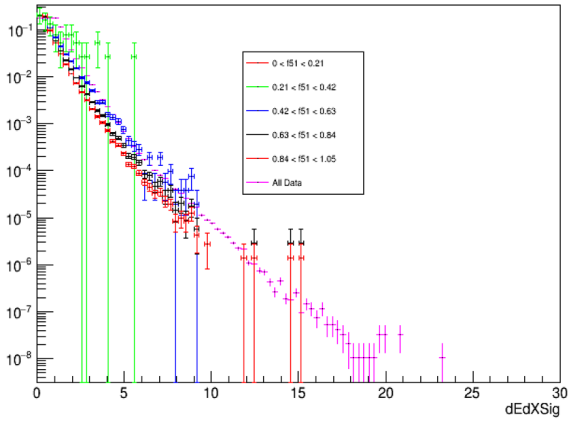


Figure 7.24: A comparison of shapes of the $dE/dx_{significance}$ distribution in slices of f_{51} the in the 2016 dataset. All curves are normalized to unit area.

The distribution of $dE/dx_{significance}$ for various slices of f_{51} displays a stronger degree of conformity. The joint distribution in data has a correlation factor of -0.009 (this number has been calculated using ROOT software [154], by using GetCovariance() function). In order to estimate the systematic uncertainty on the background, the loose cuts applied to $dE/dx_{significance}$ and f_{51} are varied. The tight cuts remain fixed at 9 and 0.85 for $dE/dx_{significance}$ and f_{51} respectively.

We have changed the loose cuts to estimate the systematic uncertainty in background estimation. Since at each set of loose cut pairs the background estimates agree with each other, as shown in table 7.20, a systematic on the background estimation can be determined by substitutes in equation 7.6. This number is taken as a systematic uncertainty in the background estimation.

$$\triangle x/x \quad = \quad 0.103/0.2918 = 0.357 \simeq 35.7\% \tag{7.6}$$

Table 7.20: The estimated background contribution to the signal region based on various loose cuts and the associated relative systematic uncertainty on the background estimate.

f_{51} loose cut	dE/dx_{sig} loose cut	X	$\triangle$ x
0.45	4	0.2918	0.1031
0.45	2	0.2918	0.1031
0.45	6	0.2918	0.1031
0.45	3	0.2918	0.1031

7.2.5 Systematic Uncertainty on the Integrated Luminosity

One of the basic parameters that is used to measure the cross section is the integrated luminosity. As we are using in this thesis 2016 Data taken in the proton-proton collision at centre of mass-energy $13\,TeV$ with integrated luminosity of $33\,fb^{-1}$. The overall uncertainty on the integrated luminosity is estimated to be $2.6\,\%$. All variations which have been discussed above are leading to very small differences in signal efficiency. Table 7.21 is summarizing The systematic uncertainties in the signal efficiency and background estimate.

Table 7.21: The Systematic Uncertainties in the signal efficiency and background estimate.

GEANT4-δ-ray (profuction off)	Spike topologies (swiss-cross and timing off)	ECAL shower shape distribution (δ-ray, spike)	dE/dx cross-talk	Luminosity	Background estimation
9.25 %	0.5 %	2.5%-0.14%	0.28%-1.11%	2.6%	35.5%

The absolute value of the total systematic error is equal to 0.36, which obtained from the following relation:

$$Total systematic error = \sqrt{\sum (systematic_uncertainty)^2} \tag{7.7}$$

7.2.6 Cross-Section Limits

The Higgs combine tool [109] is used to estimate the monopole production cross section limits. The systematic uncertainties are summarized in table 7.22. The limit placed on the number of events is scaled to a limit on cross-section by factoring in the integrated luminosity of 33 fb^{-1} and total acceptance and efficiency.

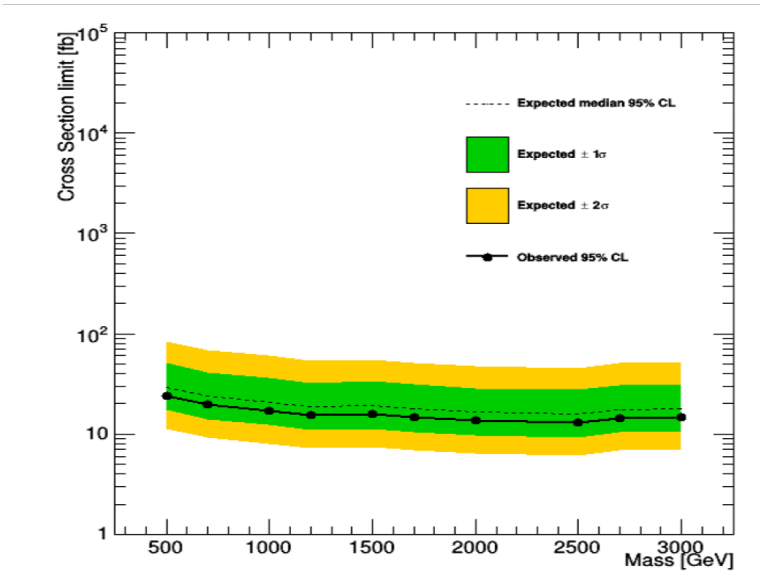


Figure 7.25: Observed 95 % CL upper limits on the cross-section for Drell-Yan spin 1/2 monopole

Table 7.22: Expected and observed production cross-section limit

Mass	500 GeV	700 GeV	1000 GeV	1200 GeV	1500 GeV	1700 GeV	2000 GeV	2500 GeV	2700 GeV	3000 GeV
Expected Limit [fb]	29.1	23.7	20.7	18.68	19.13	17.87	16.4	15.6	17.6	17.87
Observed Limit [fb]	23.9	19.59	17.1	15.39	15.77	14.69	13.53	12.93	14.5	14.7

The cross-section limits for DY pair production with spin $1/2$ are shown graphically as a function of mass, The limit obtained by this method and data is shown in figure 7.25. We calculated 0.3 expected background events, and observed 0 events. We, therefore, set an upper limit on the monopole production cross-section using CLs method [153]. The calculation includes the systematic uncertainties discussed in the previous section. The 95 % confidence limit of (23.9 for mass 500 GeV to 14.7 fb for mass 3000 GeV) on the production cross section of the Dirac magnetic monopole is illustrated, and the central limit's numerical values are tabulated in table 7.22.

Positive and negative error bands of the expected limit are plotted. The observed limit lies along the lower edge of the band of the expected limit due to the extremely low background expectation and the fact that exactly 0 event was observed in the signal region.

In conclusion: A search for magnetic monopoles as an exotic long-lived particle using a signature of a highly ionizing particle which deposits all- mostly of its energy in the ECAL crystals was performed with the CMS detector at the LHC using 33 fb^{-1} of 13 TeV proton-proton collision data. Monopole candidates were selected by extrapolating the fitted track in the tracking chamber and the shower shape in the ECAL crystals. Zero events were observed in data in the signal region. An Upper limit on the production cross-section mass limit was set for all the masses.

7.2.7 Sensitivity Differences between LHC-experiments

In this section we compare between the results of CMS-run II and ATLAS experiment-run II, with integrated luminosity of 34.4 fb^{-1} of 13 TeV proton-proton collision data (2016). Data was collected by ATLAS detector, by using a dedicated trigger for monopole that based on the high threshold hit capability of the tracker. Masses range of 200 GeV to 4000 GeV with the Drell-Yan pair

production of stable particles of spin 0 and $1/2$ are used in this search. The electric charge range in run one was $20 \leq |z| \leq 60$ and extends to $60 < |z| \leq 100$. No event was observed in the signal region, consistent with the background expectation.

By comparing The observed *CLs* upper limit on the cross-section for DY spin $1/2$ process with charge $g = 1.0\, g_D$, between ATLAS and CMS (recent results for run II). We found that our result is $4-5$ times less sensitive than the recent ATLAS results [3], figure 7.26 presents ATLAS results (black dotted line).

To improve our results we need a more dedicated trigger and a dedicated spike study using the topology of the spikes and potentially the timing to be used at the trigger level in future studies.

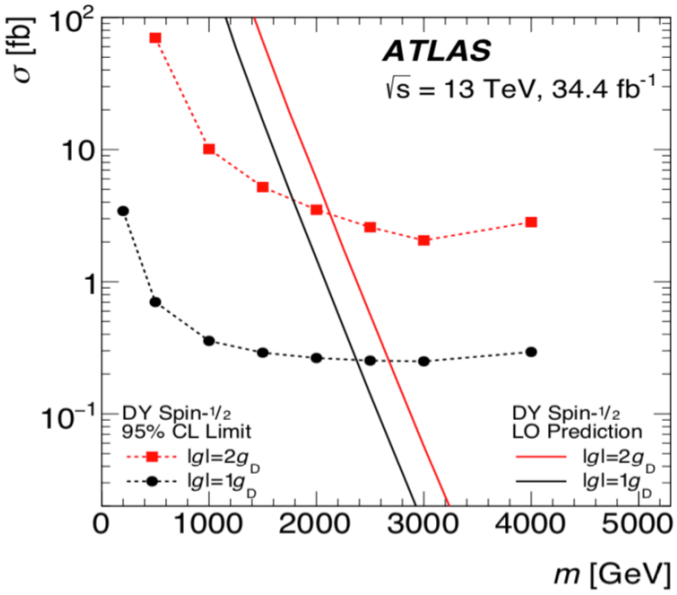


Figure 7.26: ATLAS - Observed 95 % CL upper limits on the cross-section for Drell-Yan. Plot has been taken from [3]

CHAPTER 8

MOEDAL EXPERIMENT

Searching for a magnetic monopole or other Stable Highly Ionizing – Massive particles (SMPs) at the LHC is the main objective of the MoEDAL experiment at the LHC. The MoEDAL experiment [80] is located at interaction point 8 (IP8), where LHCb detector located.

The doctoral candidate has contributed to the results of 13 TeV run II search, which was published in July 2019 with MoEDAL Collaboration. More detail about the work done will be discussed in the next sections.

8.1 MoEDAL Experiment Overview

The dedicated MoEDAL detector is composed of *Plastic Nuclear Track Detector (NTDs)* array, which performs ultra fast scanning microscopes used in offline analysis. *Magnetic Monopole Trapper (MMT)*, which is the latest subdetector system that inserted into the MoEDAL detector, and it consists of $\sim$ 1 tonne of aluminium (Al) bars placed at three points around the intersection point ($IP8$), of one of the main experiments at the LHC, which is LHCb detector, specifically in the VELO (VErtex LOcator) cavern, as shown in figure

8.1. In the next section, we will give a brief description on the technology of track-etching detectors.

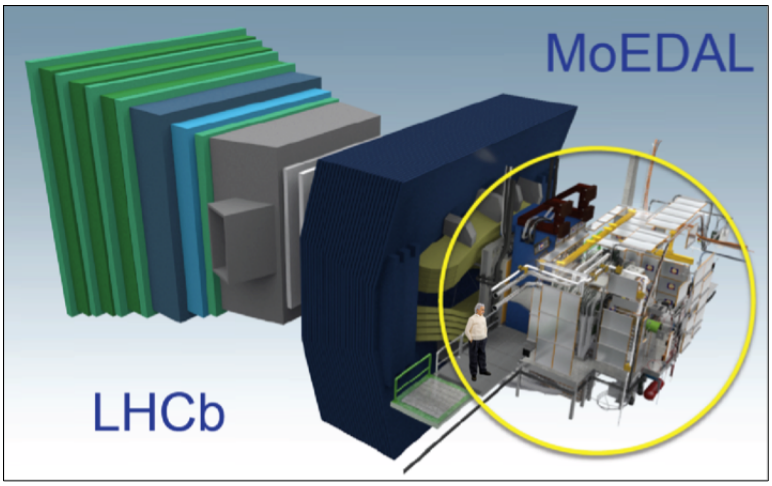


Figure 8.1: A schematic view of three-dimensional MoEDAL detector (beside the yellow circle)

Monopoles will 'burn' through the plastic sheets of the experiment or get trapped in the dense material of the trapping detector [142]. The MoEDAL experiment is composed of three main subdetectors:

- Nuclear Track-Etch Detectors (NTDs): passive sub-detector with $18\,m^2$ of CR39 and Makrrofol. more details are presented in the coming section.
- Magnetic Monopole Trapping detectors (MMTs), consist of $800\,kg$ of aluminum bars.
- MediPix chip-based online radiation monitor system

Each year, the NTD and MMT sub-detectors are removed to be exchanged by new ones and to analyze the removed ones. The main contribution of the doctoral candidate was in analyzing the aluminum (Al) bars of the MMTs using SQUID techniques.

8.1.1 Track-Etch Detectors

By the passage of a charged particle through a plastic nuclear track detector, damage is produced at the polymeric bounds level with a small region, of a shape of the cylinder, around the trajectory of that particle, which forms latent track, as shown on figure 8.2 and figure 8.3.

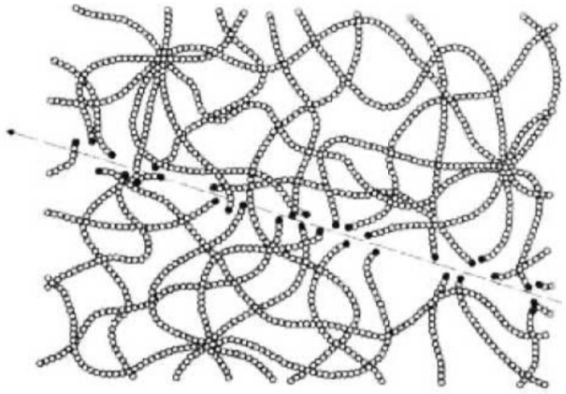


Figure 8.2: The polymeric bonds breaking caused by a crossing charged particle.

The Restricted Energy Loss (REL) is a function of the charge Z and $\beta = v/c$ of the highly ionizing particle that occurs inside the cylindrical region is proportional to the damage produced (c is the light's velocity in vacuum). This energy is equal to the total energy loss of a particle in the medium, if the incident ion's velocity is less than $1 \times 10^{-2}\, c$, otherwise, a fraction of the energy loss is efficient to form the track and it will be a reason of δ-rays production with energies less than a cut-off energy T_{cut}. The restricted-energy loss can be calculated from the Bethe-Bloch formula with energy transfers $T < T_{cut}$.

MoEDAL experiment's basic unit is a stack of 9 plastic sheets (NTDs), as shown in figure 8.4, composed as follow:

- 3 sheets of CR39[59], with $\sim 0.5\, mm$ in thickness for each sheet.
- 3 sheets of MAKROFOL [178], with $\sim 0.5\, mm$ in thickness for each sheet.

- Lexan [168] forming the 1st, middle and end sheets in the stack with $\sim 0.2\,mm$ in thickness for each sheet.

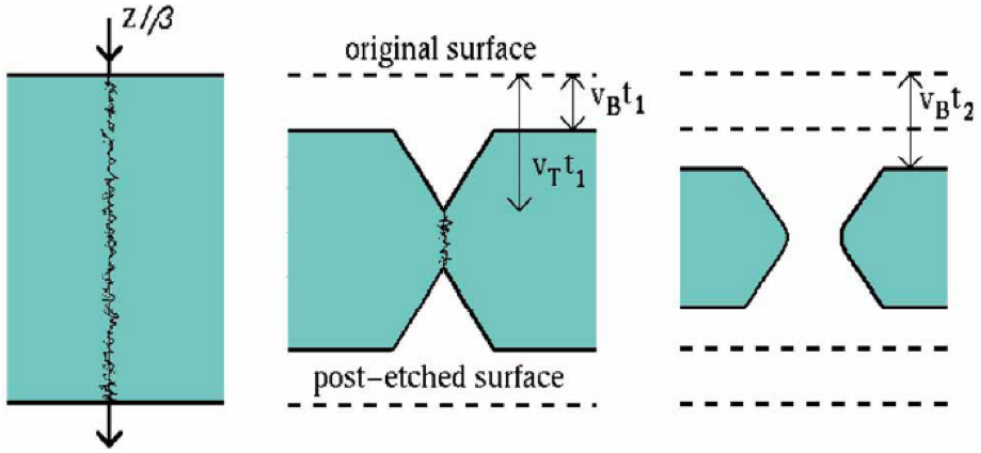


Figure 8.3: The latent track that occurred by particle's passage with charge Z and velocity $\beta = v/c$ (left). Two etch pit cones are formed on the sides of the foil (middle). A prolonged etching forms a hole (right).

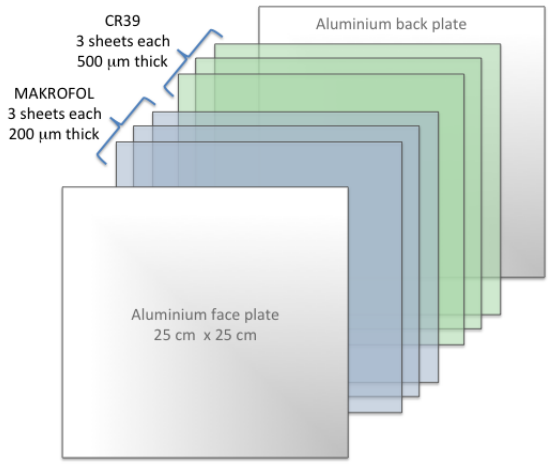


Figure 8.4: The basic MoEDAL detector stack is consisting of three sheets of CR39 and 3 sheets of MAKROFOL with Lexan sheets separating the CR39 and MAKROFOL stacks. Sheet size is $25\,cm \times 25\,cm$. An $1\,mm$ thick aluminum housing is surrounding the stack. Total thickness of the stack is $3.6\,mm$.

8.1.2 The Magnetic Monopole Trapper Detector System (MMTs)

MMTs consist of passive stacks of aluminum trapping detectors located beside the VELO detector. The main function of these stacks is to trap the monopoles and other Stable Highly Ionizing – Massive particles (SMPs) that stop within their volume. These stacks are replaced every year and then, the exposed trapping volumes are scanned and analyzed through the SQUID detector. This process takes place in a magnetically shielded room at the Laboratory of Natural magnetism at Zurich. The detection method is based on measuring a persistent current which gets induced in the superconducting coil of the sensitive SQUID magnetometer.

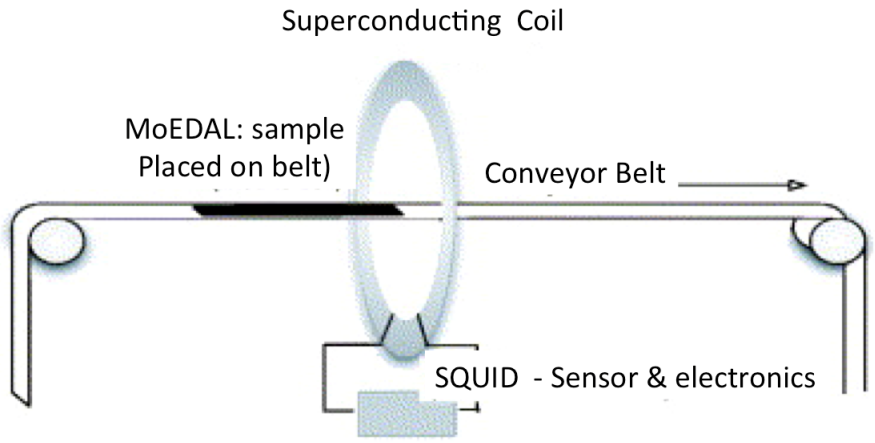


Figure 8.5: A schematic diagram for SQUID apparatus. The sample passed in steps through the coil. The current in the superconducting coil is measured after each step.

Figure 8.5 presents a schematic diagram for describing the SQUID magnetometer scanning process. Figure 8.6 shows a real photograph taken by me for the magnetically shielded room during my visit in 2018 to perform SQUID for 11 boxes with a total of 606 samples. More details regarding this technique can be found at [113].



Figure 8.6: Real photographs, taken by the author, for the magnetically shielded room at Zurich (top), the the SQUID magnetometer (middle), and the Aluminum samples (bottom)

After scanning the samples through the ”SQUID” process, the magnetic monopole trapping volumes are sent to a laboratory underground to monitor the decay of the trapped long - lived electrically charged particles, and we can find the lifetime of the particle by observing the decay rate.

8.1.2.1 Magnetometer Measurement Procedures

The procedures of the SQUID method, which has been done for all the Aluminum (Al) bars of the MMT, are as follow

- After the complete passage of the sample through the sensitive coil, output is read out before, during and after this step.
- Calibration is applied, with a convolution method, to the sample and cross-checked process with long thin dipoles mimicking a monopole of well-known charge.
- Subtract the empty holder result from the measurement. The difference between the measurements of the output current of the samples and the measurements of empty holder output, is the persistent current. If it differs from zero we have a monopole signal candidate.

8.1.3 MoEDAL Experiment Results for 13 TeV

During run II of the LHC [16], the MoEDAL experiment has extended the magnetic charge limit to be $\mid g \mid \leq 5.0\, g_D$ and the masses range become up to $1790\, GeV$ using Drell-Yan production mechanism [17, 18]. In 2018, Approximately, 2400 samples from the MMTs sub-detector were scanned with a DC SQUID long-core magnetometer, which is located at ”the Natural magnetism laboratory” at ETH Zurich’. The measured response of the magnetometer is translated into a magnetic pole P with Dirac charge g_D units, multiplying by a constant of calibration C. Two independent methods used for calibration has been performed at the beginning of the campaign, more detail is described in [85].

Based on the principle of Superposition, the first calibration method adds the performed measurements at 1 mm intervals using a dipole sample of known magnetic moment $\mu = 2.98 \times 10^6\ A.m^2$ to obtain the response of a single magnetic pole of strength $P = 9.03 \times 10^5\ g_D$. The second calibration method used a long thin solenoid that provides $P = 32.4\, g_D/\mu A$ for several ranges of currents, from $0.01\,\mu A$ to $10\,\mu A$, to be able to measure the effect of a magnetic pole of known strength directly. Figure 8.7 represents the calibration measurement's result. The calibration constant is used by tuning the measurement from the superposition method.

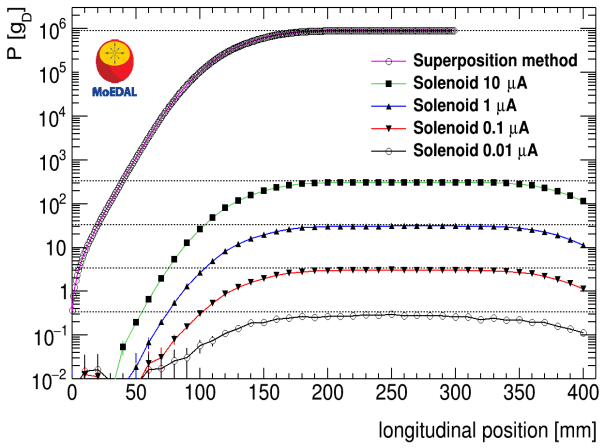


Figure 8.7: Results of the calibration measurements for several currents ranges, with the superposition method using a magnetic dipole sample, and the solenoid method with $P = 32.4\, g_D/\mu A$. The dashed lines represent the expected plateau values in units of Dirac charge.

The two calibration methods used, agree within 10 % and this value is considered as an uncertainty in the calibration of the pole strength. The response of the magnetometer is obtained to be linear and symmetric in charge with a range corresponding to $0.3 - 300\, g_D$. During the campaign, the calibration dipole sample was remeasured regularly and the value of the plateau of the calibration was shown not to vary.

8.1.3.1 MMTs Measuring Techniques

During the process of scanning the samples of the MMTs, we performed the following steps: First, we have to place the samples on a carbon-fiber movable

conveyor tray for transport through the magnetometer's sensing region, three samples at a time, with a separation distance of 46 cm. As it was found in previous studies, the speed of transportation was set to the minimum of 2.54 cm/s.

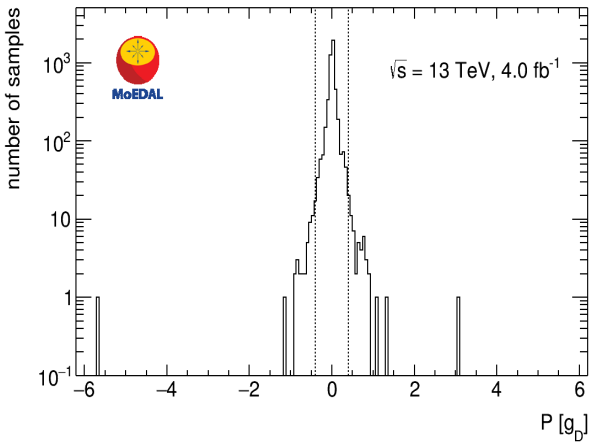


Figure 8.8: Magnetic pole strength (with Dirac charge units) measured in the 2400 Aluminium samples of the MMTs detector with exposing to 13 TeV collisions during run II, with double scanning for each sample

The magnetic charge that exists in a sample is measured as a persistent current in the superconducting coil that surrounds the transport axis of the magnetometer. This persistent current is defined as "the difference between the currents measured after (I_2) and before (I_1) passage of a sample through the sensing coil". we also have to count the contributions of the empty tray I_2^{tray} and I_1^{tray} in our measurements. The magnetic pole strength contained in a sample, expressed in Dirac charges, is thus calculated as $P = C \cdot [(I_2 - I_1) - (I_2^{tray} - I_1^{tray})]$, where C is the calibration constant. The scanning of these samples has been done twice, with the shown pole strength results in figure 8.8.

In either of the two measurements, the pole strength measurements are different from 0 by more than 0.4 g_D. A total of 87 candidate samples were identified. For repeated measurements, if a sample contains a genuine monopole would obtain the same non - zero values, while zero values would be measured when no monopole is present. Repeatly scanned process performed for the candidates samples and it was found that most of the measured pole strengths for each sample are less than the threshold of 0.4 g_D, as indicated in figure 8.9.

"The probability that a monopole of given mass, charge, energy and di-

rection would end its trajectory inside the trapping volume", is defined as the acceptance of the trapping detector, and it is determined from the information of the material traversed by the monopole [32] and the ionization energy loss of monopoles when they pass through matter [26, 60], as implemented in a simulation-based on Geant4 [31](as discussed in chapter 5). The pair-production model determines the kinematics and the overall trapping acceptance can be measured, for a given mass and charge. Uncertainties in the material description are dominating the uncertainty in the acceptance [18]. This contribution is determined by performing simulations with hypothetical material conservatively added and removed from the nominal geometry model.

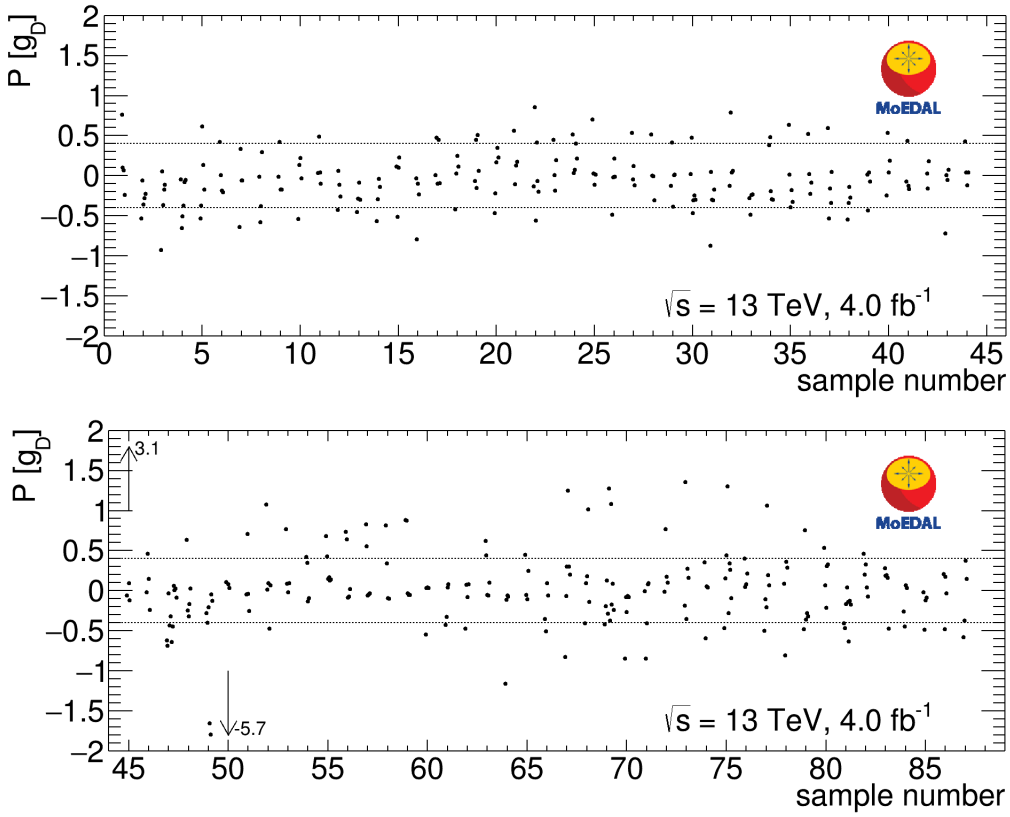


Figure 8.9: Results of multiple pole strength measurements (in units of Dirac charge) for the 87 candidates samples. At least one of the two first measurement values was above the threshold $|g| > 0.4\, g_D$. Most of the values observed below the threshold, the presence of a monopole with $|g| \geq g_D$ is excluded.

The Drell-Yan (DY) mechanism and photon fusion ($\gamma\gamma$) [38] are considered

in the presented search with spins 0, $1/2$ and 1. The value of the monopole magnetic moment (k) is zero for spin $1/2$ (the same that we used in the CMS search as described before in chapter 6), and one for spin 1. Production models were generated by MADGRAPH5_aMC@NLO [34] using the Universal Feyn-Rules Output (UFO), that described in [38]. The parton distribution functions (PDF) **NNPDF23** [42] is used for the DY model, and **LUXqed** [126] is used for photon - fusion model, which is the most accurate photon (PDF) up to date. Another modification is considered, which referred to "β-dependent coupling", with modifying photon-monopole coupling, where g is substituted by $\beta\, g$ (as described in chapter 6). Figure 8.10 represents the Feynman-like diagram for both models. Production cross-section of monopoles via $\gamma\gamma$ fusion is significantly enhanced by a factor of $\sim Z^4$ ($\sim Z^2$) for heavy ions collisions [45], where Z is the atomic number of ion.

Two contributions have controlled the acceptance behavior as a function of mass, the mass dependence of the kinematic distributions and the velocity dependence of the energy loss.

The acceptance found to be below 0.1 % over the whole mass range used (200 GeV to 5000 GeV for monopoles with charge of 6 g_D or higher as they cannot be produced with sufficient energy to pass through the material of the trapping volume. Due to this reason, the systematic uncertainties become too large.

The dominant source of systematic uncertainties arises from the amount of the material that estimated in the description of the Geant4 geometry, which results a relative systematic uncertainty of $\sim$ 10% for 1 g_D monopoles [19]. This value of the uncertainty increases when the magnetic charge reaches a point where it is too large for the analysis to be meaningful. The obtained cross-section upper limits at 95 % confidence level (CLs) for the two production models (Drell-Yan and photon-fusion monopole), with the two coupling cases, β-dependent and β-independent. As an example, spin $1/2$ for $g = 1 - 5\ g_D$ with β-dependent model (DY and $\gamma\gamma$ processes) result is shown in figure 8.11 (As an example, to be comparable with CMS experiment, we only add here the results of spin $1/2$. extra results for other spins are indicated in the publication of this search [16])

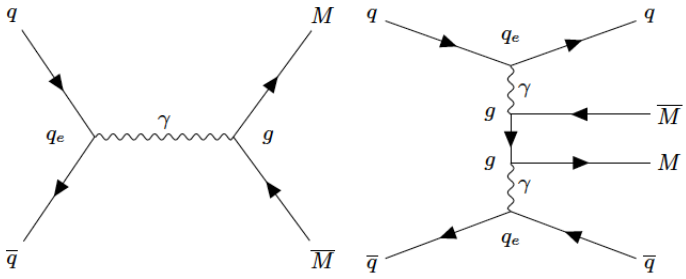


Figure 8.10: Feynman-like diagrams for monopolem - antimonopole production via the Drell-Yan (left) and photon-fusion (right) processes at the LHC.[38].

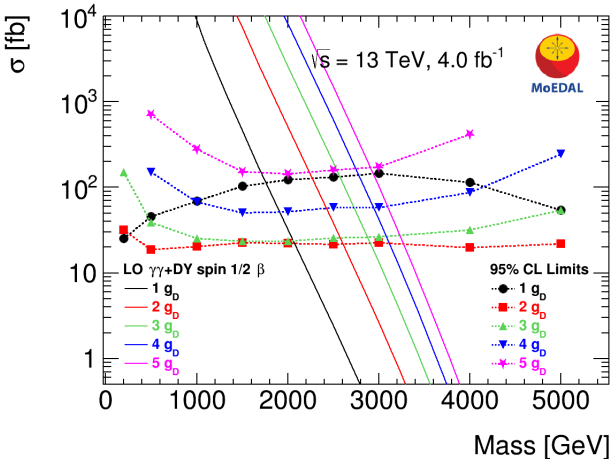


Figure 8.11: Cross-section upper limits at 95 % CLs for the combined DY and γγ monopole pair production model with β-dependent couplings in 13 TeV proton proton collisions as a function of the mass spin $1/2$. The colors correspond to different monopole charges. The solid lines are cross-section calculations at leading order.

As shown in figure 8.11, the cross-sections are represented with solid lines. All mass limits are indicated in table 8.1 for magnetic charges up to 5 g_D. The low acceptance at small mass does not allow MoEDAL to exclude the full range down to the mass limit set at the Tevatron of around 400 GeV for DY models [114], that's why no mass limit is given for the spin 0 and spin $1/2$, 5 g_D monopole with standard point-like coupling. These mass limits are only indicative since they depend on the cross sections computed by using perturbative field theory (because of the high value of the monopole-photon coupling).

Table 8.1: 95% C.L. mass limits in models of spin 0, spin $1/2$ and spin-1 monopole pair direct production in LHC pp collisions. The present results are interpreted for Drell-Yan and combined DY and photon-fusion production with both β-independent and β-dependent couplings.

Process/coupling	Spin	Magnetic charge [g_D]				
		1	2	3	4	5
		95% C.L. mass limits [GeV]				
DY	0	790	1150	1210	1130	–
DY	1/2	1320	1730	1770	1640	–
DY	1	1400	1840	1950	1910	1800
DY β-dep.	0	670	1010	1080	1040	900
DY β-dep.	1/2	1050	1450	1530	1450	–
DY β-dep.	1	1220	1680	1790	1780	1710
DY+γγ	0	2190	2930	3120	3090	–
DY+γγ	1/2	2420	3180	3360	3340	–
DY+γγ	1	2920	3620	3750	3740	–
DY+γγ β-dep.	0	1500	2300	2590	2640	–
DY+γγ β-dep.	1/2	1760	2610	2870	2940	2900
DY+γγ β-dep.	1	2120	3010	3270	3300	3270

In summary, the Aluminum samples of the MoEDAL trapping detector that exposed to 13 TeV LHC collisions were scanned using the SQUID magnetometer to search for the existence of a trapped magnetic charge. No monopole candidates survived the scanning procedures and cross-section upper limits of 11 fb was set. Previous limits of 40 fb also set by MoEDAL in the previous search [18]. We used the Drell - Yan monopole - pair and the photon-fusion direct production mechanisms. Limits for monopole masses in the range $1500-3750\,GeV$ [16] were set for magnetic charges up to $5\,g_D$ of spins 0, $1/2$ and 1, the strongest to date at a collider experiment [175] for charges ranging from two to five times the Dirac charge. For comparison, the DY mass limits set by MoEDAL experiment at 13 TeV was ranged from $450-1790\,GeV$, for previous results [18].

By comparing the sensitivity of CMS and MoEDAL experiments, for spin half monopoles, we observe that the sensitivity is similar, but the MoEDAL experiment can reach monopoles with higher magnetic charges.

CHAPTER 9

CONCLUSION

The quantization of charge is still an open question in fundamental physics. A possible solution to this question would be the existence of Dirac magnetic monopoles. Both in electroweak models [63] and grand unified theories (GUTs) [111] magnetic monopoles can occur, and this has been a strong motivation to conduct experimental searches since many years. To search for magnetic monopoles relatively simple searches techniques can be used, such as via trapping monopoles in terrestrial or extraterrestrial rocks [112, 155, 47] or in data from high energy colliders, as magnetic monopoles have a very unique signature [4, 14, 5].

P. Dirac in 1931, has predicted the existence of magnetic monopole with magnetic charge (g) equal to $n\,g_D$, where g_D is the Dirac charge, which is approximately equivalent to $68.5\,e$, where e is the electric charge. The Dirac charge is several orders larger than the elemntary electric charge. Hence the magnetic monopole coupling (monopole - photon coupling constant) is very large compared to the electric - photon coupling ($\alpha_m \sim 4700\,\alpha_e$).

Recently several experiments at the Large Hadron Collider (LHC) have searched for a magnetic monopoles with a mass range of up to a few TeV. LHC is located $100\,m$ underground between France and Switzerland, at the European Organization for Nuclear Research (CERN).

In this work, I performed a search for a magnetic monopole with the Compact Muon Solenoid experiment (CMS) at the Large hadron Collider (LHC) with proton-proton collisions at a centre of mass energy of $13\,TeV$.

There is no reliable prediction for monopole pair production cross-section, as the coupling imposed by the Dirac quantization condition is so large that perturbative techniques cannot be used to make predictions. The benchmark of the production of magnetic monopoles used in this these and many other studies such as by the ATLAS and the MoEDAL experiment, is based on the Drell-Yan process. We have used the most up to date event generation model for monopoles which has been included in Madgraph general generator recently [161]. Spin $1/2$ monopoles, with β-dependent cross section model was used, and a wide range of monopole mass points were simulated in CMS and examined (500, 700, 1000, 1200, 1500, 1700, 2000, 2500, 2700, $3000\,GeV$).

The main search in this thesis is searching for magnetic monopoles produced in the CMS experiment at the LHC with proton-proton taken at $13\,TeV$ centre of mass-energy. Because the signature of a monopole is very unique when passing through the layers of matter, such as the CMS detector, we had to develop and replace the standard energy loss measurements by a suitable method to be able to track the monopole. In the reconstruction, we used a special track combining algorithm to reconstruct the monopole track and extrapolate it to the nearest crystal of the next layer of the CMS, which is the electromagnetic calorimeter (ECAL). The energy deposits in the tracker and ECAL, were used to identify the monopole candidate and select the signal region: high ionization in the tracker and narrow energy deposition in the calorimeter. We have optimized our selection cuts and studied the relative efficiency for each major cut applied. Also we have calculated the efficiency vs. acceptance for all masses points in this search, used to calculate the cross-section production limit.

We selected a region with low background expectation, which was predicted with the data itself using a double ABCD method. Using the data collected by CMS in 2016 based on a dedicated trigger HLT_Photon175_v., corresponding to an integrated luminosity of $33\,fb^{-1}$, no event was observed in the signal region. In the absence of the observation of a signal in the data collected, we set a 95% confidence level upper limit of (23.9 to 14.7 fb) on the mass cross-section

production and the observed and expected limit are determined for all the mass points simulated (see table 7.20). Systematic uncertainties were determined and included in the limit calculations.

The doctoral candidate was the principle responsible for the whole analysis chain of magnetic monopole search in the CMS detector. The doctoral candidate was the main responsible for the whole analysis chain of the monopole search at the CMS detector through the almost 5 years of studies.

In Chapter 4 of this thesis, I have explained my main contribution during the Ph.D. period, in the service work related to the Resistive Plates chamber (RPC), which is located in the muon system of the CMS experiment. I participated in the data certification process during 2016 till 2018. Chapter 4 contains an overview of the RPCs sub-detector and mainly the performance of the endcap chambers $RE \pm 4$. In 2019, during my stay at CERN for almost 7 months, I participated in the Long Shutdown 2 (LS2) commissioning services (hardware) for $RE \pm 4$ chambers. I have participated on one of the major RPC activity that consists on dismounting of 72 super modules (SM) from the fourth Endcap muon stations RE4 at both ends to allow $RE \pm 4$ maintenance and partner inner ring muon CSC detector extraction ME4/1 for their electronics upgrade. I contributed significantly for 6 months during 2019 to the re-validation studies of $RE4$ in the Muon Static lab in CMS P5. I participated both in hardware work and data analysis. Major tasks I contributed include gas leak connections validation by performing dedicated tests and analysing the results. Also, I have performed noise study to spot any dead/noisy strips and functionality checks of RPC Front End Boards. Also, I participated actively in RE4 currents monitoring and analysis of currents using dedicated tools, to validate the SMs for reinstallation.

Finally, we have given an overview of one of the recent experiments of the LHC, a dedicated experiment to search for magnetic monopoles, located at the IP8 in the intersection point of the LHCb experiment, which is a Magnetic Monopole Trapping system detector (MoEDAL). One of the important aims of LHC experiments, especially, ATLAS and CMS, was to discover the last piece of the SM particle contents, the Higgs boson and to have a precise study of its properties. Similarly, the main goal of the MoEDAL experiment is to search for the Magnetic Monopole. Drell-Yan and photon fusion predictions

have been used as production mechanisms for monopoles with spin 0, $1/2$ and 1 with β-dependent models, for various ranges of g_D charges.

The main contribution of the doctoral candidate was performing the material analysis with a "SQUID", for the Magnetic Monopole Trapper sub-detector samples during 2018. The Magnetic Monopole Trapper is one of the main parts of the MoEDAL experiment. The "SQUID" is located in a magnetically shielded room at the Laboratory of Natural Magnetism at Zurich. The results of analyzing these samples are reported in chapter 8 [16].

By comparing the sensitivity of CMS and MoEDAL experiments, we observed that the sensitivities are similar, but the MoEDAL experiment can reach monopoles with higher magnetic charges. By comparing The observed *CLs* upper limit on the cross-section for DY spin $1/2$ process with charge $g = 1.0\,g_D$, between ATLAS and CMS for run II, we observed that our results sensitivities (CMS) is $4-5$ times less sensitive than the recent ATLAS results [3]. In order to improve our results in the future, we need more dedicated triggers for monopoles and a dedicated spike study using the topology of the spikes and potentially the timing to be used at the trigger level in future studies.

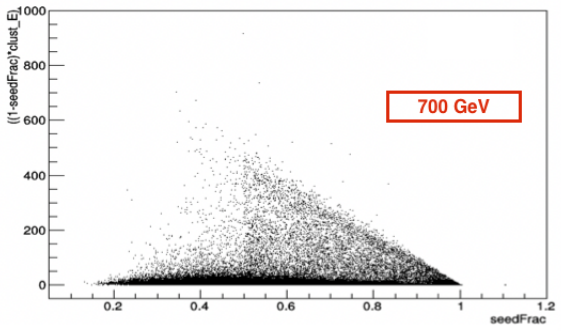
APPENDIX A

APPENDIX TITLE

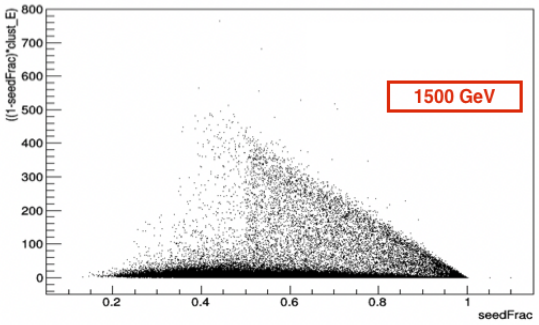
A.1 ECAL Noise

In order to estimate the impact of noise on the topological cluster shape, the amount of energy found outside of the central 5×1, $\eta - \phi$ strip versus the fraction of energy in the central strip is plotted for various minimal cuts on the cluster energy for masses 700 and 1500 GeV. The majority of ECAL clusters have a value of f_{51} nearly one. Nevertheless, when a minimal energy cut is applied, a lower bounding edge appears in the distributions representing the constraint at which noise must be present outside of the central strip to shift the measured effect f_{51}.

Figure A.1 shows these distributions for three mass points spanning the range considered with no energy cut applied. Figure A.2 shows these same distributions with 100 GeV energy cut applied to the clusters, and Figure A.3 shows these distributions and mass points after 175 GeV energy cut is applied to the cluster energy.

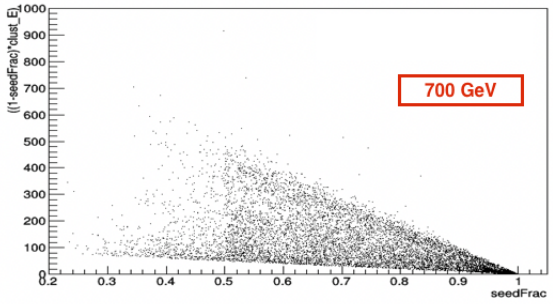


(a) 700 GeV

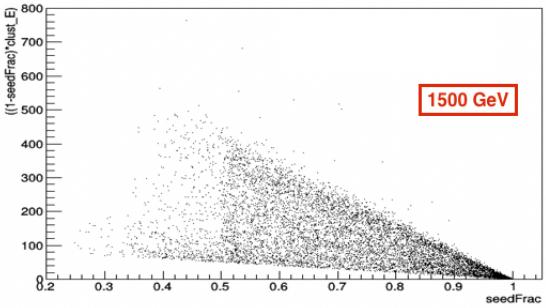


(b) 1500 GeV

Figure A.1: The energy found outside of the central strip vs. the fraction of energy found in the cluster for two monopole masses 700 and 1500 GeV respectively.

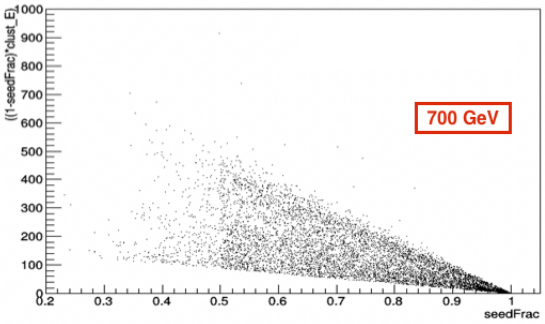


(a) 700 GeV

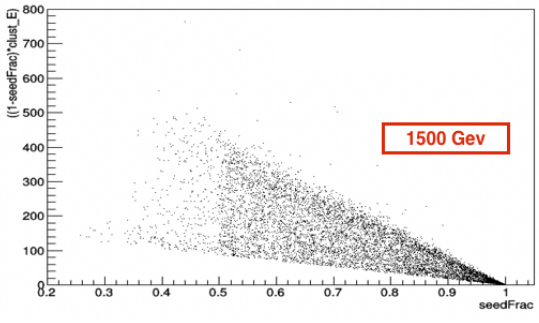


(b) 1500 GeV

Figure A.2: The energy found outside of the central strip vs. the fraction of energy found in the cluster after a 100 GeV energy cut for two monopole masses 700 and 1500 GeV respectively.



(a) 700 GeV

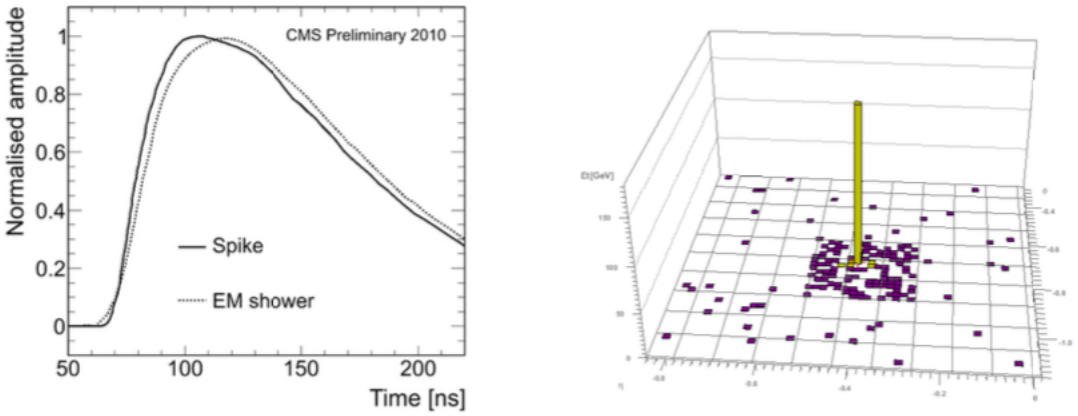


(b) 1500 GeV

Figure A.3: The energy found outside of the central strip vs. the fraction of energy found in the cluster after a 175 GeV energy cut for two monopole masses 700 and 1500 GeV respectively.

A.2 Spikes and Online Selection

Spikes are anomalous signals, a hadron hits the ECAL Barrel (EB) photo-detector APD and induce a big signal in a single channel that does not correspond to a particle passing through the crystal, hence this is a ”fake” signal. They happen in a single crystal; an electron deposits 80 % of its energy in a square of 3×3 crystals, hence topological variables can be used to discriminate spikes from electrons



(a) (b)

Figure A.4: illustration of spike shape and timing in the ECAL barrel

These hadrons are *secondary* particles, caused by a primary particle interacting with the box containing the photo-detectors, are delayed with respect to the bunch crossing, hence the time measurement can be to distinguish between spike and real particle. The characteristic of these anomalously large energy deposits, which exist in only one single crystal, is the following:

- The shape of the pulse occurred with direct ionization with the APD, is faster in time than the normal particle pulse, see figure A.4 (a).
- They have little surrounding activities (unlike electromagnetic EM shape) see figure A.4 (b).

A.2.1 Spike Mitigation Methods

Methods to mitigate the spikes are either by using topology, isolated energy deposits, or timing, differences in pulse shape

- Strip Fine-Grain Veto Bit (sFGVB), is a topological method used at L1, Semi-flexible hardware (it has the full flexibility of HLT and offline)

  Description of this method:

  The online selection (L1) employs a filter in the ECAL designed to reject anomalous "spike" clusters from forming a trigger [139]. The selection considers the number of cells in a 1×5 strip (orthogonal to the strip considered in the f_{51} variable) above $350 MeV$ for clusters with more than $12 GeV$ of total energy. If the number of cells in the 1×5 strip is more than one, then the bit for that strip is set to 1. The 5 bits, corresponding to the 5 strips in ϕ, are ORed together to form the decision. If the value is 1 the trigger tower is accepted, or if the value is 0, the trigger tower is rejected as a spike. A diagram taken from [139] is shown here in figure A.5.

  The uncertainty in the efficiency due to this spike filtering (at L1) is determined by the uncertainty in the modeling of the shower shape of energy deposits left by monopoles in the ECAL. In other words, the systematic uncertainty of the spike killing filter is considered to be uncertainty on the shower shape of the monopole energy deposits in the ECAL. It is shown in Figure 7.19 that the topological cluster shape variable f_{51} is not too sensitive to the GEANT4 simulation parameters. The variance in the number of clusters in the peak bin varies by $0.2 - 5\,\%$.

  The sFGVB has been measured to reject $> 95\,\%$ of spikes with transverse energy greater than $8 GeV$, with only a small ($< 2\,\%$) effect on the efficiency for triggering real electrons.

- HLT and offline reconstruction, at HLT and offline reconstruction, we use software tools, with full flexibility, and implement two variables **the**

Swiss-Cross: energy in a central crystal divided by energy of the 4 adjacent crystals, and **the "RecHit" timing**, the delay between the bunch crossing and the measurement of the signal peak (the signal itself has a pulse shape, with a peak at some point and a long tail)

In MC, spike cleaning is as follows, at HLT we use an "offline-like" spike cleaning, that filters the PF RecHits, so spike cleaning is applied by default when running the HLT.

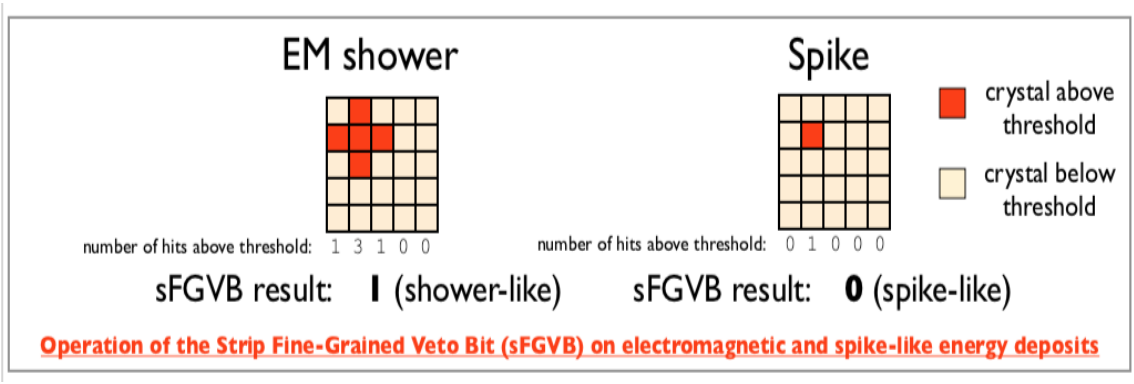


Figure A.5: A useful diagram showing the implementation of online spike filtering

As the magnetic monopole loses most of its energy in the first crystal it hits in the Ecal, most of the generated monopole has a swiss-cross value close to 1. This is one of the unique features of monopoles and we also can use this as a signature of monopoles. The definition of swiss-cross is:

$$Swiss-cross = 1 - \frac{E_4}{E_1}$$

Where E_1 is the energy deposited in the center cell and E_4 is the sum of energy deposited in the other four cells

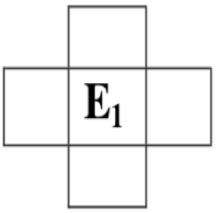
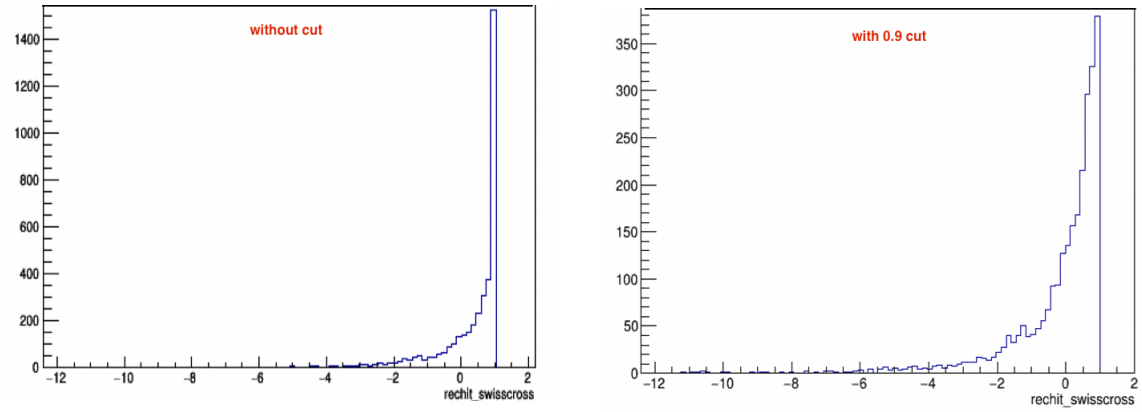


Figure A.6: Swiss-cross definition



(a) (b)

Figure A.7: Swiss cross distribution for monopole mass 1000 *GeV* before and after the cut of 0.95

In order to distinguish between monopole and spike caused by other particles, the swiss-cross variable has to be less than 0.95 and the arrival time to the Ecal to be less than 10 *ns*. We have plotted the swiss-cross for monopole mass 1000 *GeV* before and after the cut of 0.95, and it indicates that we lose most of our signal due to the existence of ”Spike”.

A.2.1.1 Implementation Monopole model in MADGRAPH5_aMC@NLO

For such relativistic fast monopoles with relative velocity $\beta = 1$, passing through materials, a large number of electron-positron pairs are produced which can be used as a sign for the monopole's presence [38]. The study of slowly moving

monopoles with $\beta << 1$, will be excluded from the present work. We are only interested here in the electromagnetic interactions of monopole of spin $S = 1/2$.

First, we need to recall some basic facts of the point-like monopole-matter scattering theory. Modern quantum field theory treatment has been used to study the classical, tree-level scattering of charged particles of massively magnetic monopoles, monopoles are relatively heavy compared to electrons with masses of TeV order.

The differential cross section for the classical scattering of electrons is described as:

$$\sigma\omega = (\frac{eg}{2\mu\nu_0 c})^2 \sum_x \frac{1}{4\sin^4(\frac{x}{2})} \left| \frac{\sin x}{\sin\theta} X\theta \right| \tag{A.1}$$

Which e, m are the charge and the mass of the electron respectively, g and M are the magnetic charge and mass in a frame where the initial velocity of the electron is ν_0 and the monopole is initially at rest. C is denoted the speed of light in vacuum and θ is the angle of scattering, μ is the reduced mass of the two body problem $mM/m+M$, in the cases of monopoles, $\mu = m$ where $M >> m$ which is of interest here. The angle $x = 2\mu\nu_o b/ \mid k \mid$, defines the cone on which the trajectory of the electron in the background of the monopole is confined, b is the impact parameter [130, 38].

For completeness, we note that the cross section diverges in two occasions:

- $\sin\theta = 0$ and $\sin x \neq= 0$, $\theta = \pi$, which is the case for a certain discrete set of cone angles.
- When $\theta X = 0$, which occurs for a certain discrete set of scattering angles θ [130, 38].

For small scattering angles, $\theta << 1$, the differential cross section can be approximated by:

$$\sigma\omega = (\frac{eg}{2\mu v_0 c})^2 \frac{1}{(\theta/2)^4}, \qquad \theta << 1 \tag{A.2}$$

A new phenomenological parameter is included in the used model to produce monopole events, which is **the magnetic-moment term** k, which is equal to 0 for spin $1/2$, and 1 for spin 1 monopoles. The existence of this parameter with the velocity – dependent coupling, may lead to a perturbative treatment of the calculations of the cross section [171]. The model used in this search to generate monopole events is the Drell-Yan production model with spin $1/2$ and velocity-dependent magnetic charge.

An appropriate implementation of the Drell-Yan process in Madgraph UFO models has been taken to serve as a useful tool to introduce monopole searches at colliders such as LHC.

A.2.1.2 Velocity–dependent magnetic charge

Last expression reduces to the standard Rutherford formula for $e\,e$ scattering upon the replacement:

$$\frac{g}{c} \rightarrow \frac{e}{v_0} \tag{A.3}$$

This assumption allows many authors including Milton [114], Schwinger [99] and collaborators to conjecture that when discussing the propagation of monopoles in matter that used for detection and capturing the monopole (interaction of monopoles with matters, electrons or quarks) or considering monopole–antimonopo pair production through Drell-Yan process, the velocity-dependent magnetic charge for monopole has to be considered in the cross-section formula

$$g \rightarrow \frac{gv}{c} = g\beta \tag{A.4}$$

And it has to be stressed that the above substitution is based on the elec-

tric–magnetic duality's assumption, which may lead to the equivalence of the electron-monopole scattering cross section (equation A.1) with Rutherford formula upon applying (equation A.4)

The monopole velocity β is used in the Drell-Yan model is given by Lorentz invariant expression in terms of the monopole mass M and the square of the center of mass-energy of the incoming particles (Photon or anti quarks), $\sqrt{s} = 2E\gamma/q$

$$\beta = \sqrt{1 - \frac{4M^2}{s}} \tag{A.5}$$

In Dirac's model, the relation between the basic magnetic charge g and the electric charge ($q\,e$) is given in the below equation with Gaussian units. However in Madgraph, Heaviside-Lorentz units are used.

$$g = \frac{1}{2\alpha} n(\frac{e}{q_e})e = 68.5e(\frac{e}{q_e})n \equiv n\frac{e}{q_e}g_D, \quad n \in \mathbb{Z} \tag{A.6}$$

Madgraph model equation:

$$q_e g = 2\pi n, \quad n \in \mathbb{Z} \tag{A.7}$$

So the unit of the magnetic charge is:

$$g_D = 2\pi/q_e \tag{A.8}$$

"There are no accurate theoretical calculations of the monopole production cross-section". Only Leading Order models can be used for the Feynman diagram. For Feynman diagram calculations, we use the perturbative approach, I.e. we have many terms in the cross-section calculations.

1. Leading Order to tree level
2. Next to leading order of first-order loop diagram to next to Leading order

or second-order loop diagram and so on.

For processes where the effective coupling is less than 1 , the terms in b and c are less than terms in a. For monopoles, the coupling is $68.5 \gg 1$ so terms b and c will be larger than terms in a, this is the reason why perturbative calculations are not possible. Here we only calculate the tree-level diagram and ignore higher order terms. We ignore them not because they are smaller in value than *LO* terms but because we don't know how to handle higher order terms.

It is reasonable to assume that a proper field theory treatment of monopole pair production would reproduce the Drell-Yan electron production with the duality transformation applied.

BIBLIOGRAPHY

[1] "https://www.physik.uzh.ch/groups/serra/StandardModel.html".

[2] Georges Aad et al. "Observation of a new particle in the search for the Standard Model Higgs boson with the ATLAS detector at the LHC". In: *Phys. Lett. B* 716.1 (2012), pp. 1–29.

[3] Georges Aad et al. *Search for magnetic monopoles and stable high-electric-charge objects in 13 TeV proton-proton collisions with the ATLAS detector*. Tech. rep. ATLAS-EXOT-2017-20-003, 2019.

[4] Georges Aad et al. "Search for magnetic monopoles and stable particles with high electric charges in 8 TeV p p collisions with the ATLAS detector". In: *Physical Review D* 93.5 (2016), p. 052009.

[5] Georges Aad et al. "Search for Magnetic Monopoles in s= 7 TeV p p Collisions with the ATLAS Detector". In: *Physical review letters* 109.26 (2012), p. 261803.

[6] Georges Aad et al. "The ATLAS experiment at the CERN large hadron collider". In: *Jinst* 3 (2008), S08003.

[7] Kenneth Aamodt et al. "The ALICE experiment at the CERN LHC". In: *Journal of Instrumentation* 3.08 (2008), S08002.

[8] R Abbasi et al. “Search for relativistic magnetic monopoles with the AMANDA-II neutrino telescope”. In: *The European Physical Journal C* 69.3-4 (2010), pp. 361–378.

[9] B Abbott et al. “Search for heavy pointlike Dirac monopoles”. In: *Physical review letters* 81.3 (1998), p. 524.

[10] M Abbrescia et al. “Properties of C2H2F4-based gas mixture for avalanche mode operation of Resistive Plate Chambers”. In: *Nuclear Instruments and Methods in Physics Research Section A: Accelerators, Spectrometers, Detectors and Associated Equipment* 398.2-3 (1997), pp. 173–179.

[11] M Abbrescia et al. “Study of long-term performance of CMS RPC under irradiation at the CERN GIF”. In: *Nuclear Instruments and Methods in Physics Research Section A: Accelerators, Spectrometers, Detectors and Associated Equipment* 533.1-2 (2004), pp. 102–106.

[12] M Abbrescia et al. “The simulation of resistive plate chambers in avalanche mode: charge spectra and efficiency”. In: *Nuclear Instruments and Methods in Physics Research Section A: Accelerators, Spectrometers, Detectors and Associated Equipment* 431.3 (1999), pp. 413–427.

[13] Marcello Abbrescia et al. *Effect of the linseed oil treatment on the performance of the resistive plate counters*. Tech. rep. 1997.

[14] A Abulencia et al. “Direct search for Dirac magnetic monopoles in p p collisions at s= 1.96 TeV”. In: *Physical review letters* 96.20 (2006), p. 201801.

[15] Maurizio Acciarri et al. “Search for anomalous Z$\rightarrow \gamma\gamma\gamma$ events at LEP”. In: *Physics Letters B* 345.4 (1995), pp. 609–616.

[16] B Acharya et al. “Magnetic monopole search with the full MoEDAL trapping detector in 13 TeV *pp* collisions interpreted in photon-fusion and Drell-Yan production”. In: *arXiv preprint arXiv:1903.08491* (2019).

[17] B Acharya et al. “Search for magnetic monopoles with the MoEDAL forward trapping detector in 13 TeV proton-proton collisions at the LHC”. In: *Physical review letters* 118.6 (2017), p. 061801.

[18] B Acharya et al. “Search for magnetic monopoles with the MoEDAL forward trapping detector in 2.11 fb-1 of 13 TeV proton–proton collisions at the LHC”. In: *Physics Letters B* 782 (2018), pp. 510–516.

[19] B Acharya et al. “Search for magnetic monopoles with the MoEDAL prototype trapping detector in 8 TeV proton-proton collisions at the LHC”. In: *Journal of High Energy Physics* 2016.8 (2016), p. 67.

[20] Bobby Acharya et al. “The physics programme of the MoEDAL experiment at the LHC”. In: *International Journal of Modern Physics A* 29.23 (2014), p. 1430050.

[21] G Acquistapace et al. *CMS, the magnet project: Technical design report*. Tech. rep. 1997.

[22] Sea Agostinelli et al. “GEANT4—a simulation toolkit”. In: *Nuclear instruments and methods in physics research section A: Accelerators, Spectrometers, Detectors and Associated Equipment* 506.3 (2003), pp. 250–303.

[23] Yakir Aharonov and David Bohm. “Significance of electromagnetic potentials in the quantum theory”. In: *Physical Review* 115.3 (1959), p. 485.

[24] SP Ahlen. “Monopole-track characteristics in plastic detectors”. In: *Physical Review D* 14.11 (1976), p. 2935.

[25] SP Ahlen. “Stopping-power formula for magnetic monopoles”. In: *Physical Review D* 17.1 (1978), p. 229.

[26] SP Ahlen and K Kinoshita. “Calculation of the stopping power of very-low-velocity magnetic monopoles”. In: *Physical Review D* 26.9 (1982), p. 2347.

[27] Steven P Ahlen. “Theoretical and experimental aspects of the energy loss of relativistic heavily ionizing particles”. In: *Reviews of Modern Physics* 52.1 (1980), p. 121.

[28] G Aielli et al. “Fluoride production in RPCs operated with F-compound gases”. In: *Nuclear Physics B-Proceedings Supplements* 158 (2006), pp. 143–148.

[29] J Allision et al. “Geant4 developments and applications. IEEE T”. In: *Nucl. Sci* 53.1 (2006), pp. 270–278.

[30] J Allison et al. “Recent developments in Geant4”. In: *Nuclear Instruments and Methods in Physics Research Section A: Accelerators, Spectrometers, Detectors and Associated Equipment* 835 (2016), pp. 186–225.

[31] John Allison et al. “Geant4 developments and applications”. In: *IEEE Transactions on nuclear science* 53.1 (2006), pp. 270–278.

[32] A Augusto Alves Jr et al. “The LHCb detector at the LHC”. In: *Journal of instrumentation* 3.08 (2008), S08005.

[33] Johan Alwall et al. “New Developments in MadGraph/MadEvent”. In: *AIP Conference Proceedings*. Vol. 1078. 1. AIP. 2008, pp. 84–89.

[34] Johan Alwall et al. “The automated computation of tree-level and next-to-leading order differential cross sections, and their matching to parton shower simulations”. In: *Journal of High Energy Physics* 2014.7 (2014), p. 79.

[35] Edoardo Amaldi et al. “Search for Dirac magnetic poles”. In: *Il Nuovo Cimento (1955-1965)* 28.4 (1963), pp. 773–793.

[36] Ugo Amaldi, Wim de Boer, and Hermann Fürstenau. “Comparison of grand unified theories with electroweak and strong coupling constants measured at LEP”. In: *Physics Letters B* 260.3-4 (1991), pp. 447–455.

[37] Pair Annihilation. “Deep Inelastic ep Scattering in Perturbation Theory”. In: *Sov. J. Nucl. Phys* 15 (1972), p. 675.

[38] S Baines et al. “Monopole production via photon fusion and Drell–Yan processes: MadGraph implementation and perturbativity via velocity-dependent coupling and magnetic moment as novel features”. In: *The European Physical Journal C* 78.11 (2018), p. 966.

[39] S Balestra et al. “Magnetic monopole bibliography-II”. In: *arXiv preprint arXiv:1105.5587* (2011).

[40] S Balestra et al. “Magnetic monopole search at high altitude with the SLIM experiment”. In: *The European Physical Journal C* 55.1 (2008), pp. 57–63.

[41] Richard D Ball et al. “Parton distributions for the LHC Run II”. In: *Journal of High Energy Physics* 2015.4 (2015), p. 40.

[42] Richard D Ball et al. “Parton distributions with LHC data”. In: *Nuclear Physics B* 867.2 (2013), pp. 244–289.

[43] Manuel Barriola, Tanmay Vachaspati, and Martin Bucher. “Embedded defects”. In: *Physical Review D* 50.4 (1994), p. 2819.

[44] G Bauer et al. “Simulating magnetic monopoles by extending GEANT”. In: *Nuclear Instruments and Methods in Physics Research Section A: Accelerators, Spectrometers, Detectors and Associated Equipment* 545.1-2 (2005), pp. 503–515.

[45] Gerhard Baur et al. “Coherent γ γ and γA interactions in very peripheral collisions at relativistic ion colliders”. In: *Physics Reports* 364.5 (2002), pp. 359–450.

[46] GL Bayatian et al. *CMS Physics: Technical Design Report Volume 1: Detector Performance and Software*. Tech. rep. CMS-TDR-008-1, 2006.

[47] Katarina Bendtz et al. “Search for magnetic monopoles in polar volcanic rocks”. In: *Physical review letters* 110.12 (2013), p. 121803.

[48] Michael Benedikt and Frank Zimmermann. “Proton colliders at the energy frontier”. In: *Nuclear Instruments and Methods in Physics Research Section A: Accelerators, Spectrometers, Detectors and Associated Equipment* 907 (2018), pp. 200–208.

[49] S Carpinteyro Bernardino et al. “Quality Certification 4 (QC4) for RE4 in the Upgrade in CMS”. In: *Journal of Physics: Conference Series*. Vol. 651. 1. IOP Publishing. 2015, p. 012005.

[50] W Bialas and DA Petyt. “Mitigation of anomalous APD signals in the CMS ECAL”. In: *Journal of Instrumentation* 8.03 (2013), p. C03020.

[51] John Betteley Birks. “Scintillations from organic crystals: specific fluorescence and relative response to different radiations”. In: *Proceedings of the Physical Society. Section A* 64.10 (1951), p. 874.

[52] Bruno Borgi et al. “The CMS electromagnetic calorimeter project: Technical design report”. In: *Technical Design Report CMS. CERN, Geneva* (1997).

[53] W Braunschweig et al. “A search for particles with magnetic charge produced ine+ e- annihilations at 543-1543-1543-1GeV”. In: *Zeitschrift für Physik C Particles and Fields* 38.4 (1988), pp. 543–550.

[54] Robert Brown, Paul Lecoq, and Hans Rykaczewski. *Changes to CMS ECAL electronics: addendum to the Technical Design Report*. Tech. rep. CMS-TDR-004-add-1, 2002.

[55] Blas Cabrera. “First results from a superconductive detector for moving magnetic monopoles”. In: *Physical Review Letters* 48.20 (1982), p. 1378.

[56] Matteo Cacciari, Gavin P Salam, and Gregory Soyez. “The anti-kt jet clustering algorithm”. In: *Journal of High Energy Physics* 2008.04 (2008), p. 063.

[57] P Camarri et al. “Streamer suppression with SF6 in RPCs operated in avalanche mode”. In: *Nuclear Instruments and Methods in Physics Research Section A: Accelerators, Spectrometers, Detectors and Associated Equipment* 414.2-3 (1998), pp. 317–324.

[58] R Cardarelli, A Di Ciaccio, and R Santonico. “Performance of a resistive plate chamber operating with pure CF3Br”. In: *Nuclear Instruments and Methods in Physics Research Section A: Accelerators, Spectrometers, Detectors and Associated Equipment* 333.2-3 (1993), pp. 399–403.

[59] Brian G Cartwright, EK Shirk, and PB Price. “A nuclear-track-recording polymer of unique sensitivity and resolution”. In: *Nuclear Instruments and Methods* 153.2-3 (1978), pp. 457–460.

[60] S Cecchini et al. “Energy Losses of Magnetic Monopoles in Aluminum, Iron and Copper”. In: *arXiv preprint arXiv:1606.01220* (2016).

[61] ATLAS collaboration atlas. publications@ cern. ch et al. “Measurements of the Higgs boson production and decay rates and constraints on its couplings from a combined ATLAS and CMS analysis of the LHC pp collision data at center of mass energy 7 and 8 TeV”. In: *Journal of High Energy Physics* 2016 (2016), pp. 1–113.

[62] S Chatrchyan et al. “The CMS experiment at the CERN LHC Journal of Instrumentation 3”. In: *S08004* (2008).

[63] YM Cho and D Maison. “Monopole configuration in Weinberg-Salam model”. In: *Physics Letters B* 391.3-4 (1997), pp. 360–365.

[64] CMS Collaboration et al. *Characterization and treatment of anomalous signals in the CMS Electromagnetic Calorimeter, 2011*. Tech. rep. CMS-AN-10-357.

[65] CMS Collaboration et al. “Muon Identification performance: hadron mis-Id measurements and RPC Muon selections”. In: *CMS Detector Performance Summary CMS-DP-2014-018* (2014).

[66] CMS Collaboration et al. “Observation of a new boson at a mass of 125 GeV with the CMS experiment at the LHC Phys. Lett. B 716 (2012) 30”. In: *arXiv preprint arXiv:1207.7235* ().

[67] CMS Collaboration et al. *The CMS experiment at the CERN LHC (Journal of Instrumentation 3 S08004, 2008) p. 158*.

[68] CMS Collaboration. “The CMS muon project: technical design report”. In: *Preprint* (1997), pp. 97–32.

[69] CMS Collaboration et al. *The CMS trigger system. JINST 12, P01020 (2017)*.

[70] CMS Collaboration et al. *The TriDAS Project Technical Design Report, vol. I: The Trigger Systems, CMS TDR CERN/LHCC 2000-038, CERN, 2000*.

[71] CMS collaboration et al. “CMS physics technical design report, volume II: physics performance”. In: *Journal of Physics G: Nuclear and Particle Physics* 34.6 (2007), p. 995.

[72] CMS collaboration et al. “CMS: The hadron calorimeter technical design report”. In: *CERN/LHCC* (1997), pp. 97–31.

[73] CMS collaboration et al. “Data Acquisition and High-Level Trigger Technical Design Report”. In: *CERN/LHCC* 26 (2002), p. 2002.

[74] CMS collaboration et al. “Description and performance of track and primary-vertex reconstruction with the CMS tracker”. In: *Journal of Instrumentation* 9.10 (2014), P10009.

[75] CMS collaboration et al. “Measurement of the differential cross section for isolated prompt photon production in pp collisions at 7 TeV”. In: *arXiv preprint arXiv:1108.2044* (2011).

[76] CMS collaboration et al. *The Muon Project, CMS Technical Design Report, CERN/LHCC 97-32*. Tech. rep. CMS-TDR-003, 1977.

[77] CMS collaboration et al. “The performance of the CMS muon detector in proton-proton collisions at s= 7 TeV at the LHC”. In: *Journal of Instrumentation* 8.11 (2013), P11002.

[78] CMS collaboration, CMS Collaboration, et al. *Particle-flow event reconstruction in CMS and performance for jets, taus and MET*. Tech. rep. CMS-PAS-PFT-09-001, 2009.

[79] H1 Collaboration et al. "A direct search for stable magnetic monopoles produced in positron-proton collisions at HERA". In: *The European Physical Journal C-Particles and Fields* 41.2 (2005), pp. 133–141.

[80] MoEDAL Collaboration et al. "Technical design report of the MoEDAL experiment". In: *CERN Preprint, CERN-LHC-2009-006, MoEDAL-TDR-1.1* (2009).

[81] OPAL collaboration et al. "Search for Charged Excited Leptons in e+ e- Collisions at sqrt (s)= 183-209 GeV". In: *arXiv preprint hep-ex/0206061* (2002).

[82] Silvia Costantini et al. "Radiation background with the CMS RPCs at the LHC". In: *Journal of Instrumentation* 10.05 (2015), p. C05031.

[83] Ian Crotty et al. "The non-spark mode and high rate operation of resistive parallel plate chambers". In: *Nuclear Instruments and Methods in Physics Research Section A: Accelerators, Spectrometers, Detectors and Associated Equipment* 337.2-3 (1994), pp. 370–381.

[84] N Dash, VM Datar, and G Majumder. "Sensitivity of the INO-ICAL detector to magnetic monopoles". In: *Astroparticle Physics* 70 (2015), pp. 33–38.

[85] A De Roeck et al. "Development of a magnetometer-based search strategy for stopped monopoles at the Large Hadron Collider". In: *The European Physical Journal C* 72.12 (2012), p. 2212.

[86] A De Roeck et al. "Sensitivity of LHC experiments to exotic highly ionising particles". In: *The European Physical Journal C* 72.4 (2012), p. 1985.

[87] Alvaro De Rújula. "Effects of virtual monopoles". In: *Nuclear Physics B* 435.1-2 (1995), pp. 257–276.

[88] Paul Adrien Maurice Dirac. "Quantised singularities in the electromagnetic field". In: *Proceedings of the Royal Society of London. Series A, Containing Papers of a Mathematical and Physical Character* 133.821 (1931), pp. 60–72.

[89] Paul Adrien Maurice Dirac. “The theory of magnetic poles”. In: *Physical Review* 74.7 (1948), p. 817.

[90] Yuri L Dokshitzer. “Calculation of the structure functions for deep inelastic scattering and e+ e- annihilation by perturbation theory in quantum chromodynamics”. In: *Zh. Eksp. Teor. Fiz* 73 (1977), p. 1216.

[91] A Dominguez et al. *CMS technical design report for the pixel detector upgrade*. Tech. rep. Fermi National Accelerator Lab.(FNAL), Batavia, IL (United States), 2012.

[92] Vasily Dzhordzhadze et al. “Accelerator Based Magnetic Monopole Search Experiments”. In: ().

[93] John Ellis, Nick E Mavromatos, and Tevong You. “The price of an electroweak monopole”. In: *Physics Letters B* 756 (2016), pp. 29–35.

[94] François Englert and Robert Brout. “Broken symmetry and the mass of gauge vector mesons”. In: *Physical Review Letters* 13.9 (1964), p. 321.

[95] M Fairbairn et al. “Stable massive particles at colliders”. In: *Physics Reports* 438.1 (2007), pp. 1–63.

[96] Mary-Cruz Fouz, CMS Collaboration, et al. “The CMS muon system”. In: *Nuclear Instruments and Methods in Physics Research Section A: Accelerators, Spectrometers, Detectors and Associated Equipment* 446.1-2 (2000), pp. 366–372.

[97] Pauline Gagnon. “The Standard Model: a beautiful but flawed theory”. In: *Quantum Diaries [cited 20171211] Available from: https://www.quantumdiaries. org/2014/03/14/the-standard-model-a-beautiful-but-flawed-theory* (2015).

[98] T Gentile et al. “Search for magnetically charged particles produced in e+ e- annihilations at s= 10.6 GeV”. In: *Physical Review D* 35.3 (1987), p. 1081.

[99] IF Ginzburg and SL Panfil. *The possibility of observation of heavy Dirac-Schwinger magnetic pole*. Tech. rep. 1982.

[100] Sheldon L Glashow. “The renormalizability of vector meson interactions”. In: *Nuclear Physics* 10 (1959), pp. 107–117.

[101] LHC Computing Grid. *Technical Design Report, ed. J. Knobloch*. Tech. rep. CERN-LHCC-2005-024, LCG-TDR-001, 2005.

[102] David Griffiths. *Introduction to elementary particles*. John Wiley & Sons, 2008.

[103] David J Gross and Frank Wilczek. "Ultraviolet behavior of non-abelian gauge theories". In: *Physical Review Letters* 30.26 (1973), p. 1343.

[104] Particle Data Group et al. "The Review of Particle Physics-Passage of particles through matter". In: *Chin. Phys. C* 38 (2014), p. 090001.

[105] Gerald S Guralnik, Carl R Hagen, and Thomas WB Kibble. "Global conservation laws and massless particles". In: *Physical Review Letters* 13.20 (1964), p. 585.

[106] Francis Halzen, Alan D Martin, and Nilotpal Mitra. "Quarks and leptons: An introductory course in modern particle physics". In: *American Journal of Physics* 53 (1985), pp. 287–287.

[107] Michel Herquet et al. "MadGraph 5: Going Beyond". In: *JHEP* 1106 (2011), p. 128.

[108] Peter W Higgs. "Broken symmetries and the masses of gauge bosons". In: *Physical Review Letters* 13.16 (1964), p. 508.

[109] *Higgs combine tools official website*. "https://github.com/cms-analysis/HiggsAnalysis-CombinedLimit/wiki".

[110] Stefan Höche. "Introduction to parton-shower event generators". In: *Journeys Through the Precision Frontier: Amplitudes for Colliders: TASI 2014 Proceedings of the 2014 Theoretical Advanced Study Institute in Elementary Particle Physics*. World Scientific, 2016, pp. 235–295.

[111] Gerardus t Hooft. "Magnetic monopoles in unified theories". In: *Nucl. Phys. B* 79.CERN-TH-1876 (1974), pp. 276–284.

[112] Hunmoo Jeon and Michael J Longo. "Search for magnetic monopoles trapped in matter". In: *Physical review letters* 75.8 (1995), p. 1443.

[113] M Dam Joergensen et al. "Searching for magnetic monopoles trapped in accelerator material at the Large Hadron Collider". In: *arXiv preprint arXiv:1206.6793* (2012).

[114] GR Kalbfleisch et al. "Limits on production of magnetic monopoles utilizing samples from the D0 and CDF detectors at the Fermilab Tevatron". In: *Physical Review D* 69.5 (2004), p. 052002.

[115] V Karimäki. *The CMS tracker system project: Technical Design Report*. Tech. rep. 1997.

[116] Yoichi Kazama, Chen Ning Yang, and Alfred S Goldhaber. "Scattering of a Dirac particle with charge Z e by a fixed magnetic monopole". In: *Physical Review D* 15.8 (1977), p. 2287.

[117] Thomas W Kephart and Thomas J Weiler. "Magnetic monopoles as the highest energy cosmic ray primaries". In: *Astroparticle Physics* 4.3 (1996), pp. 271–279.

[118] Kyoungtae Kimm et al. "Mass of the electroweak monopole". In: *Modern Physics Letters A* 31.09 (2016), p. 1650053.

[119] K Kinoshita et al. "Search for highly ionizing particles in e+ e- annihilations at s= 91.1 GeV". In: *Physical Review D* 46.3 (1992), R881.

[120] Kenichi Konishi. "The magnetic monopoles seventy-five years later". In: *String Theory and Fundamental Interactions*. Springer, 2007, pp. 471–521.

[121] Alexander Kusenko and Mikhail Shaposhnikov. "Supersymmetric Q-balls as dark matter". In: *Physics Letters B* 418.1-2 (1998), pp. 46–54.

[122] Paul Langacker. "Introduction to the Standard Model and Electroweak Physics". In: *arXiv preprint arXiv:0901.0241* (2009).

[123] Changguo Lu. "RPC electrode material study". In: *Nuclear Instruments and Methods in Physics Research Section A: Accelerators, Spectrometers, Detectors and Associated Equipment* 602.3 (2009), pp. 761–765.

[124] Rong-Shyang Lu, Cms Collaboration, et al. "Performance, calibration and alignment of the CMS preshower detector". In: *Nuclear Physics B-Proceedings Supplements* 215.1 (2011), pp. 119–121.

[125] Luciano Maiani. "The large hadron collider project". In: *Fusion engineering and design* 46.2-4 (1999), pp. 433–447.

[126] Aneesh Manohar et al. "How bright is the proton? A precise determination of the photon parton distribution function". In: *Physical review letters* 117.24 (2016), p. 242002.

[127] Alan D Martin et al. "Parton distributions for the LHC". In: *The European Physical Journal C* 63.2 (2009), pp. 189–285.

[128] Emilio Meschi et al. *Electron reconstruction in the CMS electromagnetic calorimeter*. Tech. rep. CERN-CMS-NOTE-2001-034, 2001.

[129] Robert Andrews Millikan. "On the elementary electrical charge and the Avogadro constant". In: *Physical Review* 2.2 (1913), p. 109.

[130] Kimball A Milton. "Theoretical and experimental status of magnetic monopoles". In: *Reports on Progress in Physics* 69.6 (2006), p. 1637.

[131] F. Muheim. "Week interaction, 2006, Particle physics lectures". In: *University of Edinburgh, UK* (October 2017).

[132] Bastien Luca Muster. *Search for exotic massive long-lived particles decaying semileptonically in the LHCb detector*. Tech. rep. EPFL, 2015.

[133] K Nakamura, C Amsler, Particle Data Group, et al. "Particle physics booklet". In: *Journal of Physics G: Nuclear and Particle Physics* 37.7A (2010), p. 075021.

[134] S Orito et al. "Search for supermassive relics with a 2000-m 2 array of plastic track detectors". In: *Physical review letters* 66.15 (1991), p. 1951.

[135] LM Pant. "Resistive Plate Chambers for the RE4 upgrade of the CMS endcap system". In: *Journal of Instrumentation* 7.10 (2012), P10025.

[136] CPDG Patrignani et al. "Review of particle physics". In: *Chin. Phys.* 40 (2016), p. 100001.

[137] Y Pestov et al. "A spark counter with large area". In: *Nucl. Instr. & Meth* 93 (1971), p. 269.

[138] Yu N Pestov and GV Fedotovich. *A picosecond time-of-flight spectrometer for the vepp-2m based on local-discharge spark counter*. Tech. rep. 1978.

[139] DA Petyt, CMS collaboration, et al. "Mitigation of anomalous APD signals in the CMS electromagnetic calorimeter". In: *Journal of Physics: Conference Series*. Vol. 404. 1. IOP Publishing. 2012, p. 012043.

[140] David A Petyt, CMS collaboration, et al. "Anomalous APD signals in the CMS Electromagnetic Calorimeter". In: *Nuclear Instruments and Methods in Physics Research Section A: Accelerators, Spectrometers, Detectors and Associated Equipment* 695 (2012), pp. 293–295.

[141] Antonio Pich. “The Standard model of electroweak interactions”. In: *arXiv preprint arXiv:1201.0537* (2012).

[142] James Pinfold et al. *Technical design report of the moedal experiment*. Tech. rep. 2009.

[143] JL Pinfold et al. “A Search for highly ionizing particles produced at the OPAL intersection point at LEP”. In: *Physics Letters B* 316.2-3 (1993), pp. 407–411.

[144] H David Politzer. “Reliable perturbative results for strong interactions?” In: *Physical Review Letters* 30.26 (1973), p. 1346.

[145] Alexander M Polyakov. “Particle spectrum in quantum field theory”. In: *30 Years Of The Landau Institute—Selected Papers*. World Scientific, 1996, pp. 540–541.

[146] John Preskill. “Magnetic monopoles”. In: *Annual Review of Nuclear and Particle Science* 34.1 (1984), pp. 461–530.

[147] PB Price et al. “Evidence for detection of a moving magnetic monopole”. In: *Physical Review Letters* 35.8 (1975), p. 487.

[148] Jonathan Pumplin et al. “New generation of parton distributions with uncertainties from global QCD analysis”. In: *Journal of High Energy Physics* 2002.07 (2002), p. 012.

[149] Loic Quertenmont et al. “Measurement of the hadronic activity in events with a Z and two jets and extraction of the cross section for the electroweak production of a Z with two jets in pp collisions at s= 7 TeV”. In: *Journal of High Energy Physics* 10.62 (2013), p. 101.

[150] RI Rabadan-Trejo et al. “Long-term performance and longevity studies of the CMS Resistive Plate Chambers”. In: *Journal of Instrumentation* 13.08 (2018), P08024.

[151] Arttu Rajantie. “Introduction to magnetic monopoles”. In: *Contemporary Physics* 53.3 (2012), pp. 195–211.

[152] Arttu Rajantie. “MAGNETIC”. In: *Physics Today* 69.10 (2016), p. 40.

[153] Alexander L Read. *Modified frequentist analysis of search results (the CL_{s} method)*. Tech. rep. Cern, 2000.

[154] *ROOT official website*. ”https://root.cern.ch/doc/master/classTH2.html”.

[155] Ronald R Ross et al. “Search for magnetic monopoles in lunar material using an electromagnetic detector”. In: *Physical Review D* 8.3 (1973), p. 698.

[156] Arpita Roy. “Science and the Large Hadron Collider: a probe into instrumentation, periodization and classification”. In: *Dialectical Anthropology* 36.3-4 (2012), pp. 291–316.

[157] LHC Run. “CMS Performance Note”. In: (2018).

[158] Ernest Rutherford and Hans Geiger. “An electrical method of counting the number of α-particles from radio-active substances”. In: *Proceedings of the Royal Society of London. Series A, Containing Papers of a Mathematical and Physical Character* 81.546 (1908), pp. 141–161.

[159] Abdus Salam. “Weak and electromagnetic interactions”. In: *Selected Papers Of Abdus Salam: (With Commentary)*. World Scientific, 1994, pp. 244–254.

[160] R Santonico and R Cardarelli. “Development of resistive plate counters”. In: *Nuclear Instruments and Methods in physics research* 187.2-3 (1981), pp. 377–380.

[161] Arka Santra. “Production of Magnetic Monopoles via Photon Fusion: Implementation in MadGraph”. In: *Multidisciplinary Digital Publishing Institute Proceedings*. Vol. 13. 1. 2019, p. 4.

[162] Fabio Sauli. *Gaseous radiation detectors: fundamentals and applications*. 36. Cambridge University Press, 2014.

[163] Julian Schwinger. “Magnetic charge and quantum field theory”. In: *Physical Review* 144.4 (1966), p. 1087.

[164] Julian Schwinger. “Sources and magnetic charge”. In: *Physical Review* 173.5 (1968), p. 1536.

[165] Yakov M Shnir. “Magnetic Monopole in Classical Theory”. In: *Magnetic Monopoles*. Springer, 2005, pp. 3–25.

[166] Yakov M Shnir. *Magnetic monopoles*. Springer Science & Business Media, 2006.

[167] “Silicon Strip Tracker Performance results 2018”. In: *CMS performance Note* (2018).

[168] Ravi Chand Singh and HS Virk. “Internal heating effect during electrochemical etching of Lexan polycarbonate”. In: *Nuclear Instruments and Methods in Physics Research Section B: Beam Interactions with Materials and Atoms* 29.3 (1987), pp. 579–582.

[169] Albert M Sirunyan, CMS collaboration, et al. “Particle-flow reconstruction and global event description with the CMS detector”. In: *JINST* 12.10 (2017), P10003.

[170] Torbjorn Sjostrand. “PYTHIA 8 status report”. In: *arXiv:0809.0303* 69 (2008).

[171] Torbjörn Sjöstrand, Stephen Mrenna, and Peter Skands. “A brief introduction to PYTHIA 8.1”. In: *Computer Physics Communications* 178.11 (2008), pp. 852–867.

[172] Torbjörn Sjöstrand, Stephen Mrenna, and Peter Skands. “PYTHIA 6.4 physics and manual”. In: *Journal of High Energy Physics* 2006.05 (2006), p. 026.

[173] J Skarha et al. *Construction of the CDF silicon vertex detector*. Tech. rep. Fermi National Accelerator Lab., Batavia, IL (United States), 1992.

[174] Are Strandlie and Rudolf Frhwirth. “Discrimination between different types of material in track reconstruction with a Gaussian-sum filter”. In: *IEEE transactions on nuclear science* 53.6 (2006), pp. 3842–3849.

[175] Masaharu Tanabashi et al. “Review of particle physics”. In: *Physical Review D* 98.3 (2018), p. 030001.

[176] Stefaan Tavernier. “Interactions of particles in matter”. In: *Experimental techniques in nuclear and particle physics*. Springer, 2009, pp. 23–53.

[177] Max Tegmark et al. “Cosmological parameters from SDSS and WMAP”. In: *Physical review D* 69.10 (2004), p. 103501.

[178] Ž Todorović. “Makrofol track detectors: Application in high energy nuclear physics”. In: *International Journal of Radiation Applications and Instrumentation. Part D. Nuclear Tracks and Radiation Measurements* 17.1 (1990), pp. 23–26.

[179] Michael Tytgat et al. “The upgrade of the CMS RPC system during the first LHC long shutdown”. In: *Journal of Instrumentation* 8.02 (2013), T02002.

[180] Tanmay Vachaspati and Manuel Barriola. “A new class of defects”. In: *Physical review letters* 69.13 (1992), p. 1867.

[181] Steven Weinberg. “A model of leptons”. In: *Physical review letters* 19.21 (1967), p. 1264.

[182] Edward Witten. “Dyons of charge eθ/2π”. In: *Physics Letters B* 86.3-4 (1979), pp. 283–287.

[183] Tai Tsun Wu and Chen Ning Yang. “Concept of nonintegrable phase factors and global formulation of gauge fields”. In: *Physical Review D* 12.12 (1975), p. 3845.

[184] H Wells Wulsin. “Performance of the Cathode Strip Chamber endcap muon detectors in Run 2”. In: *arXiv preprint arXiv:1510.08908* (2015).

[185] E Cerron Zeballos et al. “High rate resistive plate chambers”. In: *Nuclear Instruments and Methods in Physics Research Section A: Accelerators, Spectrometers, Detectors and Associated Equipment* 367.1-3 (1995), pp. 388–393.

ملخص الرسالة باللغة العربية

"البحث عن احادي القطب المغناطيسي بتجربة CMS في مصادم الهدرونات الكبير"

معظم القوانين والنظريات الطبيعية الاساسية توضح مفاهيم التفاعلات الأساسية لنشأه الكون ولقد بذل العلماء مجهود ضخم لتحقيق واثبات كثير من النظريات ومنها نظرية طبيعة التماثل وهي واحدة من النظريات الموحدة. يشغل تفكير كثير من العلماء التماثل بين الكهربية والمغناطيسية، وبالرغم من العمل الجاد الذي تم ومازال الا انه ما زال هناك جزء غير مكتمل الفهم والوضوح، ألا وهو وجود آحادي القطب المغناطيسي، وهو عباره عن جسيم اولي منفرد في فيزياء الجسيمات الأولية ويحمل احد القطبين المغناطيسيين دون الاخر.

لقد تنبأ بول ديراك عام ١٩٣١ بوجود آحادي القطب المغناطيسي، وهذا ان وجد فانه يحمل شحنه مغناطيسيه وسوف يساعد في تفسير النظرية الموحدة. وشحنة احادي القطب المغناطيسي كبيرة جدا (تعادل ما يقرب من ٦٨.٥ مرة شحنه الالكترون)، وايضا سوف يساعد في تفسير نظريه تكميم الشحنة، وتوحيد معادلات ماكسويل (الكهربية والمغناطيسية).

تقدم الرسالة شرح تفصيلي للبحث العلمي الذي تم في ما يقرب من خمس سنوات و في البحث عن احادي القطب المغناطيسي في تجربه الملف اللولبي الميوني المدمج بالمصادم الهدروني الكبير نستخدم طاقات عالية ١٣ تيرا الكترون فولت لتعجيل اشعة من البروتونات عكس الاتجاه للتمكن من حدوث تصادم بين الشعاعين و دراسة نواتج هذه التصادمات، و مناقشة المهام التي تم تنفيذها في التجربة خلال فترة زيارة المختبر الأوروبي لفيزياء الجسيمات الأولية (سيرن) ، و أيضا تفاصيل الاشتراك بتجربة اخري في المصادم الهدروني الكبيرLHC و هي تجربة صياد احادي القطب المغناطيسي MoEDAL .

معظم تجارب المصادم الهدروني الكبير LHC تبحث عن احادي القطب المغناطيسي بطرق كثيرة و مختلفة تبعا لطبيعة و تركيب الكواشف بكل تجربة و قد قمنا في نهاية هذا البحث بالمقارنة بين النتائج المختلفة الخاصة بهذه التجارب، مثل تجربه اطلس و غيرها.

تم استخدام برنامج Monte Carlo للمحاكاة خاص بتجربة CMS لإنتاج ملفات قابلة للدراسة وحساب كفاءتها باستخدام المتغيرات اللازمة للبحث للتمكن لإجراء نفس الخطوات للبيانات الحقيقة الناتجة من تصادم البروتونات داخل التجربة.

تم البحث عن احادي القطب المغناطيسي داخل الكواشف المختلفة الخاصة بالتجربة وذكرت التفاصيل المتعلقة بكل وسيلة. تتكون التجربة من ٤ كواشف رئيسية، اقرب كاشف لحدوث التصادم هو كاشف المسارات Tracker الخاصة بكل جسيم و هو هام جدا لتحديد نوع المسار و بداية تكوينه ، يليه كاشف الجسيمات الكهرومغناطيسية Electromagnetic Calorimeter (ECAL) و هو

مكون من حوالي ٧٥٨٤٨ كريستال للكشف عن الالكترونات و الفوتونات و الجسيمات المشابهة لهم. وقد ينتهي مسار الجسيم في واحد من هذه الكواشف ويفقد معظم طاقته الي ان يتم وقوفه تماما في إحدى هذه الكواشف و هذا ما يحدث في حاله الإلكترونات و الفوتونات. أما في حاله احادي القطب المغناطيسي فانه يتم تحديد مساره في كاشف المسارات ويتم أيضا تحديد وجوده في كاشف الجسيمات الكهرومغناطيسية من خلال صفاته المميزة عن أي جسيم اخر مشحون بشحنة كهربية، و ذلك للأسباب التالية:

١- مسار احادي القطب المغناطيسي ينحني في اتجاه z و ليس x-y كما هو الشائع حدوثه مع الجسيمات المشحونة الأخرى و هذا بسبب المجال المغناطيسي القوي في اتجاه موازي للانبوبة الضخمة التي تحتوي علي اشعة البروتونات و نقطة حدوث التصادم

٢- يفقد احادي القطب المغناطيسي كل طاقته في كريستالة واحده (في المنتصف) في حيز ٢٥ كريستال (٥ * ٥) و تسمي Cluster علي عكس الجسيمات الأخرى مثل الإلكترون فانه يفقد ٨٠ ٪ من طاقته في المنتصف في كريستاله واحدة و باقي طاقته يتم توزيعها علي باقي الكريستال المجاورة

قيمة الازدواج المغناطيسي Magnetic Coupling constant بين احادي القطب المغناطيسي و الفوتون اكبر ٤٧٠٠ مرة من ثابت الازدواج بين الالكترون و الفوتون ، لهذا السبب فان حساب قيمة المقطع المستعرض للتصادم Cross section في حالة احادي القطب المغناطيسي صعب الحصول عليه بالطرق المتعارف عليها. ولهذا السبب يجب اختيار نموذج مناسب لإنتاج العينات (الملفات) في برنامج المحاكاة.

تم اختيار النموذج الأفضل و هو Drell-Yan لإنتاج العينات الخاصة بجسيم احادي القطب المغناطيسي لأنه النموذج المستخدم في التجارب الأخرى و تم انتاج ١٠ عينات تبدأ من ٥٠٠ جيجا الكترون فولت حتي ٣٠٠٠ جيجا الكترون فولت بشحنة قدرها ١ شحنة ديراك.

بعد اجراء كل خطوات البحث و النتائج المشروحة في الرسالة، لم يرصد أي دليل واضح لجسيم آحادي القطب المغناطيسي (كما حدث في التجارب الأخرى) حتي الان بالإمكانيات الحالية للمصادمات الكبرى و لكن يمكن الحصول عليه بتحديث بعض الأجزاء و رفع قيمة الطاقة المستخدمة لتعجيل البروتونات و في هذه الحالة من المحتمل وجوده و لكن بكتلة اكبر من ٣٠٠٠ جيجا الكترون فولت.

أيضا تم المشاركة في المهام المتعلقة بكاشف اللوحات فائقة المقاومة والكشف عن كفاءة البيانات الحقيقة الناتجة من التصادم في النظام الميوني للتجربة، و إقامة بعض الاختبارات للأجزاء المختلفة لهذا الكاشف في فترة إغلاق تشغيل المصادم الهدروني الكبير لإجراء التحديثات و التصليحات

اللازمة لبعض الكواشف بعد فترة التشغيل الثانية الكبرى اللازمة لتهيئه كل تجارب المصادم لفترة تشغيل ثالثه في عام ٢٠٢١.

تشتمل الرسالة على ثماني فصول بالإضافة إلي فصل تاسع خاتمه يلخص نتائج ما تم.

الفصل الأول:

يتناول هذا الفصل مقدمة عامة عن الأسس والنظريات الأولية الخاصة بالدراسة المقدمة مثل نظرية النموذج المعياري ونظرية ما بعد النموذج المعياري.

الفصل الثاني:

يستعرض هذا الفصل شرح تفصيلي لنظرية آحادي القطب المغناطيسي وخصائص هذا الجسيم مع نبذه مختصره عن انواعه الأخرى في النظريات المختلفة وأيضا في التجارب الأخرى السابقة. يتناول أيضا هذا الفصل جزء هام جدا عن كيفية مرور الجسيمات المشحونة خلال المادة وبالأخص احادي القطب المغناطيسي.

الفصل الثالث:

يتضمن هذا الفصل شرح تفصيلي كامل للمصادم الهدروني الكبير LHC و تركيب تجرب CMS و الكواشف المختلفة التي يتم بداخلها الكشف عن الجسيمات الأولية الناتجة من تفاعل البروتونات بداخلها.

الفصل الرابع:

يشمل هذا الفصل الشرح الكامل لكاشف اللوحات فائقة المقاومة RPC الذي يوجد في النظام الميوني بتجربة CMS و المهام التي نفذتها طالبة الدكتوراه في الفترة من ٢٠١٦ – ٢٠١٩.

الفصل الخامس:

هذا الفصل يوضح تفصيلا للتفاعلات الناتجة من التصادمات المتتالية للبروتونات منذ بداية حدوث التصادم الي انتشار الجسيمات الناتجة في كواشف التجربة وأيضا يتم توضيح كيفية حفظ وتسجيل البيانات الناتجة من هذه التفاعلات. كما يتم شرح البرامج المستخدمة في المحاكاة لتكوين الملفات اللازمة التي تحتوي على كل معلومات هذه الدراسة.

الفصل السادس:

يشرح هذا الفصل كيفية تكوين الجسيمات طويله العمر و كيفية انتاج جسيم آحادي القطب المغناطيسي خطوة بخطوة في تجربه ال CMS مع شرح تفصيلي كامل عن النموذج المستخدم.

الفصل السابع:

يتناول هذا الفصل شرح تفصيلي عن خطه الدراسة وكيفية تطبيق كل خطوه علي البيانات الخاصة بالملفات التي تم تكوينها عن طريق برامج المحاكاة و أيضا علي البيانات الحقيقية الناتجة من تصادمات البروتونات التي حدثت في التجربة. كما يستعرض النتائج الخاصة بهذه الدراسة وكيفية حساب نهاية انتاج المقطع المستعرض Cross section production Limit عن طريق برنامج احصائي خاص بالتجربة Higgs combine tools software .

الفصل الثامن:

يتضمن هذا الفصل تجربه اخري من تجارب المصادم الهدروني الكبير و هي تجربه الصياد احادي القطب المغناطيسي MoEDAL و بالأخص ما قامت به طالبه الدكتوراه سنه ٢٠١٨ عند زيارتها للتجربة و ما ترتب عليه من نتائج، مع مقارنه بين الدراسات العملية الأخري بين تجارب المصادم الهدروني الكبير التي تبحث عن نفس الجسيم.

الفصل التاسع:

يحتوي هذا الفصل علي ملخص باللغة الانجليزية للنتائج المطروحة في الرسالة المقدمة.

جامعة بني سويف
كلية العلوم – قسم الفيزياء

جامعة أنتورب
كلية العلوم – قسم الفيزياء

البحث عن احادي القطب المغناطيسي بتجربة CMS في مصادم الهدرونات الكبير

اعداد

الباحثة / **مي محمد حسن عبد المجيد الصاوي**
مدرس مساعد – قسم العلوم الأساسية – كلية الهندسة بالجامعة البريطانية في مصر

رسالة مقدمة للحصول على درجة الدكتوراه المزدوجة
دكتوراة الفلسفة في الفيزياء - جامعة بني سويف ـ مصر
دكتوراة الفلسفة في الفيزياء - جامعة أنتورب ـ بلجيكا

الأستاذ الدكتور/ هاني صالح حمدي
أستاذ الفيزياء الذرية – قسم الفيزياء
كلية العلوم – جامعة بني سويف.

الأستاذ الدكتور/ ألبرت دي روك
أستاذ فيزياء الجسيمات الأولية – قسم الفيزياء
كلية العلوم – جامعه أنتورب - عضو المختبر الأوروبي لفيزياء الجسيمات (CERN).

الأستاذ الدكتور/ علي محمد خلف
أستاذ الفيزياء النظرية – قسم الفيزياء
كلية العلوم - جامعة الازهر

٢٠١٩